

Fundamental measurements and modeling of prescribed fire behavior in the naturally heterogeneous fuel beds of southern pine forests

RC-2640

Final Report

USDA Forest Service (USFS)

Pacific Southwest Research Station

Albany, CA

David R. Weise¹, Thomas H. Fletcher², Timothy J. Johnson³, WeiMin Hao⁴, Mark Dietenberger⁵, Marko Princevac⁶, Bret Butler⁴, Sara McAllister⁴, Joseph J. O'Brien⁷, E. Louise Loudermilk⁷, Roger D. Ottmar⁸, Andrew T. Hudak⁴, Akira Kato⁹, Babak Shotorban¹⁰, Shankar Mahalingam¹⁰, William E. Mell⁸, Charles R. Boardman⁵, Tanya L. Myers³, Stephen P. Baker⁴, Benjamin C. Bright⁴, Joseph C. Restaino⁸

¹ USFS PSW Research Station, ² Brigham Young University, ³ Pacific Northwest National Laboratory, ⁴ USFS RM Research Station, ⁵ USFS Forest Products Laboratory, ⁶ University of California – Riverside, ⁷ USFS Southern Research Station, ⁸ USFS PNW Research Station, ⁹ Chiba University, ¹⁰ The University of Alabama in Huntsville

The authors of this report are responsible for the content and accuracy. The opinions expressed in the report do not reflect any position of the U.S. Department of Agriculture, the Pacific Northwest National Laboratory, Brigham Young University, University of California-Riverside, The University of Alabama in Huntsville, or Chiba University.

Table of Contents

Table of Contents	i
List of Tables	iv
List of Figures.....	vi
List of Acronyms	xii
Keywords	xiii
Acknowledgements	xiii
Abstract.....	xiv
Executive Summary	xvi
1 Introduction	xvi
2 Objective.....	xvi
3 Technical Approach	xvii
Objective 0 – Fuel characterization	xix
Objective 1 – Measurement of pyrolysis products	xix
Objective 2 – Determining effects of heat transfer	xix
Objective 3 - High-fidelity physics-based modeling	xx
4 Results and Discussion	xx
Objective 1 – Measurement of pyrolysis products	xxi
Objective 2 – Determining effects of heat transfer	xxiii
Objective 3 – High-fidelity physics-based modeling.....	xxiv
5 Implications for Future Research	xxiv
1 Introduction	1
2 Objective.....	1
2.1 Specific hypotheses addressed by this project	1
3 Technical Approach	2
3.1 Background	3
3.2 Objective 0 – Fuel characterization.....	6
3.2.1 Solid fuel properties (FPL).....	7
3.2.2 Fuel beds used in wind tunnel fires	10
3.2.3 Sampling fuels at Ft. Jackson (field scale).....	11
3.3 Objective 1 – Measurement of pyrolysis products.....	18
3.3.1 High and low-heating rate experiments (BYU)	18
3.3.2 Optical absorption methods for detection of pyrolysis gases.....	20

3.3.3	Measurement of pyrolysis in a wind tunnel experiment	22
3.3.4	Measurement of pyrolysis in Ft. Jackson field burns.....	26
3.3.5	Compositional data analysis (CoDA).....	27
3.3.6	Summary statistics.....	28
3.4	Objective 2 – Determining effects of heat transfer	29
3.4.1	Bench-scale tests	29
3.4.2	Wind tunnel fires.....	30
3.4.3	Ft. Jackson field burns.....	32
3.5	Objective 3 – High-fidelity physics-based modeling.....	34
3.5.1	Gpyro & FDS bench-scale	34
3.5.2	FDS modeling of wind tunnel fires	37
3.5.3	Specific heat and FDS Vegetation module	38
4	Results and Discussion	39
4.1	Objective 0 – Fuel characterization.....	39
4.1.1	Solid fuel properties	39
4.1.2	Wind tunnel fuel beds	39
4.1.3	Fuels and fuel consumption at Ft. Jackson.....	39
4.2	Objective 1 - Measurement of pyrolysis products	52
4.2.1	High and low-heating rate experiments	52
4.2.2	Wind tunnel experiment.....	62
4.2.3	Linear mixed model	64
4.2.4	Effect of fuel bed.....	64
4.2.5	Canister composition of wind tunnel versus field.....	71
4.2.6	Static and dynamic FTIR measurements.....	76
4.2.7	Field pyrolysis measurements at Ft. Jackson	85
4.3	Objective 2 – Determining effects of heat transfer	91
4.3.1	Bench-scale tests	91
4.3.2	Wind tunnel fires.....	98
4.3.3	Ft. Jackson field burns.....	105
4.4	Objective 3 – High-fidelity physics-based modeling.....	135
4.4.1	Gpyro & FDS bench-scale	135
4.4.2	FDS wind tunnel scale.....	141
4.4.3	Specific heat and Vegetation module.....	145
5	Conclusions and Implications for Future Research/Implementation.....	148

6 Literature Cited	150
---------------------------------	------------

List of Tables

Table 1. Synopsis of experiments conducted at 3 scales to measure composition of pyrolysis gases associated with live plants common to the southeastern United States.	6
Table 2. Southern plant species used in pyrolysis experiments.....	8
Table 3. Summary of physical and chemical characteristics determined for southern fuels.....	10
Table 4. Schematic illustrating the construction of balances of groups of compositional parts of scientific interest determined by sequential binary partition. “+” denotes parts in numerator and “-” denotes parts in denominator of balance (an additional 74 balances not shown completed the full partition). PG denotes permanent gases (CH ₄ , CO, CO ₂ , H ₂).	28
Table 5. Kinetic parameters for materials used in Arrhenius multistep pyrolysis scheme.....	38
Table 6. Initial proximate and ultimate analysis of plant species [63].	40
Table 7. Plant physical dimensions [63].	41
Table 8. Density of a fresh leaf by species (g cc ⁻¹).	42
Table 9. Size measurements of plants used in wind tunnel pyrolysis experiment. Sample size of 40 plants per species.	42
Table 10. Properties and characteristics of wind tunnel and field fires burned to measure pyrolysis gases. Environmental conditions measured prior (less than 5 minutes) of start of experiment. Values rounded to appropriate number of significant digits.....	43
Table 11. Pre- and post-burn fuel loading samples by fuel class of two-year roughs in longleaf pine stands at Ft. Jackson, SC. Units are g m ⁻² . Eight sample points were measured per plot. Time – Pre = preburn loading, Post = postburn loading.	47
Table 12. Mean fuel loading by component (g m ⁻²) in longleaf pine forest at Ft. Jackson, SC burned to collect pyrolysis gas samples.....	50
Table 13. Estimated fuel consumption by component in longleaf pine forest at Ft. Jackson, SC..	50
Table 14. Moisture content (percent, dry-weight basis) prior to ignition by fuel category in longleaf pine stands at Ft. Jackson, SC.....	50
Table 15. Shrub fuel loading estimated by 2D destructive sampling and 3D nondestructive sampling (g m ⁻²).	52
Table 16. Summary of pyrolysis product yields for live species for four heating modes.	54
Table 17. Summary of light gas analysis during pyrolysis of live plants for three heating modes.	54
Table 18. Estimated harmonic mean (\bar{x}_H) and 95 percent confidence intervals for activation energy (kJ mol ⁻¹) for fresh and air-dried foliage from plants native to the southern U.S. Both classic and bootstrap estimates are reported.	59
Table 19. Summary statistics for pyrolysis and flaming combustion canisters collected during wind tunnel fires in fuel beds of longleaf pine needles with selected plants from the southeastern U.S. Concentration in ppm. Number of samples: flaming = 67, pyrolysis = 86.	66
Table 20. Variation array of gas composition for pyrolysis and flaming combustion measured in a wind tunnel. Mean log-ratio and log-ratio variance ($\hat{\tau}_{ij}$) for each pair of gases are found below and above the diagonal, respectively.	67
Table 21. Influence of fuel bed type and environmental variables on the composition of pyrolysis gases measured in a wind tunnel.....	70

Table 22. Custom balances of gases for wind tunnel and field experiments determined by sequential binary partition. “+” and “-” denote gases in the numerator and denominator, respectively.	70
Table 23. Pairwise comparisons of fuel bed effect on selected balances of pyrolysis gases measured in a wind tunnel. For each balance, fuel beds that did not differ are indicated by the same letter with the letter values ordered from smallest to largest. P-values adjusted to control for false discovery rate at 0.05 [132].	71
Table 24. Effects of air temperature, fire phase and location on composition of gases measured	72
Table 25. Pairwise comparisons of location and fire phase effects on selected balances of gases measured in canisters. For each balance, effects that did not differ are indicated by the same letter with the letter values ordered from smallest to largest. P-values adjusted to control for false discovery rate at 0.05 [132].	75
Table 26. Experimental wind tunnel fires measured by Bruker T37 spectrometer using static or dynamic mode.	77
Table 27. Mixing ratios for compounds identified using a Bruker T37 spectrometer in experimental wind tunnel fires in static mode. Values are ppm except H ₂ O and CO ₂ (% , pph)..	82
Table 28. Geometric mean, standard deviation, and 95% confidence interval for pyrolysis gases measured in wind tunnel using Bruker T37 spectrometer. Note that the geometric mean and standard deviation were calculated from the data after closure [120]. Pyrolysates are sorted in decreasing order based on mean relative amount.	85
Table 29. Emission ratios relative to CO (ppb/ppm) and standard deviations (1 σ) for the present study of the five compounds detected for the first time via IR and for three other previous biomass burning studies.	87
Table 30. Mixing ratios for compounds identified using a Bruker T37 spectrometer in experimental prescribed burns at Ft. Jackson, SC. Values are ppm.	88
Table 31. Geometric mean, standard deviation, and 95% confidence interval for pyrolysis gases measured in experimental prescribed burns in longleaf pine at Ft. Jackson, SC using Bruker T37 spectrometer. Note that the geometric mean and standard deviation were calculated from the data after closure [120]. Pyrolysates are sorted in decreasing order based on mean relative amount. Number of samples = 10.	89
Table 32. Partial list of gas-phase compounds detected by infrared absorption spectroscopy during the laboratory-scale and field-scale experiments conducted as part of SERDP project RC-2640.	90
Table 33. Mean maximum heat flux for each heat transfer mode and associated fluxes (expressed as proportion of maximum) and wind information observed at same time as maximum. Harmonic mean and 95 percent confidence interval shown. Fluxes in kW m ⁻² , wind velocity m s ⁻¹ , angle in degrees. Flow into face of sensor, away from face, upward and downward is 0°, 180°, 90° and 270°, respectively.	123
Table 34. Experimental and simulated rate of spread in longleaf pine needle fuel beds burned in a low speed wind tunnel.	145
Table 35. Data sets created by SERDP project RC-2640 to be archived in the Forest Service Research Data Archive (https://www.fs.usda.gov/rds/archive/).	165

List of Figures

Figure 1. Conceptual diagram of heat transfer mechanisms and processes in heterogeneous fuel beds for prescribed fires (adapted from [2]).	3
Figure 2. Schematic linking processes and activities/data to RC-2640 experimental and modeling work.	6
Figure 3. Specialized holder used for foliage samples in cone calorimeter.	9
Figure 4. Vertical stereo photographs of wind tunnel fuel bed used to provide 3D image.	11
Figure 5. Location of six experimental burn units at Ft. Jackson, SC. Background image illustrates individual tree crowns from the canopy height model interpolated from airborne laser scanning data at 0.5 m x 0.5 m resolution. Figure from [66].	12
Figure 6. Plot layout for prefire and postfire fuel measurements at the two 2017 burn units: 16D2 (left) and 16D1 (right).	13
Figure 7. Plot layout for the 2018 burn units: 24A7, 24B8, 16D1 and 16D5.	14
Figure 8. Forest floor pin plot layout.	15
Figure 9. 3D shrub fuel plots.	17
Figure 10. Flat-flame burner setup used to measure pyrolysis products resulting from heating southern wildland fuels at a high rate.	19
Figure 11. Schematic of programmable heater used for generating pyrolysis products from southern wildland fuels at a low heating rate.	20
Figure 12. Cartoon representation of generalized infrared spectrometer.	21
Figure 13. Measured IR spectrum (May 2018) and individual spectral contributions for the major components and associated residual with and without acrolein included in the fit.	21
Figure 14. Setup of wind tunnel canister sample points.	23
Figure 15. (a) Cartoon rendering of block layout for the extractive T37 spectrometer/gas cell with inlet tubing. The gas cell and FTIR system are shown as yellow and purple boxes, respectively. Also shown is the Quantum Cascade Laser system (blue); the laser system directly probed the flame. (b) Both systems on site at RFL.	24
Figure 16. Setup of 3 instruments used to measure composition of gaseous pyrolysis products in mixed fuel beds of longleaf pine needles and small shrubs.	26
Figure 17. Fuel bed composed of longleaf pine needles and <i>Lyonia lucida</i> plants. Sample probe to collect pyrolysis gases for the Bruker Tensor 37 is indicated by the arrow.	26
Figure 18. Gathering pyrolysis phase gas samples using an extractive wand coupled to a pump and gas canister (not seen) during prescribed burns at Ft. Jackson, SC, May 2018.	27
Figure 19. Flat-flame burner heating a pyrolyzing foliage sample.	29
Figure 20. Simple schematic of background oriented Schlieren configuration used to nonintrusively estimate the flow field surrounding pyrolyzing plants. ZD is the distance of the flame from the background noise pattern, ZB is the distance of the camera lens from the background, ϵy represents the deflection angle caused by the flame-generated distortion, L is the flame zone width, f is the focal length of the camera, $\Delta y'$ represents displacement in the camera sensor plane and Δy represents displacement in the background plane.	30
Figure 21. Sensor setup to measure plant mass loss on an electronic scale with total and radiant heat fluxes using Schmidt-Boelter type thermopiles (grey cylinders).	31
Figure 22. Type K thermocouple tree designed to measure air temperature around a single plant in the wind tunnel experiments.	31
Figure 23. Air temperature thermocouples placed in a subset of the wind tunnel experiments. The	

blue circles represent thermocouples placed in the fuel bed and the brown circle represents the plant scale.....	32
Figure 24. Example of Fire Behavior Package (left) and Insitu Video Camera package (right) deployed to measure horizontal heat fluxes and record visible flame and smoke movement in wildland fires.	33
Figure 25. Boom-mounted IR camera used to measure shrub leaf temperatures during prescribed burns at Ft. Jackson, SC.....	34
Figure 26. Isometric view of the computational domain with the vertically oriented solid fuel over the flat flame burner.....	36
Figure 27. Multistep scheme to model pyrolysis in longleaf pine needle fuel beds using the Fire Dynamics Simulator	38
Figure 28. Prefire coverage of predominantly sparkleberry shrubs in (a) burn unit 16D1 and (b) burn unit 16D2 two years after most recent burn.	42
Figure 29. Natural logarithm relations between measured shrub fuel bulk density and voxel density derived from TLS	51
Figure 30. Example of mass loss over time during fast pyrolysis for live and air-dried <i>Ilex glabra</i> leaves. Air-dried denoted “dead plant”.....	52
Figure 31. Comparison of pyrolysis product yields vs. final temperature for longleaf pine litter obtained in a pyrolyzer (solid lines) at 0.5 °C/s and from the flat flame burner system (dashed lines) under different modes of heating (radiation only (550 °C), convection only (750 °C), and radiation plus convection (800 °C))......	53
Figure 32. Light gas species observed during pyrolysis of live sparkleberry plotted as a function of final temperature.....	54
Figure 33. Distribution of tar compounds for the fast pyrolysis of longleaf pine.	55
Figure 34. Mole percent phenol in tar during pyrolysis of 14 live plant species. Error bars represent the 95% confidence interval.....	56
Figure 35. Distribution of functional groups in tar for pyrolysis of live longleaf pine foliage. ...	57
Figure 36. Harmonic mean and bootstrapped 95 percent confidence interval for activation energy measured in a pyrolyzer for common plant species from the southern U.S.	58
Figure 37. Distribution of pyrolysis rates as a function of conversion based on the KAS method for all live plant species at 300 °C.	60
Figure 38. DTG and TG curves for live water oak resulted from experimental data and multiple-reaction DAEM model in heating rates of 10, 20, and 30 °C min ⁻¹	61
Figure 39. Observed mean composition of canister samples from wind tunnel and field fires in longleaf pine fuel beds in original units.....	63
Figure 40. Observed mean composition of samples of pyrolysis and flaming combustion gases in wind tunnel fires by chemical type after closure.	65
Figure 41. Deviations of fitted geometric mean to overall geometric mean (in log-ratio scale) for fuel beds organized by individual gas (upper) and for individual gases organized by fuel bed (lower left), and differences in mean balances (group versus overall) between gases for fuel beds (lower right).	69
Figure 42. Effect of location on gas composition of pyrolysis samples collected in a wind tunnel and in prescribed burns in longleaf pine stands located at Tall Timbers Pebble Hill Plantation and Fort Jackson in the southeastern U.S. Composition expressed as deviation (log-ratio scale) from overall geometric mean by gas. Values below zero indicate gas concentrations less than the overall mean and values above zero indicate greater concentrations.	73

Figure 43. Observed relative concentration of gases in canister samples analyzed by GCMS from pyrolysis and flaming combustion in wind tunnel and field burns in longleaf pine fuel beds.	74
Figure 44. Observed mean composition of samples of pyrolysis and flaming combustion gases in wind tunnel fires by chemical type after closure.	76
Figure 45. Measured and scaled reference spectra for C_2H_2 and naphthalene, and corresponding residuals with and without naphthalene included in the fit for the a) original spectrum collected at 0.6 cm^{-1} and the deresolved spectra at b) 1 cm^{-1} , c) 2 cm^{-1} , and d) 4 cm^{-1} . The reference spectra for CO_2 , HCN and H_2O are not shown (HCN was not included in fit when the resolution was 4 cm^{-1} ; for resolutions 1, 2 and 4 cm^{-1} , H_2O was not included in the fit when naphthalene was removed from the fit). Spectra are offset for clarity.	78
Figure 46. Burn 86 time-resolved measured IR spectra (November 2018) for regions $1150\text{--}800\text{ cm}^{-1}$ and $2250\text{--}2000\text{ cm}^{-1}$ respectively. The top series of spectra show the presence of ethene (C_2H_4), propene (C_3H_6) and nitrous acid ($HONO$) become more evident during the pyrolysis phase of the burn and reach their highest mixing ratios as seen in scans 15-20, and ammonia (NH_3) at its highest mixing ratio during the flaming and smoldering phases of the fire. The bottom series of spectra depicts the progression of the burn relative to carbon monoxide (CO), with mixing ratios increasing and peaking during the pyrolysis phase while decreasing during the flaming portion of the flame. Spectra were taken at 1 cm^{-1} resolution every 2.5 seconds.	80
Figure 47. (a) MWIR absorption spectrum shortly after ignition (10:40:41.9 - 0.1 s average). Concentrations from the fit Figure 13 are 893 ppm CO_2 , 10 ppm CO , 2690 ppm H_2O , and $T_{fit}=314\text{ K}$. (b) LWIR absorption spectrum (10:39:59.3 - 0.1 s average) showing plume from denatured alcohol used to ignite the flame. Concentrations from the fit are 6 ppm $MeOH$ and 72 ppm $EtOH$, and $T=298\text{ K}$ (fixed). For both (a) and (b), the top panel (left axis) shows the experimental absorbance (black) and the best fit (orange). The top panel (right axis) shows selected library spectra, offset for clarity. The bottom panel shows the fit residuals.	81
Figure 48. Relative concentrations of gases measured using FTIR in wind tunnel (RFL) and field burns (FJSC). RFL samples are known to be pyrolysis samples. FJSC samples have not yet been classified as flaming or pyrolysis samples using logistic regression as in section 4.2.5.	91
Figure 49. Fuel surface temperatures for (a) radiation-only (inkberry), (b) convection-only (inkberry) and (c) combined convection and radiation (wax myrtle) heating modes ([125]).	92
Figure 50. Mass loss over time for live foliage samples heated by convection only in a flat-flame burner.	94
Figure 51. Mass loss over time for live foliage samples heated by convection and radiation in a flat-flame burner/radiant panel apparatus.	96
Figure 52. Influence of heating mode on selected balances of pyrolysis gases. Average difference for a balance is the difference between mean value for heating mode and overall mean value. Average difference less than 0 indicates either relatively less in the numerator or relatively more in the denominator; positive values, vice-versa.	97
Figure 53. Example of long wave infrared imagery collected in experimental fires in wind tunnel experiments in fuel beds of longleaf pine needles and small shrubs. Dark circles indicate location of plants.	98
Figure 54. Time trace of surface fuel temperature below FTIR sample probe determined from FLIR thermal camera. Fuel bed composed on longleaf pine needles and small shrubs.	99
Figure 55. Example of mass and mass loss rate of a single plant in a fuel bed of longleaf pine needles measured in a wind tunnel experiment.	100
Figure 56. Summary of mass and mass loss data for different fuel bed configurations of longleaf	

pine needles with nursery shrubs. Treatment number refers to the combination of plant species and wind speed.....	100
Figure 57. Example of temperatures measured by thermocouple tree array (Figure 22) in wind tunnel fires.	101
Figure 58. Total and radiant heat flux measured by sensors placed below the fuel bed upwind and downwind of mass loss plant in a wind tunnel experiment (Figure 21).	102
Figure 59. Convective heat flux estimated using Background-Oriented Schlieren methods for 4 replicate burns in a wind tunnel.	103
Figure 60. Maximum (top) and median (bottom) convective heat fluxes estimated using Background-Oriented Schlieren for all fuel bed configurations for experimental wind tunnel fires.	103
Figure 61. Relationship between eddy diffusivity against convective Froude number.	104
Figure 62. Relationship between convective heat flux and convective heat Froude number.	105
Figure 63. Fire behavior package 6 set up for plot 24Bt.	106
Figure 64. Fire behavior package 6 during burn in 24Bt. This package saw a peak total heat flux of 10.9 kW m^{-2} , peak air temperature of 423°C , and registered a peak wind speed of 3 m s^{-1} . .	107
Figure 65. Fuel loading on plot 24Bs. A peak total heat flux of 30 kW m^{-2} was registered for this burn along with a peak air temperature of 1042°C and a peak horizontal wind speed of 4 m s^{-1}	108
Figure 66. An example of fuel loading in plot 24As.	109
Figure 67. Fire behavior in 24As where a peak total heat flux value of 17.5 kW m^{-2} was registered along with a peak air temperature of 954°C and peak wind speed of 4.5 m s^{-1}	110
Figure 68. A sensor package set up to monitor fire behavior in the reference plots of plot 24At.	111
Figure 69. Fire behavior in the reference plots of plot 24At. Instruments registered a peak total heat flux of 19.3 kW m^{-2} , a peak air temperature of 714°C , and a peak horizontal wind speed of 3.6 m s^{-1}	112
Figure 70. Instrumentation set up to monitor fire behavior in plot 16D5 reference plots.	113
Figure 71. Fire behavior in plot 16D5 reference plots. A peak total heat flux of 10.9 kW m^{-2} was registered for burn 5 along with a peak air temperature of 511°C , peak horizontal wind speed of 3.8 m s^{-1}	114
Figure 72. Fuel loading in plot 16D6. A peak total heat flux of 12.4 kW m^{-2} was registered along with a peak air temperature of 631°C and peak horizontal wind speeds of 4 m s^{-1}	115
Figure 73. Fuel loading for plot 16D1. A peak total heat flux of 17.8 kW m^{-2} was registered along with a peak air temperature of 930°C and peak horizontal wind speeds of 4.3 m s^{-1}	116
Figure 74. Instantaneous horizontal and vertical air flow measured by FBPs in low intensity prescribed burns in longleaf pine at Ft. Jackson, SC and Tall Timbers Pebble Hill Plantation. Note that positive horizontal flow is into the FBP and negative vertical flow is parallel to the gravity vector.	117
Figure 75. Instantaneous air temperature measured with FBPs in low intensity prescribed burns in longleaf pine at Ft. Jackson, SC, and Tall Timbers Pebble Hill Plantation.	118
Figure 76. Maximum, arithmetic mean and minimum heat fluxes measured during experimental prescribed fires in longleaf pine at Ft. Jackson, SC.	119
Figure 77. Components of air flow and air temperatures measured during experimental prescribed fires in longleaf pine at Ft. Jackson, SC.	120
Figure 78. Heat fluxes measured using Fire Behavior Packages in prescribed burns in longleaf	

pine at Ft. Jackson, SC, and Tall Timbers Research Station Pebble Hill Plantation. Harmonic mean with 95 percent confidence interval shown.	122
Figure 79. Frequency distribution of wind speed (m s^{-1}) into sensor by direction categories summarized by plot from FBPs deployed in experimental burns in longleaf pine at Ft. Jackson, SC and Tall Timbers Pebble Hill Plantation shown as bar charts.	125
Figure 80. Frequency distribution of wind speed (m s^{-1}) into sensor by direction categories from FBPs deployed summarized by experimental burns in longleaf pine at Ft. Jackson, SC and Tall Timbers Pebble Hill Plantation shown in polar coordinates.	126
Figure 81. New heat flux package consisting of radiometer, a disk anemometer and thermocouples deployed in experimental prescribed burns in longleaf pine at Ft. Jackson, SC.	127
Figure 82. Flame ionization detector used to estimate flame residence time buried in longleaf pine forest floor at Ft. Jackson, SC. Red arrow indicates detector.	127
Figure 83. Uncorrected radiant flux measured in experimental prescribed fires in longleaf pine at Ft. Jackson, SC with new heat flux (HF) package.	128
Figure 84. Flame residence time estimated by new flame ionization detector in experimental prescribed fires in longleaf pine, Ft. Jackson, SC.	129
Figure 85. Location (red circles) of foliage sampled for leaf temperature during prescribed burn 24A in longleaf pine at Ft. Jackson, SC.	130
Figure 86. Location (red circles) of foliage sampled for leaf temperature during prescribed burn 24A in longleaf pine at Ft. Jackson, SC.	130
Figure 87. LWIR (7-14 μm) false color image of leaf temperature sampling locations during prescribed burn 16D1 in longleaf pine at Ft. Jackson, SC. Purple indicates high water content foliage, orange indicates sun flecks in litter, lavender is shaded litter.	131
Figure 88. IR image of leaf temperature sampling locations during prescribed burn 16D5 in longleaf pine at Ft. Jackson, SC.	132
Figure 89. IR image of leaf temperature sampling locations during prescribed burn 16D6 in longleaf pine at Ft. Jackson, SC.	133
Figure 90. Example thermal image of plot 24A. The gas sampling wand is visible in the lower left.	134
Figure 91. Shrub leaf temperatures estimated from IR images during experimental prescribed burns in longleaf pine at Ft. Jackson, SC.	135
Figure 92. Time histories of (a) mass normalized by initial mass and (b) mass loss rate. Exp #1-4 are for experiments performed on four manzanita leaves with unspecified FMCs [148]. FMC 40%/76%/120% are the three FMCs modeled in the study.	136
Figure 93. Color contours of oxygen mass fraction at $t=11.5$ s for a simulated horizontal manzanita leaf heated in a flat flame burner.	137
Figure 94. Time evolution of vertically oriented leaf normalized mass. Dotted lines indicate 95% confidence intervals for experimental data [219].	138
Figure 95. Time evolution of the leaf mass normalized by the leaf initial mass for (a) convection-only and (b) combined convection and radiation heating modes in the previous experiments [46] (symbolized dashed line) and the current computations (solid line).	139
Figure 96. (a) Temperature; (b) vertical (z-component) velocity; and (c) oxygen volume fraction versus y at $x=0\text{m}$ and $z=0.045\text{m}$ in the gas domain surrounding the leaf at $t = 6\text{s}$ for the combined heating modes of convection and radiation. The thick line in the middle indicates the horizontal position of the leaf.	140
Figure 97. Profiles of evaporation (a,b), liquid moisture mass fraction (c,d) and temperature (e,f)	

for an external radiant flux of 40 kW m^{-2} . FMC = 26 and 100 %, left and right, respectively. EM is equilibrium model and AM is Arrhenius model.	141
Figure 98. Contour plot of temperature at different time steps estimated using a single step pyrolysis scheme in a longleaf pine fuel bed under no wind conditions.	142
Figure 99. Comparison of measured fuel bed surface temperature with simulations using single step and multi-step pyrolysis schemes for longleaf pine needle fuel beds burned under 3 wind velocities (none, 0.44 m s^{-1} , 1 m s^{-1}) in a wind tunnel.	143
Figure 100. Temperature contours in a vertical plane in the wind tunnel centerline for single and multistep pyrolysis schemes for 3 wind velocities: (a) 0 m s^{-1} , (b) 0.44 m s^{-1} , (c) 1 m s^{-1}	143
Figure 101. Simulated flame zone width (depth) along the fire front for single and multi-step pyrolysis schemes.	144
Figure 102. The mass loss with time for different wind speeds a): single-step reaction. b): multi-step reaction.	145
Figure 103. Specific heat capacity measured in a DSC for foliage from 11 species of plants native to the southeastern U.S. [163]	146
Figure 104. Pyrolysis emissions: a) trace gases b) major mass flows derived.	147

List of Acronyms

ASTM	American Society for Testing and Materials
BOS	Background Oriented Schlieren
BYU	Brigham Young University
CFD	Computational fluid dynamics
CI	Confidence interval
CoDA	Compositional data analysis
DAF	Dry ash free
DoD	Department of Defense
EGA	Evolved gas analysis
ER	Emission ratio
FBP	Fire Behavior Package
FDS, WFDS	Fire Dynamics Simulator, Wildland extension of the Fire Dynamics Simulator
FFB	Flat flame burner
FMC	Fuel moisture content (mass of water on dry mass basis)
FPL	Forest Products Laboratory (USFS Madison)
FTIR	Fourier Transform InfraRed spectroscopy
GA	Genetic algorithm
GC	Gas chromatography or chromatograph
Gpyro3D-FDS	Linked Gpyro3D and Fire Dynamics Simulator models
HRR	Heat release rate
IVC	In situ Video Camera
JFSP	Joint Fire Science Program
KBr	Potassium bromide
LES	Large eddy simulation
LiDAR	Light Detection and Ranging
LWIR	Longwave infrared (7.5 to 13.5 μm)
MCE	Modified combustion efficiency
MCT	Mercury cadmium telluride
MLR	Mass loss rate
MS	Mass spectrometry or spectrometer
OPAG-22	Open Path Gas Analyzer
PI	Principal Investigator
PM	Particulate matter
PNNL	Pacific Northwest National Laboratory
PPM	Parts per million
RFL	Riverside Fire Laboratory (USFS Riverside)
SERDP	Strategic Environmental Research and Development Program
SIP	Small Instrumented Plot
SON	Statement of Need
TCD	Thermal conductivity detector
TGA	Thermal gravimetric analyzer
TLS	Terrestrial lidar scan

T37	Bruker Tensor 37 FTIR Spectrometer
UAH	The University of Alabama in Huntsville
UAS	Unmanned autonomous system
UCR	University of California – Riverside
USDA	U.S. Department of Agriculture
USDI	U.S. Department of the Interior
USFS	U.S. Forest Service

Keywords

pyrolysis, combustion, activation energy, longleaf, Pinus, FTIR, spectroscopy, CO, CO₂, CH₄, phenol, trace gases, Vaccinium, heat flux

Acknowledgements

This complex project required the support provided by the partner institutions including the fire management staff at Ft. Jackson, SC. The support provided by the technical staffs at US Forest Services labs in Seattle, WA, Moscow, ID, Missoula, MT, Madison, WI, Athens, GA, and Riverside, CA was integral to accomplishing this task. The work performed by the technical staffs and students at Brigham Young University, The University of Alabama in Huntsville, University of California – Riverside, University of Washington, Chiba University and the Pacific Northwest National Lab utilized equipment and produced data critical to this project. The financial support provided by the business management staffs at all institutions was invaluable to the conduct and accountability of the project. The financial support provided by the SERDP program through project RC-2640 made this project possible. The efforts of all personnel, likely numbering over 100 individuals, in making this project a success is acknowledged and greatly appreciated. Lastly, the guidance and mentoring on compositional data analysis provided to the P.I. by Dr. Javier Palarea-Albaladejo, Biomathematics and Statistics Scotland and Department of Computer Science, Applied Mathematics and Statistics, University of Girona, Girona, Catalonia, Spain, greatly improved the statistical analyses of the various compositional data created by this project.

Abstract

The Department of Defense (DoD) uses prescribed fire to manage millions of acres across a variety of ecosystems in the United States to accomplish multiple objectives. To properly implement prescribed fire and limit potential escapes, an improved understanding is needed of fundamental science questions related to combustion and fire propagation in natural fuel beds that are a mix of both live and dead fuels. This study examined aspects of pyrolysis, the thermal breakdown of solid wildland fuels to produce the gases that combust resulting in fire. To improve the understanding and modeling capability of pyrolysis in physics-based fire spread models, three goals were identified: 1) provide more detailed description of pyrolysis and the evolution of its products for a greater variety of southern fuels than is currently known, 2) determine how convective and radiative heat transfer from flames to live fuel particles influenced pyrolysis and ignition at laboratory and field scales and 3) gain more detailed insight into pyrolysis, combustion and heat transfer processes in wildland fire spread through the use of high-fidelity physics-based models.

These goals were achieved by accomplishing three technical objectives (tasks) which were supported by a 0th foundational task: 0) characterize the physical, chemical, compositional and spatial structure of wildland fuels used in this project, 1) characterize pyrolysis products by measurement of a variety of live and dead foliar fuels in laboratory and small-scale field experiments, 2) determine the effects of convective and radiant heat transfer on pyrolysis and 3) perform high-fidelity physics-based modeling of pyrolysis for bench-scale and wind tunnel experiments. Physical and chemical properties were determined using a variety of analytical methods. Wildland fuels were described using a variety of traditional 2D and innovative 3D sampling methods using LiDAR and terrestrial laser scanning. Pyrolysis gases were generated from single leaves at bench-scale by slow heating in pyrolyzer and fast heating using combinations of convective and radiant heating in a flat-flame burner. Pyrolysis gases from fuel beds of live and dead fuels were measured in a wind tunnel and in the field in small, prescribed burns at Ft. Jackson, SC by capturing gases in canisters or in real-time using nonintrusive FTIR spectroscopy. Bench scale, wind tunnel and field gases were identified using GC/MS and GC/FID. Wind tunnel and field gases were also identified using static and dynamic (time-dependent) gas collection and identification using FTIR spectroscopy. Data were analyzed using a variety of statistical methods. Modeling of bench-scale pyrolysis experiments was accomplished using the GPYRO model coupled with the FDS model. Wind tunnel experiments were modeled using the FDS model.

Composition of foliar fuels was found to be appreciably different from wood. 3D description of fuel beds provided more information for physics-based fire models than traditional 2D sampling. The statistical field of compositional data analysis was applied to pyrolysis and combustion gas mixtures for the first time. In the bench-scale measurements, the relative amounts of pyrolysis gases were affected by moisture content and heating mode (convective versus radiant). First successful measurement and description of pyrolysis gases under realistic fire conditions was accomplished, both in the wind tunnel and in the low intensity prescribed burns at Ft. Jackson. Fuel heating rates, maximum fuel temperatures and fuel conditions were found to be similar for the wind tunnel fires and the prescribed burns. The relative amounts of pyrolysis gases differed, however, between the wind tunnel and the field experiments. Dynamic changes in gas composition measured by FTIR were correlated with fire phase determined by IR camera in wind tunnel experiments. The GPYRO model was modified substantially to improve modelling of evaporation from foliar fuels. Replacement of an Arrhenius-based model with an equilibrium

model for evaporation had greater impact on high fuel moisture fuels. Drying dynamics from the equilibrium model is more consistent with the physics of evaporation. Modeling revealed that fluid dynamics play a distinctive role in evaporation, pyrolysis, ignition, combustion and burnout behavior of leaves. Fluid flow was influenced by leaf orientation (horizontal or vertical). The addition of radiative heating to a combined heat flux reduced the time that a fuel particle lost 50 percent of initial mass by only a third suggesting that convective heating had a greater impact on pyrolysis and burning of an individual leaf.

The primary benefits of the project are the information and modeling related to pyrolysis of intact wildland fuels. Prior pyrolytic work strove to minimize the effects of heat transfer and fuel moisture on pyrolysis. The present study showed that heat transfer mode and fuel moisture are both important factors that should be considered when modeling pyrolysis in modern physics-based fire models. Similarly, results from laboratory fires under standard conditions differed from field measurements. Comparison of results under standard conditions with bench-scale results in oxidizing and non-oxidizing environments will be limited to a small subset of the measured gases and is outside the scope of this project. Improvements to the modeling of evaporation and a more complex pyrolysis and combustion framework in GPYRO-FDS better model these processes; however, the impact of these improvements on fire spread predictions is unknown and needs to be explored in future work to determine if the improvements warrant the additional complexity. The introduction of compositional data analysis, a branch of statistics thus far overlooked by the wildland fire community and a significant outcome of this project, has the potential to provide scientific results based on statistical analyses suited to the nature of many types of wildland fire data describing the composition of things.

Executive Summary

1 Introduction

The Department of Defense (DoD) uses prescribed fire to manage millions of acres across a variety of ecosystems in the United States to 1) prepare sites for military training, 2) reduce hazardous fuel, and 3) obtain fire's ecological benefits. In the southern U.S., many DoD lands contain stands of longleaf and loblolly pine with a variety of understories including wiregrass, palmetto-gallberry, and turkey oak that generally burn at relatively low fire line intensities (heat release rates). Installations also manage dwarf pitch pine, sand pine, and pond pine stands which can burn with high intensity. All of these fuel bed types are 1) heterogeneous in nature, 2) contain multiple fuel components, and 3) contain a mixture of live and dead fuels, all important characteristics influencing the combustion process and fire propagation. To properly implement prescribed fire and limit potential escapes, an improved understanding is needed of those fundamental science questions related to combustion and fire propagation in heterogeneous fuel beds that are a mix of live and dead fuels.

2 Objective

In the U.S. currently, widely used operational fire behavior models are based on data from homogenous beds of dead fuels and associated theory. However, most prescribed fires at DoD installations occur in heterogeneous fuel beds with a mixture of live and dead biomass, under differing conditions. The objective of this project was to address several fundamental questions to improve our understanding and modeling capability of fire propagation in natural fuel beds including

- 1) detailed description of pyrolysis and the evolution of its products for a greater variety of southern fuels than is currently known,
- 2) how convective and radiative heat transfer from flames to live fuel particles influences pyrolysis and ignition at laboratory and field scales, and
- 3) more detailed insight into pyrolysis, combustion and heat transfer processes in wildland fire spread through the use of high-fidelity physics-based models.

This project thus directly responded to SON RCSON-16-02 "Improved Understanding of Wildland Fire Combustion Processes for Department of Defense Management Ecosystems" and all 4 of the SON objectives by focusing on natural fuel beds managed with prescribed fire in southern pine forests. While the SON included fine to landscape scale, RC-2640 focused on scale ranging from fine to small-scale field experiments. The project increased knowledge of open combustion processes at particle (0.001 to 0.01 m) to fuel bed (1-10s of m²) scales (SON Objective 1) by measuring the mechanisms of pyrolysis, ignition, and heat transfer (SON Objective 3) in several live fuels and a single dead fuel at particle and fuel bed-scales (SON Objective 2). The role of fuel characteristics (live and dead, structure and composition) on heat transfer, pyrolysis, and ignition were examined experimentally in the lab and in the field (SON Objective 3). Physics-based modelling of fires was conducted for the lab experimental setups (SON Objective 4) with a focus on pyrolysis and ignition in live shrub canopies. An improved understanding of pyrolysis and how it is affected by heat transfer in heterogeneous fuel beds will eventually lead to an improved ability to predict fire behavior such that managers can more readily achieve desired fire effects with prescribed burning.

The project was structured to address several specific null hypotheses related to the objectives of

the study. Data and modeling were collected and performed to test these hypotheses. Most of the hypotheses were tested during the project and the results reported. The data are available to test the H_5 hypothesis.

H₁: Composition and concentrations of gaseous and tar pyrolysis products do not differ between southern species; a common pyrolysis scheme can thus be used in models.

H₂: The rate at which foliage is heated does not affect the composition and concentrations of dominant gaseous pyrolysis or tar pyrolysis products.

H₃: Heat transfer mechanisms (radiation and convection) do not affect the composition and concentrations of dominant gaseous pyrolysis products.

H₄: The water content of foliage does not affect the composition and concentrations of dominant gaseous and tar pyrolysis products.

H₅: Laboratory-scale measurements of the production of gaseous pyrolysis products under controlled conditions cannot be correlated with field-scale measurements under prescribed fire conditions.

H₆: Inclusion of an advanced pyrolysis mechanism for live and dead wildland fuels does not improve fire behavior predictions by the high-fidelity physics-based models.

H₇: Improving the evaporation mechanism for moisture content in wildland fuels does not improve fire behavior predictions by the high-fidelity physics-based models.

H₈: Simulation of pyrolysis and ignition of wildland fuels is not improved with 3D fuels characterization and can be just as effectively simulated in 2D.

H₉: Foliar fuels are not different from solid wood and can be modelled using parameters associated with wood.

3 Technical Approach

Laboratory and field experiments focused on pyrolysis coupled with sufficient description of fuel characteristics and heat transfer mechanisms and physics-based modeling were used to improve our understanding of combustion processes in mixed (heterogeneous) fuel beds managed with prescribed fire on DoD installations. Our conceptual model (Figure 1) of the physics and chemistry of fire spread in heterogeneous fuel beds builds upon previous formulations. The formulations generally included the heat transfer mechanisms listed. Conduction, while important when fuel particles physically contact, was not focused on because it is a relatively slow mechanism in wildland fuels. Treatment of pyrolysis varies somewhat between the formulations ranging from assuming Arrhenius-type production of pyrolysates to simply assuming a higher heat content for the fuel. Dead fuels dominate fire spread in many fuel types and thus dominate operational models; however, live fuels are an important contributor in many forested systems where prescribed burning is routinely used. Our approach included using well-controlled, traditional methods such as thermogravimetric analysis and wildland fire flames to study the thermal decomposition (pyrolysis) of live fuels and the resulting gaseous products.

Pyrolysis is strongly affected by the solid fuel particle temperature which is a function of heat transfer from the flame to the unburnt live fuels. We determined the effects of various heating modes on the production of pyrolysates for live southern fuel types. Pyrolyzate production is a precursor to the ignition of live fuels and previous work has typically studied dried, ground fuel samples. Involvement of live fuels in the spreading flame front is an important consideration

when planning prescribed burns under a forest canopy. While the focus of the present work was on heterogeneous fuel beds located in the southern United States, these results may benefit other coniferous forests managed with low intensity prescribed fire that also have surface fuel beds of conifer litter, live shrubs and regenerating trees.

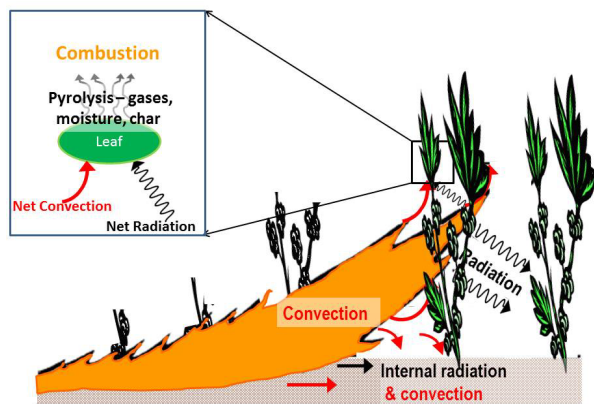


Figure 1. Conceptual diagram of heat transfer mechanisms and processes in heterogeneous fuel beds for prescribed fires.

	Analytical	Bench	Wind Tunnel	Field
Objectives				
3. Physics-based modeling	Kinetics—TGA, DAEM, components	Modified Gpyro/FDS	FDS/Vegetation Module
2. Heat transfer effects	Heating rate in Pyrolyzer (N ₂) & TGA/DSC (He)	Heating mode (convective/radiative) & heating rate (fast/slow)	Natural flames, measured flame & fuel temperature, radiative & convective	Natural flames, measured flame & fuel temperature, radiative & convective
1. Pyrolyzate composition/quantity	Light gases & tars chemistry	Light gases & tars yields—heated bed and cone calorimetry	Composition of light gases and tars	Composition of light gases
0. Fuel characteristics	Live fuel chemical analysis	Physical properties—H ₂ O activity	Controlled fuel loading, composition	Natural loading, 3D structure, composition, consumption

Figure 2. Schematic linking processes and activities/data to RC-2640 experimental and modeling work.

Previous pyrolysis work has typically used ground-up samples, thus eliminating any effects caused by moisture content, fuel particle shape, or heating mode. Thermal gravimetric analysis (TGA) coupled with gas chromatography-mass spectrometry (GC-MS) and evolved gas analysis (EGA) have been used for decades to describe the composition and energy content of pyrolysis products. We measured pyrolysis products (permanent gases (PG), light gases and tars (condensable gases)) at three scales – from tightly controlled heating rate bench-scale measurements at BYU and the Forest Products Laboratory (FPL) to laboratory burn-scale in a wind tunnel at RFL where fuel bed composition was controlled and flame length and rate of spread were relatively constant resulting in consistent heating rates to small field-scale burns (0.09 ha) in similar fuels under similar weather conditions at Fort Jackson in South Carolina. The BYU experimental apparatus consisted of a flat-flame burner with mm-size flames producing hot post-combustion gases (convective heating) and a radiant panel (radiant heating). The burner surface was water-cooled reducing possible radiant heating from the surface and the fuel gas mixture produced thin blue flames with no soot resulting in negligible radiant flux. FPL heating experiments were performed using enhanced cone-calorimeter techniques developed for this study. In all instances intact fuels from living plants were used instead of ground and dried fuel samples. A schematic showing linkages between the various experiments, model development and testing performed during this project (Figure 2) illustrates both similarities and differences in the experiments due to scale differences and ability to control conditions. At each scale measurements associated with the three objectives and fuel description were conducted. The methods associated with accomplishing the objectives are organized by experimental scale within each objective. A summary of the experiments performed at the three scales can be found in Table 1.

Table 1. Synopsis of experiments conducted at 3 scales to measure composition of pyrolysis gases associated with live plants common to the southeastern United States.

Scale	Experimental Summary
Bench (BYU)	87 slow-heating, 87 radiant, 87 convective, 87 radiant & convective
Wind tunnel	91 experimental fires (22 dormant season, 69 growing season)
Field	7 Ft. Jackson (5/1/18 – 24Bt, 24Bs; 5/2/2018 – 24As, 24At; 5/3/2018 – 16D5, 16D6, 16D6); 2 Tall Timbers (4/2017)

Objective 0 – Fuel characterization

Combining our knowledge of important southern fuels and plants with the species available through commercial nurseries able to ship the materials to Utah, Wisconsin and California, 14 plant species were selected: *Aristida stricta*, *Schizachyrium scoparium*, *Ilex glabra*, *Ilex vomitoria*, *Lyonia lucida*, *Morella cerifera*, *Persea palustris*, *Vaccinium arboreum*, *Vaccinium darrowii*, *Pinus palustris*, *Quercus nigra*, *Quercus virginiana*, *Sabal minor*, *Serenoa repens*. Plant size varied between species. One of the dominant shrub species at Ft. Jackson is sparkleberry (*Vaccinium arboreum*). It was chosen to link bench-scale measurements to field-scale measurements. Specialized small scale tests available at FPL and physical properties obtained at BYU and other facilities characterized these plant materials. Early in the project we determined that conventional wood wet chemistry could only account for about one-half of the live leaf dry mass, described as hemicellulose, cellulose, and klason lignin so additional standardized tests determined the leaf components of glucose, fructose, starch, crude protein, and minerals along with modifications to the standard tests for determining lipids, pectin, phenolic, and silicates. Composition and fuel loading of wind tunnel fuels were known. Two types of sampling to assess loading of surface and understory fuels at Ft. Jackson were used: 1) traditional, 2D plot methods and 2) novel 3D methods using LiDAR and terrestrial laser scanning to describe the shrub component of the fuel bed.

Objective 1 – Measurement of pyrolysis products

A flat-flame burner (FFB) apparatus and a pyrolyzer were used to study pyrolysis of foliar samples at high ($4 - 195\text{ }^{\circ}\text{C s}^{-1}$) and low ($0.5\text{ }^{\circ}\text{C s}^{-1}$) heating rates. Tar vapors were condensed in condensers and were analyzed by GC-MS after solvent extraction using a Thermo Scientific™ Trace™ 1310 (GC) equipped with a thermal conductivity detector (TCD) was used with an HP 5890 GC combined with an HP 5972 MS. Non-condensable gases were collected in gas sampling bags for transfer to gas analysis devices.

Canister samples were collected in the wind tunnel and field burn experiments. Composition of the gas samples in the wind tunnel canisters and some of the field canisters were analyzed using a GC. The other field canisters were analyzed the evening of each fire using a Bruker Tensor 37 (T37) extractive FTIR. For the wind tunnel experiments, the T37 was used in two modes, static and dynamic) to determine lumped (static) and time resolved (dynamic) composition of pyrolysis gases. Canister samples were collected either in advance of the flame (wind tunnel) or at the base of the flame (field).

Objective 2 – Determining effects of heat transfer

In the bench-scale tests in the pyrolyzer and the flat-flame burner, the heating rates were known.

Temperatures of the leaf samples were measured using a longwave IR (LWIR) camera. In the wind tunnel experiments, convective heat flux around the nursery plants was estimated using a background-oriented schlieren technique; radiative and total heat fluxes into the pine needle fuel bed were measured using Schmidt-Boelter heat flux sensors. A downward viewing LWIR camera recorded the temperature of the fuel bed as the fire advanced in the wind tunnel. Custom built Fire Behavior Packages containing a total and radiant heat flux sensor, a narrow angle radiometer, thermocouples and mass flow sensors were deployed at Ft. Jackson to measure horizontal heat fluxes from the fires to the shrubs. A nadir downward looking IR camera was used to measure leaf temperatures of the shrubs. Traditional statistical analyses of pyrolysis product yields and composition were used initially. Recognition that these data did not meet the assumptions underlying traditional statistical analyses resulted in the application of compositional data analysis (CoDA) techniques to these data which was a new approach for the wildland fire and atmospheric science communities.

Objective 3 - High-fidelity physics-based modeling

Three modeling studies relevant to the bench-scale FFB experiments were performed to gain further understanding of pyrolysis, ignition and flaming of solid fuels representing manzanita (*Arctostaphylos glandulosa*) leaves. While this species is native to California and Oregon, its overall leaf characteristics such as leaf morphology and heat content are similar to southern species such as inkberry, fetterbush, and swamp bay resulting in similar physical (as opposed to chemical) response in these studies. All simulations were validated against the experimental data previously obtained using the FFB. In the first study, the leaf was oriented horizontally in the hot upward convective stream exiting the FFB. Pyrolysis, ignition and combustion of a thin solid fuel representing a broadleaf were studied. In the second study, the leaf was oriented vertically and held above the FFB. Pyrolysis, ignition, and combustion of a leaf-like solid fuel representing a vertically oriented manzanita leaf were computationally investigated using modified Gpyro3D coupled with FDS. In the third study, the effect of heating mode, convection vs radiation vs combined convection-radiation, was investigated for a leaf in the FFB apparatus equipped with a radiative panel. A fourth modeling study was performed to investigate two moisture evaporation approaches (Arrhenius vs equilibrium) in dead and live fuels. Lastly, FDS version 6.7 was used to simulate pyrolysis and combustion of fuel beds of longleaf pine needles only (0.396 kg m⁻²) in the wind tunnel. Because the detailed chemical analysis of the foliage of 12 of the plant species in this study and other prior work has shown that foliar fuels are different from wood, this project developed a model of specific heat capacity based on the foliar composition using a combination of theoretical and statistical modeling. The characterization of the physical and chemical composition of the nursery plants revealed the inadequacies of the existing Vegetation module in FDS which enables FDS to simulate wildland and wildland-urban interface fire and this new model has been developed as an alternative. At present time it has not been added to FDS, but the formulation is available in the literature.

4 Results and Discussion

Fuels were characterized for all sets of experiments. Proximate and ultimate analysis of the nursery plants produced values that were typical of living vegetation. Proximate analysis determined moisture, ash, volatile matter and fixed carbon content; ultimate analysis determined C, H, O, N and S. Fuel loading at Ft. Jackson was within the range of loadings reported for unburnt stands at Eglin Air Force Base in Florida and for mixed slash (*Pinus elliottii* Engelm.) and longleaf pine stands in central Georgia. The low intensity fires at Ft. Jackson do not typically

consume all surface fuels so there is a residual duff layer in these stands. 3D shrub fuels were successfully modeled using plot data and TLS measures; however, the shrub component, while significant in terms of vertical distribution and its influence on fire behavior, was only a minor portion of the fuel consumption.

Objective 1 – Measurement of pyrolysis products

During fast pyrolysis in the FFB, live foliage samples lost initial mass at a slower rate and pyrolysis took longer to complete compared to air-dried foliage samples. This difference in mass loss rate is attributed to the fact that more water was present in the foliage of the live plants as previous studies have shown. Figure 3 shows a comparison of the pyrolysis product yields from longleaf pine litter in the different heating modes as a function of temperature (even though the heating rates and background gas composition were different). The tar yields from the pyrolyzer peaked at 500 °C and then decreased due to secondary reactions of tar. However, the tar yields in the FFB system continued to increase with final temperature, reaching over 60% of the mass of the dry plant. This difference in trend indicates that temperature alone cannot be used to describe pyrolysis behavior, but that heating rate and perhaps the temperature of the ambient environment also contribute to pyrolysis behavior. On a weight basis CO was the most prevalent species, followed by CO₂, with much smaller amounts of CH₄ and H₂. On a molar basis, H₂ comprised about 30 mol% of the light gas. The amount of CO increased with increasing severity of the heating, while the amount of CO₂ decreased (Figure 4). Plant-to-plant variations in light gas species were relatively small, especially considering that the light gas only comprised about 25 wt% of the pyrolysis gases.

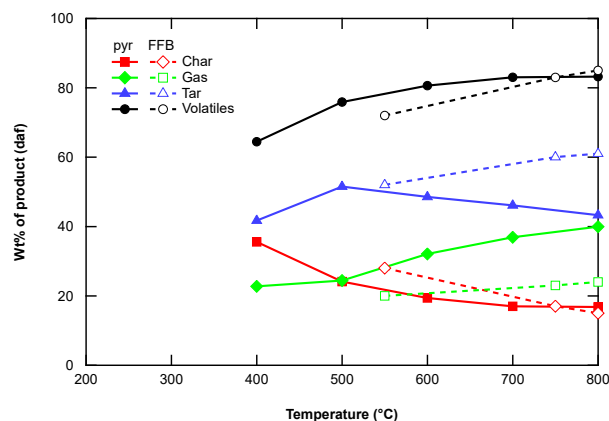


Figure 3. Pyrolysis product yields (percentage of total mass (dry ash free basis)) vs. final temperature for longleaf pine litter obtained in a pyrolyzer (solid lines) at 0.5 °C/s and from the flat flame burner system (dashed lines) under different modes of heating: radiation only (550 °C), convection only (750 °C), and radiation plus convection (800 °C).

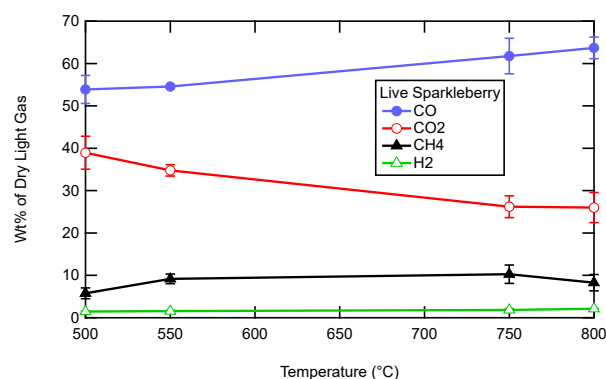


Figure 4. Light gas species observed during pyrolysis of live sparkleberry plotted as a function of final temperature.

Tars are gases evolved in the pyrolysis environment that condense when cooled to room or ice temperature. The initial tar species released from a surface may react further in a hot environment to (a) crack apart and form smaller light gas species, or (2) polymerize to form larger species called polyaromatic hydrocarbons (PAH) which can eventually polymerize to form soot. The yellow part of flames is due to radiant emission from hot soot particles formed largely from the tar. Soot is the dominant source of radiation from flames.

The GC/MS analysis of tars was able to determine 60 tar species with concentrations of more than 1 mol% of the tar in the FFB experiments, and over 30 compounds in the pyrolyzer experiments. There were many more compounds than these but in such low concentrations that signal-to-noise became a problem. Figure 3 shows the distribution of compounds measured in the FFB system in the three heating modes for longleaf pine (live, dead, and pine litter). Large variations in the amount of individual tar species were observed as a function of plant species. One of the major tar species that were observed in every experiment was phenol for all four modes of heating (Figure 5). The yields of phenol and 1,2-benzenediol were quite different for each plant species, with no clear trend with heating mode that is common to all plant species. An example of the effects of heating mode, rate and temperature on tar composition summarized in groups can be easily seen (Figure 6).

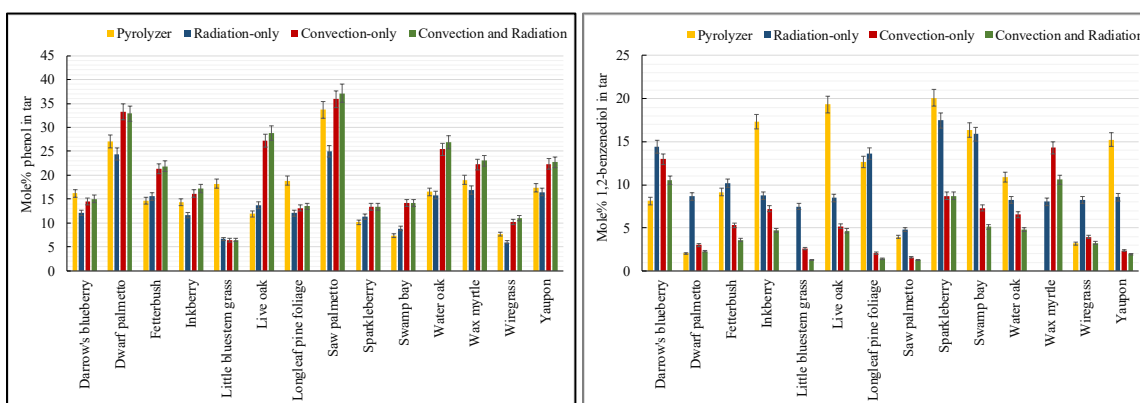


Figure 5. Mole percent phenol (left) and 1,2-benzenediol (right) in tar during pyrolysis of 14 live plant species. Error bars represent the 95% confidence interval.

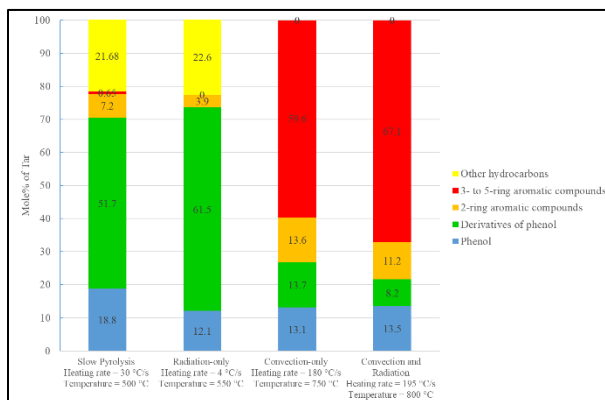


Figure 6. An example of heating mode on distribution of functional groups in tar for pyrolysis of live longleaf pine foliage.

Using compositional data analysis (CoDA) permitted the proper application of multivariate analysis (and other statistical methods) to the bench-scale pyrolysis data. The composition of the pyrolysis gases was significantly affected by plant species, moisture content, heating mode. Pairwise comparisons of log-ratios of groups of pyrolysis products (balances) showed that the relative amounts of the various groupings differed between most heating modes; however, only a few of the groupings were affected by the foliage moisture status (Table 2).

In the 88 wind tunnel experiments, 22 light gases were identified in the 153 canister samples and 35 gases were identified using the FTIR in 37 experiments. Of these gases, 8 were common to both instruments (CO , CO_2 , CH_4 , C_2H_2 , C_2H_4 , C_2H_6 , C_3H_6 and C_4H_6). The bench-scale experiments measured CO , CO_2 and CH_4 . While we compared gas composition at the bench, wind tunnel and field scales separately, we did not compare the relative amount of CO , CO_2 and CH_4 across the 3 scales. At Ft. Jackson, 42 canisters were collected for GC/MS and 7 were collected for FTIR analysis. Logistic regression correctly classified 74 percent of the wind tunnel samples as pyrolysis or flaming and this model applied to the Ft. Jackson canisters identified 17 of the 42 as pyrolysis samples. As expected, gas composition differed significantly between pyrolysis and flaming combustion. The gas composition was also affected by the sample location (wind tunnel vs field) (Figure 7). Fuel heating rates, maximum fuel temperatures and fuel conditions (loading, moisture content) were similar between the wind tunnel experiment and the field prescribed burns thus warranting comparison.

The dynamic FTIR wind tunnel samples afforded the opportunity to link the measured concentrations of gases to the infrared imagery to examine association with different stages of the preheating, pyrolysis and combustion phases (Figure 8). The top series of spectra show the presence of ethene (C_2H_4), propene (C_3H_6) and nitrous acid (HONO) become more evident during the pyrolysis phase of the burn and reach their highest mixing ratios as seen in scans 15-20, and ammonia (NH_3) at its highest mixing ratio during the flaming and smoldering phases of the fire. The bottom series of spectra depicts the progression of the burn relative to carbon monoxide (CO), with mixing ratios increasing and peaking during the pyrolysis phase while decreasing during the flaming portion of the flame.

A great deal was learned from the Ft. Jackson FTIR measurements, including about the technique itself. First amongst these is that when using IR spectroscopy deriving the mixing ratios from the congested spectra obtained from wildland smoke samples is far more challenging than in other applications due to multiple overlapping spectral features. Sophisticated software and analysis are required with careful iterative analysis carried out in selected spectral “microwindows.” Using such methods, successful analysis was carried out that resulted in first infrared detection of five compounds generated during prescribed forest fire burns: methyl nitrite ($\text{CH}_3\text{ON}=\text{O}$), allene (1,2-propadiene, $\text{CH}_2=\text{C}=\text{CH}_2$), the aromatic compound naphthalene (C_{10}H_8), and the two aldehydes acrolein ($\text{CH}_2=\text{CHCHO}$) and acetaldehyde (CH_3CHO). Most of the compounds (excluding acetaldehyde), had their primary features become apparent only after the larger spectral features had been fitted and subtracted.

Table 2. Pairwise comparison of heating mode and moisture status effects on balances of gas compounds produced by the pyrolysis of 15 plant species native to the southeastern United States. “X” indicates a significant difference. Slow=pyrolyzer, Rad=radiative only, Conv=convective only, RadConv=combined radiative and convective.

Balance	Heating Mode						Moisture
	Rad-Slow	Conv-Slow	RadConv-Slow	Conv-Rad	RadConv-Rad	RadConv-Conv	Air dried-Fresh
Tars vs permanent gas (PG)	X	X	X	X	X	X	
CO vs Other PG		X	X	X	X	X	X
H ₂ vs CH ₄	X	X	X		X	X	X
Tars vs Phenol	X	X			X	X	X
Primary vs Other Tars	X	X	X	X	X	X	
Other Tars vs Phenol derivs	X	X	X	X	X	X	
Acid, Alcohol vs Other HC	X	X		X	X		
Aldehyde vs Ketone	X	X	X	X	X		
Acid vs Alcohol	X	X		X	X	X	
Benzene vs Rings	X	X	X	X	X	X	
2&3 vs 4&5 Ring	X	X	X	X	X	X	
2 vs 3-Ring Tars	X	X	X	X	X	X	
4 vs 5-Ring Tars		X	X	X	X	X	

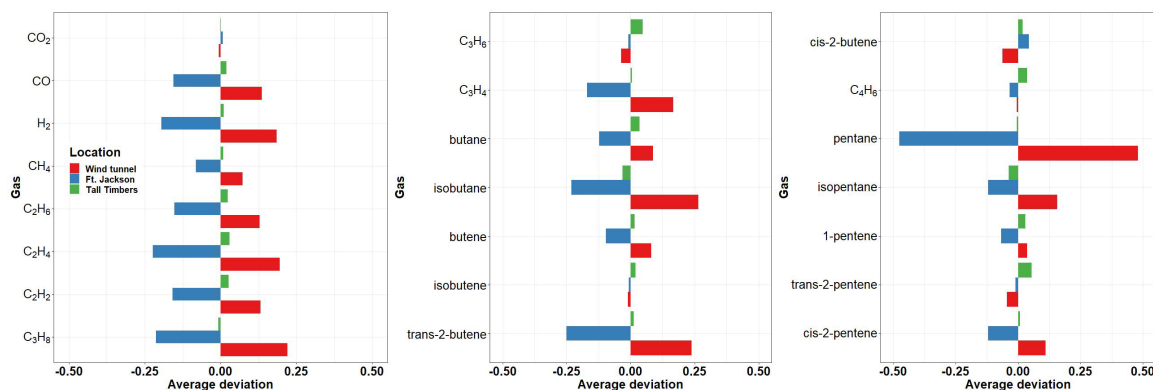


Figure 7. Effect of location on gas composition of pyrolysis samples collected in a wind tunnel and in prescribed burns in longleaf pine stands located at Tall Timbers Pebble Hill Plantation and Fort Jackson in the southeastern U.S. Composition expressed as deviation (log-ratio scale) from overall geometric mean by gas. Values below zero indicate gas concentrations less than the overall mean and values above zero indicate greater concentrations.

Burn 86 – Sparkleberry and 1 kg long-leaf pine needles

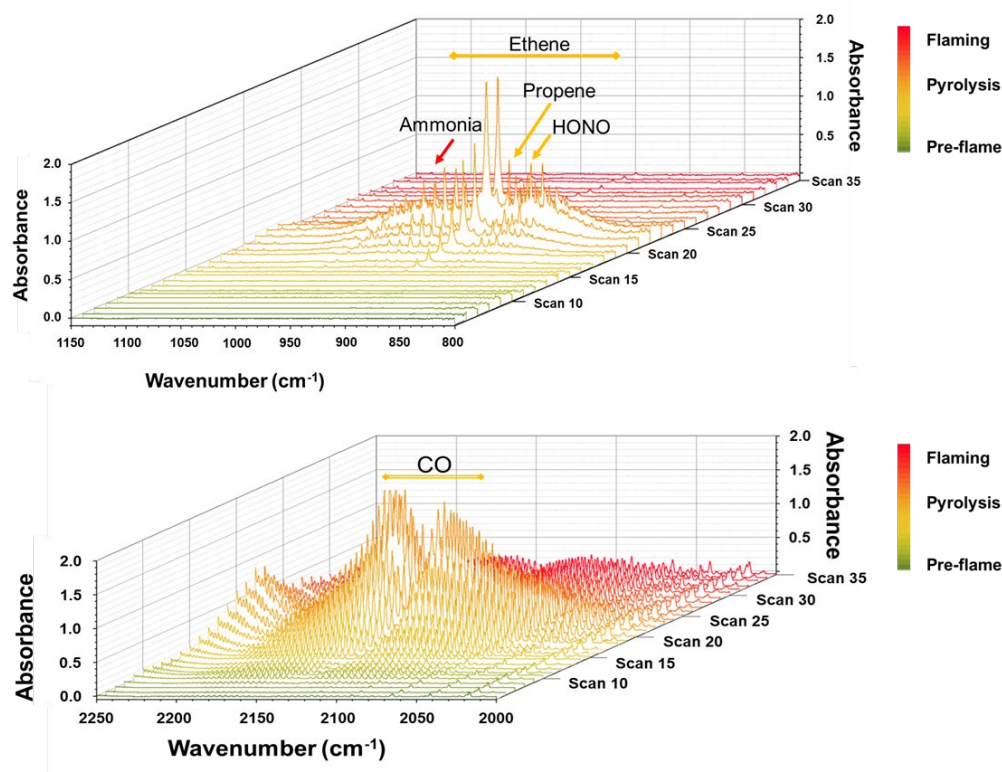


Figure 8. Burn 86 time-resolved measured IR spectra (November 2018) for regions 1150-800 cm⁻¹ and 2250-2000 cm⁻¹ respectively.

Objective 2 – Determining effects of heat transfer

Infrared images taken using an IR camera during the pyrolysis of the leaves indicate that the leaves did not heat isothermally under convective heating. At the beginning of the experiments, there were temperature gradients within the leaves; the edges of the leaves had higher temperatures than the middle of the leaves. As time passed, the heat traveled from the edges towards the center until the temperature was uniform across the entire leaf. The maximum fuel surface temperature measured during the convection-only experiments was 750 °C.

Maximum observed fuel temperatures in the wind tunnel experiments were similar (on the order of 650 °C). Temperatures derived from the time sequence of IR images (Figure 9) were synchronized with FTIR data to produce Figure 8. Heat fluxes into the wind tunnel fuel bed ranged up to 25 kW m⁻². The horizontal convective fluxes estimated by the background oriented schlieren were generally 1 or 2 orders of magnitude smaller. In contrast, the horizontal heat fluxes measured in the Ft. Jackson burns (Figure 10) were on the order of 5-15 kW m⁻² which were like other reported values for similar vegetation types.

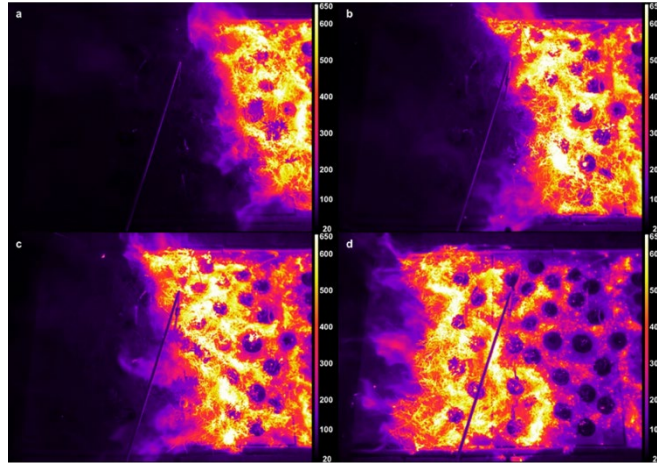


Figure 9. FLIR thermal images of fire progression through a fuel bed of longleaf pine needles and inkberry plants.

Objective 3 – High-fidelity physics-based modeling

The GPyro model was modified substantially to improve modelling of evaporation from foliar fuels. Replacement of an Arrhenius-based model with an equilibrium model for evaporation had greater impact on high fuel moisture fuels. Drying dynamics from the equilibrium model is more consistent with the physics of evaporation (Figure 11). Modeling revealed that fluid dynamics play a distinctive role in evaporation, pyrolysis, ignition, combustion and burnout behavior of leaves. Fluid flow was influenced by leaf orientation (horizontal or vertical). The addition of radiative heating to convective heating reduced the time to combust 50 percent of the initial mass by 1/3 suggesting that convective heating had a greater impact on pyrolysis and burning of an individual leaf compared to radiative heating.

5 Implications for Future Research

This project has applied new techniques to characterize and model evaporation and pyrolysis in wildland fuels with an emphasis on the live shrub component of fuel beds treated with prescribed burning in the southern United States. While it has been known for several decades that the composition of these fuels is complex and affected by the conditions under which pyrolysis has occurred, these subtleties have not been incorporated into wildland fire models for a variety of reasons. Several unique contributions have resulted from this project. The use of actual fuels that retained their original shape and water content thus reintroducing the effects of water and heat transfer into the results provide a more realistic characterization of pyrolysis that likely occurs in the wildland setting. While prior pyrolysis work with biomass has occasionally occurred in an oxidizing environment, most work has typically occurred in inert environments. Our measurement of gas concentrations in an oxidizing environment may have underestimated pyrolysis gases because the sampling technique was not sufficiently quick to capture the gases before oxidation. Post project future work can compare the gas composition resulting from the inert environments of the pyrolyzer and flat-flame burner with the oxidizing environments of the wind tunnel and field burns at Ft. Jackson to determine what the effects are using the collected data. It will be key to perform this analysis using compositional data analysis techniques because the information in the relative amounts of gases within the composition are contained within the ratios of the gases and not the absolute amounts. If future work shows that the gas ratios do not

change between the inert and oxidizing environments, then the applicability of bench-scale results to model the larger scale, oxidizing environment where prescribed fires take place is strengthened. The dynamic FTIR data illustrated that pyrolysis gas composition was not static; further analysis is required to confirm trends as these data were acquired late in the project. Application of the improved spectral analysis techniques which resulted in the first infrared detection of five gas compounds during prescribed forest fire burns may potentially improve our ability to non-intrusively identify other compounds previously identified only using intrusive sampling methods. While the focus of the present work was on heterogeneous fuel beds located in the southern United States, these results may benefit other coniferous forests managed with low intensity prescribed fire that also have surface fuel beds of conifer litter, live shrubs and regenerating trees.

Detailed analytical work supported the hypothesis that foliar fuels are quite different chemically from wood and should be modeled accordingly. While this difference is currently modeled using different heat content for foliar fuels in fire spread models, this difference also extends to the composition of the pyrolysis and combustion products. Fuel heat content, while important to fire spread and fire energy release, may be less important to smoke and air quality issues which strongly impact the ability to use prescribed fire. Most physically based fire models do not contain a sophisticated description of the chemistry of combustion due to lack of information on combustion pathways and computational demands. The gas composition information developed by this project can be used to methodically examine the effects of increased chemical computations on the prediction of fire behavior versus the computational demand which is needed future work. Improved chemical computations may provide a description of the chemical composition of pyrolysis and combustion products which can be used in smoke production and transport models. Examining the improvement in model prediction resulting from increased detail in chemical complexity is a logical next step building upon this project. Similarly, scaling up the modeling of moisture from a single leaf to entire shrubs or dead litter fuel beds to determine the improvement by using the equilibrium moisture model instead of the more common Arrhenius model is a logical next step in the development of improved physics-based fire models.

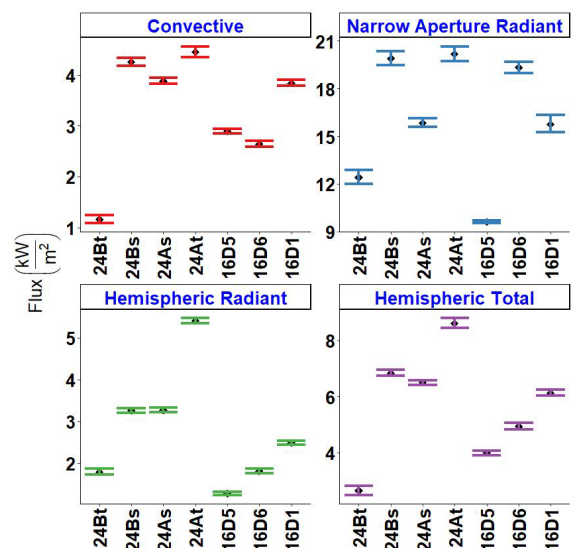


Figure 10. Fire behavior in plot 24As (left) and (right) heat fluxes measured using Fire Behavior Packages in prescribed burns in longleaf pine at Ft. Jackson, SC. Harmonic mean with 95 percent confidence interval shown.

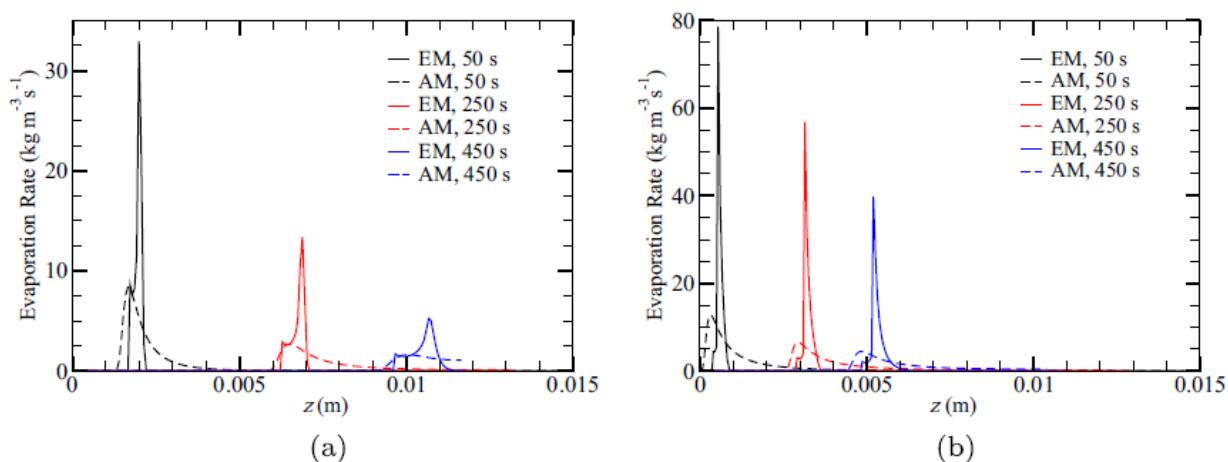


Figure 11. Profiles of evaporation (a,b) for an external radiant flux of 40 kW m^{-2} . FMC = 26 and 100 %, left and right, respectively. EM is equilibrium model and AM is Arrhenius model.

1 Introduction

The Department of Defense (DoD) uses prescribed fire to manage millions of acres across a variety of ecosystems in the United States to 1) prepare sites for military training, 2) reduce hazardous fuel, and 3) obtain fire's ecological benefits. In the southern U.S., many DoD lands contain stands of longleaf and loblolly pine with a variety of understories including wiregrass, palmetto-gallberry, and turkey oak that generally burn at relatively low fire line intensities [1] (heat release rates). Installations also manage dwarf pitch pine, sand pine, and pond pine stands which can burn with high intensity. These fuel bed types are 1) heterogeneous in nature, 2) contain multiple fuel components, and 3) contain a mixture of live and dead fuels, all important characteristics influencing the combustion process and fire propagation. To properly implement prescribed fire and limit potential escapes, an improved understanding is needed of those fundamental science questions related to combustion and fire propagation in heterogeneous fuel beds that are a mix of live and dead fuels [1].

2 Objective

Today's widely used operational fire behavior models are based on data from homogenous beds of dead fuels and associated theory [2]. However, most prescribed fires at DoD installations occur in heterogeneous fuel beds with a mixture of live and dead biomass. The objective of this project was to address several fundamental questions to improve our understanding and modeling capability of fire propagation in natural fuel beds including

- 4) detailed description of pyrolysis and the evolution of its products for a greater variety of southern fuels than is currently known,
- 5) how convective and radiative heat transfer from flames to live fuel particles influences pyrolysis and ignition at laboratory and field scales, and
- 6) more detailed insight into pyrolysis, combustion and heat transfer processes in wildland fire spread through the use of high-fidelity physics-based models.

This project thus directly responded to SON RCSON-16-02 "Improved Understanding of Wildland Fire Combustion Processes for Department of Defense Management Ecosystems" and all 4 of the SON objectives by focusing on heterogeneous fuel beds managed with prescribed fire in southern pine forests. The project increased knowledge of open combustion processes at particle (0.001 to 0.01 m) to fuel bed (1-10s of m²) scales (SON Objective 1) by measuring the mechanisms of pyrolysis, ignition, and heat transfer (SON Objective 3) in several live fuels and a single dead fuel at particle and fuel bed-scales (SON Objective 2). The role of fuel characteristics (live and dead, structure and composition) on heat transfer, pyrolysis, and ignition were examined experimentally in the lab and in the field (SON Objective 3). Physics-based modelling of fires was conducted for the lab experimental setups (SON Objective 4) with a focus on pyrolysis and ignition in live shrub canopies. An improved understanding of pyrolysis and how it is affected by heat transfer in heterogeneous fuel beds will eventually lead to an improved ability to predict fire behavior such that managers can more readily achieve desired fire effects with prescribed burning.

2.1 Specific hypotheses addressed by this project

H₁: Composition and concentrations of gaseous and tar pyrolysis products do not differ between southern species thus a common pyrolysis scheme can be used in models.

H₂: The rate at which foliage is heated does not affect the composition and concentrations of dominant gaseous pyrolysis or tar pyrolysis products.

H₃: Heat transfer mechanisms (radiation and convection) do not affect the composition and concentrations of dominant gaseous pyrolysis products.

H₄: The water content of foliage does not affect the composition and concentrations of dominant gaseous and tar pyrolysis products.

H₅: Laboratory-scale measurements of the production of gaseous pyrolysis products under controlled conditions can be correlated with field-scale measurements under prescribed fire conditions.

H₆: Inclusion of an advanced pyrolysis mechanism for live and dead wildland fuels does not improve fire behavior predictions by the high-fidelity physics-based models.

H₇: Improving the evaporation mechanism for moisture content in wildland fuels does not improve fire behavior predictions by the high-fidelity physics-based models.

H₈: Simulation of pyrolysis and ignition of wildland fuels is not improved with 3D fuels characterization and can be just as effectively simulated in 2D.

H₉: Foliar fuels are not different from solid wood and can be modelled using parameters associated with wood.

These hypotheses were tested with data derived from the technical objectives. As the physical and chemical characteristics of the wildland fuels are foundational to understanding the three technical objectives, a 0th technical objective is identified in this final report. The work was previously included in the original three objectives, but it has been elevated as a separate objective due to its foundational nature. The original three and the elevated foundational technical objectives were:

- 0) characterize the physical, chemical, compositional and spatial structure of wildland fuels used in this project
- 1) characterization of pyrolysis products by measurement for a variety of live and dead foliar fuel particles in laboratory and small-scale field experiments
- 2) determination of the effects of convective and radiant heat transfer on pyrolysis
- 3) performance of high-fidelity physics-based modeling of pyrolysis and ignition for bench-scale, wind tunnel and small-scale field experiments.

3 Technical Approach

Laboratory and field experiments focused on pyrolysis coupled with sufficient description of fuel characteristics and heat transfer mechanisms and physics-based modeling were used to improve our understanding of combustion processes in mixed (heterogeneous) fuel beds managed with prescribed fire on DoD installations. Our conceptual model (Figure 1) of the physics and chemistry of fire spread in heterogeneous fuel beds builds upon previous formulations [2–5]. The formulations generally included the heat transfer mechanisms listed. Treatment of pyrolysis varies somewhat between the formulations ranging from assuming Arrhenius-type production of pyrolysates to simply assuming a higher heat content for the fuel. Fuel bed formulations also varied somewhat [2–5]. Dead fuels dominate fire spread in many fuel types and thus dominate operational models; however, live fuels are an important contributor in many forested systems where prescribed burning is routinely used [6–8]. Our approach included using well-controlled, traditional methods and wildland fire flames to study the thermal decomposition (pyrolysis) of live fuels and the resulting gaseous products which may ignite producing the visible flame.

Pyrolysis is strongly determined by the solid fuel particle temperature which is a function of heat transfer from the flame to the unburnt live fuels. With this approach, we determined the effects of various heating modes on the production of pyrolysates for live southern fuel types. Pyrolyzate production is a precursor to the ignition of live fuels and previous work has typically studied dried, ground fuel samples. Involvement of live fuels in the spreading flame front is an important

consideration when planning prescribed burns under a forest canopy. While the focus of the present work was heterogeneous fuel beds located in the southern United States, these results may benefit other coniferous forests in the U.S. managed with low intensity prescribed fire that also have surface fuel beds of conifer litter, live shrubs and regenerating trees.

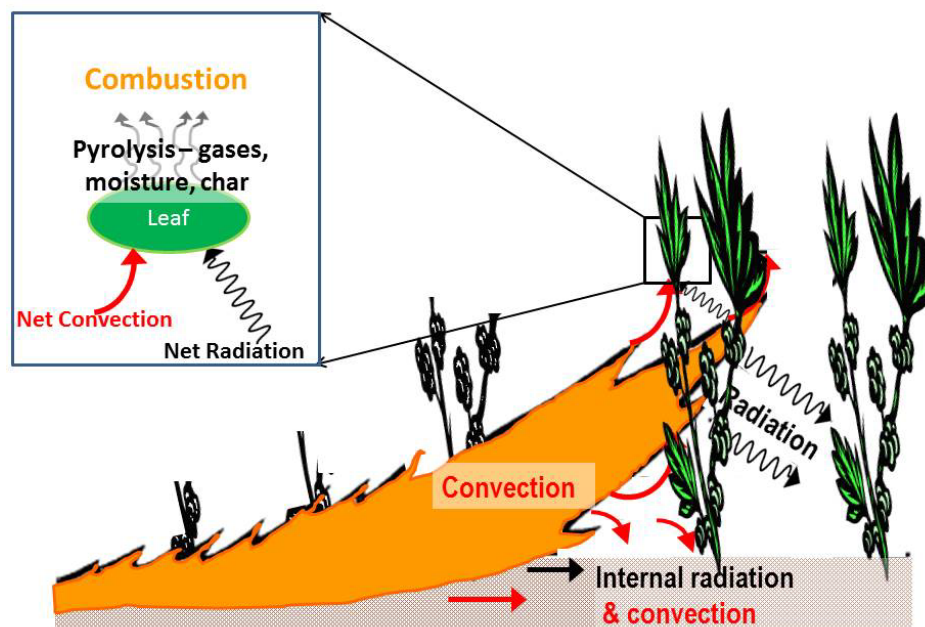


Figure 1. Conceptual diagram of heat transfer mechanisms and processes in heterogeneous fuel beds for prescribed fires (adapted from [2]).

3.1 Background

While controlled burning has been used in southern forests for millennia, the collective knowledge of how to use fire as a management tool was not codified until 1965 and subsequently updated [9]. This prescribed fire guide presented firing techniques and weather information to manipulate fire behavior to achieve resource objectives; most of the fire behavior information was based on experience and observation and the original data are difficult to find. For example, the fire behavior presented in the Southern Forestry Smoke Management Guidebook [10] was estimated using the Rothmel operational model and a custom palmetto-gallberry fuel model [6]. Much of the focus of fire research in the southern U.S. has been linking pre-fire conditions to fire behavior to fire effects. Until recently, detailed study and modeling of the physical mechanisms of fire spread, particularly prescribed fire spread, in southern fuels was generally limited to the work of Byram and Nelson [11–14].

Chemical study of southern fuels has generally focused on determining the heat content and heat of combustion [15,16]; the evolution of combustible gases from heating (pyrolysis) of gallberry, palmetto, and wax myrtle has been studied using ground samples [17–21]. Hough’s work examined a wide variety of southern fuels and found that the low heat content for live fuels ranged from high values of 20,570 and 22,190 kJ kg⁻¹ for gallberry leaves and sand pine fresh needles to low values of 19,385 and 16,425 kJ kg⁻¹ for wiregrass and herbaceous species, respectively. While this limitation is true for prescribed fire behavior in much of the U.S., its impact is perhaps most acute in the southern U.S. where 2.6×10⁶ ha are prescribed burned annually [22]. As the SERDP Fire Science Strategy [1] reiterates, fuel consumption and fire behavior are closely linked to smoke production and transport and the ecological effects of fire which are typically the values and risks with which society is most

concerned.

Current operational fire spread models were developed based on homogeneous fuel beds composed of a single fuel type consisting of dead fuels such as pine needles or machined wood [2]. Few laboratory experiments used heterogeneous fuel beds composed of different fuel types or a mix of live and dead fuels and fuel particle sizes [12,23]. It is important to note that predictions using the Rothermel model in mixed fuel beds of the machined wood fuels did not match well with observations [24]. While the Rothermel model was recently reformulated to recognize the heterogeneity in natural fuel beds, it has not been widely validated [25]. In contrast, the majority of all field-based fire behavior experiments have occurred in natural fuel beds that are inherently heterogeneous [13,14,26,27]. Fons described fire spread in light forest fuels as a series of ignitions wherein heat is transferred from burning fuel particles to unburnt fuel particles [3] through convective and radiative heat transfer. Conduction was assumed to be important in thermally thick fuels.

From this early formulation, various laboratory, field, and numerical experiments have been conducted to determine the relative importance of convection and radiation to ignition and fire spread in simple and complex fuel beds [28–30]. Laboratory work has shown the importance of wind to fire spread in moist dead and live fuels [31,32] even though it was not specifically labeled as convection. Recent work has shown that radiative heat transfer at levels experienced in wildland flames is not sufficient to ignite fine fuels [33–35] and further that convective heating is an important factor to successful fire spread in live fuel beds [36,37]. Recent field measurements have been performed at Eglin Air Force Base designed to quantify the amount of heat transferred by radiation and convection to unburnt fuels during prescribed burns [38,39]. New mathematical models include additional physics which led to the need for additional measurements, particularly of the basic heat and chemical processes occurring in fire. This need has been addressed through both field [40,41,41,42] and laboratory experiments [43].

It has long been recognized that wildland fire spread involves two main processes – pyrolysis and combustion. In operational models, pyrolysis has not been explicitly included; however, fuel types such as palmetto-gallberry and pocosin that produce more volatiles than dead wood does are assigned higher heat content values to compensate for this omission [6,15,19]. As computational resources have increased, the treatment of pyrolysis and chemical reactions of combustion have been described mathematically and included in fire models [44] including a recent model based on coupling the Gpyro3D and Fire Dynamics Simulator (FDS) models [45,46]. Validation and comparison of these model components in wildland fuels is limited. Biomass pyrolysis can be classified based on heating rate and solid residence time [47,48]: slow (very low heating rate $< 1\text{ }^{\circ}\text{C s}^{-1}$, 300-700 $^{\circ}\text{C}$, residence times of hours to days), fast (high heating rate $> 10\text{-}200\text{ }^{\circ}\text{C s}^{-1}$, residence time of 0.5 – 10 s), and flash (heating rate $10^3\text{-}10^4\text{ }^{\circ}\text{C s}^{-1}$, residence time $< 0.5\text{ s}$). Prior pyrolysis work has argued the need to conduct experimental work under well-controlled conditions due to the complexity of thermal behavior chemically and physically as opposed to conducting this work during actual fires under field conditions with limited control of conditions [49]. However, we find no quantitative comparison of results from the well-controlled experiments with results from actual fires to support application of this approach.

The FDS model, developed and tested extensively for structural fires, has been modified (WFDS) to accommodate wildland fuel beds with limited testing thus far [50]. While it has long been recognized that fuel moisture content of live fuels is a significant source of water in the combustion environment [11], modeling of the impact of this moisture on chemical reactions involved in flames has only recently been initiated [51]. Recognition that the composition of live fuels changes seasonally due to physiological processes with attendant impact on ignition and fire spread has also recently resurfaced as a topic of investigation with regard to pyrolysis and combustion [52,53]. There is extensive

literature concerning pyrolysis of biomass, particularly as it relates to potential energy sources [e.g. 21]; however, the biomass is typically modified physically and sometimes chemically so application of the results in the wildland fire setting are questionable.

Primary pyrolysis products are defined as the gases that are released directly from the fuel due to changes in temperature, as indicated by the inset box in Figure 1. In biomass fuels and coals, these primary pyrolysis products consist of CO, CO₂, H₂O, light hydrocarbons, and heavy hydrocarbons and char [54]. The heavy hydrocarbons that condense at room temperature are often referred to as tars. After these pyrolysis gases are released, they heat up inside the flame and the heavier hydrocarbons react further, and this reaction of pyrolysis gases is called secondary pyrolysis. Secondary pyrolysis may crack the heavier hydrocarbons to form lighter gases or may polymerize the tars to form soot. The orange color of wildland flames is due to radiation from tiny soot particles in the fuel-rich part of the flame. Unburned secondary pyrolysis products appear as smoke which is composed of permanent gases and particulate matter formed from char and condensed gases produced by primary and secondary gases. As a quantitative example of secondary pyrolysis, pyrolysis of a birch wood gave almost 60% tars at 500°C, but the tars decreased to only 5% if the pyrolysis products reached 900°C [55]. Primary pyrolysis models of cellulose, hemicellulose, and lignin have been developed for biomass fuels [56–58]. A chemical structure approach [59] was combined with models of secondary tar pyrolysis to model the high heating rate pyrolysis of biomass fuels [60]. These models and others will be investigated for application to live fuels in this project.

Previous pyrolysis work has typically used ground-up samples, thus eliminating any effects caused by moisture content, fuel particle shape, or heating mode. Thermal gravimetric analysis (TGA) coupled with gas chromatography-mass spectrometry (GC-MS) and evolved gas analysis (EGA) [61,62] have been used for decades to describe the composition and energy content of pyrolysis products. We measured pyrolysis products (permanent gases (PG), light gases and tars (condensable gases)) at three scales – from tightly controlled heating rate bench-scale measurements at BYU and the Forest Products Laboratory (FPL) to laboratory burn-scale in a wind tunnel at RFL where fuel bed composition was controlled and flame length and rate of spread were relatively constant resulting in consistent heating rates to small field-scale burns (0.09 ha) in similar fuels under similar weather conditions at Fort Jackson in South Carolina. The BYU experimental apparatus consisted of a flat-flame burner with mm-size flames producing hot post-combustion gases (convective heating) and a radiant panel (radiant heating). The burner surface was water-cooled reducing possible radiant heating from the surface and the fuel gas mixture produced thin blue flames with no soot resulting in negligible radiant flux. FPL heating experiments were performed using enhanced cone-calorimeter techniques developed for this study. In all instances intact fuels from living plants were used instead of ground and dried fuel samples. A schematic showing linkages between the various experiments, model development and testing performed during this project (Figure 2) illustrates both similarities and differences in the experiments due to scale differences and ability to control conditions. At each scale measurements associated with the three objectives and fuel description were conducted. The methods associated with accomplishing the objectives are organized by experimental scale within each objective. A summary of the experiments performed at the three scales can be found in Table 1.

Table 1. Synopsis of experiments conducted at 3 scales to measure composition of pyrolysis gases associated with live plants common to the southeastern United States.

Scale	Experimental Summary
Bench (BYU)	87 slow-heating, 87 radiant, 87 convective, 87 radiant & convective
Wind tunnel	91 experimental fires (22 dormant season, 69 growing season)
Field	7 Ft. Jackson (5/1/18 – 24B-triangle, 24B-square; 5/2/2018 – 24A-square, 24A-triangle; 5/3/2018 – 16D5, 16D6, 16D6); 4 Tall Timbers (4/2018)

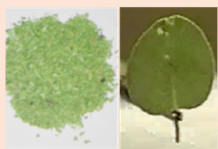



	Analytical	Bench	Wind Tunnel	Field
<i>Objectives</i>				
<i>3. Physics-based modeling</i>	Kinetics—TGA, DAEM, components	Modified Gpyro/FDS	FDS/Vegetation Module
<i>2. Heat transfer effects</i>	Heating rate in Pyrolyzer (N ₂) & TGA/DSC (He)	Heating mode (convective/radiative) & heating rate (fast/slow)	Natural flames, measured flame & fuel temperature, radiative & convective	Natural flames, measured flame & fuel temperature, radiative & convective
<i>1. Pyrolyzate composition/quantity</i>	Light gases & tars chemistry	Light gases & tars yields—heated bed and cone calorimetry	Composition of light gases and tars	Composition of light gases
<i>0. Fuel characteristics</i>	Live fuel chemical analysis	Physical properties—H ₂ O activity	Controlled fuel loading, composition	Natural loading, 3D structure, composition, consumption

Figure 2. Schematic linking processes and activities/data to RC-2640 experimental and modeling work.

3.2 Objective 0 – Fuel characterization

Combining our knowledge of important southern fuels and plants with the species available through commercial nurseries able to ship the materials to Utah, Wisconsin, and California (a challenge due to agricultural restrictions), 14 plant species were selected (Table 2). Because of quantity and price, the plant size ordered was generally a cell pack meaning the plants were 1-2 years old; plant size varied between species. One of the dominant shrub species at Ft. Jackson is sparkleberry (*Vaccinium arboreum*). Since this plant is deciduous, the foliage can cause a significant increase to prescribed fire behavior during the growing season. Sparkleberry was chosen to be the live plant species to link

bench-scale measurements to field-scale measurements.

3.2.1 *Solid fuel properties (FPL)*

Various physical properties of the live and dead leaves suitable for pyrolysis modeling were scant or inadequate in the literature for utilization in FDS or GPYRO. Specialized small scale tests were available at FPL and in some cases complement the physical properties tests obtained at BYU [63] and other facilities. In order to perform calculations related to gas and tar composition as well as modeling the plants with physical fire behavior models, many chemical and physical properties of the plant material in Table 2 were determined using a variety of methods (Table 3).

Detailed methods associated with describing the composition of the selected species are described elsewhere [64]. Early in the project we determined that conventional wood wet chemistry could only account for about one-half of the live leaf dry mass, described as hemicellulose, cellulose, and klason lignin. It was found that additional standardized tests for determining the leaf components of glucose, fructose, starch, crude protein, and minerals along with modifications to the standard tests for determining lipids, pectin, phenolics, and silicates, while accounting for interferences, was sufficient for obtaining 100% of the dry leaf mass [64]. Those components that would be the dominating mass fractions (lipids, protein, hemicellulose, cellulose, and structural lignin) were measured. Further tests on the sub-structures of hemicellulose indicated the primary presence of xylan, cellulose as being very amorphous, and lignin as having more phenolic units such as condensed tannins. These tests comprehensively show the live leaf to be sufficiently different from that of wood and biomass to merit new bench scale tests with Proximate/Ulimate Analysis, TGA, DSC, evolved gas analysis, water activity meter, and cone calorimeter for deriving the heat/mass properties for use in pyrolysis models, such as in FDS.

The development of analytical tests for pectin, phenolics, and silicates were easily adapted from the literature, whereas the test for lipids proved to be challenging. At first, our intention was to obtain extractives in the most extreme way known, including the soxhlet extraction with acetone/water. This led to significant interferences of carbohydrates, phenolics, and others which were already measured in other tests. Literature review indicated some presence of terpenoids and essential oils, leading us to use hexane solvent to dissolve those compounds. The living cell walls contained high amounts of high molecular weight lipids that needed stainless steel beads intense mashing of live leaves to lower molecular weights along with isopropanol solvent to help open up the cell walls that then, along with other classes of lipids, dissolved initially in the 50 hexane/50 isopropanol, followed by 90 acetone/10 water to ensure the dissolving of wide range of polar and non-polar lipids. Since only about 5% of the extractive dry mass was determined to be carbohydrates, and unlikely to contain protein and phenolic, given the nature of solvents the other portion (95%) can definitely be determined as lipids. The lipids have a large range of pyrolysis temperatures giving off volatiles with very high heat of combustion due to their small oxygen contents.

Table 2. Southern plant species used in pyrolysis experiments.

Common name	Scientific name ¹	Experiment	Nursery
Wiregrass	<i>Aristida stricta</i> Michx.	B (bench-scale)	Sandhill Native Growers, Arcadia, FL
Little bluestem	<i>Schizachyrium scoparium</i> (Michx.) Nash	B	Hoffman Nursery, Rougemont, NC
Inkberry	<i>Ilex glabra</i> (L.) A. Gray	B,W (wind tunnel)	Ornamental Plants and Trees, Hawthorne, FL (OPT)
Yaupon	<i>Ilex vomitoria</i> Aiton ‘Schelling Dwarf’	B	OPT
Fetterbush	<i>Lyonia lucida</i> (Lam.) K. Koch	B,W	OPT, Van Der Giessen Nursery, Semmes, AL (VDG)
Wax myrtle	<i>Morella cerifera</i> (L.) Small	B	OPT
Swamp bay	<i>Persea palustris</i> (Raf.) Sarg.	B	OPT
Sparkleberry	<i>Vaccinium arboreum</i> Marshall	B,W,F (field)	OPT, VDG
Darrow’s blueberry	<i>Vaccinium darrowii</i> Camp “Rosa’s Blush”	B,W	OPT, VDG
Longleaf pine foliage	<i>Pinus palustris</i> Mill.	B	OPT
Longleaf pine litter	<i>Pinus palustris</i> Mill.	B,W,F	The Pine Straw Store, Augusta, GA
Water oak	<i>Quercus nigra</i> L.	B	OPT
Live oak	<i>Quercus virginiana</i> Mill.	B	OPT
Dwarf palmetto	<i>Sabal minor</i> (Jacq.) Pers.	B	OPT
Saw palmetto	<i>Serenoa repens</i> (W. Bartram) Small	B	OPT

1. USDA, NRCS. 2018. The PLANTS Database ([USDA Plants Database](https://plants.sc.egov.usda.gov/) , 20 Oct 2021). National Plant Data Team, Greensboro, NC 27401-4901 USA; Radford, A.E., Ahles, H.E., Bell, C.R. 1968. Manual of the vascular flora of the Carolinas, University of North Carolina Press, Chapel Hill, NC

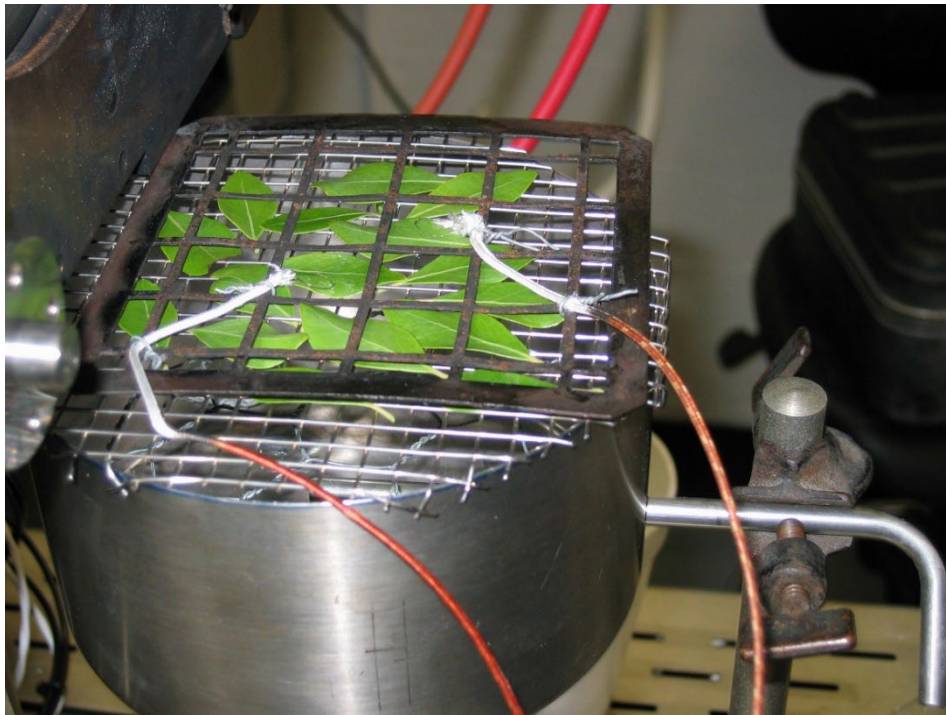


Figure 3. Specialized holder used for foliage samples in cone calorimeter.

Table 3. Summary of physical and chemical characteristics determined for southern fuels.

Property	Quantity	Reference
Moisture content	wt %	ASTM D7582
Ash content	wt %	ASTM D7582
Volatile Matter	wt %	ASTM D7582
Fixed Carbon	wt %	ASTM D7582
Sulfur	wt %	ASTM D4239
Carbon	wt %	ASTM D5291
Hydrogen	wt %	ASTM D5291
Nitrogen	wt %	ASTM D5291
Oxygen by Difference	wt %	ASTM D5291
Low Heat Value	kJ/g	ASTM E711
High Heat Value	kJ/g	ASTM E711
Water	%	ASTM D6304
Mineral content (Total N, P, K, Ca, Mg, S, Total mineral)	wt%	University of Wisconsin Forage Lab
Silicon content	wt%	FPL analytical laboratory
Mineral content (Zn, Mn, B, Fe, Cu)	ppm	University of Wisconsin Forage Lab
Proximate composition analysis (cellulose, pectin, starch, soluble sugar, hemicellulose, protein, lipids, soluble lignin, structural lignin, and silicates)	wt%	FPL analytical laboratory with HPLC and chemical kits
Density	kg/m ³	FPL greenhouse
Thickness	mm	FPL greenhouse
Emissivity		FPL greenhouse
Heat capacity of various dried residues	J/g K	DSC
Pyrolysis kinetics of components	A, E _a , and z ₀	TGA and cone calorimeter/Gpyro
Thermal conductivity, ignition criterion, & combustion properties via enhanced cone tests		

3.2.2 Fuel beds used in wind tunnel fires

Eighty-eight fuel beds 2 m long and approximately 1 m wide composed of longleaf pine needles and various combinations of fetterbush (*Lyonia lucida* (Lam.) K. Koch), sparkleberry (*Vaccinium arboreum* L.), blueberry (*V. darrowii* Camp) and inkberry (*Ilex glabra* (L.) A. Gray) (Table 1) were burned under 0 and 1 m s⁻¹ wind conditions in November 2017 (fires 3 – 49), February 2018 (50-73) and November 2018 (74-97). Fuel moisture content and fuel loading as well as ambient temperature and relative humidity in the wind tunnel varied between experiments. The living plants were well-watered resulting in normal levels of moisture content. The dead pine needle moisture content resulted from the needles equilibrating to the ambient conditions of the unconditioned building housing the wind tunnel. The longleaf pine needle dry mass ranged from 862 to 943 g uniformly distributed over the 2 m² fuel bed. Dry mass of the live plants could not be measured without killing the plants. Assuming the dry mass of the stem and foliage of a single plant ranged from 5 to 15 g resulted in a live plant dry mass ranging from 150 to 600 g in the high-density fetterbush fuel beds. Fuel beds were ignited with a line fire which spread the length of the fuel bed.

We initially planned to use a camera-based stereo photogrammetric technique [65] to describe the 3D nature of the wind tunnel fuel beds (Figure 4), but the nursery plants were smaller than anticipated and the technique was unable to separate the plants from pine needles.

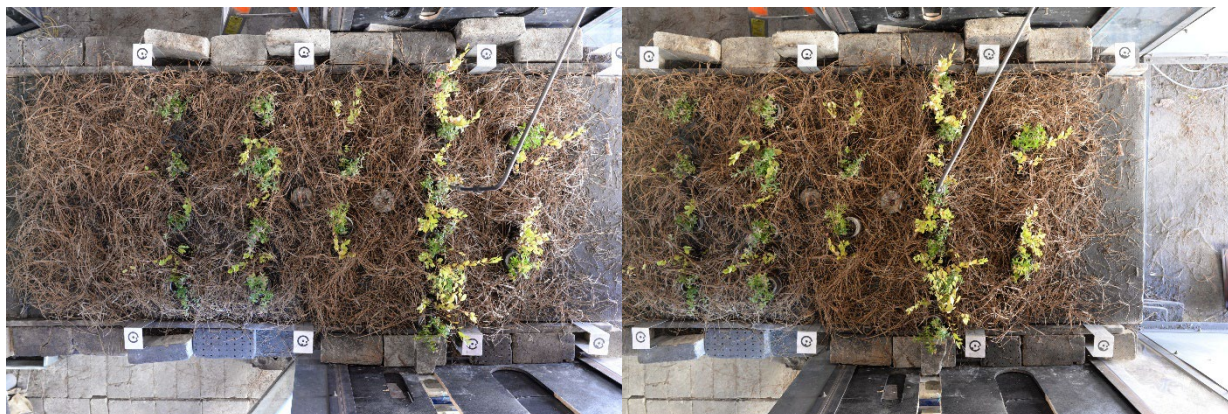


Figure 4. Vertical stereo photographs of wind tunnel fuel bed used to provide 3D image.

3.2.3 *Sampling fuels at Ft. Jackson (field scale)*

The methods outlined here contributed to baseline fuels data. The baseline data provides extensive fuel and fuel consumption information that can be correlated with pyrolysis data. Fuels were characterized at six research burn units located within three management blocks (16D, 24A, 24B) on Fort Jackson, South Carolina (Figure 5).

We used two types of sampling to assess loading of surface and understory fuels: 1) traditional, 2D methods and 2) novel 3D methods as detailed in this report and summarized in [66]. The novel 3D methods were only applied to measuring shrub fuels, which comprised a minor component of total consumption, but which may have had disproportionate influence on the pyrolysis products sampled in this study. Fuels were sampled before and after both the 2017 and 2018 burns. The two 2017 burns were considered “practice burns” to test our fuel sampling design and whether it needed modification to improve our ability to achieve our project objectives during the primary burn season of 2018. Modifications were made to our 2017 sampling design which merit explanation here.

In 2017, four paired clip plots (four prefire and four postfire) 0.5-m \times 0.5-m in size horizontally (0.25 m²), were established to estimate fuel consumption of shrubs, grass, fine downed woody debris (<7.62 cm diameter), litter, and duff in 2017 (Figure 6). Based on a preliminary analysis of the 2017 samples in these “practice” plots, the plot size was quadrupled and the sampling effort doubled in 2018 to overcome higher-than-anticipated fuel variation; i.e., eight prefire and eight postfire 1-m \times 1-m clip plots were established to estimate fuel consumption of shrubs, grass, and fine downed woody debris in 2018 (Figure 7). The paired plots were laid out systematically at 5-m (2017) or 8-m (2018) intervals, with 2 m (2017) or 6 m (2018) separating each pre- and post-fire pair. Because of the high variability in litter and duff depth observed in 2017, 16 consumption pins per paired consumption plot (Fig. 4) were added in 2018 to measure litter and duff consumption [67].

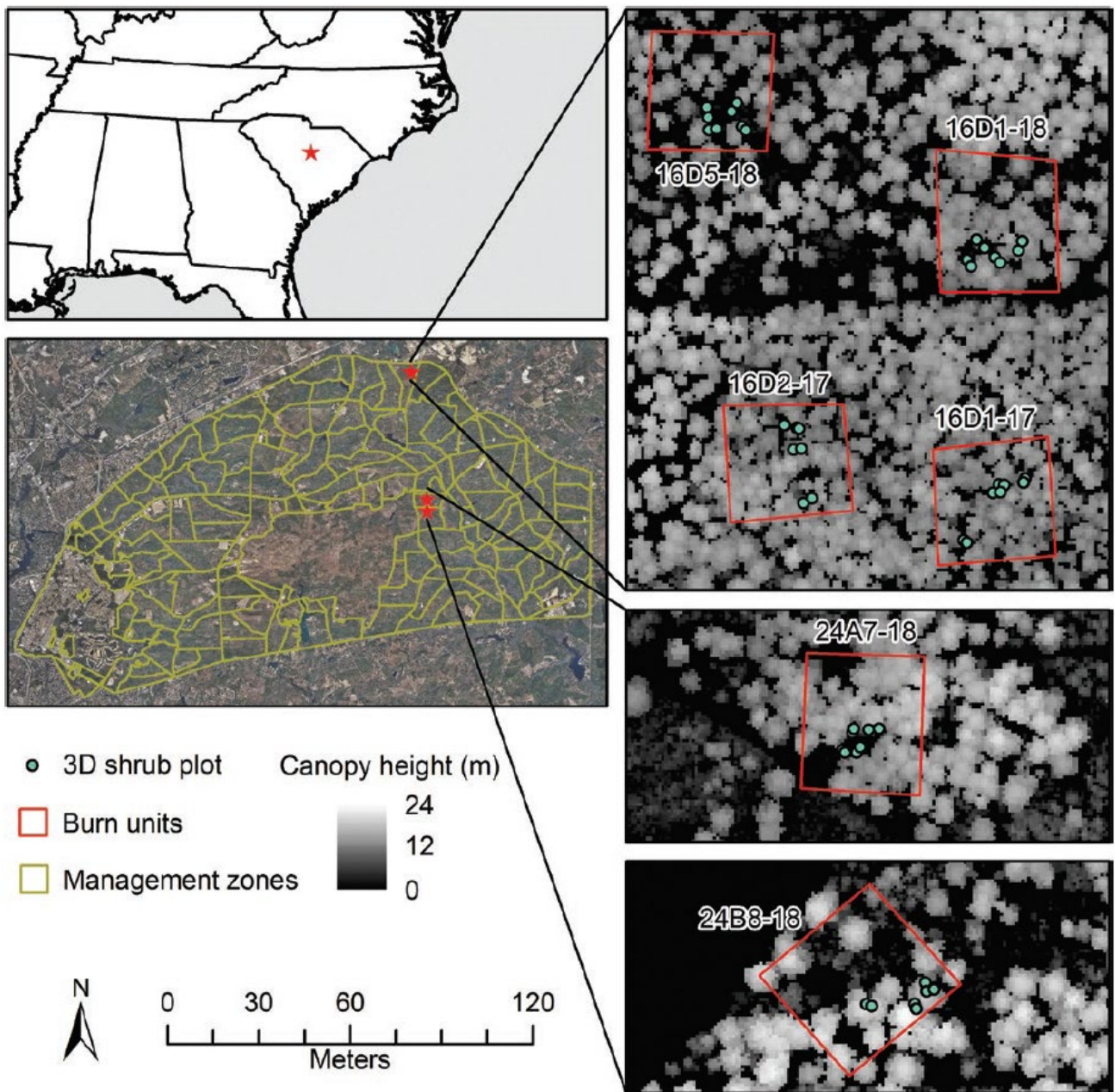


Figure 5. Location of six experimental burn units at Ft. Jackson, SC. Background image illustrates individual tree crowns from the canopy height model interpolated from airborne laser scanning data at 0.5 m x 0.5 m resolution. Figure from [66].

3.2.3.1 Traditional Fuel Loading, Moisture, and Consumption Measures

Destructive harvest sample plots (clip plots) were systematically arranged in six 40 m x 40 m burn units to measure biomass of shrubs, herbs (grasses and forbs), downed woody debris (1-hr, 10-hr, 100-hr and 1000-hr), litter and duff. In 2018, forest floor fuels (i.e., litter and duff) were measured with depth measurements (forest floor pins). We calculated loading of surface fuel strata prior to and after prescribed burn events. Prefire data were collected less than one week prior to each burn to minimize changes in the fuelbed due to vegetative growth or windfall. Post-fire data were collected within two days of the burn event to minimize changes in fuels due to rainfall and re-growth. We collected fuel moisture grab samples from the same fuel strata immediately prior to ignition. Both loading and fuel moisture data were averaged for the 40 m x 40 m research burns.

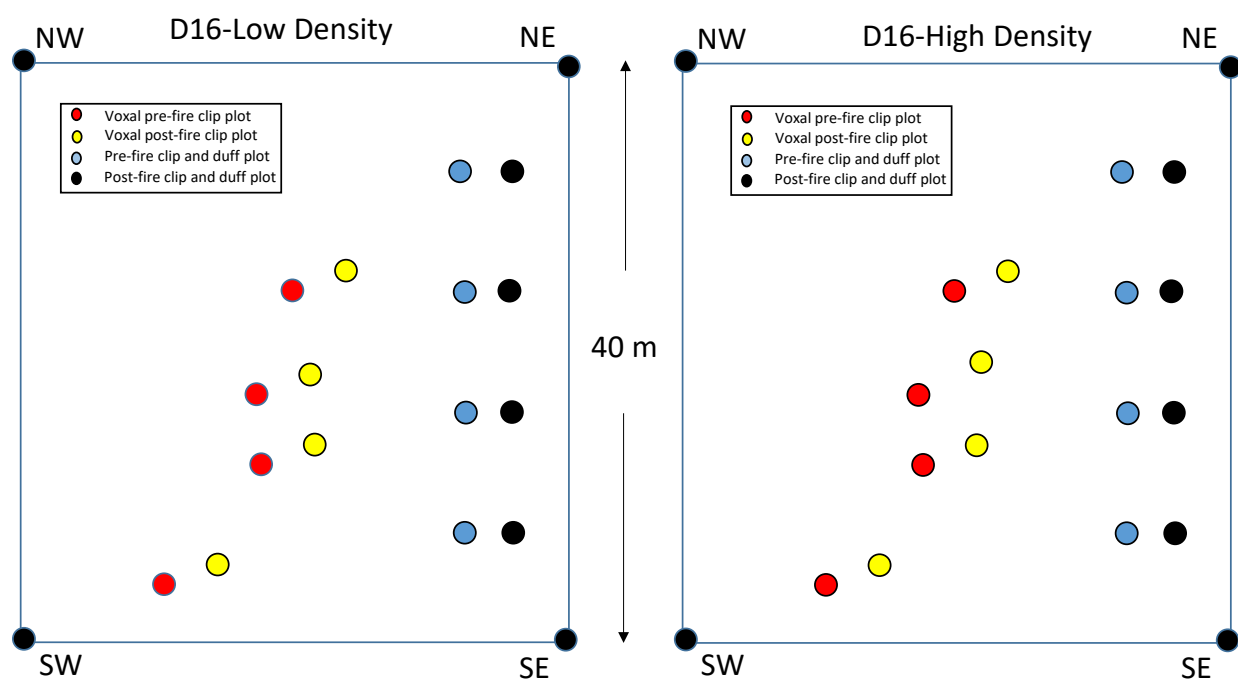


Figure 6. Plot layout for prefire and postfire fuel measurements at the two 2017 burn units: 16D2 (left) and 16D1 (right) [66].

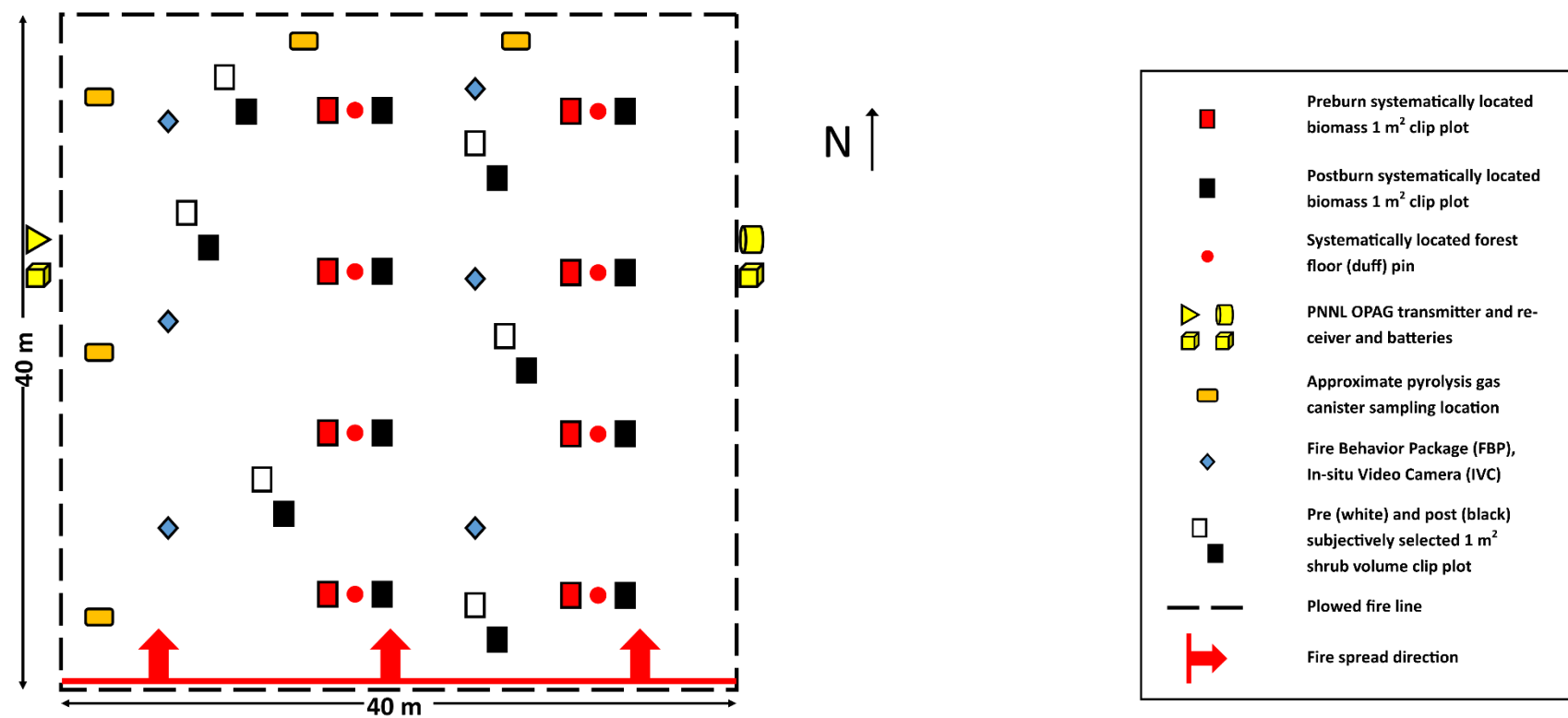


Figure 7. Plot layout for the 2018 burn units: 24A7, 24B8, 16D1 and 16D5 [66].

Forest Floor Pin Plots. Eight forest floor pins were installed for each plot in 2018 (Figure 8). For this project we placed 15.25 cm nails at half meter intervals from plot center in the four cardinal directions and marked them with red pin flags. To measure forest floor depth we pushed nails into the ground until the top of the nail was flush with the top of the surface material. When the nail could not be driven to this level we recorded the distance from the top of the nail to the top of the surface material. When obstructions like logs, tree bases, or rocks were encountered we did not install forest floor pins. The exception was when litter covered a log; in this case we drove a nail into the log to a depth where it was unlikely to fall over.

When sampling prefire forest floor depth, we measured the distance from the top of the pin to the bottom of the litter layer. When duff was encountered, we measured distance to the litter/duff interface [68], however most depth measurements were from the top of the litter layer down to mineral soil. Litter was defined as whole or broken leaves and needles, and duff as partially decomposed organic matter. Litter type was recorded for each pin and if multiple litter types were present, we recorded the dominant type within a 2 cm area around the nail. When no litter or duff was present, we recorded MS for mineral soil. After the fire, each nail was re-located and the distance from the nail head to the duff surface or mineral soil was re-measured. Using a representative bulk density for the litter and duff of a forest floor type for the region [69], the prefire depth and postfire reductions in litter and duff were converted to loading. Ash was not classified as litter or duff because it does not represent unburned biomass.

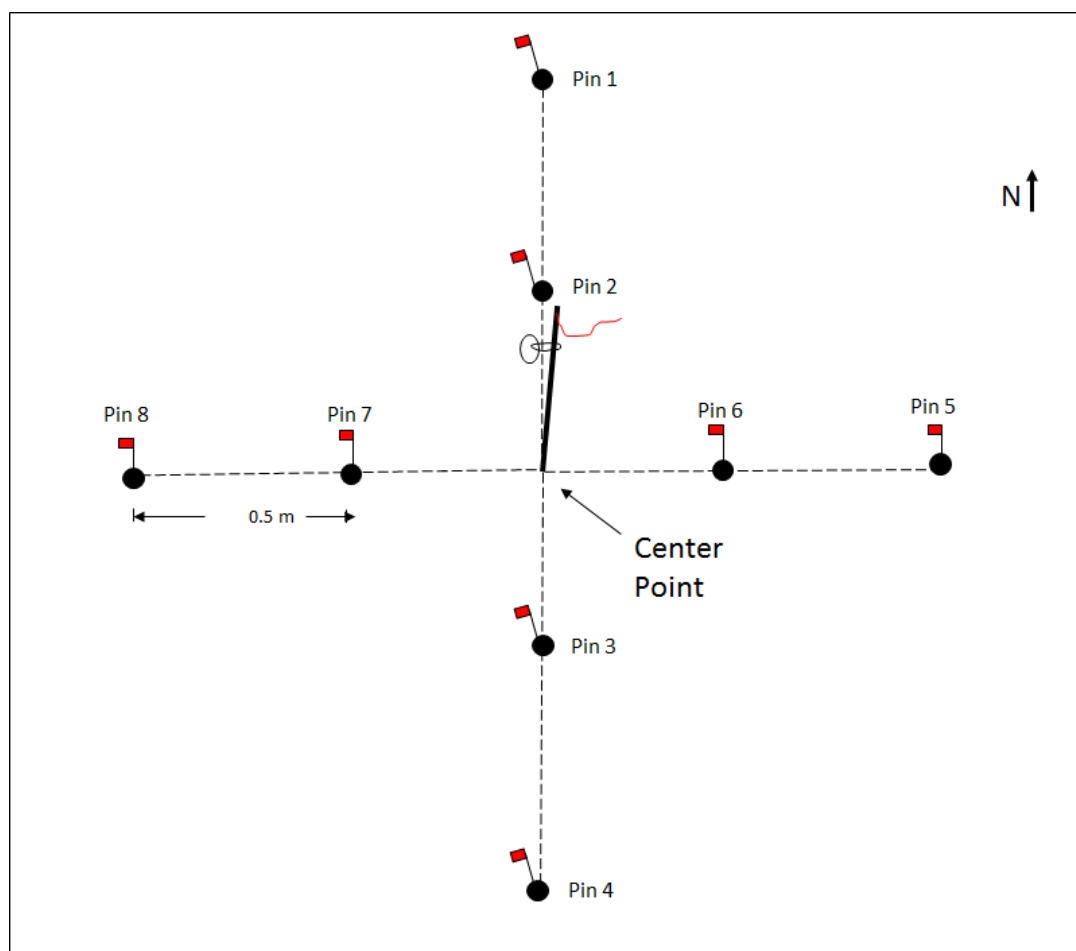


Figure 8. Forest floor pin plot layout.

2-Dimensional Biomass Inventory. Clip plot boundaries were marked with a one-inch diameter PVC

frame with an inside length of 1.0 meter (in 2018). The frame was placed flush with the forest floor and a plot photo was taken from 2 m south of the plot. Downed woody debris and standing vegetation fuel strata were clipped at ground level and sorted into labeled paper bags. Vegetation was clipped along a vertical plane extending 1.83 m up from the clip plot boundaries in order to obtain a volumetric sample. The procedure for sampling prefire and postfire clip plots was the same. Sample bags were stapled shut, tracked on a data sheet, and placed in large durable garbage bags for transport.

Day-of-Burn Fuel Moisture. Ten fuel moisture samples for each fuel stratum were collected before ignition to correlate fuel moisture levels to consumption. Fuel moisture samples were placed in 12" x 12" 4-millimeter thick zip-lock plastic bags. Samples fully occupied bag volume and care was taken to completely seal bags. Maximizing sample bag volume reduces the percent error associated with handling and weighing samples. Fuel moisture samples represented the composition of species, particle sizes, and arrangement in burn units. For instance, graminoids had greater cover than forbs and consequently, our herbaceous samples contained more grass than forb clippings. We collected individual samples from a large area (~ 400 m²) to reduce the influence of microsite characteristics. Once a bag was sufficiently filled with material and fully sealed, we recorded the time and date of the collection on the bag and placed it in a garbage bag for safe transport.

The wet weight of all samples was recorded within one hour of collection and again in the evening in order to test if wet weights of fuel moisture samples changed over the course of a day. We did not sample 1000-hr fuels in each unit, as those fuels were not always present. All samples were collected within 1 hour prior to ignition, and fine fuels (i.e., litter, suspended litter, 1-hr) were collected during the ignition of a burn unit.

Drying Procedures. Fuel loading and fuel moisture samples were shipped to the Pacific Wildland Fire Sciences Laboratory in Seattle and oven-dried in convection ovens for 48 hours at 70° C within two weeks of collection. Within 7 days of collection samples were opened and allowed to air dry. Fuel consumption of the shrubs, grass, and small down woody debris was calculated by subtracting the postfire loading from the prefire loading for each fuel category.

Plot Geolocation. At each plot, the center of the forest floor pins (Figure 8) and the NW corner of post-fire clip plots were monumented with welding rods and the NW corner of prefire clip plots were monumented with conduit. Each conduit was marked with red flagging and sequentially numbered steel tags. When post-fire clip plots were close to the 3D shrub fuel plots (described below), they were offset 1 to 2 m to the west to avoid interference.

We took photos from 2 m south of every clip and forest floor plot. Photos were taken from a standing position at eye level. Plot coordinates were collected with a resource-grade Global Navigation Satellite System (GNSS) receiver (Geo7X, Trimble Inc.) at the plot monuments (welding rods, metal conduit) located at the northwest corners of clip plots and in the center of forest floor pin plots and 3D shrub fuel plots.



Figure 9. 3D shrub fuel plots.

3.2.3.2 3D Shrub Fuel Plots

Four paired 3D shrub plots (four prefire and four postfire) per burn unit were subjectively selected within each burn unit, choosing sparkleberry shrubs (or shrub clumps) of comparable size in close proximity. Shrubs were clipped beginning from the shrub top (<2 m) and clipping at 0.1-m vertical intervals down to ground level (Figure 9). All shrub material was clipped, bagged, and labeled separately by vertical strata at 10 cm intervals. Frame design, construction, and 3D sampling protocol are further described in [70], and details with regard to RC-2640 can be found in [66].

The 3D shrub plots were marked by metal conduit in the center of the shrub plot, for more accurate geolocation of the shrub (or shrub clump) selected for sampling. Reflective tape was used at the top of the conduit to make it more visible in the TLS point cloud. The ability to see the conduit in the point cloud data proved critical, as the geolocation even after differential correction could be off by 1-2 m, which is a larger error than the 0.5m x 0.5m sample plot. Therefore, the conduit locations were considered preliminary and just used to find the correct conduit in the point cloud; later, each 3D shrub plot conduit location was adjusted such that it aligned with the “virtual” conduit visible in the point cloud. This markedly improved the accuracy of the relationship between the 3D shrub plot biomass samples and point cloud data [66].

3.2.3.3 Terrestrial Lidar Scanning (TLS)

The TLS used for the pre- and post-fire point cloud data was a LMS 511 (SICK Inc.). The portable TLS system was set up on a tripod for ease of movement to positions in the burn unit less affected by tree boles or dense shrub clumps that cause occlusion. A minimum of eight scans per burn unit were collected, including at each plot corner plus the mid points between plot corners along the square boundary. In 2018, a minimum of two scans per 3D shrub plot were collected; sometimes, three to four scans were required to ensure that shrubs were scanned without occlusion by trees or other objects. Before scanning a new area, four to eight reflective targets were positioned around the periphery of the scan area; these targets remained stationary and provide relative tie points for merging point clouds from separate scans as the TLS was moved around the plot. Further details may be found in [66].

3.2.3.4 Unmanned Aerial Vehicles (UAV)

Quad-copter drones equipped with 3-band or 4-band digital cameras were flown above treetop level at both the 2017 and 2018 burns. Photogrammetric points were derived from these stereo images using Structure from Motion (SfM) techniques and explored to characterize understory fuels. However, the point cloud data proved too noisy to do so reliably so the UAV datasets were removed from the present analysis which focused on the TLS point cloud datasets alone. We conclude that photogrammetric point cloud data lack the canopy penetration capability of lidar, and thus have greatly reduced sensitivity to understory and surface fuel variation beneath the overstory. We recommend UAV-mounted lidar as a remote sensing tool with great potential for providing useful information about understory and surface fuel conditions.

3.3 **Objective 1 – Measurement of pyrolysis products**

While most pyrolysis work applied to wildland fire is based on slow-heating, in wildland fire reported air heating rates near foliar fuels ranged 30 to 5000 °C s⁻¹ [2,71–74]. While a fuel particle will not necessarily heat at the same rate as the adjacent air due to its thermal properties [75] and the nature of the heat transfer method [76,77], the rate of temperature rise in wildland fuel particles is more akin to fast pyrolysis rates. Higher heating rates and high temperatures are also typical of pyrolysis in wood-based structures [78].

3.3.1 *High and low-heating rate experiments (BYU)*

A flat-flame burner (FFB) apparatus was used to study pyrolysis of foliar samples from the plants in Table 2. The apparatus described in [79] was increased in size and a glass chimney was added to eliminate entrainment (Figure 10) [80]. A horizontal fuel sample was attached to a horizontal rod and was suspended in the middle of the glass duct. The rod was attached to a Mettler¹ Toledo XS204 scale. The scale was programmed to record the change of mass by a LabView code using a National Instruments SCXI-1000 module. The temperature at the level which the sample was loaded was measured by a K-type thermocouple with 0.38 mm bead diameter (OMEGA Engineering). The flat-flame burner structure was placed on wheels which enabled the structure to be moveable. The flat-flame burner was operated under fuel-rich conditions with an equivalence ratio of 1.13. The fuel-rich condition prevented the presence of O₂ in the hot (810 °C) post-flame gas, providing pyrolysis conditions inside the glass duct. A mixture of methane (CH₄) and hydrogen (H₂) was used as the fuel and air was used as the oxidizer. The flow rates of gases were 258.8 L/min, 16.63, and 26.56 for air, hydrogen, and methane, respectively. The post-flame gases were mainly N₂, CO₂, H₂O, CO, and H₂. The pyrolysis sampling system consisted of a glass funnel connected to stainless steel tubing wrapped with heating tape and insulation with hot and cold traps to separate the pyrolysis products in two stages.

Pyrolysis products were analyzed using (1) a Thermo Scientific™ Trace™ 1310 gas chromatograph (GC) equipped with, a thermal conductivity detector (TCD), and (2) a HP 5890 GC combined with a HP 5972 mass spectrometer (MS). High molecular weight hydrocarbons which are not detectable by GC-MS were condensed in the hot trap. In the cold trap, the remaining hydrocarbons were condensed to be analyzed by GC-MS after solvent extraction using dichloromethane GC grade from Sigma-Aldrich, Inc. The non-condensable gases were collected in Tedlar® gas collection bags and analyzed with GC-TCD. Additional measurements included: (1) mass of the sample versus time; (2) gas temperature above the burner at the level of the sample (3) surface temperature distribution of the sample using a FLIR mid-infrared camera, (4) temperatures of the transfer line at four points; (5) radiative, convective, and total heat flux. Three replications of each experimental combination were run for a total of 342 observations. Additionally we used FTIR technology from PNNL in some of

¹ The use of trade or firm names in this publication is for reader information and does not imply endorsement by the U.S. Department of Agriculture of any product or service.

these experiments but were unable to extract meaningful data from the measurements due to a variety of issues [67]. Particulate matter was not collected in the present study since it forms from small pieces of char and condensed gases. The objective of the project, as defined in the original proposal, was to characterize pyrolysis product yields and to characterize the composition of both the permanent gases and some of the condensable gases produced during primary and secondary pyrolysis.

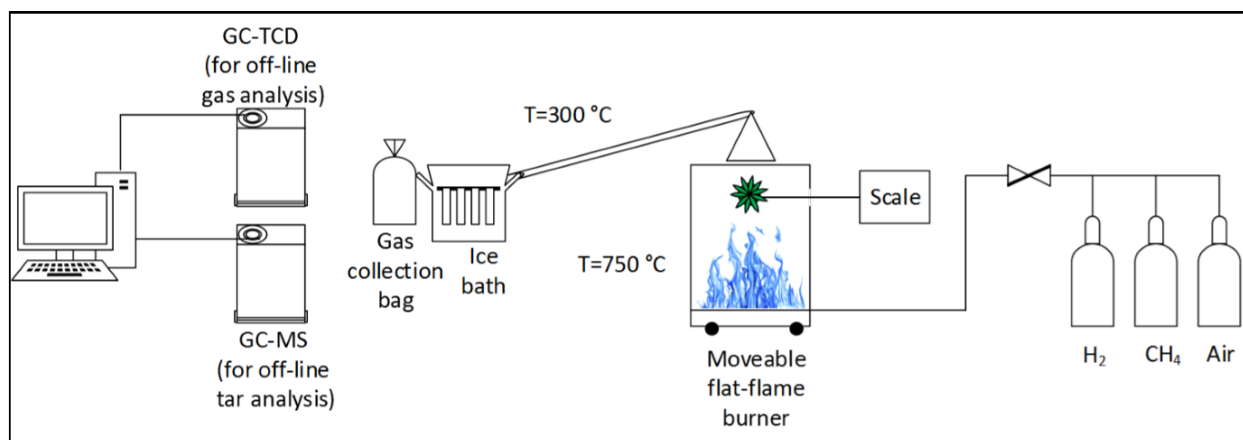


Figure 10. Flat-flame burner setup used to measure pyrolysis products resulting from heating southern wildland fuels at a high rate.

An apparatus used previously to measure pyrolysis products from oil shale [81,82] was used to measure pyrolysis products at slow heating rate and low temperature to generate gas and tar samples (Figure 11). Prior to performing the pyrolysis composition experiments, a study was performed varying temperature (400–800 °C), slow heating rate (5–30 °C min⁻¹), and carrier gas flow rate (50–350 ml min⁻¹) to find the optimum conditions for maximum tar yield. The results showed that the highest tar yield was obtained at a temperature of 500 °C, heating rate of 30 °C min⁻¹, and sweep gas flow rate of 100 ml min⁻¹ [83]. Approximately 2 grams of sample were positioned in a U-like 19 mm stainless steel tube placed in the heater. A small flow of 300 ml min⁻¹ of N₂ was used to purge the pyrolysis gases and provide an oxygen-free environment for pyrolysis. Gas condensers were constructed by packing fine glass wool into test tubes and using rubber stoppers to close the top. The stoppers had two holes drilled into them through which 6.35 mm stainless steel tubing was tightly fitted. The gases entered and passed through the glass wool before exiting. Four condensers were placed in an ice bath filled with dry ice to aid condensation. Tar vapors were condensed in condensers and were analyzed by GC-MS after solvent extraction using GC grade dichloromethane. A Thermo Scientific™ Trace™ 1310 (GC) equipped with a thermal conductivity detector (TCD) was used with an HP 5890 GC combined with an HP 5972 MS. Non-condensable gases were collected in gas sampling bags for transfer to gas analysis devices. The reaction was stopped at 500 °C and the apparatus was cooled to prevent further reaction. Three replications of experiments in this apparatus resulted in 87 observations of pyrolysis composition.

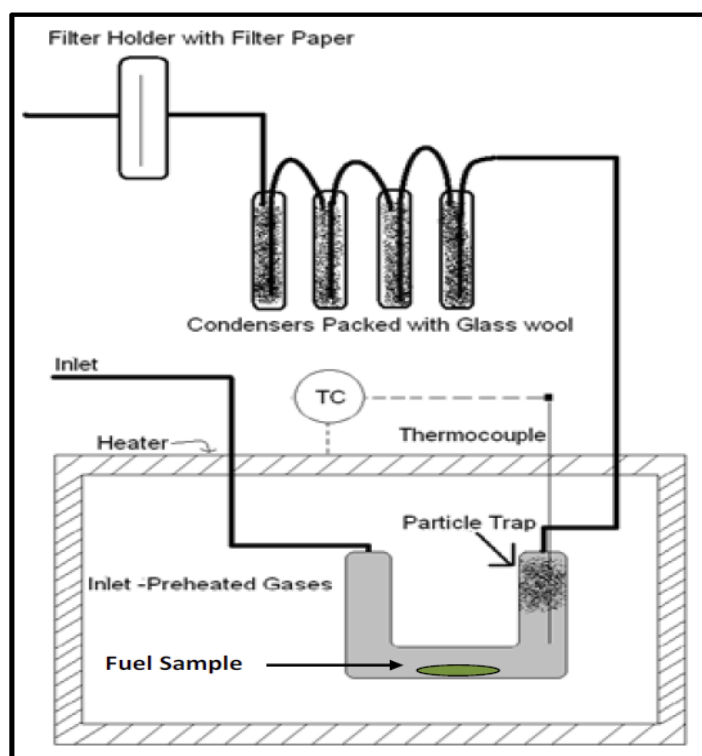


Figure 11. Schematic of programmable heater used for generating pyrolysis products from southern wildland fuels at a low heating rate.

3.3.2 Optical absorption methods for detection of pyrolysis gases

Regardless of whether via FTIR or via laser methods, the basic principles of an infrared spectrometer measurement are seen in Figure 12. In either case the spectrometer consists of the IR light source (i.e. a laser or a broadband IR source such as a glow bar), a wavelength selector or modulator, the sample, and an infrared-sensitive detector such as a cooled mercury–cadmium–telluride (MCT) semiconductor. For all experiments a background spectrum must be recorded or approximated; this is the I_o reference spectrum. This is followed by recording the sample (I) spectrum; in the present case this is where the smoke either drifts into the beam (for an open path experiment) or is let into the gas cell (for a laboratory experiment). The data typically consist of the reference or I_o spectrum (where no sample, or only a “blank” is present), the sample (I) spectrum, and finally the absorbance spectrum A which are related by the Beer-Lambert Law: $A = \epsilon l C = -\log_{10} (I/I_o)$ where ϵ is the infrared extinction coefficient as a function of wavelength (an intrinsic property of the molecule) [84] (Figure 12). The use of spectroscopy and the Beer-Lambert law is extensive throughout science, especially in chemistry and physics. The program used for quantitative spectral analysis during the course of the SERDP program was the MALT5 program [85,86] which is now commercially available.

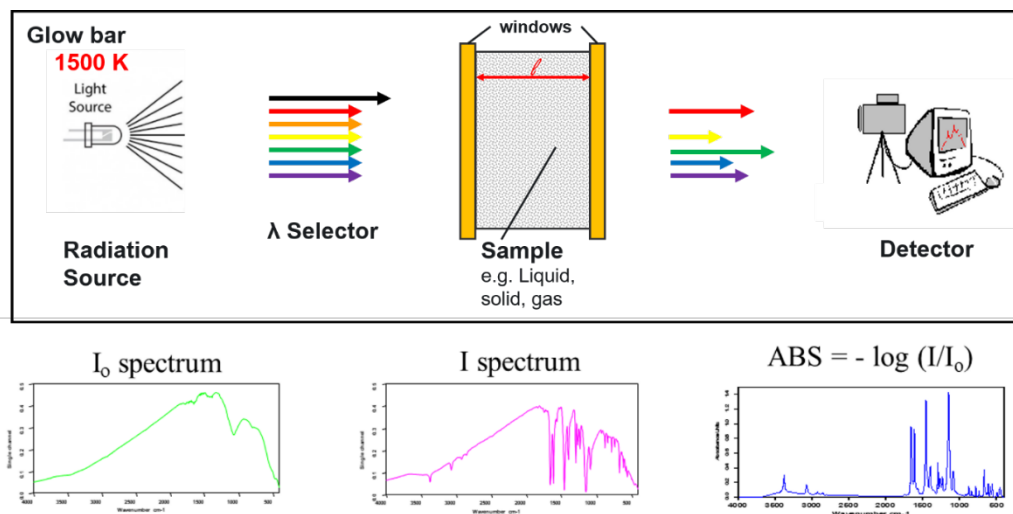


Figure 12. Cartoon representation of generalized infrared spectrometer.

The MALT program analyzes the spectra once they have been converted to absorbance mode as seen in the lower right-frame of Figure 12. The data from fires, however, are never “pristine” spectra such as those seen in the Figure – there is always instrumental noise and there are always multiple chemical species (analytes) in the beam of the infrared instrument; spectra with multiple analytes thus tend to be very “busy” or “cluttered”. To disentangle such spectra the MALT software uses both broadband reference spectra from the PNNL database [87–91] and absorption line intensities from HITRAN [92] [in units of $\text{cm}^{-1}/(\text{molec} \times \text{cm}^{-2})$] to iteratively fit a simulated spectrum to the measured spectrum by optimizing the fit so as to minimize the mean-squared residual, i.e. the difference between the measured and simulated spectra. Parameters such as path length, resolution, apodization, temperature, pressure, spectral domain, target compounds and overlapping compounds are all used as inputs to the spectral fit. The MALT analysis technique has previously been used in both open-path and extractive FTIR systems with active sources [93–97].

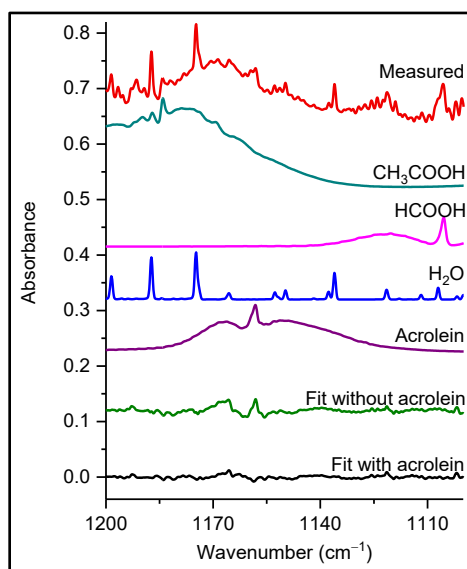


Figure 13. Measured IR spectrum (May 2018) and individual spectral contributions for the major components and associated residual with and without acrolein included in the fit.

As an example of the complexity of the spectral analysis, Figure 13 displays a very congested biomass burning spectrum (red trace) with individual contributions for several species included in the fit [contributions for furfural ($\text{C}_4\text{H}_3\text{OCHO}$), acetaldehyde, CH_4 , and C_2H_4 are included, but not

plotted] as well as the residual with and without acrolein ($\text{C}_3\text{H}_4\text{O}$) included in the fitting process. All spectra are at 0.6 cm^{-1} resolution and have been offset for clarity. The calculated mixing ratio of acrolein in this measured spectrum is 99.9 ppm. When acrolein is not included in the fit, features near 1168 and 1158 cm^{-1} that resemble acrolein are observed in the residual spectrum as seen in the green trace. When acrolein is included in the fit, the features are removed. Part of the confirmation strategy is thus to process the experimental spectra with/without the target gas in the fit and then to visually inspect the residual. In each case an IR-active vibrational mode is used for each species in the fit, typically the species' strongest band in the longwave IR window, along with a list of species with overlapping bands in that domain. Throughout the study, MALT was used to identify multiple gas-phase species emitted during the burns and quantify the gas mixing ratios via spectroscopy, five gases for the first time as detailed below.

As previously reported by RC-1649 [98], the spectral characteristics of many gases associated with biomass and wildland fuels are unknown. RC-1649 substantially increased the number of gases associated with smoke emissions in the spectral database. As part of the present project, spectra for additional gases were developed or improved and are now available in the spectral database [99]. The experimental methods and evaluation of results are presented in detail elsewhere [89,100,101]. The gases added to the database include hydroxyacetone, crotonaldehyde, methyl vinyl ketone as well as the *ortho*-, *meta*-, and *para*- isomers of xylene. It is unknown if these compounds are produced by pyrolysis or, if produced, occur in detectable concentrations. However, the spectra are now available for use in the processing algorithms which will be used to identify the pyrolysis gases by FTIR instruments.

3.3.3 *Measurement of pyrolysis in a wind tunnel experiment*

In the 88 wind tunnel fires (Table 10) pyrolysis gases were sampled in real-time using a variety of methods and instruments (Figure 14, Figure 15, Figure 16, Figure 17).

3.3.3.1 Canister sampling

Sampling pyrolysis gases in an open environment is a challenge as pyrolysis is a transient process. The location and timing of the gas sample probe is critical to effectively capturing pyrolysis products. In the wind tunnel experiments, the sampling approach was to fill a sample canister with multiple small aliquots of pyrolysis gases and sample a separate canister to characterize flaming emissions for comparison. Installed along the length of the fuel bed was an array of 8 stainless-steel sample tubes, connected to a pump/manifold collection system with separate switches to control each point (Figure 14). As the flame progressed along the fuel bed the spotter called out when to initiate and end sampling, with a short sampling interval at each tube. One canister at the first point collected flaming emissions only, a different collection method was used for this canister – flaming emissions were collected for 30 seconds well before the flame front reached the sample probe. One pyrolysis canister per fire was sampled, filled with the small aliquots of pyrolysis gases.

Pyrolysis Sampling Points Setup

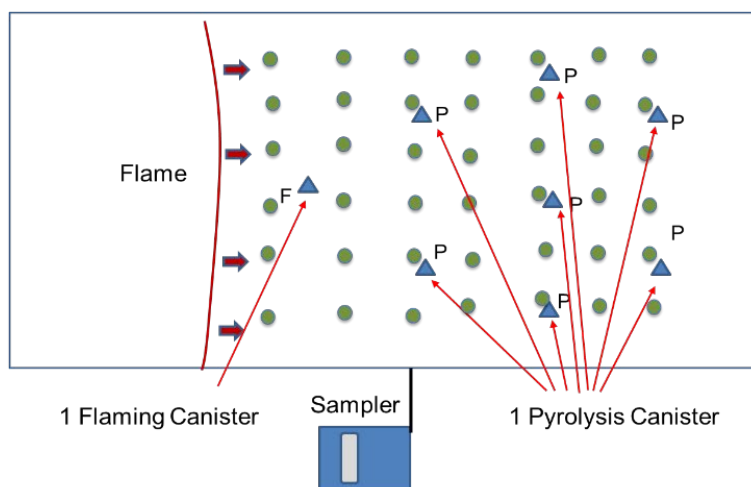


Figure 14. Setup of wind tunnel canister sample points.

The gas samples were collected in 850 ml stainless steel SUMMA canisters. Background air samples were taken during the experiment and analyzed. The canister samples of emissions were analyzed (EPA method TO-14A) for CO₂, CO, CH₄, and C₂ to C₅ hydrocarbon gases with an Agilent model 7890 gas chromatograph configured with two columns running simultaneously. A 1/8" diameter, 2 m Carbosphere packed column with a nickel catalyst methanizer was used for analysis of CO₂ and CO. flame ionization detector (FID). The second column, a 0.53 mm diameter x 50 m length Agilent AI/S column, separates hydrocarbons and methane. Both columns go to FID detectors and run simultaneously. Chromatogram data were collected and processed by Agilent OpenLab software. A multipoint set of 3 standards bracketing the sample concentrations were analyzed with each set of samples to construct a standard curve for each compound. Based on the integrated peak areas, the sample concentrations were calculated from the standard curves and written into a spreadsheet for analysis. NIST SRM gas standards for CO, CO₂, CH₄, and propane were run each day to validate the standard curve. Duplicate GC runs of canisters were performed for each sixth sample. For measurement of H₂ concentrations a Trace Analytical RGA3 reduction gas analyzer was used. This is a chromatographic instrument with a molecular sieve column, and UV mercuric oxide detector that provides highly sensitive precise measurement of trace level H₂. The range is 0 – 10 ppm H₂, most samples were diluted with UHP nitrogen to be in this range. An H₂ standard (Scott Specialty Gases) was used for calibration. Chromatograms of H₂ from this instrument were collected and integrated with Agilent OpenLab software interfaced to the instrument. On a subset of canisters with significant detectable pyrolysis gases, GC/MS analysis was performed using an Agilent 6890 GC with an HP-5 .320mm x 30 m column, He carrier gas, and Agilent 4590N MS detector.

Fire-integrated emission factors were calculated using the carbon mass balance (CMB) approach [102] in which the concentrations of emitted carbon-containing species are a proxy for the mass of dry fuel consumed during the fire. The “fire-averaged approach” was used in this first attempt to capture pyrolysis gases instead of using temporal sampling. The emission factor for species *I* emitted by a fuel with carbon mass fraction (x_c) of the dry fuel mass is given by:

$$EF_i = \frac{m_i}{\Delta CO + \Delta CO_2 + \Delta PM_C + \sum \Delta HC} x_c$$

where m_i is the mass of species *I* emitted, PM_C is the mass of particulate-phase carbon and $\sum \Delta HC$

is the sum of the total mass of C contained in gas-phase hydrocarbons, estimated as the sum of the measured C_{1-6} hydrocarbons. Δ denotes the amount above background atmospheric concentrations.

Combustion efficiency (CE) – the fraction of fuel carbon converted to carbon as CO_2 – was estimated by modified combustion efficiency $MCE = CO_2 / (CO + CO_2)$ [103–105]. Pure flaming has an MCE near 0.99 while the MCE of smoldering varies from 0.65 to 0.85) and is typically near 0.90 for prescribed fires that are a mix of the two phases. It is important to note that as a result of the present study, MCE has been recently shown to be an index that is not statistically independent of other wildland fire emissions [106] and should not be used as a predictor for other emission factors. As pyrolysis gases arise before combustion, the utility of this ratio is unknown for pyrolysis.

3.3.3.2 FTIR detection

During the November 2017 and November 2018 wind tunnel burns we coupled FTIR instruments. For the November 2018 burns only, a quantum cascade laser (QCL) direct-probe system was added as well. No measurements were taken as part of the February 2018 burns. A conceptual layout and photograph of the instruments coupled to the tunnel are seen in Figure 15. In February 2018, a TELOPS instrument was also deployed, but the sensor saturated due to proximity to the flame so no useful data were extracted (Figure 16).

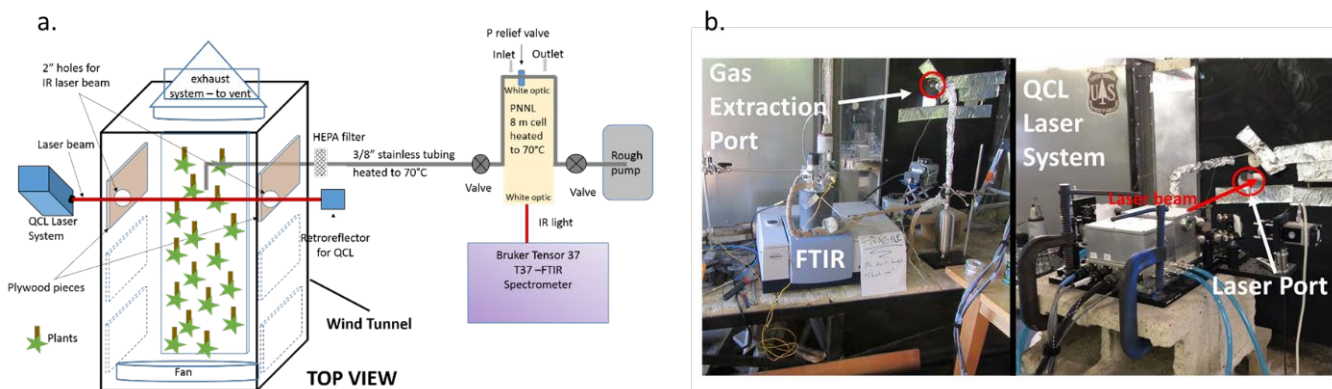


Figure 15. (a) Cartoon rendering of block layout for the extractive T37 spectrometer/gas cell with inlet tubing. The gas cell and FTIR system are shown as yellow and purple boxes, respectively. Also shown is the Quantum Cascade Laser system (blue); the laser system directly probed the flame. (b) Both systems on site at RFL.

The extractive Bruker Tensor 37 (T37) spectrometer/gas cell system was coupled via heated inlet tubing (70 °C) to extract the gases before, during and after the passage of the flame front down the wind tunnel. The White cell was held at approximately 55 °C to keep the gases and particulates from condensing inside the cell. Data were analyzed as described in 3.3.2. The chief research objective was to determine the specific (small) gases associated with the different phases of consumption of the plants, particularly the pyrolysis phase. Ideally, we wished to understand if there were differences in the gas composition for the different plant species, e.g., sparkleberry vs. yaupon. An added objective was to use temporal resolution in the acquisition for some of the experiments to try to understand the composition during the different phases of the burn.

For the wind tunnel experiments, the resolution of the T37 was set to 4 cm^{-1} , the acquisition mode was set to double sided, forward-backward, the apodization function was Blackman-Harris 3-Term, and phase correction mode was Mertz [107] with a zero filling factor of 2. To increase temporal resolution, the number of scans was set to 1 with continuous measurements to obtain a spectral time resolution of 0.2 seconds. This instrument configuration is referred to as an “extractive FTIR” because it consists of a probe with 3/8” metal tubing connected to extract the gas into the White cell

using a roughing pump. The probe was placed above a plant during measurements (Figure 17) and gases were extracted from the wind tunnel into the gas cell before, during and after the flame had passed the plant. Absorbance spectra (A) were collected in real time. The reference measurement was collected when the instrument and gas cell were purged with high purity nitrogen gas; N_2 does not absorb in the IR.

The other FTIR instrument used for gas phase measurements was the Bruker OPAG-22, which is an open path gas analyzer. Unlike the extractive FTIR, this instrument is non-disrupting since it does not remove any of the gases from the wind tunnel, i.e. it does not perturb the sample. The OPAG was mounted on a tripod on one side of the wind tunnel with the glow bar IR source on the opposite side. The path between the OPAG and the source was 1.2 m and was directly in line with a row of plants (Figure 16). The OPAG is equipped with a KBr beam splitter and a Stirling-cycle cooled MCT detector. Interferograms were collected in the range of 4000 to 0 cm^{-1} at a resolution of 2 cm^{-1} and at an acquisition mode set to double-sided forward-backward. To achieve better time resolution between measurements, interferograms were converted to spectra via post process procedures. The apodization function was Blackman-Harris 3-Term [108] and phase correction mode was Mertz [107] with a zero-filling factor of 2. The number of scans per measurement was set to 1 and the measurements were repeatedly collected to obtain a time profile with a resolution (time between spectra) of 0.53 seconds. The third instrument deployed was the TELOPS, an infrared hyperspectral imaging system that has high spectral and spatial resolution. Like the OPAG, the TELOPS was mounted on a tripod on one side of the wind tunnel with a blackbody source on the opposite side (Figure 16).

FTIR spectral analysis has been, and continues to be, both versatile and powerful. However, the method is somewhat limited in its time response. The best temporal resolution demonstrated in the wind tunnel fires was on the order of 10-30 seconds. For rapidly moving flame fronts there can be ambiguity as to the fire phase from which the gases were captured (pyrolysis v. combustion, combustion v. smoldering). The flames in the wind tunnel and field tend to be more chaotic in nature and there may be some cross-contamination of the pyrolysis gases with flame gases produced in the combustion reactions. One of the project goals was to try to better decouple the signals/phases to better understand the discrete pyrolysis and combustion processes. To achieve both better temporal resolution and better sensitivity, a QCL system was used in the wind tunnel for the November 2019 experiments. In previous applications QCL systems had demonstrated increased sensitivity as well as increased temporal resolution as compared to other optical systems [e.g. 109]. Whereas the FTIR requires seconds to minutes per spectrum, the QCL can collect >100 spectra/second. The QCL system was deployed in tandem to the FTIR system but with a different optical configuration. Instead of an extractive tube, the QCL IR open path laser beam directly traversed the gas plume inside the tunnel via optical ports. The QCL laser data acquisition was synchronized with time stamps as to associate the data with the different phases of the fire processes: pre-heating, pyrolysis, flaming, smoldering, etc.

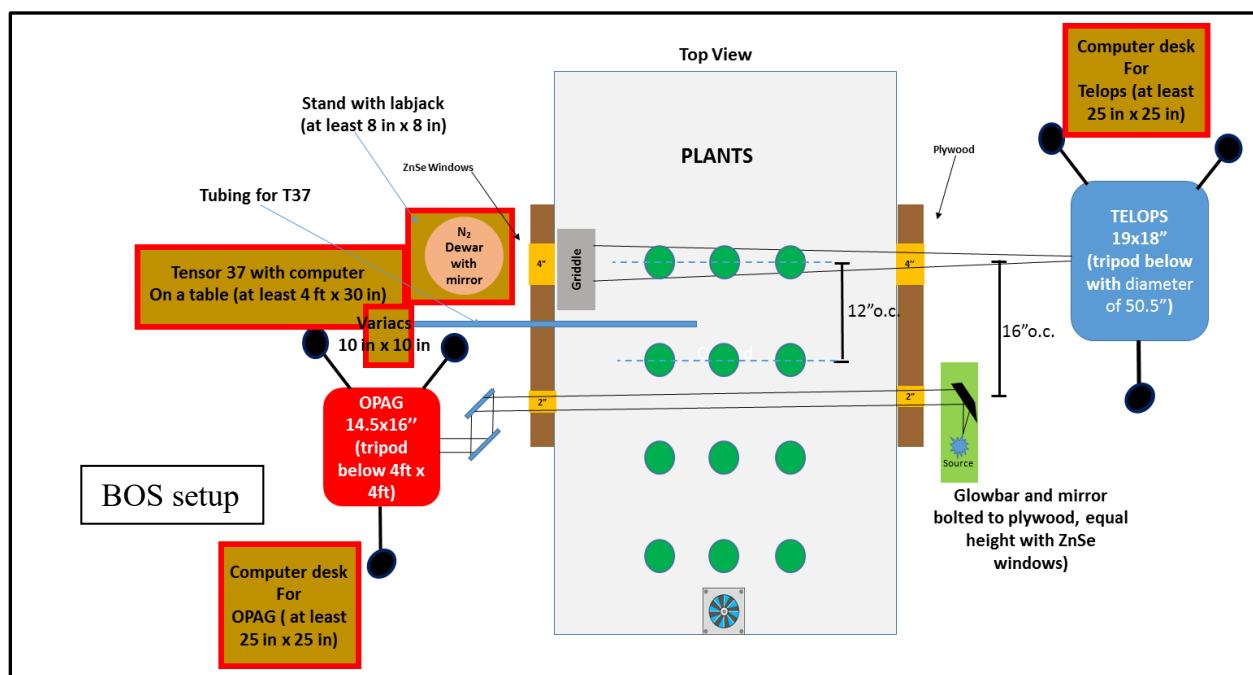


Figure 16. Setup of 3 instruments used to measure composition of gaseous pyrolysis products in mixed fuel beds of longleaf pine needles and small shrubs.



Figure 17. Fuel bed composed of longleaf pine needles and *Lyonia lucida* plants. Sample probe to collect pyrolysis gases for the Bruker Tensor 37 is indicated by the arrow.

3.3.4 Measurement of pyrolysis in Ft. Jackson field burns

A trial field deployment was conducted at Fort Jackson in May 2017 in order to test techniques in area 16D at Ft. Jackson. As a result of the deployment, the fuel measurement and canister gas sampling techniques were modified. Details of the trial deployment can be found in the Interim Technical Report [67]. The revised methods were used in 4 experimental burns at the Tall Timbers Research Station Pebble Hill Plantation prior to the Fort Jackson burns to gain experience. A 2.5 m sampling probe of 6 mm stainless steel tubing connected to the sampling package with flexible stainless tubing. The sampling package consists of a swing Piston KNF Neuberger Pump, 12-volt gel cell rechargeable battery, stainless steel tubing to a pressure relief valve and gauge. The flow rate to fill the canisters was 15 liters/ minute. There were 2 identical canister sampling packages, with one for 0.85 l SUMMA canisters (25 psia) for GC analysis (3.3.3.1), and a second package for 3-liter SUMMA canisters (20 psia) for FTIR analysis (3.3.3.2). The reliability of SUMMA canisters used in

both the wind tunnel gas collection and in the Ft. Jackson field sampling have been evaluated in several studies and have been found to be acceptable [e.g. 110–112]. The sampling strategy was to identify plants along the edge of the plot that had sufficient foliage to ignite and allow the chance of sampling pyrolysis. As the flame front advanced, we positioned the probe ahead of flame front as it approached (Figure 18). We sampled at the base of approaching flame, taking short interval sample aliquots when it was likely that pyrolysis was occurring.



Figure 18. Gathering pyrolysis phase gas samples using an extractive wand coupled to a pump and gas canister (not seen) during prescribed burns at Ft. Jackson, SC, May 2018.

3.3.5 *Compositional data analysis (CoDA)*

As part of this project we have established that smoke emissions and pyrolysis mixtures meet the characteristics of so-called compositional data and that compositional data analysis (CoDA) techniques should be applied using data that originated from earlier SERDP projects [106,113,114]. Pyrolysis mixtures are inherently multivariate and the quantity of each part of the composition (mixture) is relative to the other parts of the composition. This multivariate, relative nature of the data is also true for other aspects of fire data such as fuel composition and species composition. In CoDA today, in order to use familiar statistical techniques such as exploratory data analysis, linear regression, multivariate analysis of variance, time series analysis, etc., the mainstream approach is to translate compositions from the simplex (the sample space where they reside) to the ordinary real space using log-ratio transformations [115–118]. The linear algebra theory supporting these transformations also provides the underpinnings for “standard” or “classical” statistics routinely used in the sciences [119]. Several texts describe the theory and methods of compositional data analysis [115,118,120–123].

As this is a relatively new field of statistics that we have introduced to the wildland fire community and most of the team are not familiar with it, only a portion of the data in this report were analyzed using CoDA techniques. In the initial publications from the BYU pyrolysis studies, hypotheses H_1 to H_7 were tested using familiar methods that were applied to the original data (mole fraction or mass fraction) [63,83,124,125]. The BYU data have been reanalyzed in light of our recent awareness of this field of statistics [126] and additional manuscripts are currently in development and review for the wind tunnel and field fires. Applying CoDA methods to analyze the compositional aspects of the data consisted of estimating values of a composition that were below detection limits (BDL) using techniques suitable to the relative nature of compositional data with the *zCompositions* package [127,128]. The data were then transformed into various log-ratios using the *Compositions* package [115] and standard statistical techniques such as multivariate analysis of variance and logistic

regression were applied to the log-ratios. The log-ratio approach eliminated the possibility of “spurious correlation” [120]. Spurious correlation can occur when analyzing data expressed as proportions and the results of the numerical analyses are influenced by the presence or absence of one or more parts of the composition [129]. These analyses were performed using the R statistical package [130]. Multivariate analysis of variance (MANOVA) was used to test hypotheses H₁ to H₇. Scientifically meaningful log ratios of groups of pyrolysis compounds known as balances [131] were formed (Table 4) and the effects of heating mode and rate, moisture content, and plant species were tested. Pairwise comparisons between the levels of these experimental factors were made while controlling the false discovery rate to keep the experiment-wise Type 1 rate at 0.05 [132]. The relationship between pyrolysis composition in the bench-scale data and the lab and field scale data (hypothesis H₈) was examined by 1) using the wind tunnel pyrolysis canister data to predict which field canister data resulted from pyrolysis using logistic regression and 2) using MANOVA and pairwise comparisons to determine if scale was significant.

Table 4. Schematic illustrating the construction of balances of groups of compositional parts of scientific interest determined by sequential binary partition. “+” denotes parts in numerator and “-” denotes parts in denominator of balance (an additional 74 balances not shown completed the full partition). PG denotes permanent gases (CH₄, CO, CO₂, H₂).

	Compositional Part or Group														
	CO	H ₂	CO ₂	CH ₄	Phenol	Phenol Deriv	Acid	Alcohol	Aldehyde	Ketone	Benzene	2-ring	3-ring	4-ring	5-ring
Tars vs PG ¹	-	-	-	-	+	+	+	+	+	+	+	+	+	+	+
CO vs Other PG	+	-	-	-											
H ₂ vs CH ₄		+		-											
Tars vs Phenol					-	+	+	+	+	+	+	+	+	+	+
Primary vs Other Tars						-	+	+	+	+	-	-	-	-	-
Other Tars vs Phenol derivs						-					+	+	+	+	+
Acid, Alcohol vs Other HC							+	+	-	-					
Aldehyde vs Ketone									+	-					
Acid vs Alcohol							+	-							
Benzene vs Rings											+	-	-	-	-
2&3 vs 4&5 Ring												+	+	-	-
2 vs 3-Ring Tars												+	-		
4 vs 5-Ring Tars														+	-

3.3.6 Summary statistics

Several measures of central tendency exist (e.g. mean, median). There are several types of means as well. Unlike the arithmetic mean $\left(A_n = \frac{1}{n} \sum_{i=1}^n a_i \right)$ which can be used with both positive and negative

numbers, the geometric $\left(G_n = \sqrt[n]{\prod_{i=1}^n a_i} \right)$ (for proportions) and harmonic $\left(H_n = n / \sum_{i=1}^n (1/a_i) \right)$ (for rates)

means can only be used with positive values. It is well-known that $A_n \geq G_n \geq H_n$. Oftentimes the arithmetic mean, the mean that is most familiar of these three, has been reported in many of the

published articles resulting from this project. While the values of these means are often close, in this report, both the published arithmetic mean values as well as recomputed values applying the mean that is appropriate to the measure are reported. Specifically, the geometric mean is reported for fuel loading and pyrolysis gas composition since these data are compositional. The harmonic mean is computed for various rates such as rate of spread, heat fluxes and activation energies.

3.4 Objective 2 – Determining effects of heat transfer

3.4.1 Bench-scale tests

In this study, the pyrolysis of 14 live plant species native to the forests of the southern United States was investigated at four heating conditions using (1) a low heating rate pyrolyzer (Figure 11), (2) a thermal gravimetric analyzer (TGA) at slow heating rates, and (3) a flat-flame burner (FFB) apparatus under three different heating modes (Figure 10). The pyrolyzer was operated at $0.5\text{ }^{\circ}\text{C s}^{-1}$ up to final temperatures as high as $800\text{ }^{\circ}\text{C}$ using intact leaf samples of approximately 1 gram in order to collect sufficient amounts of pyrolysis products (light gases and tar) for subsequent analysis. The TGA was operated with 2 mg samples of leaves at heating rates of 10, 20, and $30\text{ }^{\circ}\text{C min}^{-1}$ up to final temperatures of $800\text{ }^{\circ}\text{C}$ in order to determine kinetic rate coefficients for models of pyrolysis. The FFB system was operated with whole leaf samples (approximately 1 gram) in three different modes of heating: (1) radiation-only, where the plants were pyrolyzed under a moderate heating rate of $4\text{ }^{\circ}\text{C s}^{-1}$ (radiative flux of 50 kW m^{-2}) in a stream of N_2 , reaching a final temperature of $550\text{ }^{\circ}\text{C}$; (2) convection-only, where the FFB apparatus was operated in fuel-rich mode with a sample heating rate of $180\text{ }^{\circ}\text{C s}^{-1}$ (convective heat flux of 100 kW m^{-2}), reaching a final temperature of $750\text{ }^{\circ}\text{C}$; and (3) a combination of convection and radiation, where the plants were exposed to both convective and radiative heat transfer mechanisms (heating rate of $\sim 195\text{ }^{\circ}\text{C s}^{-1}$ with a final temperature of 800°C) in fuel-rich post-flame gases (Figure 19). Foliage from watered living plants, unwatered air-dried plants, and dead longleaf pine litter were exposed to the different heating rates.

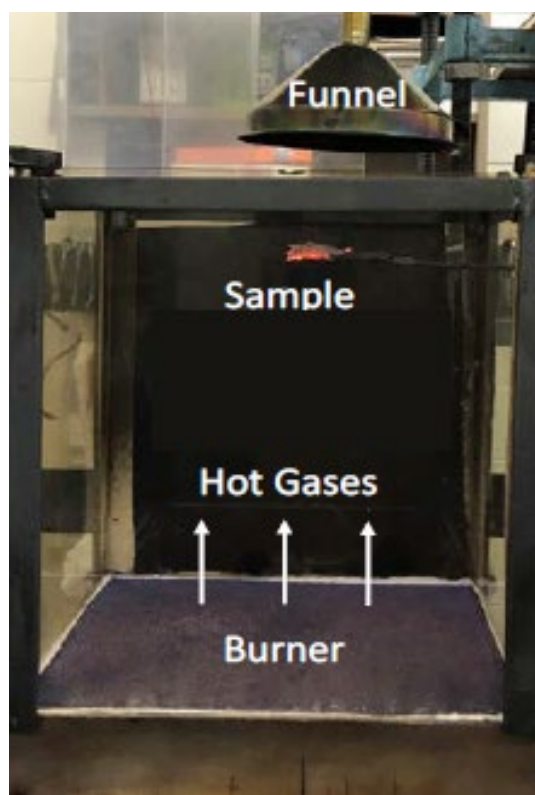


Figure 19. Flat-flame burner heating a pyrolyzing foliage sample.

3.4.2 Wind tunnel fires

In the wind tunnel experiments, the objective of heat transfer measurements was to estimate convective and radiative fluxes to the live plants contained in the fuel bed. While UCR has used a variety of techniques previously to describe the flow field around experimental laboratory fires [133–135], the use of smoke tracers and introduced particles in the present experiment was precluded by the gas sampling objective. The TPIV technique [133] could not be used because the large glass windows in the wind tunnel are opaque to the infrared spectrum. A background-oriented Schlieren (BOS) approach was selected to determine the flow field in the flame and surrounding the plants [136–138]. The BOS setup (Figure 20) was located upwind of the PNNL gas sampling instruments (Figure 16) to visualize hot gases around a turbulent diffusive flame and help to describe the flow fields around the fire as it spread in a porous vegetative fuel bed. Convective flux to the plants in the wind tunnel was estimated using BOS [139]. Total and radiant heat fluxes at the top of the fuel bed were measured using 2 Schmidt-Boelter sensors (Figure 21). A longwave infrared (LWIR) camera provided a nadir view of the fuel bed and measured radiance from the fuel bed will be converted into temperature. A system of K-type thermocouples was created to mimic temperature profile around a single plant and was deployed in a subset of the wind tunnel fires (Figure 22). The thermocouple tree system was replaced with 14 thermocouples, which were scattered through the fuel bed. The configuration of this thermocouple setup can be seen in Figure 23. This configuration created the opportunity to record the temperature of the gases at the moments that they were analyzed by the FTIR system.

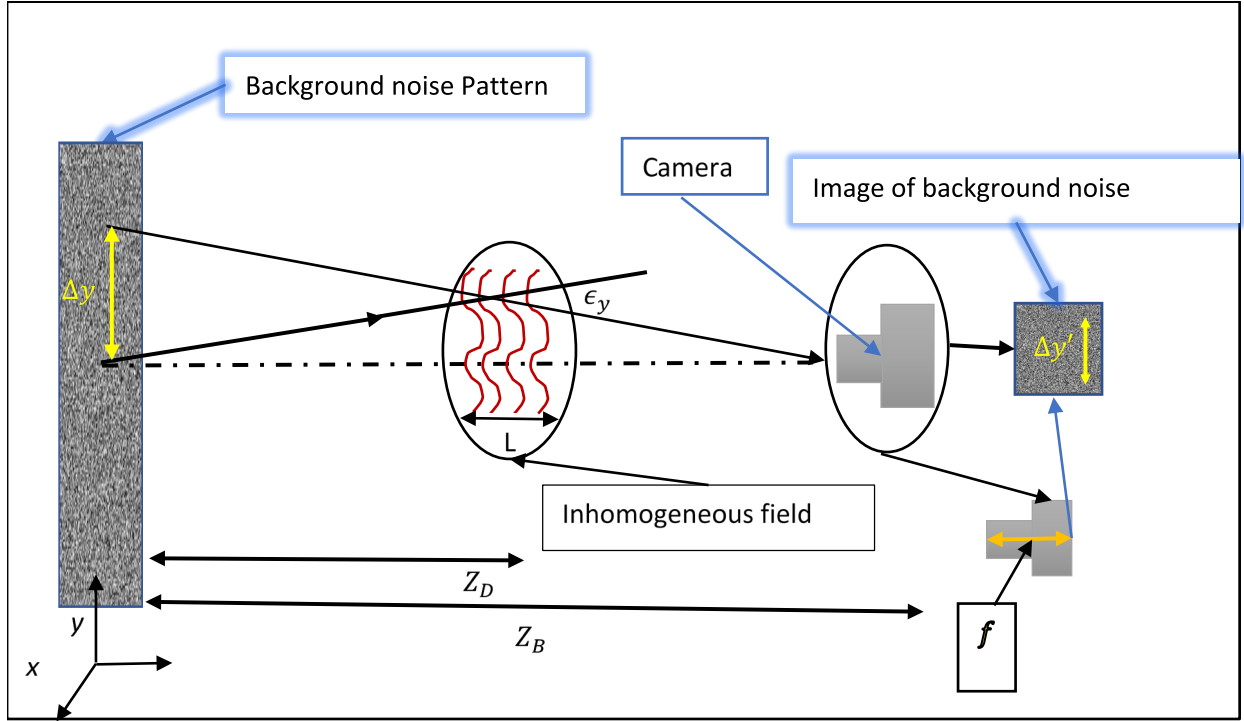


Figure 20. Simple schematic of background oriented Schlieren configuration used to nonintrusively estimate the flow field surrounding pyrolyzing plants. Z_D is the distance of the flame from the background noise pattern, Z_B is the distance of the camera lens from the background, ϵ_y represents the deflection angle caused by the flame-generated distortion, L is the flame zone width, f is the focal length of the camera, $\Delta y'$ represents displacement in the camera sensor plane and Δy represents displacement in the background plane.

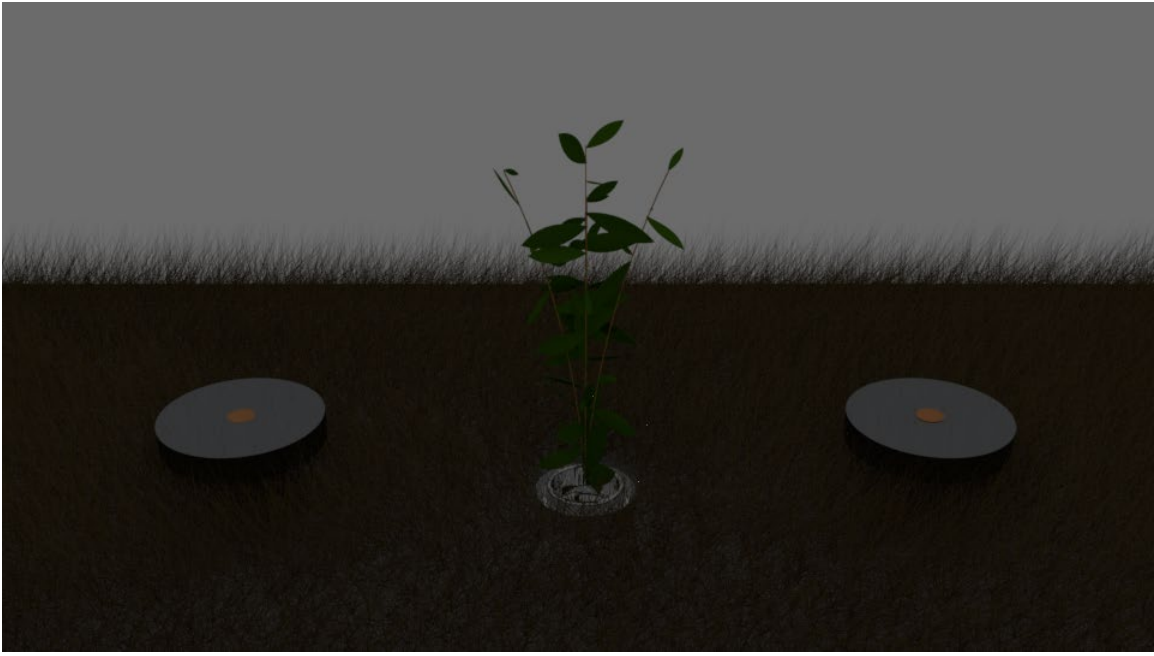


Figure 21. Sensor setup to measure plant mass loss on an electronic scale with total and radiant heat fluxes using Schmidt-Boelter type thermopiles (grey cylinders).

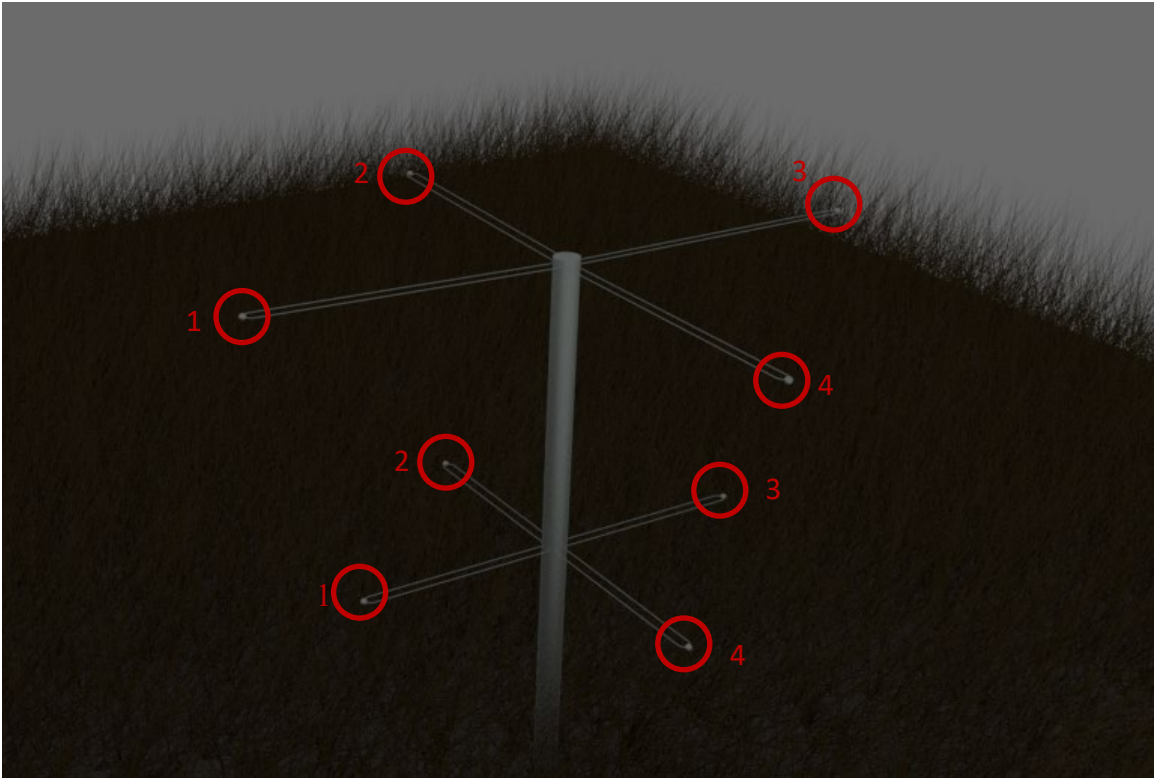


Figure 22. Type K thermocouple tree designed to measure air temperature around a single plant in the wind tunnel experiments.

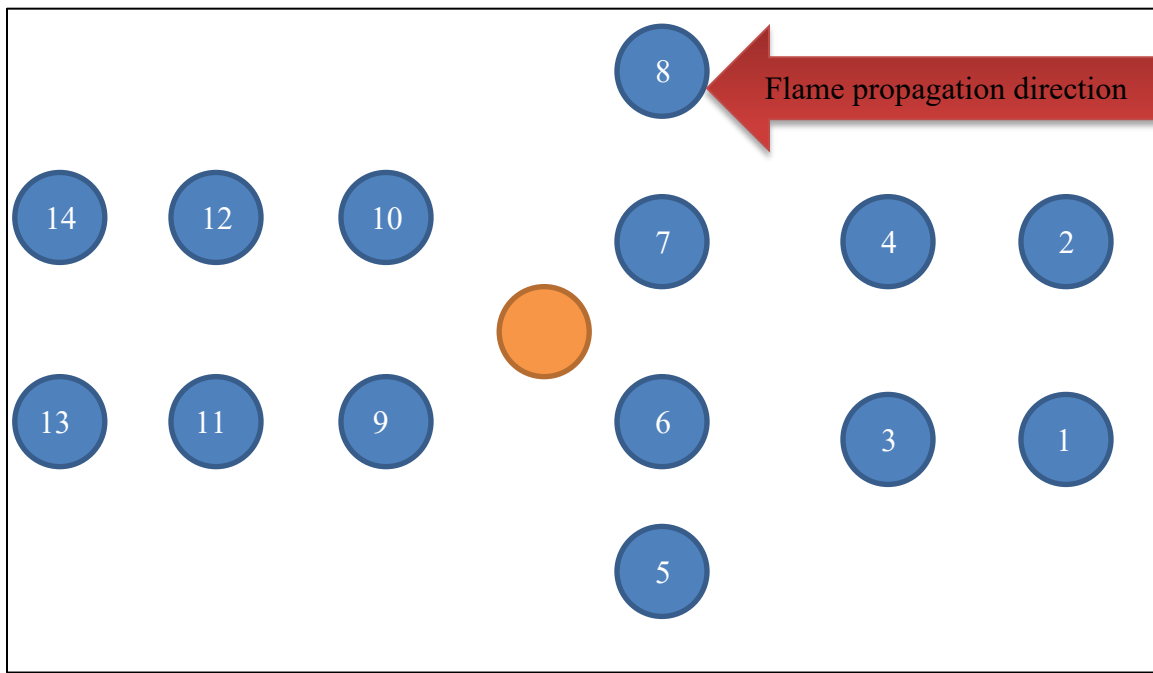


Figure 23. Air temperature thermocouples placed in a subset of the wind tunnel experiments. The blue circles represent thermocouples placed in the fuel bed and the brown circle represents the plant scale.

3.4.3 *Ft. Jackson field burns*

3.4.3.1 Horizontal radiative and convective fluxes from flames

Actual measurements of fire intensity benefit wildland fire behavior research and modeling by providing data for evaluating and developing fire models. Past measurements consisted primarily of observations of rate of spread, gas temperatures and fuel consumption and have been both field based [140–142] and laboratory based [2,43,142]. Such studies provided useful data and observations; however with the advent of modern numerical computers, the complexity of wildland fire models has increased [143–145]. However quantitative measurements of energy and mass transport in wildland fire have been relatively sparse. The reasons are likely related to the risks and hazards to humans and equipment associated with wildland fires as well as the high degree of uncertainty in the weather and fuel conditions. Additionally, only recently has the technology become readily available at a cost that allows scientists to capture the desired measurements over the range of possible conditions. Some studies have been published that focus on relating fire intensity to emissions [102], others on statistical modeling of fire behavior [146].

For burns conducted at Pebble Hill Plantation and Fort Jackson a field deployable, fire resistant, programmable sensor array mounted in a fire-resistant enclosure and coupled with a video imaging system was used to characterize energy release from flames [147]. The sensor system was coupled with a digital video system. Two enclosures comprise the system. The primary sensor package is termed the Fire Behavior Flux Package (FBP). It measures 27 cm by 15 cm by 18 cm and in its current configuration weighs approximately 5.3 kg (Figure 24). Various enclosure materials have been used from mild steel, stainless steel and aluminum; the latest design consists of 3.7mm thick aluminum welded at the seams. A 12 volt 2.2Ah sealed lead acid battery or 8 AA dry cells provide power to the logger. The dataloggers used are Campbell Scientific® model CR1000. The dataloggers are capable of logging over one million samples, providing 20 hours of continuous data logging at 1hz. This logger is user-programmable and accepts a wide range of analog and digital inputs and outputs. It is thermally stable and has been relatively insensitive to damage incurred in shipping and

handling. The second part of the system is a fireproof enclosure housing a video camera and is termed the In-situ Video Camera (IVC). The IVC measures 10 cm by 18 cm by 19 cm and is constructed of 1.6 mm aluminum with a weight of approximately 1.8 kg (Figure 24). The front of the IVC has two circular windows nominally 45 and 20 mm in diameter. A double lens configuration of high temperature PYREX® glass and a second lens of hot mirror coated glass (Edmund Optics) is mounted in the ports. This multi-layer dielectric coating reflects harmful infrared radiation (heat), while allowing visible light to pass through. Both the FBP and IVC are designed to be mounted tripods. The preferred tripods consist of wall galvanized 2.5 cm diameter mild steel pipe with one extendable leg to facilitate deployment on slopes. Once mounted on the tripods a layer of 2.5 cm thick ceramic blanket enclosed in a single layer of fiberglass reinforced aluminum foil is wrapped around the boxes to provide further thermal protection. The packages are typically deployed so that the sensors are directed towards the oncoming fire front. The FBP is oriented to “look” at the expected fire approach direction, while the IVC is positioned to image both the FBP and approaching fire front. Once the FBP and IVC’s are mounted on tripods, they are powered up. The FBP’s have LEDs to indicate that the logger is indeed running, the IVC’s also have an LED to indicate that they are running and have entered “sleep” mode when they are being used with the remote automatic trigger system.

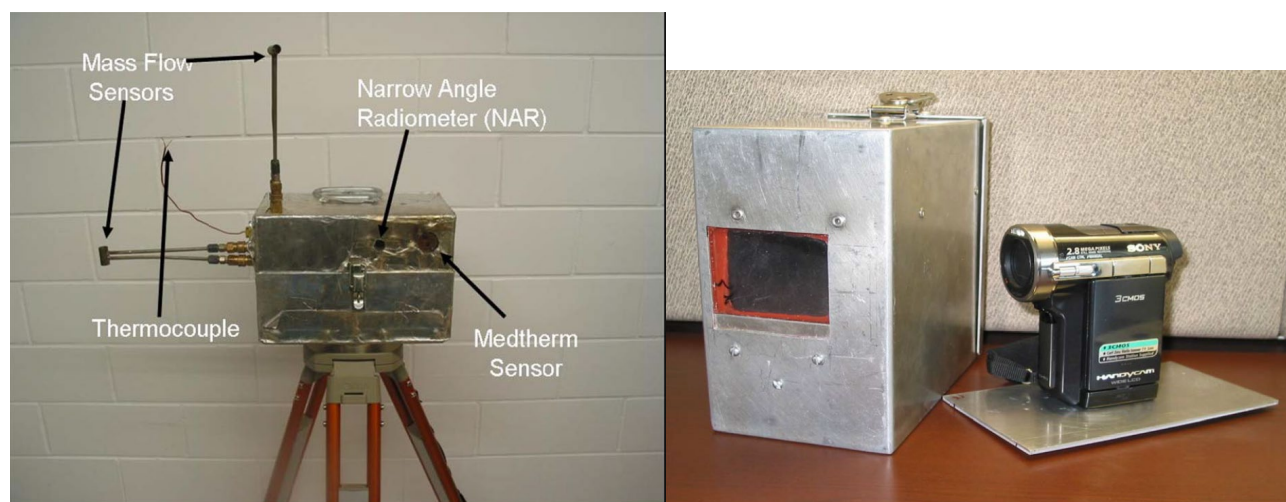


Figure 24. Example of Fire Behavior Package (left) and Insitu Video Camera package (right) deployed to measure horizontal heat fluxes and record visible flame and smoke movement in wildland fires.

3.4.3.2 Leaf Temperature Measurements

In each of three Fort Jackson burns live sparkleberry shrubs were sampled for leaf temperature in advance of the flaming front up to the point where leaves were consumed. FLIR Inc. A-655 thermal imagers were used to capture radiant heat flux from the leaf surfaces from a near nadir perspective (Figure 25). The camera range was set for high gain which meant temperatures over 500 °C would saturate the image. However, lower gain would mean losing measurements at temperatures relevant to pyrolysis and tissue desiccation. Camera distance was approximately 2 meters from the measured leaf surface giving individual pixel sizes of approximately 6 mm². A 1 m² steel frame (1x1 m) delineated the shrubs in two adjacent plots and was used to calibrate pixel size. Data were collected at 1 Hz. In each 1 m² plot, two circular sub-samples of 30 pixels were averaged over unobstructed leaves towards the top of a sparkleberry bush with the view comprised of approximately 6-8 leaves. Fire radiative power was recorded at 1 second intervals, leaf temperatures were derived by rearranging the Stefan-Boltzmann equation assuming an emissivity of 0.98. High-definition visual imagery was also captured to document the timing and location of the gas sampling tube (3.3.4) and

the flaming front.

3.5 Objective 3 – High-fidelity physics-based modeling

The physics-based modeling, while initially proposed to include all three experimental scales (Figure 2), was not done for the field experiments for 2 primary reasons. Firstly, as the intent of the field experiments was to collect as many pyrolysis samples as possible within the time onsite, the experimental plots were small and ignited using closely spaced strip head fires thus effectively negating free-burning fire spread. Secondly, many of the physical properties necessary to use FDS were unavailable and would have been assumed resulting in questionable results.



Figure 25. Boom-mounted IR camera used to measure shrub leaf temperatures during prescribed burns at Ft. Jackson, SC.

3.5.1 *Gpyro & FDS bench-scale*

Three modeling studies relevant to the FFB experiments (3.3.1) were performed to gain further

understanding of pyrolysis, ignition and flaming of solid fuels representing manzanita (*Arctostaphylos glandulosa*) leaves. While this species is not native to the southern U.S., its overall characteristics are like southern species such as inkberry, fetterbush, and swamp bay. All simulations were validated against the experimental data previously obtained using the FFB [80,148,149].

In the first study [150], the leaf was oriented horizontally in the hot upward convective stream exiting the FFB. Pyrolysis, ignition and combustion of a thin solid fuel representing a broadleaf were studied [150]. The computational configuration resembled a previous experimental FFB setup [148] where horizontally oriented manzanita leaves were burned. This setup is considered an earlier version of the FFB apparatus used in the present SERDP project. To conduct the modeling, first, a critical modification was made on Gpyro3D [151], and then it was coupled with Fire Dynamic Simulator (FDS) for simulations [152].

Gpyro3D and Gpyro2D by default assume that heating does not change the volume of the object (no shrinkage or swelling). It additionally assumes that the total volume of the condensed phase, i.e., solid or liquid, does not change in a computational cell. The combination of these two assumptions creates inconsistencies when there is a volatilizing condensed phase species such as moisture. It also imposes an unphysical algebraic constraint between the apparent densities of the char and the charring condensed phase species. We relaxed the latter assumption here by introducing volumetric averaging operations and accounting for the void formation because of moisture loss or charring. Such an operation is defined by

$$\bar{\alpha} = \frac{1}{\delta V} \int_{\delta V} \alpha dV$$

where δV is a finite volume and α indicates a typical property of the condensed phase such as density. Accordingly, we revised the differential equations and source codes to modify Gpyro3D. A detailed mathematical description of this modification made on the equations is provided elsewhere [150]. The modeled fuel thickness and surface area were in the range of the measured values for live manzanita leaves. Three different fuel moisture contents (FMC) were examined, namely 40, 76, 120%.

In the second study [153], the leaf was oriented vertically and held above the FFB. Pyrolysis, ignition, and combustion of a leaf-like solid fuel representing a vertically oriented manzanita leaf were computationally investigated [153] using modified Gpyro3D [150] coupled with FDS. Four different treatments of dry dead (FMC 4%), rehydrated dead (26%), dehydrated live (34%) and fresh live (63%) studied in experiments in the FFB facilities of BYU, were simulated [80]. The fuel condition in computations was set identical to that in the previous work [150] except for the orientation and FMC of the leaf. Computed time history of the normalized mass of the leaves was compared against the experimental data to validate the model.

In the third study [154], the impact of the heating mode, viz. convection vs radiation vs combined convection-radiation, was investigated for a leaf in the FFB apparatus equipped with a radiative panel to supply thermal radiation. Simulations were performed using the modified Gpyro3D coupled with FDS to investigate pyrolysis, ignition and flaming of a vertically oriented leaf subjected to the heating mode. Three modes were considered: upward convective heating; external thermal radiation heating; and convective heating combined with thermal radiation heating.

Figure 26 displays the computational configuration which resembles the reference experimental setup where the burning experiments were performed on freshly harvested manzanita leaves [46,155,156]. The entire computational domain is a rectangular box with dimensions of 0.18×0.25×0.32 m in x, y and z, respectively. The initial FMC of the fuel is 65%. The other specifics

of the modeled leaf can be found in [150,153]. The approximation of the leaf face shape by a rectangle is a simplification imposed by the constrain that Gpyro3D is a structure grid-based model with a limitation on dealing with non-rectangular domains. The center of the solid fuel is located 4 cm above the FFB exit and 11 cm from the radiant panel. The FFB supplying the convective heating is represented by the bottom surface, viz. burner, in the computational domain. This surface has dimensions of 0.18×0.25 m ($x \times y$) through which hot gases exiting the FFB enter the domain at 1000°C with 10 mol% oxygen at a velocity of 0.6 m/s. The radiant panel is represented by a vertical heated wall with dimensions of 0.18×0.32 m along x and z . The heated wall temperature was maintained at 952°C throughout the simulation, which provided $\sim 50 \text{ kW/m}^2$ radiation heat flux at the leaf location, consistent with the reported radiant heat flux in the reference experiments. Other lateral surfaces of the domain are considered as the solid walls with fixed ambient temperature while the top surface is considered an open boundary.

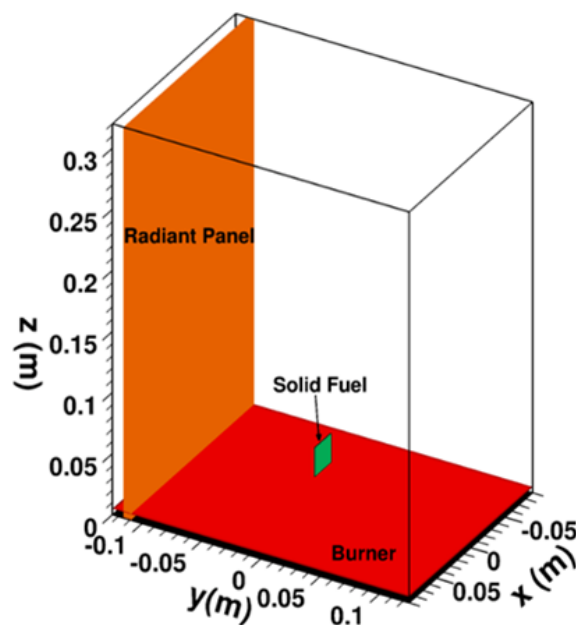


Figure 26. Isometric view of the computational domain with the vertically oriented solid fuel over the flat flame burner.

The fourth modeling study [133] was performed to investigate the moisture evaporation approaches in dead and live fuels. The fuel moisture evaporation precedes and significantly influences the pyrolysis and burning processes of the fuel. In this work, two moisture evaporation modeling approaches, namely the Arrhenius model and the equilibrium model are examined in a shrinking biomass fuel slab subject to external radiant heating. In the equilibrium model, evaporation is treated as a phase-change thermodynamic process whereas in the Arrhenius model, it is treated as a chemical process. We made an extensive revision in Gpyro source code to include the equilibrium model, as this model is substantially more sophisticated than the Arrhenius model, which is the default approach for moisture evaporation treatment in Gpyro. This extension works for one-dimensional configurations, e.g., fuel slabs, for now. In a fuel slab, the dimension of the fuel in one direction (slab thickness direction) is much smaller than the other two dimensions. Thus, it was assumed that the heat and mass transfer occur at a much higher rate in the direction of the slab thickness. Consequently, the transport processes in the direction of the other two larger dimensions is neglected.

To gain a better understanding of the fuel shrinkage, we developed a continuum description for the mass and energy conservation laws in the form of integral-differential equations for a pyrolyzing,

shrinking objects under one dimensional assumption. Such a description, which provides fundamental governing equations, is lacking for shrinking objects in the previous Gpyro works. In continuum description, for example, the mass conservation of the condensed phase in one dimensional configuration reads

$$\frac{d}{dt} \int_{z_t(t)}^{z_b(t)} \bar{\rho} dz = \int_{z_t(t)}^{z_b(t)} \dot{\omega}_{fg}''' dz$$

where d/dt is the material derivative (Lagrangian derivative), $\bar{\rho}$ is the weighted bulk (mean apparent) density of the condensed phase and $\dot{\omega}_{fg}'''$ is the net mass reduction rate of the condensed phase per unit volume. It is noted that the continuum description (differential equations) presented in Gpyro documents for 1, 2 and 3D configurations are only valid under no shrinkage (or swelling) assumption [151]. Under the shrinkage assumption, Gpyro documents [151] only provide a numerically discretized form of the equations for one dimensional configurations. Here, it was shown that this form is the outcome of application of the finite volume approach for spatial discretization and the Euler approach for time discretization. We performed a validation study for both equilibrium and Arrhenius evaporation models using the experimental data of cone calorimeter experiments [157]. We considered two fuel moisture contents of 26% and 100% (on dry-mass basis) representing dead and live fuels, respectively.

In the final study, the modeling approach is being improved to include the major pyrolysis gases that were identified by the BYU group in this SERDP project and their associated chemical reactions in the leaf scale burning simulations for improved representation of the combustion process. Our efforts so far suggest that the challenge here is a need for a finer grid in the FDS domain (Figure 26). To conduct the simulations in a finer grid over a practical computational time, we may have to reduce the overall computational domain to be limited to a region surrounding the leaf while being large enough to capture the whole flame without compromising its shape. We expect to produce validated results of this study soon. A manuscript describing the completed study is under review [158].

3.5.2 FDS modeling of wind tunnel fires

FDS version 6.7 was used to simulate pyrolysis and combustion of fuel beds of longleaf pine needles only (0.396 kg m^{-2}) in the wind tunnel. The governing equations as implemented in FDS 6 are described elsewhere [46]. Three different wind conditions including $U=0, 0.44$, and 1 m/s were investigated. The turbulence model was mainly described based on the two turbulent transport coefficients: the turbulent viscosity and the turbulent diffusivity. The Schmidt number and Prandtl number were used to identify the turbulent diffusivity, and both were given a value of 0.5 [152]. In this study, the eddy viscosity was calculated based on the Deardorff model [159,160]. Two schemes, a single-step reaction and a multi-step reaction (Figure 27) modelled the pyrolysis process. In the single-step reaction, the pine needle fuel was considered as cellulose, while for the multi-step reaction the pine needles were modeled as a combination of cellulose, hemicellulose, and lignin (Table 5). To validate the numerical methodology, the temperature and flame spread rate data were compared with the wind tunnel measurements. Different quantities such as temperature at fuel bed surface, flame shape, flame spread rate, flame width and fuel mass loss rate were analyzed in this study. The numerical model used in FDS and the modeling schemes are described in detail elsewhere [161] which is retrievable from the RC-2640 files in SEMS2.

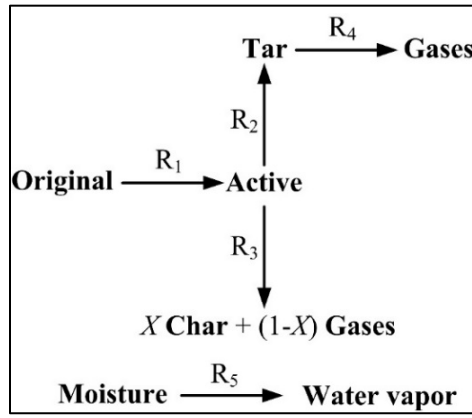


Figure 27. Multistep scheme to model pyrolysis in longleaf pine needle fuel beds using the Fire Dynamics Simulator [50,150].

Table 5. Kinetic parameters for materials used in Arrhenius multistep pyrolysis scheme.

Reaction	Pre-exponential (A) (s^{-1})	Activation energy E (kJ/mol)
R1-cellulose	2.8×10^{19}	242.4
R2-cellulose	3.28×10^{14}	196.5
R3-cellulose	1.3×10^{10}	150.5
R1-hemicellulose	2.1×10^{16}	186.7
R2-hemicellulose	8.75×10^{15}	202.4
R3-hemicellulose	2.6×10^{11}	145.7
R1-lignin	9.6×10^8	107.6
R2-lignin	1.5×10^9	143.8
R3-lignin	7.7×10^6	111.4
R4	4.28×10^6	108
R5	5.13×10^{10}	88

3.5.3 Specific heat and FDS Vegetation module

Because the detailed chemical analysis of the foliage of 12 of the plant species in this study [64] and other prior work ([52,162]) has shown that foliar fuels are different from wood, a model of specific heat capacity based on the foliar composition was formulated using a combination of theoretical and statistical modeling [163]. The characterization of the physical and chemical composition of the nursery plants revealed the inadequacies of the existing Vegetation module in FDS to simulate wildland and wildland-urban interface fire. The current Vegetation module was formulated and parameterized for Douglas-fir (*Pseudotsuga menziesii*) foliage based on Susott's work [17,50]. Based on information from the present study, modifications to the Vegetation module for pyrolysis and ignition of live fuel foliage have been formulated [164].

4 Results and Discussion

4.1 Objective 0 – Fuel characterization

4.1.1 Solid fuel properties

Proximate and ultimate analysis of the 14 plant species were typical of living vegetation (Table 6). Leaf size differed between species (Table 7). Density of the fresh leaves of the shrub species was relatively constant; longleaf pine needles had the largest density (Table 8).

4.1.2 Wind tunnel fuel beds

A description of the plant sizes used in the wind tunnel fires is found in Table 9. While the plants were similar in height, the crown dimensions differed between the three species used. The wind tunnel fuel beds were generally similar in terms of live and dead fuel moisture content (Table 10) even though ambient conditions in the wind tunnel were changed to simulate dormant season conditions (fires 55-73). The conditions the wind tunnel and field fires were burned under and the resulting fire behavior are also included in Table 10.

4.1.3 Fuels and fuel consumption at Ft. Jackson

Photographs of the burn plots showed relatively open stands with variable levels of sparkleberry and other shrub fuels (Figure 28). Eight 2D fuel samples were collected in each of four burn plots at Ft. Jackson (Table 11). The estimated duff fuel loading is within the range of loading reported for unburnt stands at Eglin Air Force Base in Florida [165] and for mixed slash (*Pinus elliottii* Engelm.) and longleaf pine stands in central Georgia [166]. Fuel loading data are compositional in nature and were analyzed as such. The data were summarized using the geometric mean and standard deviation, measures appropriate for the relative nature of fuels data. It is important to note that the geometric standard deviation is related to the geometric mean by multiplication and division which is denoted by “*” [167] (Table 12). This results in the confidence interval being estimated as

$$\left[\exp\left(\log(\bar{x}_g) - t_{n,1-\alpha} s_g / \sqrt{n}\right), \exp\left(\log(\bar{x}_g) + t_{n,1-\alpha} s_g / \sqrt{n}\right) \right]$$

where \bar{x}_g, s_g are the geometric mean and standard deviation, n is the sample size, and $t_{n,1-\alpha}$ is from Student's t-distribution. Note that treating fuel loading data as compositional data and using the confidence interval above, the estimates for fuel loading will always be positive. By expressing the loadings on a relative basis using the closure operation $C(\mathbf{x})$, [115,120]

$$C(\mathbf{x}) = \frac{[x_1, x_2, \dots, x_D]}{\sum_{i=1}^D x_i} \quad (1)$$

associated with compositional data [115,120], the center (geometric mean) of the fuel loading vector (proportions) shows the relative dominance of duff and litter in the pre-burn fuel loadings (0.594 and 0.339, respectively). The closure operation is sometimes called “normalizing the data”. Even though the area is typically burned on a 3-year interval, there was a surprising amount of duff present in the stands. This duff accumulation can pose a potential problem as long-term smoldering can result in elevated soil temperatures potentially lethal to fine roots as has been found in ponderosa pine (*Pinus ponderosa*) and giant sequoia-mixed conifer stands in the western U.S. [168,169] and reported more recently in longleaf pine [165,170]. In the preburn samples, the geometric standard deviation for cones, 100 hr dead woody and the herbaceous/forb fuel types was large. This high variability is reflected in the relative high percentages of the total variance accounted for by these fuels (Table 12).

Table 6. Initial proximate and ultimate analysis of plant species [63].

Common name	MC ¹	Proximate analysis			Ultimate analysis						
		Ash	VM	FC	C	H	N	S	O	LHV	HHV
Wiregrass	135	4.34	81.7	18.3	47.42	6.34	3.31	0.25	42.68	17.74	19.34
Little bluestem	217	4.12	84.9	15.1	51.22	5.66	2.22	0.15	40.75	17.63	19.09
Inkberry	85	1.88	80.2	19.8	54.63	6.42	0.87	0.11	37.97	20.94	22.52
Yaupon	104	4.89	86.2	13.8	51.34	6.28	1.46	0.18	40.74	19.79	21.43
Fetterbush	91	2.24	77.7	22.3	54.36	5.81	0.80	0.12	38.91	19.00	20.57
Wax myrtle	118	2.41	77.4	22.6	50.65	5.44	2.31	0.14	41.46	19.98	21.36
Swamp bay	116	1.84	79.6	20.4	52.48	6.11	1.36	0.17	39.88	20.50	22.10
Sparkleberry	103	3.10	79.0	21.0	52.49	7.71	0.74	0.16	38.90	18.96	20.90
Darrow's blueberry	104	2.85	n.a.	n.a.	n.a.	n.a.	n.a.	n.a.	n.a.	n.a.	n.a.
Longleaf pine foliage	207	2.02	79.7	20.3	51.37	3.00	1.21	0.11	44.31	19.26	20.11
Longleaf pine litter	15 ⁴	1.77	78.3	21.7	52.31	6.09	2.31	0.06	39.23	19.59	21.10
Water oak	170	4.18	80.6	19.4	50.06	5.57	1.47	0.1	42.80	18.23	19.96
Live oak	103	2.71	80.9	19.1	49.57	6.01	2.30	0.15	41.97	18.21	19.81
Dwarf palmetto	164	3.26	89.8	10.2	47.36	5.93	2.14	0.66	43.91	19.04	20.61
Saw palmetto	112	3.19	76.4	23.6	49.49	5.48	0.90	0.17	43.96	19.09	20.56

1. Moisture content dry weight basis of BYU samples

2. VM = volatile material, FC = fixed carbon. Values are wt% dry-ash free. ASTM D7582.

3. C, H, N, S, O – values are % dry mass; LHV = low heating value, HHV = high heating value (kJ g⁻¹, dry-ash free basis). ASTM D5291, D4239, E711

4. Moisture content of the pine litter reported in Table 2 of [63] is incorrect. The correct value is reported in [171].

Table 7. Plant physical dimensions [63].

Common name	Thickness (mm)		Length (mm)		Width(mm)		Stem diameter (mm)		Width/Length
	Mean	CI ¹	Mean	CI	Mean	CI	Mean	CI	
Wiregrass	0.31	0.04	154	49					
Little bluestem	0.11	0.03	175	67	2.3	0.6			0.01
Inkberry	0.32	0.06	29	5	15.0	3.0	2.0	0.8	0.52
Yaupon	0.31	0.09	11	3	6.0	2.0	1.4	0.2	0.55
Fetterbush	0.20	0.08	27	6	15.0	4.0	1.2	0.4	0.56
Wax myrtle	0.19	0.04	33	4	12.0	2.0	0.7	0.2	0.36
Swamp bay	0.30	0.06	104	8	27.0	4.0	3.4	0.5	0.26
Sparkleberry	0.24	0.05	20	4	8.0	2.0	0.6	0.2	0.40
Darrow's blueberry	0.23	0.06	22	5	7.0	4.0	0.7	0.4	0.32
Longleaf pine foliage	0.42	0.04	106	4					
Longleaf pine litter	0.46	0.03	104	4					
Water oak	0.18	0.03	63	17	16.0	7.0	2.2	0.8	0.25
Live oak	0.33	0.05	61	9	29.0	6.0	3.0	1.2	0.48
Dwarf palmetto	0.21	0.04	120	25	9.0	3.0			0.08
Saw palmetto	0.22	0.06	95	22	14.0	4.0			0.15

1. 95 percent confidence interval based on sample size of three.

Table 8. Density of a fresh leaf by species (g cc⁻¹).

Common name	Density Samples			
	1	2	3	Mean
Inkberry	0.936	0.911	0.903	0.917
Yaupon	0.903	0.927	0.883	0.904
Fetterbush	0.973	0.896	0.943	0.937
Wax myrtle	1.054	1.017	0.972	1.014
Swamp bay	0.964	0.882	0.895	0.914
Sparkleberry	0.950	1.025	1.029	1.001
Longleaf pine foliage	1.756	1.202	1.301	1.420
Water oak	1.019	0.969	1.251	1.080
Live oak	0.905	0.920	0.978	0.935
Dwarf palmetto	0.840	0.786	0.942	0.856
Saw palmetto	1.019	1.155	1.125	1.099

Table 9. Size measurements of plants used in wind tunnel pyrolysis experiment. Sample size of 40 plants per species.

Species	Height (cm)	Crown ^a		
		Diameter 1 (cm)	Diameter 2 (cm)	Area (cm ²)
<i>Ilex glabra</i>	17.0(2.6)	11.2	9.7	318.4
<i>Lyonia lucida</i>	22.7(2.9)	18.5	16.4	856.7
<i>Vaccinium arboreum</i>	20.6(2.6)	18.9	15.8	879.8

^a Crown diameter 1 is maximum crown diameter and crown diameter 2 was measured perpendicular to crown diameter 1. Crown area = $\pi d_1 d_2$.

**Figure 28. Prefire coverage of predominantly sparkleberry shrubs in (a) burn unit 16D1 and (b) burn unit 16D2 two years after most recent burn.**

Table 10. Properties and characteristics of wind tunnel and field fires burned to measure pyrolysis gases. Environmental conditions measured prior (less than 5 minutes) of start of experiment. Values rounded to appropriate number of significant digits.

Fire	Location	Fuel bed ^a	Wind ^b	Spread rate ^c (m s ⁻¹)	Maximum Temperature ^d (°C)	Heating rate ^e (°C s ⁻¹)	Fuel moisture (%)		Air temperature (°C)	Relative Humidity (%)
							Dead	Live		
3	RFL	Needles only	N	0.006			11		25.3	47
4	RFL	Needles only	N	0.006			12		22.6	52
5	RFL	Needles only	N	0.005			13		22.6	53
8	RFL	Needles only	N	0.004	439	95	15		20.4	67
9	RFL	Needles only	N	0.005	660	57	16		23.7	50
10	RFL	Needles only	N	0.006	578	85	11		22.6	50
11	RFL	Needles only	N	0.005	612	103	12		21.5	56
12	RFL	High Inkberry	N	0.005	615	282	11	117	20.4	56
13	RFL	Low Inkberry	N	0.005	398	51	12	120	18.7	62
14	RFL	High Inkberry	N	0.005	438	18	10	128	19.8	61
15	RFL	Low Inkberry	N	0.005	630	314	8	120	21.5	51
16	RFL	Low Inkberry	N	0.005	660	54	8	108	24.2	46
17	RFL	High Inkberry	N	0.006			8	116	24.2	35
18	RFL	High Inkberry	N	0.005	552	42	8	117	24.8	30
19	RFL	Low Inkberry	N	0.005	605	48	9	117	24.8	31
20	RFL	Low Inkberry	N	0.005	427	12	15	136	21.5	52
21	RFL	High Inkberry	N	0.005	660	66	14	104	22.0	42
22	RFL	Low Inkberry	N	0.006	563	33	12	99	24.2	34
23	RFL	High Inkberry	N	0.006	612	27	10	106	25.3	29
24	RFL	Low Inkberry	N	0.006	660	99	9	100	25.3	28
25	RFL	High Inkberry	N	0.006	616	72	10	122	25.3	33

26	RFL	Longleaf	Y	0.011	660	32	10		22.6	31
27	RFL	Longleaf	Y	0.010	590	107	10		21.5	31
28	RFL	Low Inkberry	Y	0.009	462	28	12	93	20.4	34
29	RFL	High Inkberry	Y	0.009	660	60	9	108	23.1	32
30	RFL	High Inkberry	Y	0.009	643	76	10	120	24.2	29
31	RFL	Low Inkberry	Y	0.009	590	59	7	133	26.4	21
32	RFL	High Inkberry	N	0.006	606	200	8	116	26.4	24
33	RFL	High Inkberry	Y	0.011	614	24	8	117	25.9	26
34	RFL	High Inkberry	Y	0.010	597	34	11	121	22.6	40
35	RFL	High Inkberry	N	0.005	557	23	10	113	23.1	42
36	RFL	High Inkberry	N	0.005	644	65	10	93	23.7	36
37	RFL	High Inkberry	N	0.005	660	42	10	124	26.4	29
38	RFL	High Inkberry	N	0.005	610	29	9	102	27.0	26
41	RFL	Blueberry	N	0.005	508	15	10	118	26.4	33
42	RFL	Blueberry	N	0.006	524	148	10	130	27.0	33
44	RFL	Fetterbush	N	0.005	645	38	9	104	25.9	42
45	RFL	Fetterbush	N	0.006	545	29	6	106	24.2	42
46	RFL	Fetterbush Blueberry	N	0.004	569	20	12	135	18.7	37
47	RFL	Fetterbush	N	0.005	482	18	11	105	21.5	31
48	RFL	Fetterbush Blueberry	N	0.006	602	25	10	131	23.1	25
49	RFL	Fetterbush	N	0.006	638	48	10	103	24.2	49
51	RFL	Longleaf	Y	0.015	430	55	11		6.7	75
52	RFL	Fetterbush	Y	0.015	567	65	10	79	6.1	59
53	RFL	Blueberry	Y	0.018	414	208	11	148	11.7	39
55	RFL	Fetterbush	Y	0.019	509		10		6.1	43
56	RFL	Longleaf	Y	0.018	660	167	10		9.4	35
57	RFL	Blueberry	Y	0.017	528	48	12	130	5.6	73
58	RFL	Fetterbush Blueberry	Y	0.027	417	39	11	138	5.6	70
59	RFL	Longleaf	Y	0.017	532	291	11		7.8	58
60	RFL	Fetterbush	Y	0.020	660	88	10	103	8.3	50

61	RFL	Fetterbush Blueberry	Y	0.021	472	140	10	127	6.7	67
62	RFL	Longleaf	Y	0.019	513	378	10		6.7	63
63	RFL	Blueberry	Y	0.016	218	171	12	128	7.2	63
64	RFL	Fetterbush	Y	0.015	315	329	12	93	6.1	73
65	RFL	Fetterbush Blueberry	Y	0.017	523	148	10	139	6.7	62
66	RFL	Blueberry	Y	0.019	479	113	11	137	7.2	63
67	RFL	Longleaf	Y	0.020	514	72	10		7.2	63
68	RFL	Fetterbush	Y	0.022	601	102	10	103	7.8	63
69	RFL	Fetterbush	Y	0.016	471	443	12	102	7.8	78
70	RFL	Blueberry	Y	0.017	478	179	11	150	7.8	78
71	RFL	Fetterbush Blueberry	Y	0.016	341	39	12	132	6.1	73
72	RFL	Blueberry	Y	0.018	533	43	9	128	8.3	74
73	RFL	Fetterbush Blueberry	Y	0.023	516	17	9	107	10.0	65
74	RFL	Longleaf	Y	0.011	419	400	12		20.0	96
75	RFL	Longleaf	Y	0.009	405	104	13		20.8	59
76	RFL	High Inkberry	Y	0.010	373	10	12	97	23.9	48
77	RFL	Fetterbush	Y	0.009	648	21	9	106	28.3	35
78	RFL	Sparkleberry	Y	0.010	304	16	9	105	28.9	19
79	RFL	High Inkberry	Y	0.010	190	39	9	100	28.3	26
80	RFL	Sparkleberry	Y	0.011	435	8	9	108	23.2	15
81	RFL	Fetterbush	Y	0.011	273	75	7	79	23.3	12
82	RFL	Sparkleberry	Y	0.009	132	49	8	107	25.6	12
83	RFL	High Inkberry	Y	0.010	343	23	7	92	27.8	11
84	RFL	Fetterbush	Y	0.010		41	8	135	27.8	10
85	RFL	Fetterbush	Y	0.010	294	22	7	102	28.9	9
86	RFL	Sparkleberry	Y	0.013	288	21	7	100	13.9	33
87	RFL	High Inkberry	Y	0.014	419	56	8	92	12.8	33
88	RFL	Fetterbush	Y	0.014	199	52	7	99	12.8	39
89	RFL	High Inkberry	Y	0.011	630	37	7	89	29.4	18

90	RFL	Sparkleberry	Y	0.008	468	20	7	106	28.9	19
91	RFL	Fetterbush	Y	0.009	236	48	8	109	29.4	18
92	RFL	High Inkberry	Y	0.010	612	58	9	95	21.7	30
93	RFL	Fetterbush	Y	0.009	223	4	8	89	26.1	24
94	RFL	Sparkleberry	Y	0.009	648	94	8	111	29.4	23
95	RFL	Sparkleberry	Y	0.012	526	28	7	116	25.6	24
96	RFL	Fetterbush	Y	0.012	388	5	8	88	28.9	21
97	RFL	Sparkleberry	Y	0.011	439	11	8	86	28.9	22
101	TTRS	Subxeric Woodland	Y						28	25
102	TTRS	Subxeric Woodland	Y						28	25
201	FJSC	Fall-line Sandhills	Y				7	211	24	26
202	FJSC	Fall-line Sandhills	Y		599	259	7	211	28	18
203	FJSC	Fall-line Sandhills	Y				12	212	21	53
204	FJSC	Fall-line Sandhills	Y		648	372	12	212	27	34
205	FJSC	Fall-line Sandhills	Y		264	107	13	177	22	59
206	FJSC	Fall-line Sandhills	Y		231	117	6	191	26	43
207	FJSC	Fall-line Sandhills	Y		264	107	6	191	29	30

^a Each wind tunnel fuel bed contained 1000 g of longleaf pine needles. After adjusting for fuel moisture content, longleaf pine needle mass ranged from 862 to 943 g. Fuel consumption not measured; however, virtually all longleaf pine needle mass was consumed by flaming combustion with minimal residual smouldering combustion. Ft. Jackson (FJSC) and Tall Timbers Pebble Hill Plantation (TTRS) classification from [172,173].

^b N = no concurrent air flow, Y = concurrent air flow of nominally 1 m s⁻¹

^c Calculated quasi-steady fire rate of spread (fuel bed length / transit time).

^d Maximum uncorrected radiometric leaf temperature (T_i) measured by 7-13 μ m thermal camera.

^e Maximum heating rate = $\max \left[(T_i - T_{i-1}) / (t_i - t_{i-1}) \right], T_i > T_{i-1}$

Table 11. Pre- and post-burn fuel loading samples by fuel class of two-year roughs in longleaf pine stands at Ft. Jackson, SC. Units are g m⁻². Eight sample points were measured per plot. Time – Pre = preburn loading, Post = postburn loading.

Plot	Time	Duff	Litter	1000hr	100hr	10hr	1hr	Cones	Susp. Litter	Shrubs	Herbs
16D5	Pre	896.07	367.39	0.00	264.34	69.45	89.61	20.16	64.96	969.99	0.00
16D5	Pre	67.21	239.70	0.00	0.00	13.44	6.72	0.00	0.00	11.20	4.48
16D5	Pre	250.90	268.82	0.00	0.00	64.96	8.96	15.68	0.00	60.48	0.00
16D5	Pre	4610.27	407.71	0.00	277.78	221.78	17.92	147.85	0.00	6.72	0.00
16D5	Pre	1314.98	669.81	0.00	250.90	537.64	134.41	172.49	51.52	548.84	0.00
16D5	Pre	1711.49	779.58	0.00	0.00	232.98	4.48	253.14	20.16	232.98	0.00
16D5	Pre	0.00	463.72	0.00	0.00	53.76	4.48	215.06	0.00	89.61	4.48
16D5	Pre	2965.99	313.62	0.00	0.00	448.03	47.04	15.68	4.48	1232.09	0.00
16D5	Post	875.91	26.88	0.00	49.28	51.52	0.00	13.44	2.24	403.23	0.00
16D5	Post	67.21	6.72	0.00	152.33	31.36	0.00	0.00	0.00	6.72	2.24
16D5	Post	132.17	17.92	0.00	0.00	26.88	4.48	0.00	0.00	20.16	0.00
16D5	Post	4610.27	31.36	0.00	0.00	51.52	0.00	4.48	0.00	2.24	0.00
16D5	Post	1314.98	42.56	0.00	0.00	11.20	0.00	13.44	0.00	31.36	0.00
16D5	Post	1711.49	15.68	0.00	0.00	49.28	0.00	0.00	0.00	0.00	0.00
16D5	Post	0.00	24.64	0.00	598.13	42.56	0.00	0.00	0.00	35.84	0.00
16D5	Post	1978.07	4.48	0.00	282.26	15.68	2.24	6.72	0.00	11.20	0.00
16D1	Pre	3944.94	636.21	0.00	0.00	71.69	33.60	152.33	0.00	0.00	0.00
16D1	Pre	2309.62	703.41	0.00	0.00	647.41	129.93	271.06	91.85	35.84	0.00
16D1	Pre	3803.81	629.49	0.00	0.00	125.45	33.60	0.00	8.96	170.25	0.00
16D1	Pre	1010.32	439.07	0.00	0.00	208.34	49.28	6.72	8.96	38.08	0.00
16D1	Pre	6666.75	589.16	0.00	0.00	15.68	8.96	87.37	0.00	2.24	0.00
16D1	Pre	239.70	557.80	0.00	0.00	58.24	2.24	38.08	0.00	0.00	0.00
16D1	Pre	546.60	403.23	0.00	0.00	132.17	60.48	33.60	0.00	13.44	0.00
16D1	Pre	5772.92	737.02	0.00	0.00	479.40	15.68	22.40	15.68	11.20	0.00
16D1	Post	3944.94	42.56	0.00	26.88	82.89	2.24	8.96	0.00	0.00	0.00
16D1	Post	2289.45	0.00	0.00	0.00	4.48	2.24	6.72	0.00	15.68	0.00
16D1	Post	3642.52	40.32	0.00	0.00	38.08	4.48	8.96	0.00	4.48	0.00

16D1	Post	784.06	38.08	0.00	0.00	2.24	0.00	2.24	0.00	0.00	0.00
16D1	Post	5210.64	60.48	0.00	47.04	24.64	2.24	0.00	0.00	17.92	0.00
16D1	Post	239.70	0.00	0.00	436.83	0.00	0.00	0.00	0.00	0.00	0.00
16D1	Post	506.28	38.08	0.00	0.00	20.16	0.00	0.00	0.00	118.73	0.00
16D1	Post	5714.67	96.33	0.00	0.00	15.68	2.24	4.48	0.00	2.24	0.00
24A	Pre	6928.85	1404.59	0.00	0.00	291.22	38.08	4.48	17.92	38.08	0.00
24A	Pre	4737.96	963.27	0.00	0.00	40.32	4.48	0.00	0.00	33.60	0.00
24A	Pre	3165.36	943.11	0.00	0.00	112.01	8.96	0.00	0.00	11.20	0.00
24A	Pre	6610.74	898.31	0.00	0.00	29.12	13.44	0.00	42.56	98.57	0.00
24A	Pre	10770.74	878.15	0.00	0.00	94.09	38.08	71.69	35.84	150.09	0.00
24A	Pre	2945.82	519.72	0.00	0.00	8.96	0.00	0.00	0.00	2.24	0.00
24A	Pre	3649.24	822.14	0.00	703.41	174.73	58.24	60.48	47.04	58.24	0.00
24A	Pre	6272.48	875.91	0.00	0.00	56.00	0.00	2.24	0.00	2.24	0.00
24A	Post	5755.00	62.72	0.00	0.00	125.45	0.00	0.00	0.00	0.00	0.00
24A	Post	4480.34	82.89	0.00	170.25	40.32	0.00	13.44	0.00	0.00	0.00
24A	Post	3046.63	85.13	0.00	0.00	33.60	0.00	0.00	0.00	414.43	0.00
24A	Post	6272.48	26.88	0.00	0.00	6.72	0.00	2.24	0.00	0.00	0.00
24A	Post	10571.36	60.48	0.00	0.00	123.21	0.00	0.00	2.24	33.60	0.00
24A	Post	2905.50	29.12	0.00	0.00	35.84	0.00	0.00	2.24	259.86	0.00
24A	Post	3232.57	38.08	0.00	96.33	51.52	0.00	0.00	0.00	42.56	0.00
24A	Post	6191.83	172.49	0.00	582.44	60.48	0.00	0.00	0.00	33.60	0.00
24B	Pre	318.10	909.51	0.00	0.00	141.13	60.48	201.62	69.45	430.11	67.21
24B	Pre	2211.05	972.23	0.00	636.21	62.72	22.40	212.82	35.84	51.52	35.84
24B	Pre	2067.68	510.76	0.00	0.00	8.96	8.96	0.00	17.92	15.68	44.80
24B	Pre	439.07	573.48	0.00	0.00	224.02	49.28	35.84	20.16	199.38	82.89
24B	Pre	4280.96	474.92	0.00	813.18	4.48	2.24	0.00	38.08	51.52	71.69
24B	Pre	288.98	461.48	2939.10	678.77	114.25	11.20	0.00	0.00	82.89	138.89
24B	Pre	244.18	217.30	0.00	286.74	22.40	0.00	0.00	8.96	44.80	145.61
24B	Pre	107.53	315.86	0.00	0.00	49.28	24.64	0.00	8.96	13.44	64.96
24B	Post	179.21	150.09	0.00	0.00	20.16	2.24	91.85	0.00	4.48	0.00
24B	Post	2130.40	56.00	0.00	0.00	2.24	0.00	13.44	0.00	105.29	2.24

24B	Post	1608.44	98.57	0.00	0.00	210.58	2.24	0.00	0.00	116.49	13.44
24B	Post	439.07	141.13	0.00	103.05	11.20	0.00	0.00	0.00	11.20	31.36
24B	Post	4021.11	134.41	0.00	179.21	89.61	0.00	0.00	0.00	150.09	0.00
24B	Post	192.65	49.28	0.00	147.85	156.81	0.00	0.00	0.00	271.06	8.96
24B	Post	235.22	42.56	0.00	497.32	6.72	0.00	0.00	0.00	82.89	0.00
24B	Post	26.88	0.00	0.00	232.98	6.72	0.00	0.00	0.00	0.00	0.00

Table 12. Mean fuel loading by component (g m⁻²) in longleaf pine forest at Ft. Jackson, SC burned to collect pyrolysis gas samples.

Component	Fuel loading ^a		Center ^b		Var ^c	
	Pre-burn	Postburn	Pre-burn	Postburn	Pre-burn	Postburn
Litter	566.9*1.4	16.2*3.3	3.39E-01	1.82E-02	2.0	6.6
Duff	994.9*4.4	852.0*4.7	5.94E-01	9.57E-01	7.7	6.8
Cones	1.2*18.2	0.04*4.7	7.15E-04	4.42E-05	20.3	16.1
Suspended Litter	0.4*6.4	0.002*2.5	2.36E-04	2.31E-06	13.5	4.5
1 hr	7.7*3.5	0.009*7.6	4.63E-03	1.03E-05	5.8	9.6
10 hr	80.3*1.7	19.6*2.7	4.80E-02	2.20E-02	1.9	2.8
100 hr	0.03*19.5	0.3*4.7	1.53E-05	3.15E-04	19.2	30.0
1000 hr	0.001*2.5	0.001*1.0	9.51E-07	1.12E-06	6.0	1.2
Herbs	0.03*209.4	0.004*8.8	1.66E-05	4.50E-06	18.4	7.9
Shrubs	23.3*6.5	2.5*5.1	1.39E-02	2.81E-03	5.2	14.5

a. Geometric mean is related to geometric standard deviation by multiplication and division, represented by “*”.

b. Mean (center) composition for 4 0.1 ha plots. Eight sample points located in each plot.

c. Percentage of total (metric) variance (124.15) contributed by fuel component.

Table 13. Estimated fuel consumption by component in longleaf pine forest at Ft. Jackson, SC.

Component	Fuel consumption ^a		
	Mean	L95	U95
Litter	544.8	411.5	693.4
Duff	113.4	49.9	368.9
Cones	1.1	0.1	14.5
Suspended Litter	0.4	0.1	1.1
1 hr	7.7	2.8	21.2
10 hr	45.6	20.0	105.0
Shrubs	19.9	5.1	121.2

a. Geometric mean, lower (L95) and upper (U95) confidence intervals estimated using a bootstrap method (function *Gmean* in *DescTools* package [174]).

Table 14. Moisture content (percent, dry-weight basis) prior to ignition by fuel category in longleaf pine stands at Ft. Jackson, SC.

Plot	Duff	Litter	1000hr	100hr	10hr	1hr	Cones	Susp. Litter	Shrubs	Herbs
24A	50	11		25	14	12	11	11	212	145
24B	26	6	46	22	13	7	14	8	211	205
16D1	45	4			8	7	13	7	191	20
16D5	44	11		11	11	14	13	12	177	60

The relatively low intensity fires did not significantly consume the duff fuels (Table 12) which accounted for nearly 96 percent of the post-burn loading. The duff, 1000 hr and 100 hr fuels were relatively moist (Table 14) in these spring burns. The live shrub foliage fuel moistures were also high. Note that litter was the primary fuel that was consumed by the burns. Further analysis of fuel consumption and pyrolysis products considering their compositional nature is planned.

3D shrub fuels were modeled from prefire 3D shrub fuel plot and TLS measures, and postfire 3D

shrub fuel plot and TLS measures. Little difference was noted in the prefire vs postfire logarithmic relationships between 3D shrub bulk density destructively sampled in the field and 3D occupied voxel density quantified from the TLS point cloud data [66] (Figure 29). Therefore, a generalized logarithmic function predicted shrub fuel load in 3D from both the pre- and post-fire datasets such that by differencing the outputs, shrub fuel consumption was estimated. The variance in these estimates between the 2017 and 2018 burn units was greatly reduced compared to the variance in consumption estimates calculated from the traditional, 2D fuel samples [66]; the latter were concluded to under sample shrub fuel variability across the burn units. However, the traditional fuel measures were critical for estimating consumption of the duff, litter, downed woody debris, and herbaceous fuel components. Indeed, shrub fuels comprised only a minor portion of total consumption (Table 12).

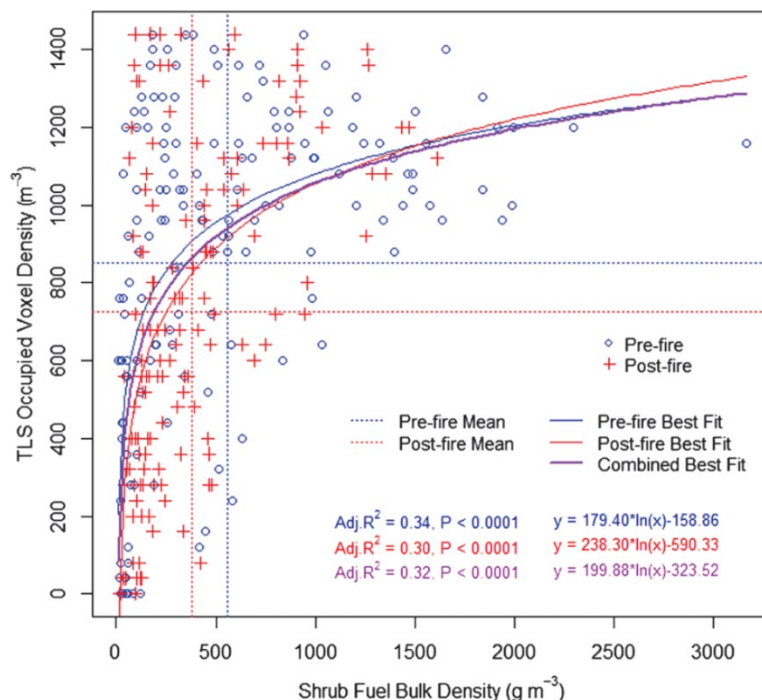


Figure 29. Natural logarithm relations between measured shrub fuel bulk density and voxel density derived from TLS [66].

The 3D approach provided preburn and postburn estimates of fuel loading that yielded consumption estimates that were all positive. This contrasts with the 2D destructive sampling estimates that resulted in fuel consumption that was negative (greater fuel loading following the fire). The approach should be tested in other settings, such as at Tall Timbers Research Station, where similar datasets have been collected [175]. Moreover, other fuel components besides shrubs need to be modeled in 3D, although TLS and other point cloud data have reduced sensitivity to less erect fuel structures, most notably downed woody debris, litter and duff fuels [176].

Table 15. Shrub fuel loading estimated by 2D destructive sampling and 3D nondestructive sampling (g m^{-2}).

Plot	2D			3D		
	Preburn	Postburn	Consumption	Preburn	Postburn	Consumption
16D1-17	47.83	162.79	-114.96	106.11	72.44	33.67
16D2-17	2.60	356.30	-353.70	150.85	87.78	63.07
16D1-18	33.63	20.18	13.45	107.62	70.37	37.25
16D5-18	394.54	65.01	329.53	76.55	39.21	37.34
24A7-18	49.32	98.63	-49.32	70.21	47.29	22.92
24B8-18	112.09	91.91	20.18	159.46	127.92	31.54

4.2 Objective 1 - Measurement of pyrolysis products

4.2.1 High and low-heating rate experiments

The results in this section are separated into 2 sections. In the first section, results as originally published are presented. These data were analyzed and interpreted as absolute values that can be analyzed using traditional statistical methods that assume that the range of the data is $(-\infty, \infty)$. In the second section, the data were reanalyzed as compositional data wherein the range of the data is $[0, \infty)$, strictly positive, using traditional statistical methods after being transformed using log-ratios.

During fast pyrolysis in the FFB, live foliage samples lost initial mass at a slower rate and pyrolysis took longer to complete compared to air-dried foliage samples (Figure 30) [171]. This difference in mass loss rate is attributed to the fact that more water was present in the foliage of the live plants as previous studies have shown.

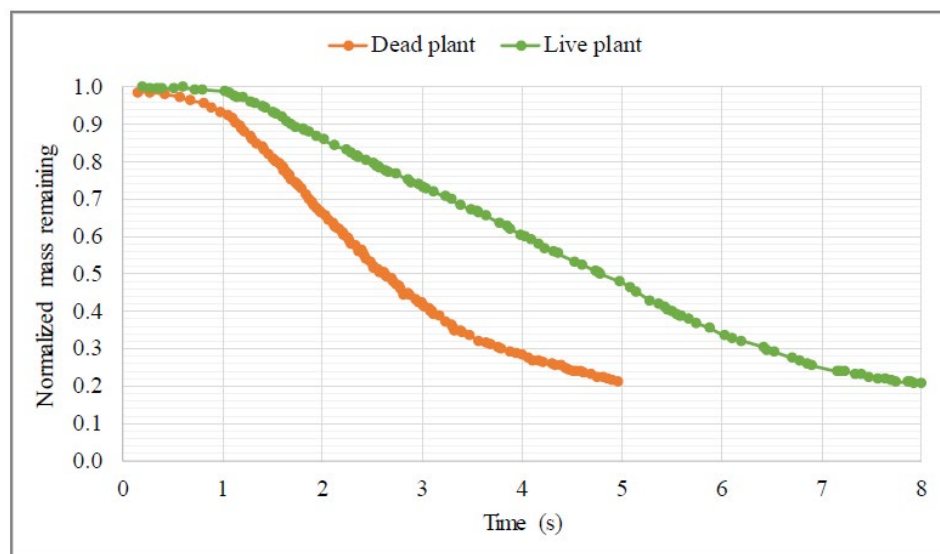


Figure 30. Example of mass loss over time during fast pyrolysis for live and air-dried *Ilex glabra* leaves. Air-dried denoted “dead plant”.

Figure 31 shows a comparison of the pyrolysis product yields from longleaf pine litter in the different heating modes as a function of temperature (even though the heating rates and background gas composition were different). The tar yields from the pyrolyzer peaked at 500 °C and then decreased

due to secondary reactions of tar. However, the tar yields in the FFB system continued to increase with final temperature, reaching over 60% of the mass of the dry plant. This difference in trend indicates that temperature alone cannot be used to describe pyrolysis behavior, but that heating rate and perhaps the temperature of the ambient environment also contribute to pyrolysis behavior. Table 16 shows a summary of the pyrolysis yield data for all plants in the four different heating modes.

A summary of the light gas species analysis is given in Table 17. The light gas species are presented here as a percent of the dry light gases on a weight basis. CO is the most prevalent species, followed by CO₂, with much smaller amounts of CH₄ and H₂ on this basis. On a molar basis, H₂ comprised about 30 mol% of the light gas. The amount of CO increased with increasing severity of the heating, while the amount of CO₂ decreased. This is illustrated in Figure 32 for live sparkleberry. Plant-to-plant variations in light gas species were relatively small, especially considering that the light gas only comprised about 25 wt% of the pyrolysis gases.

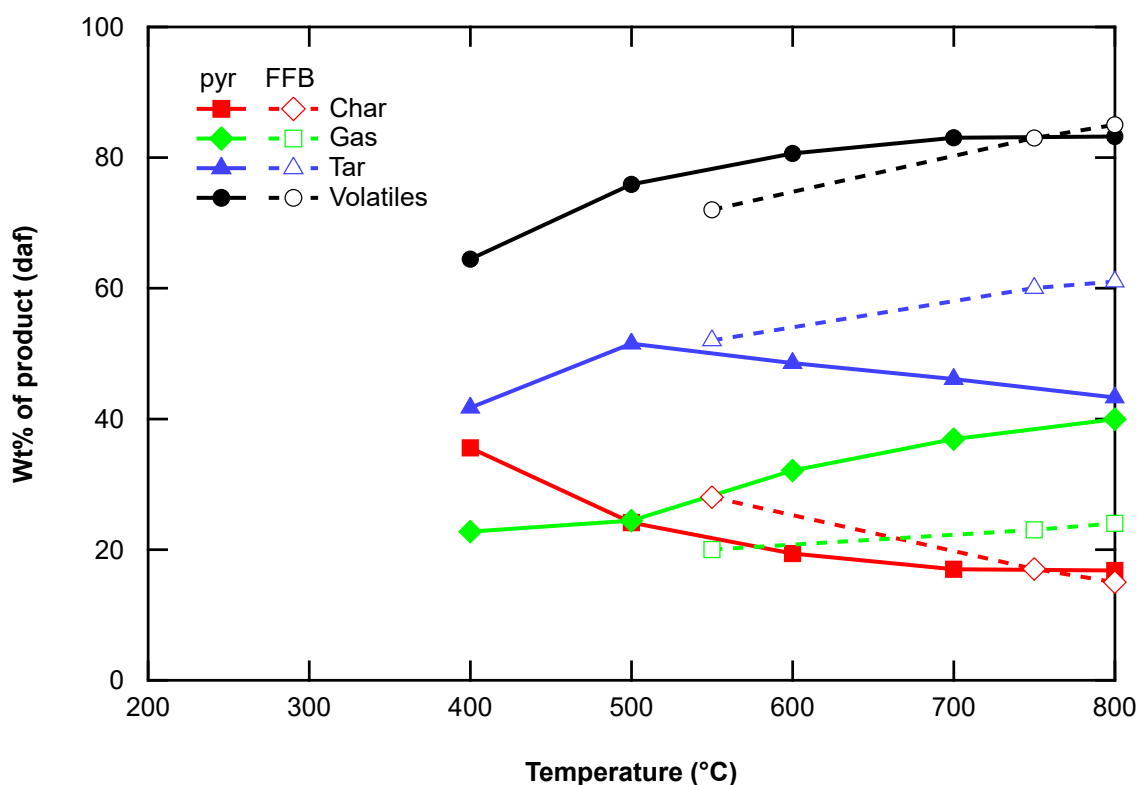


Figure 31. Comparison of pyrolysis product yields vs. final temperature for longleaf pine litter obtained in a pyrolyzer (solid lines) at 0.5 °C/s and from the flat flame burner system (dashed lines) under different modes of heating (radiation only (550 °C), convection only (750 °C), and radiation plus convection (800 °C)).

Table 16. Summary of pyrolysis product yields for live species for four heating modes.

Heating modes	Apparatus	Tar yield ^a	Light gas yield ^a	Char yield ^a
Slow heating to 500 °C [27]	Pyrolyzer	44-54	16-24	27-34
Radiation-only	FFB	49-57	16-23	24-29
Convection-only [27]	FFB	53-62	18-25	17-22
Convection and Radiation	FFB	55-63	20-27	14-19

^a wt% on a dry, ash-free (daf) basis

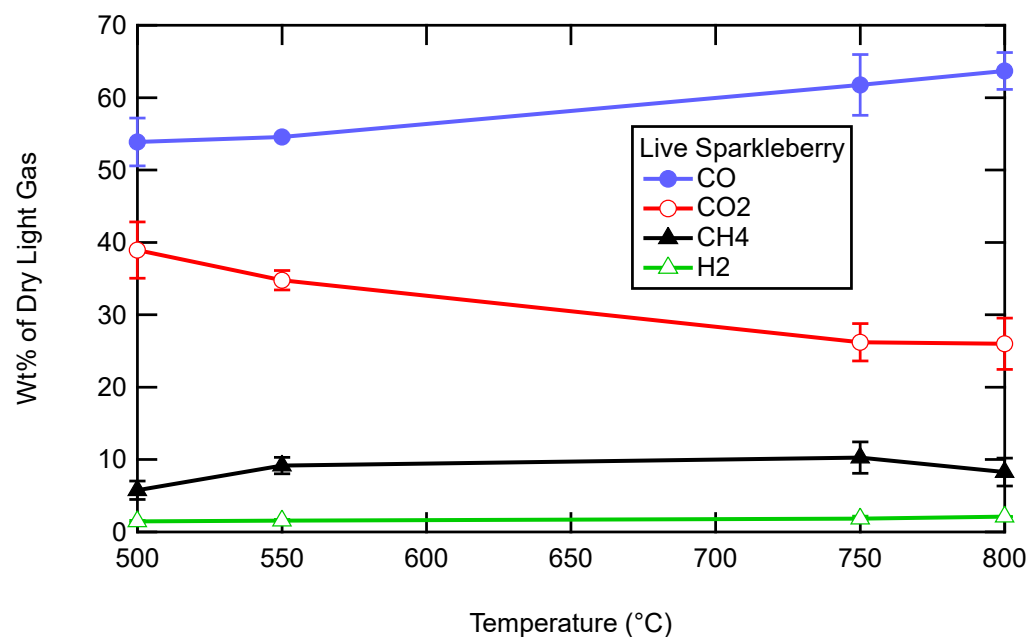
Table 17. Summary of light gas analysis during pyrolysis of live plants for three heating modes.

Heating mode	Apparatus	H ₂		CO		CO ₂		CH ₄	
		Avg ^a	Rng ^b	Avg	Rng	Avg	Rng	Avg	Rng
Slow heating to 500 °C	Pyrolyzer	1.4	1.1-1.7	52.1	47-58	38.4	34-42	8.1	5-11
Radiation-only	FFB	1.5 ^c	1.3-1.9	53.4	51-56	36.0	33-39	9.1	8-10
Convection-only	FFB	1.7	1.3-2.1	59.8	53-63	29.5	25-35	8.9	6-11
Convection and Radiation	FFB	2.0	1.7-2.4	63.6	60-66	26.8	25-30	7.6	6-8

^a Average

^b Range

^c Wt% on a dry light gas-only basis

**Figure 32. Light gas species observed during pyrolysis of live sparkleberry plotted as a function of final temperature.**

Tars are gases evolved in the pyrolysis environment that condense when cooled to room or ice

temperature. The initial tar species released from a surface may react further in a hot environment to (1) crack apart and form smaller light gas species, or (2) polymerize to form larger species called polyaromatic hydrocarbons (PAH) which can eventually polymerize to form soot. The yellow part of flames is due to radiant emission from hot soot particles formed largely from the tar. Soot is the dominant source of radiation from flames.

The GC/MS analysis of tars was able to determine 60 tar species with concentrations of more than 1 mol% of the tar in the FFB experiments, and over 30 compounds in the pyrolyzer experiments. There were many more compounds than these but in such low concentrations that signal-to-noise became a problem. Figure 33 shows the distribution of compounds measured in the FFB system in the three heating modes for longleaf pine (live, dead, and pine litter).

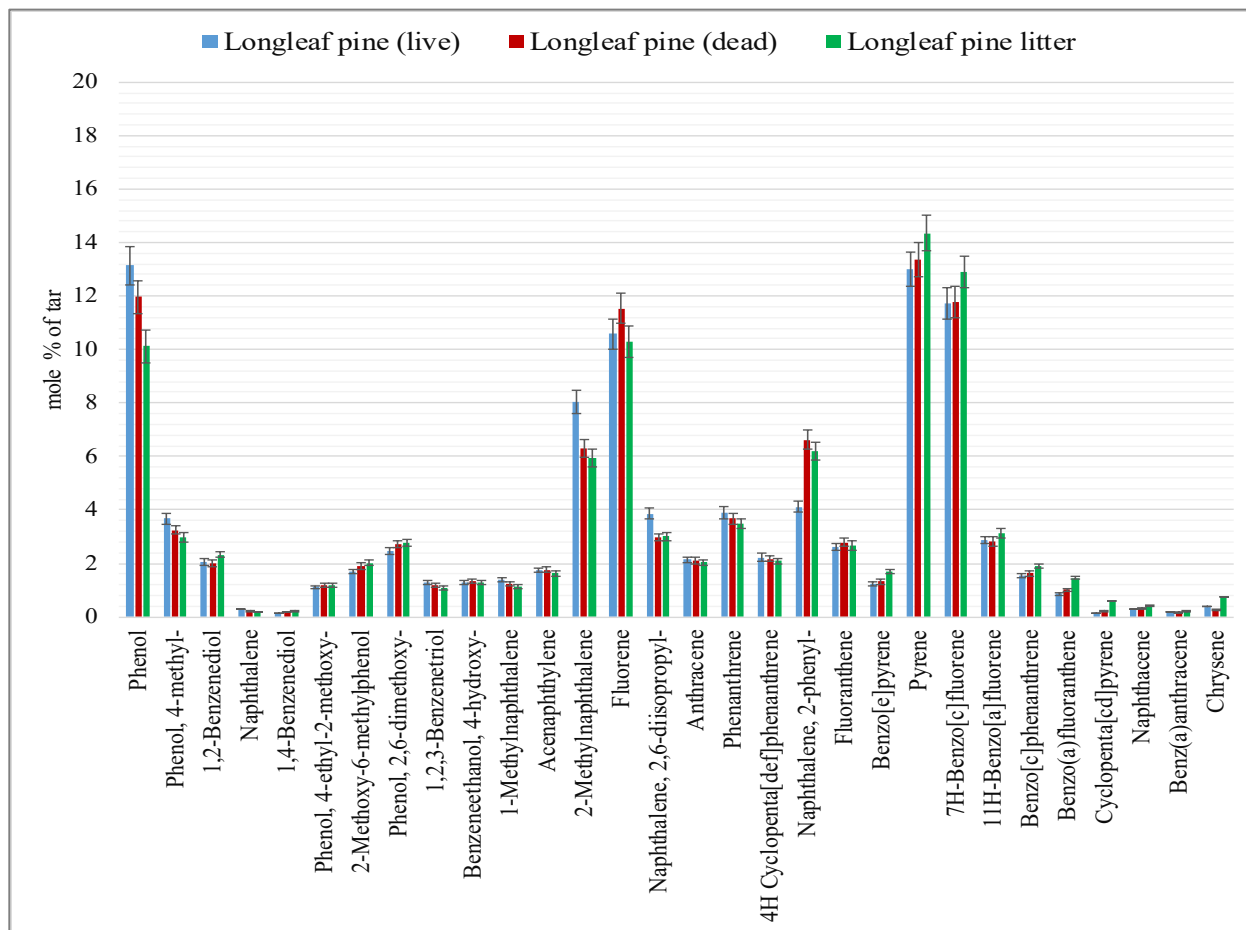


Figure 33. Distribution of tar compounds for the fast pyrolysis of longleaf pine.

Large variations in the amount of individual tar species were observed as a function of plant species. One of the major tar species that were observed in every experiment was phenol as shown in Figure 34 for all four modes of heating. The yields of each of these two tar species are quite different for each plant species, with no clear trend with heating mode that is common to all plant species. The different types of tar species were grouped for easier interpretation (**Figure 35**).

Pyrolysis kinetics were determined for fresh and air-dried foliage samples from the 14 species as well as longleaf pine litter. Since activation energy is a rate, the harmonic mean and associated 95 percent confidence intervals were estimated (Table 18, Figure 36) from the activation energies estimated for the 10 to 90 percent conversion levels [177]. Both the classic confidence interval and a nonparametric bootstrap confidence interval are presented [178]. While it is not desirable to use confidence intervals to compare equality of multiple means since the error rate is not controlled, for

most species except wax myrtle and Darrow's blueberry, the 95 percent confidence intervals for the harmonic means overlapped between the fresh samples and the air-dried samples. The confidence intervals reported in the Fall 2019 In-Progress Review were in error.

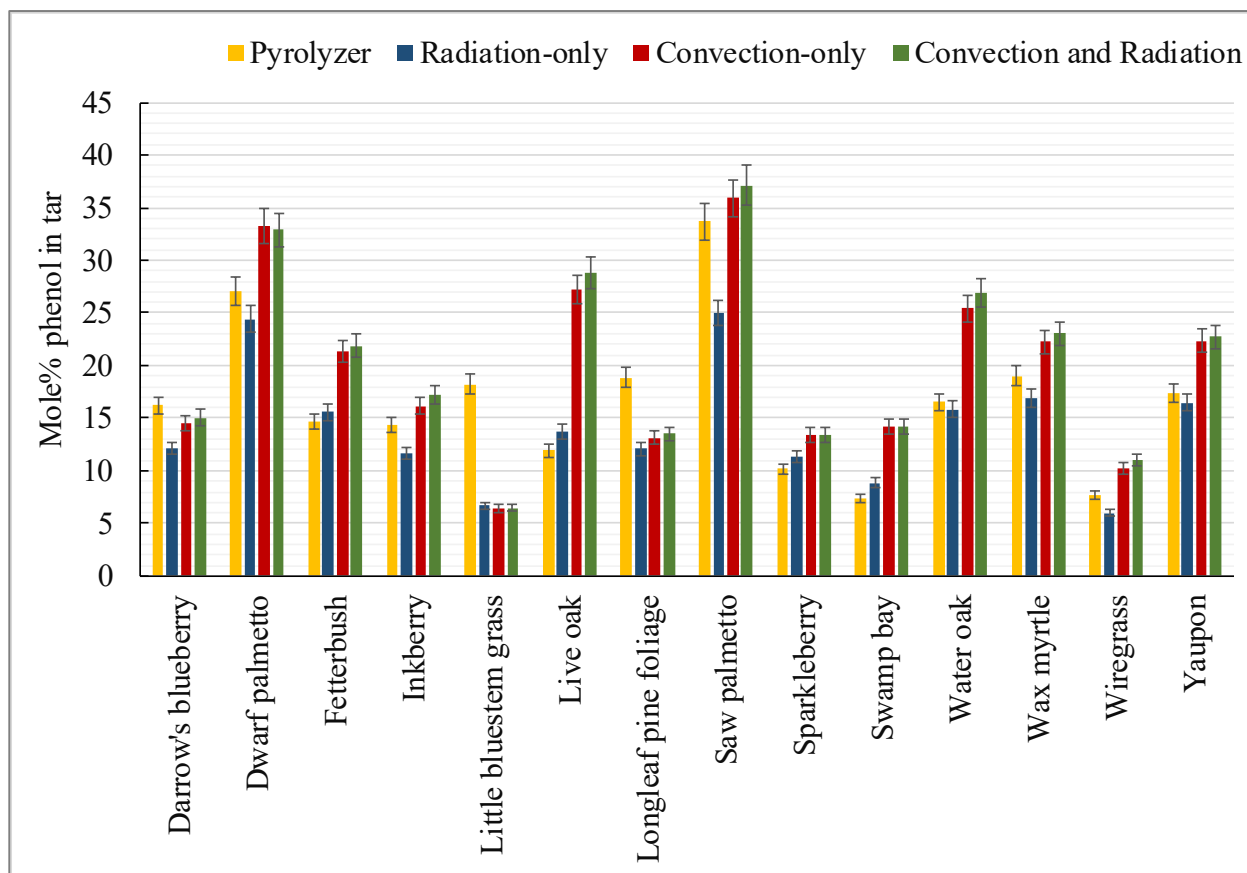


Figure 34. Mole percent phenol in tar during pyrolysis of 14 live plant species. Error bars represent the 95% confidence interval.

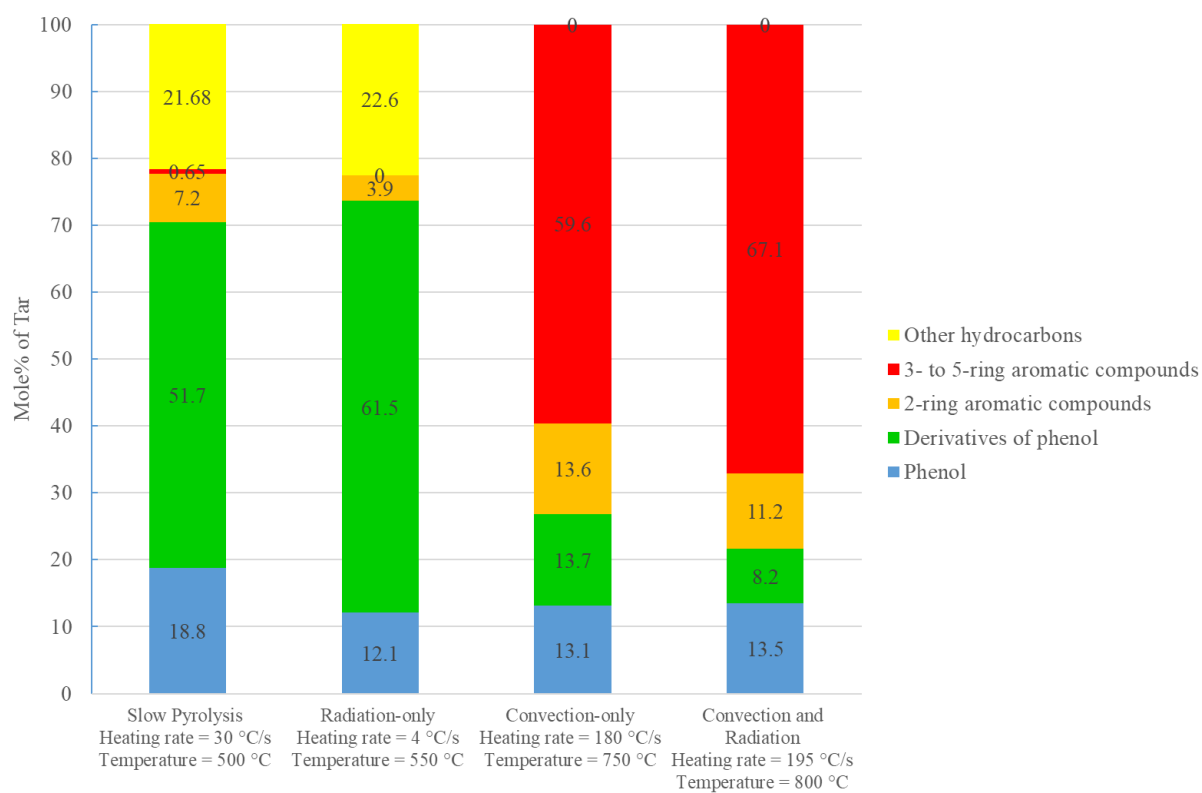


Figure 35. Distribution of functional groups in tar for pyrolysis of live longleaf pine foliage.

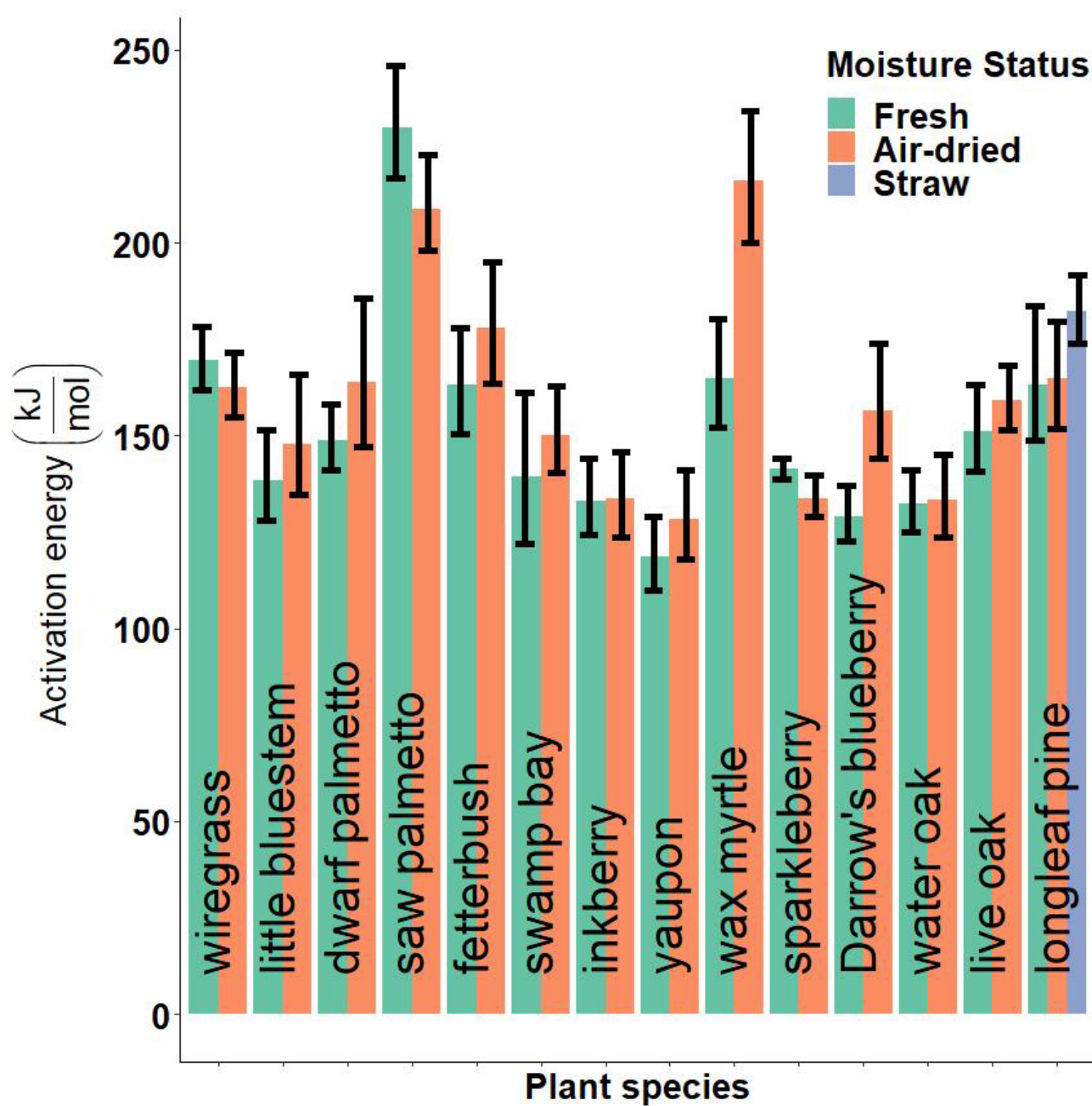


Figure 36. Harmonic mean and bootstrapped 95 percent confidence interval for activation energy measured in a pyrolyzer for common plant species from the southern U.S.

Table 18. Estimated harmonic mean (\bar{x}_H) and 95 percent confidence intervals for activation energy (kJ mol⁻¹) for fresh and air-dried foliage from plants native to the southern U.S. Both classic and bootstrap estimates are reported.

Plant Species	Fresh			Air-dried		
	\bar{x}_H	Classic CI	Bootstrap CI	\bar{x}_H	Classic CI	Bootstrap CI
Wiregrass	1.69E+2	(1.60E+2, 1.80E+2)	(1.62E+2, 1.78E+2)	1.63E+2	(1.53E+2, 1.74E+2)	(1.55E+2, 1.71E+2)
Little bluestem	1.39E+2	(1.26E+2, 1.55E+2)	(1.28E+2, 1.51E+2)	1.48E+2	(1.31E+2, 1.69E+2)	(1.35E+2, 1.64E+2)
Inkberry	1.33E+2	(1.22E+2, 1.47E+2)	(1.24E+2, 1.44E+2)	1.34E+2	(1.21E+2, 1.49E+2)	(1.24E+2, 1.46E+2)
Yaupon	1.19E+2	(1.08E+2, 1.32E+2)	(1.10E+2, 1.29E+2)	1.28E+2	(1.16E+2, 1.44E+2)	(1.18E+2, 1.41E+2)
Fetterbush	1.63E+2	(1.48E+2, 1.82E+2)	(1.51E+2, 1.79E+2)	1.78E+2	(1.60E+2, 2.00E+2)	(1.64E+2, 1.96E+2)
Wax myrtle	1.65E+2	(1.50E+2, 1.84E+2)	(1.52E+2, 1.80E+2)	2.16E+2	(1.96E+2, 2.40E+2)	(2.00E+2, 2.34E+2)
Swamp bay	1.40E+2	(1.19E+2, 1.69E+2)	(1.23E+2, 1.64E+2)	1.50E+2	(1.37E+2, 1.65E+2)	(1.40E+2, 1.64E+2)
Sparkleberry	1.41E+2	(1.38E+2, 1.45E+2)	(1.39E+2, 1.44E+2)	1.34E+2	(1.27E+2, 1.41E+2)	(1.28E+2, 1.40E+2)
Darrow's blueberry	1.29E+2	(1.21E+2, 1.39E+2)	(1.23E+2, 1.37E+2)	1.57E+2	(1.40E+2, 1.77E+2)	(1.44E+2, 1.73E+2)
Longleaf pine foliage	1.63E+2	(1.44E+2, 1.88E+2)	(1.48E+2, 1.82E+2)	1.65E+2	(1.49E+2, 1.84E+2)	(1.53E+2, 1.80E+2)
Longleaf pine litter				1.82E+2	(1.72E+2, 1.94E+2)	(1.74E+2, 1.92E+2)
Water oak	1.32E+2	(1.23E+2, 1.43E+2)	(1.26E+2, 1.41E+2)	1.34E+2	(1.21E+2, 1.49E+2)	(1.23E+2, 1.46E+2)
Live oak	1.51E+2	(1.38E+2, 1.67E+2)	(1.40E+2, 1.64E+2)	1.59E+2	(1.50E+2, 1.70E+2)	(1.52E+2, 1.68E+2)
Dwarf palmetto	1.49E+2	(1.39E+2, 1.60E+2)	(1.41E+2, 1.58E+2)	1.64E+2	(1.44E+2, 1.91E+2)	(1.47E+2, 1.85E+2)
Saw palmetto	2.30E+2	(2.14E+2, 2.49E+2)	(2.17E+2, 2.45E+2)	2.09E+2	(1.94E+2, 2.26E+2)	(1.96E+2, 2.23E+2)

Two types of kinetic models were used to fit the TGA data: model-free forms and simple specified forms. A model-free form using iso-conversional techniques was used to fit the main pyrolysis peak after moisture evaporation at 5 different heating rates (10 to 30 °C min⁻¹), resulting in activation energies as a function of conversion for live and dead samples of each plant species.

Figure 37 shows a comparison of the pyrolysis rates of all live plant species as a function of conversion in the first pyrolysis peak centered around 300 °C. At a conversion of 0.2, there is a factor of almost 5 difference in the pyrolysis rates between different plant species. Pyrolysis rates were also shown to be different for live vs. dead samples of the same plant species.

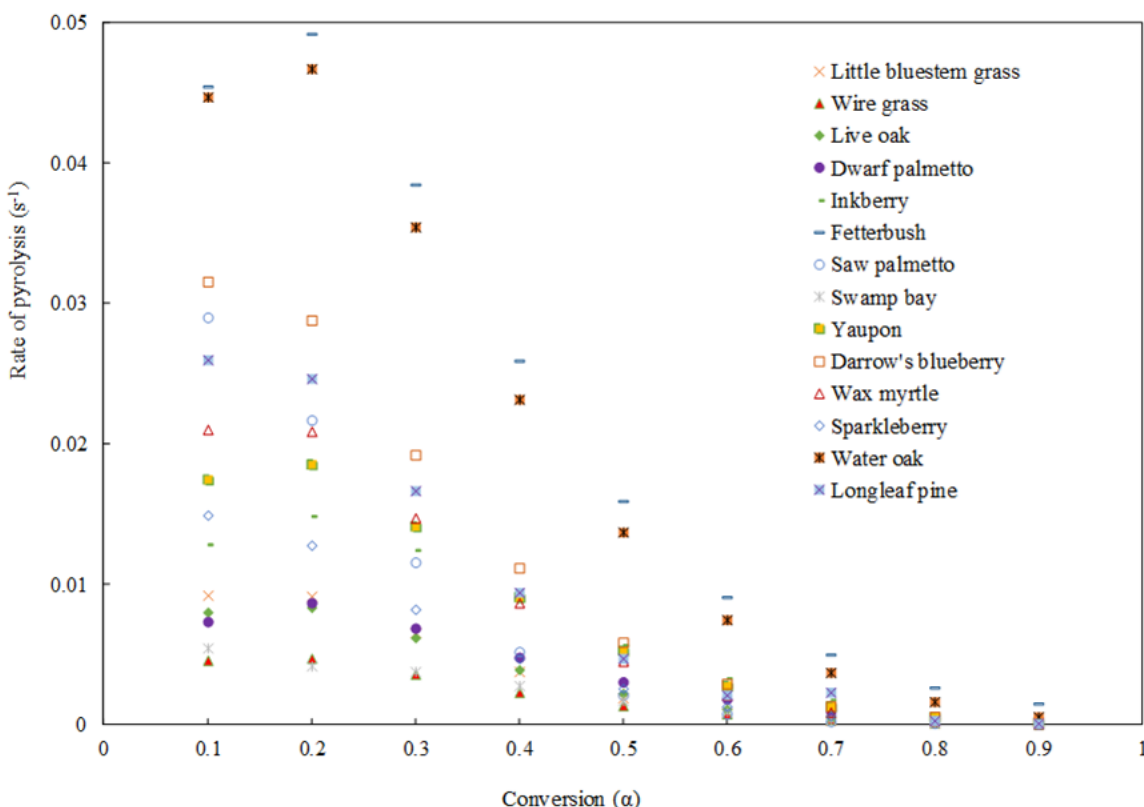


Figure 37. Distribution of pyrolysis rates as a function of conversion based on the KAS method for all live plant species at 300 °C. [177].

Engineering models of combustion generally require a specified simple model form that hopefully can describe the pyrolysis behavior over a wide range of heating rates, such as from smoldering or from rapid fire spread. A first-order 1-step model was shown to be inadequate for describing pyrolysis rates at multiple heating rates. A distributed activation energy model (DAEM) was therefore used to determine rate coefficients from the data. Each peak was modeled with a different component. Some species required only one component, while other plant species required up to 5 components. Figure 38 shows an example of the curve fit to pyrolysis data from water oak at three different heating rates using the same set of coefficients. DTG stands for the derivative of the TGA data. An attempt was made to correlate the activation energies found for each component in this analysis with the corresponding content of hemicellulose, cellulose, and lignin based on temperatures of peaks from the biomass literature. The results indicated no correlation between the activation

energies and the corresponding contents of hemicellulose, cellulose, and lignin. This lack of correlation is not too surprising since the chemical analysis of live plants revealed many more components than just hemicellulose, cellulose, and lignin. The multiple-reaction DAE model gave the best fit to the pyrolysis data at multiple heating rates when multiple peaks were observed. The multiple pyrolysis peaks were attributed to decomposition of hemicellulose, cellulose, and lignin, based on literature observations for biomass. The order of activation energies for pyrolysis of all plant species indicated that hemicellulose and extractives decompose more readily than cellulose and finally lignin [179].

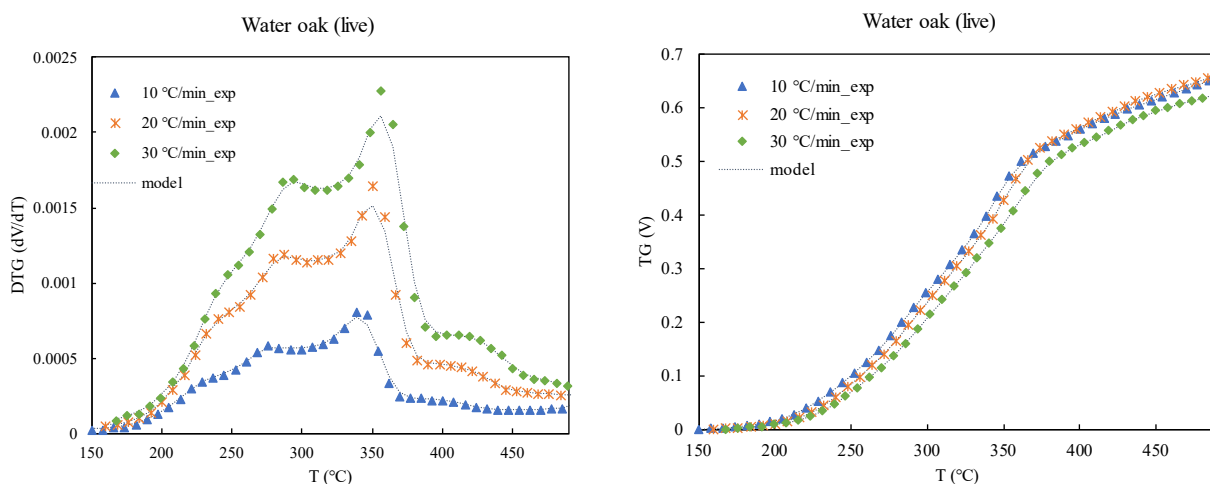


Figure 38. DTG and TG curves for live water oak resulted from experimental data and multiple-reaction DAEM model in heating rates of 10, 20, and 30 °C min⁻¹.

Reanalysis of the composition of pyrolysis gases from the bench-scale experiments consisted of analyzing the data expressed as mole fractions. Mass and mole fractions are compositionally equivalent as perturbation is used to change the units [115]. The 4 light gases and 322 organic compounds contained in the tar comprised a data set where each sample contained 326 parts (compounds). In the original data, mole fraction was calculated separately for the light gases and tars. In the full data set, 89.19 percent of the values were below detection limits (BDL). Nearly 190 of the identified compounds were detected in only single combinations of plant species by heating mode. After removing the compounds which were measured in less than 4 of 60 heating mode/species combinations, $D = 88$ compounds remained with a BDL rate of 64.05%. Thus, in the current analysis, each sample consisted of a vector where parts were the measured mole fractions. An average of 52 compounds were measured in the pyrolyzer while averages of 34, 37 and 30 compounds were recorded for the FFB radiation, convection and radiation+convection modes, respectively [126].

Plant species affected the amount of phenol, primary and secondary/tertiary tars relative to permanent gases and relative amounts of single- and multi-ring compounds. Plant moisture status affected the amount of CO relative to other permanent gases, of H₂ to CH₄ and tars to phenol. Heating mode and rate strongly influenced pyrolysate composition. Slow heating produced more primary tars relative to multi-ring tars than fast heating convective and combined radiant and convective heating modes. Slow heating produced relatively more compounds with fewer rings and fast heating produced relatively more multi-ring compounds. The use of compositional balances to form log-ratios contrasting subsets of parts of interest enabled hypothesis testing to examine relative differences in the amounts of gaseous pyrolysis products caused by plant species, moisture content and heating mode (Table 4). The results of this hypothesis testing have more formal rigor than was

previously presented, by respecting the relative nature of the data. We have definitively shown that plant species affected several different ratios of groups of pyrolysates and are assured that the results are not an artifact of the analysis, which can then be used to make various inferences and decisions. The effects of heating mode, which was confounded with heating rate, were shown to definitively affect the composition of pyrolysis products and we are assured that these results are not an artifact of the analysis. Increased heating rate resulted in less primary tars relative to other tars; the radiation-only mode, which also had the lowest environmental temperature, produced the greatest quantity of primary tars relative to other tars. The higher heating rates also produced more H_2 relative to CH_4 . The production of phenol relative to tars was more complex. The pyrolyzer and the FFB combination of radiation and convection, which represented the lowest and highest heating rates, produced less tar relative to phenol than radiant and convective heating alone, which represented the intermediate heating rates. The relative amounts of the pyrolysis products did not differ between fresh and air-dried foliage samples. The presence of H_2O in the samples would not affect the ratios between the other gases, suggesting water's role may only be as a diluent. It is important to note that the effects of plant species, heating mode and moisture status are independent of the units used to describe the composition due to the use of CoDA.

4.2.2 *Wind tunnel experiment*

While most pyrolysis work applied to wildland fire is based on slow-heating, in wildland fire reported air heating rates near foliar fuels ranged 30 to 5000 $^{\circ}C\ s^{-1}$ [2,71–74] which are more akin to fast and flash pyrolysis heating rates represented in the bench scale tests by the FFB experiments than the slow pyrolysis heating rates. As can be seen in Table 10, the estimated heating rates in both the wind tunnel and field fires suggest fast pyrolysis. Mean spread rate of all fires was 0.008 (0.004 – 0.027) $m\ s^{-1}$. In the wind tunnel, visually estimated flame heights for the no wind fires ranged from 0.3 to 0.6 m with an estimated flame depth of 0.3 m based on a residence time of 28 s derived from an average longleaf pine needle diameter of 0.0015 m [180–182]. Flame heights for the wind-aided fires were similar and the flame lengths were longer. These flame heights fall at the lower end of the range reported for low intensity prescribed burns in southern fuel beds [14,183,184]. An overhead view of a fuel bed containing inkberry and the flame for a no wind fire can be found elsewhere [185]. Vertical total and radiant fluxes into the fuel bed ranged up to 25- and 14- $kW\ m^{-2}$, respectively [186,187]. Horizontal convective fluxes from the plume to the leaves ranged up to 0.8 $kW\ m^{-2}$ [139]. Harmonic mean spread rate (0.008 $m\ s^{-1}$), longleaf pine heat of combustion (19,000 $kJ\ kg^{-1}$) [188], dry fuel loading (0.45 $kg\ m^{-2}$) and flame depth (0.3 m) yielded a fireline intensity of 68 $kW\ m^{-1}$ and combustion rate of 228 $kW\ m^{-2}$ [11,182] for the wind tunnel fires. The heating rates, rate of spread and estimated flame lengths from the wind tunnel and field fires were similar supporting comparison between the sampled gas compositions.

In total, 88 fires were burned in the wind tunnel. The wet fuel loading of the longleaf pine needles was typically 0.5 $kg\ m^{-2}$, mean (min, max) fuel moisture content of the needles was 9.8 (6, 15.6) percent and the live foliage was 112.5 (73.2, 173.6) percent. In the wind tunnel, environmental conditions simulated growing season (dead fuel moisture = 9.6%, air temperature = 297 K, relative humidity = 35%) and dormant season (dead fuel moisture = 10.6%, air temperature = 280.6 K, relative humidity = 63%) weather. Twenty-nine gases were identified in the wind tunnel and field burn canisters. Seven of the gases were observed at levels which occurred mostly below detection limit, so they were dropped from the analysis resulting in a composition with $D = 22$ gases. In the wind tunnel fires, the geometric mean concentrations ranged from a high of 3840 ppm for CO_2 to a low of 0.0019 for cis-2-pentene (Table 19). The original concentrations were summarized as geometric mean * geometric standard deviation. Overall, CO_2 was the dominant gas observed in the wind tunnel canister samples followed by CO , H_2 , and CH_4 (Table 19) based on relative amounts.

Geometric mean concentrations for wind tunnel and field gas samples ranged over seven and eight orders of magnitude, respectively (Figure 39, Table 19). While the relative concentrations of CO, CO₂, and CH₄ in the wind tunnel were similar between the pyrolysis and flaming combustion samples, the relative concentration of H₂ doubled in the pyrolysis canisters (Figure 40). Relative concentrations of many of the higher molecular weight trace gases were greater in the pyrolysis samples, likely due to the decreased relative amount of CO₂. The relative amount of isobutane and isopentane varied greatly accounting for 43.2 percent of the total variance (Table 19). In the variation arrays (Table 20) for pyrolysis and flaming combustion samples, a mean log-ratio less than 0 indicated that amount of the gas in the numerator was relatively smaller than the gas in the denominator. Less CH₄ (-5.0) was present than H₂ (-4.1) relative to CO₂ in the pyrolysis samples.

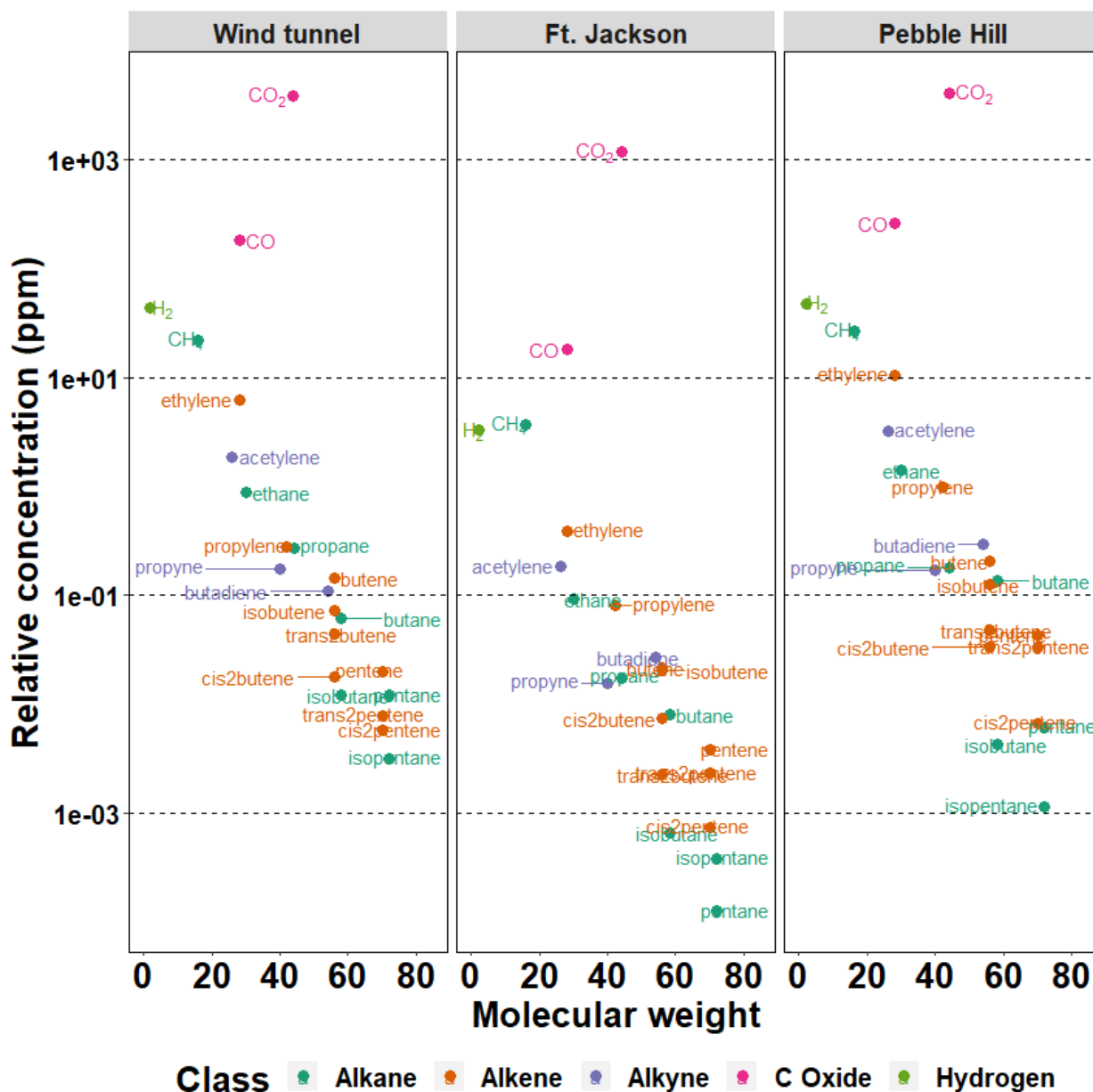


Figure 39. Observed mean composition of canister samples from wind tunnel and field fires in longleaf pine fuel beds in original units.

The log-ratios of CH₄ to H₂ in the pyrolysis (-0.9) and flaming combustion (-0.4) samples also show that less CH₄ relative to H₂ was present in the wind tunnel samples suggesting that relatively more of the H₂ was oxidized. The relatively greater concentration of H₂ is important to note as most pyrolysis modelling considers CH₄ to be more abundant [e.g. 189] based on mass fraction.

The variance of a log-ratio can be viewed as an indicator of the proportionality between two parts (see footnote b in Table 20). The smaller the value of $\hat{\tau}_{ij}$, the more constant the log-ratio is which may indicate proportionality. While there were several log-ratio variances that were less than 1 for both pyrolysis and flaming combustion samples (Table 20), we chose to identify the parts which accounted for most of the variability. Isobutane, isopentane, propene and pentane accounted for over half of the total variance (Table 19) even though these gases were relatively small parts of the compositions. Greater proportionality between parts across a range of fuel types might be used to as an indicator about how to simplify description of pyrolysis.

4.2.3 Linear mixed model

Since the flaming and pyrolysis samples were collected in a single experiment, we initially fit a linear mixed model with a random effect for the paired nature of the measurements and a factor for the sample type (flaming or pyrolysis). A likelihood ratio test indicated that the random effect term was not statistically significant ($\chi^2 = 0$, p-value = 1). Model estimates showed that there was a statistically significant difference in the *ilr* coordinates between flaming and pyrolysis phase samples (F-value_{1,128} = 15.88, p-value = 0.0001). This difference can be seen in the summary statistics for the two phases (Table 19, Figure 40). All mean log-ratios of the gases with CO₂ were larger for the pyrolysis samples compared to the flaming samples, indicating that either relatively less CO₂ or more of an individual gas was present in the pyrolysis samples (Table 20).

4.2.4 Effect of fuel bed

Since the *ilr* coordinates differed between pyrolysis and flaming combustion, analysis of the effect of fuel bed on pyrolysis composition was restricted to the 86 wind tunnel pyrolysis samples. The fuel bed effect was statistically significant (Table 21). Based on the ANOVA parameterization, the intercept term represented the longleaf needle fuel bed with no live plants of any species. The fuel bed effect captured the change in pyrolysis composition (all parts collectively) caused by the addition of live plants to the longleaf pine needles. Natural logarithms of fuel moisture content, air temperature (K) and relative humidity were used [115]. None of the environmental variables were statistically significant (Table 21). Average deviation plots (Figure 41) illustrated the relative differences in fuel bed effects. For several gases, the mean of sparkleberry relative to the overall mean often had the largest (or smallest) average deviations compared to the other fuel beds.

Pairwise comparisons between fuel bed types for the custom balances were made (Table 23). Fuel bed significantly affected only the *ilr* coordinates for the measured amount of alkanes relative to other NMOCs. Sparkleberry fuel beds produced relatively more alkanes (C₂H₆, C₃H₈, C₄H₁₀, C₅H₁₂) than other NMOCs (C₂H₂, C₂H₄, C₃H₄, C₃H₆, C₄H₆, C₄H₈ and C₅H₁₀). Overall, these results suggest that fuel bed did not significantly affect the composition of the pyrolysis gases in the wind tunnel even though live plant mass may have ranged to as high as 30 percent of the total fuel bed mass. The lack of an effect of fuel bed on the Zhou and Westbrook balances suggests that these pyrolysis mechanisms might be used in modeling for a variety of fuel bed types containing longleaf pine needles.

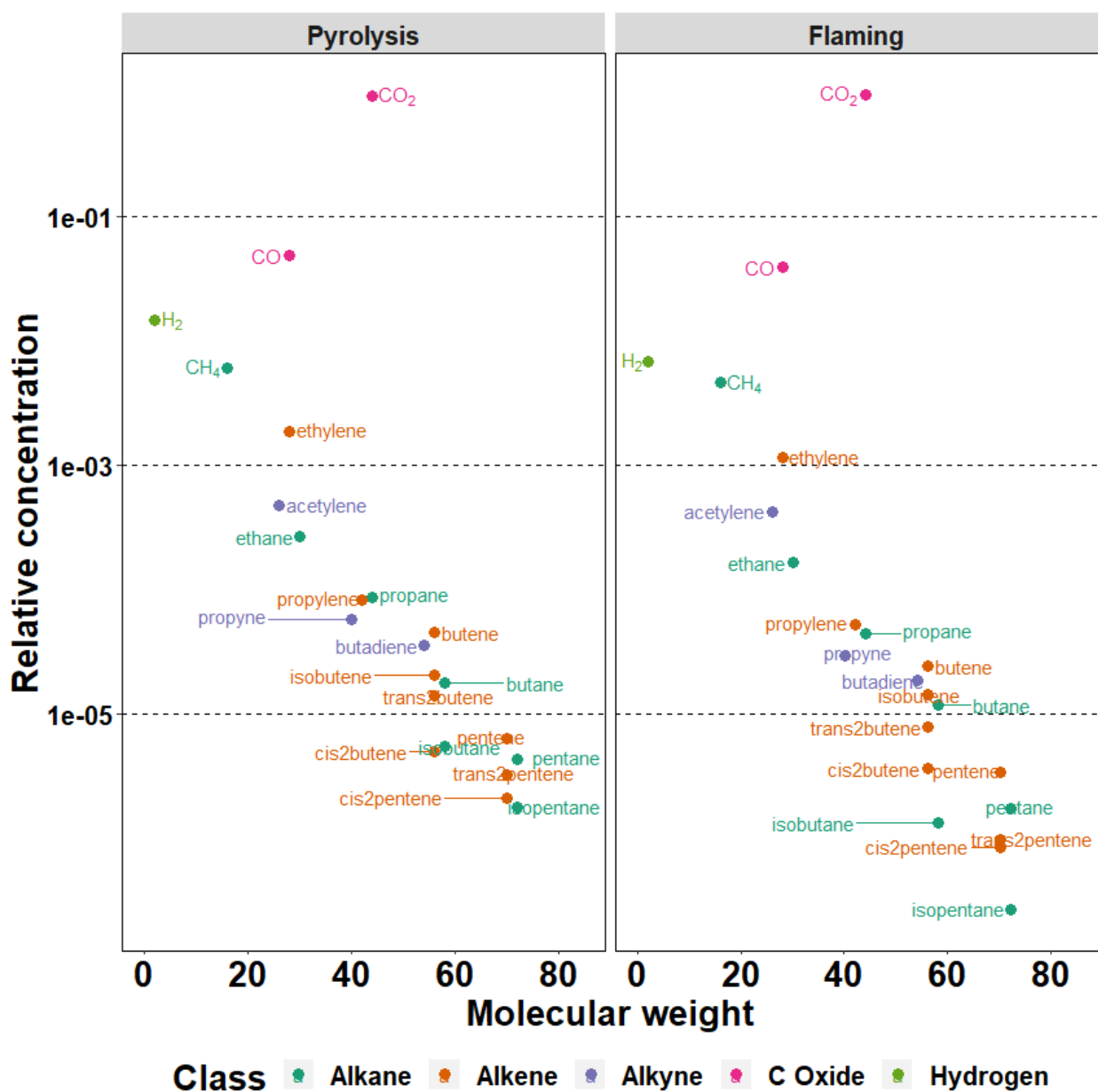


Figure 40. Observed mean composition of samples of pyrolysis and flaming combustion gases in wind tunnel fires by chemical type after closure.

Table 19. Summary statistics for pyrolysis and flaming combustion canisters collected during wind tunnel fires in fuel beds of longleaf pine needles with selected plants from the southeastern U.S. Concentration in ppm. Number of samples: flaming = 67, pyrolysis = 86.

Gas	Concentration ^a				BDL ^b	Wind tunnel Centre ^c		Var ^d	
	Wind tunnel	Ft. Jackson	Pebble Hill			Pyro	Flam	Pyro	Flam
carbon dioxide (CO ₂)	3.84e+03*4.82e+00	1.18e+03*2.34e+00	4.06e+03*3.17e+00	0.0		9.28E-01	9.47E-01	3.6	2.8
carbon monoxide (CO)	1.80e+02*1.34e+01	1.82e+01*7.31e+00	2.62e+02*1.25e+01	0.0		4.82E-02	3.91E-02	3.0	3.5
hydrogen (H ₂)	4.32e+01*1.07e+01	3.27e+00*3.98e+00	4.75e+01*1.21e+01	0.0		1.47E-02	6.87E-03	1.6	1.9
methane (CH ₄)	2.20e+01*6.86e+00	3.69e+00*1.87e+00	2.69e+01*7.44e+00	0.0		6.07E-03	4.60E-03	0.8	0.8
ethane (C ₂ H ₆)	9.14e-01*1.27e+01	9.24e-02*4.19e+00	1.41e+00*1.13e+01	8.1		2.81E-04	1.72E-04	0.2	0.4
ethylene (C ₂ H ₄)	6.33e+00*1.81e+01	3.91e-01*9.69e+00	1.05e+01*1.61e+01	3.5		1.88E-03	1.14E-03	0.8	2.0
acetylene (C ₂ H ₂)	1.74e+00*1.45e+01	1.84e-01*6.57e+00	3.22e+00*3.80e+01	7.6		4.80E-04	4.12E-04	3.5	3.6
propane (C ₃ H ₈)	2.56e-01*1.83e+01	1.74e-02*5.21e+00	1.81e-01*8.84e+00	11.6		8.33E-05	4.29E-05	2.0	1.8
propylene (C ₃ H ₆)	2.93e-01*1.47e+01	8.14e-02*8.34e+00	9.82e-01*3.82e+01	17.7		8.56E-05	5.25E-05	7.3	6.8
propyne (C ₃ H ₄)	1.88e-01*1.82e+01	1.57e-02*5.94e+00	1.70e-01*1.84e+01	19.7		6.01E-05	3.38E-05	0.7	1.9
butane (C ₄ H ₁₀)	6.72e-02*1.59e+01	7.97e-03*5.26e+00	1.37e-01*1.27e+01	27.8		2.24E-05	1.22E-05	1.1	2.5
isobutane (C ₄ H ₁₀)	2.07e-02*1.34e+02	6.68e-04*3.40e+01	4.27e-03*1.78e+01	50.0		3.50E-06	3.73E-06	25.2	15.0
butene (C ₄ H ₈)	1.41e-01*1.21e+01	2.17e-02*4.68e+00	2.04e-01*1.72e+01	14.1		4.42E-05	2.35E-05	0.5	0.9
isobutene (C ₄ H ₈)	7.30e-02*9.03e+00	2.07e-02*2.75e+00	1.26e-01*1.05e+01	17.7		2.12E-05	1.23E-05	1.7	1.3
trans2butene (C ₄ H ₈)	4.84e-02*2.04e+01	2.27e-03*1.12e+01	4.77e-02*1.08e+01	31.3		1.40E-05	8.41E-06	2.8	1.7
cis2butene (C ₄ H ₈)	1.82e-02*9.46e+00	7.30e-03*2.89e+00	3.36e-02*1.41e+01	37.9		5.03E-06	4.93E-06	3.7	1.9
butadiene (C ₄ H ₆)	1.05e-01*1.22e+01	2.70e-02*4.25e+00	2.97e-01*1.95e+01	18.2		3.38E-05	1.60E-05	3.6	3.5
pentane (C ₅ H ₁₂)	1.28e-02*5.78e+01	1.26e-04*2.71e+01	6.17e-03*7.98e+01	52.5		3.69E-06	1.67E-06	9.3	8.0
isopentane (C ₅ H ₁₂)	2.13e-03*2.95e+02	3.84e-04*6.14e+01	1.15e-03*2.91e+01	58.1		1.21E-06	1.84E-07	18.8	26.9
pentene (C ₅ H ₁₀)	2.17e-02*1.37e+01	3.81e-03*7.88e+00	4.27e-02*1.28e+01	40.9		6.43E-06	3.81E-06	2.5	1.7
trans2pentene (C ₅ H ₁₀)	7.56e-03*2.42e+01	2.31e-03*6.83e+00	3.35e-02*6.34e+00	58.6		2.31E-06	1.26E-06	3.3	7.1
cis2pentene (C ₅ H ₁₀)	6.56e-03*1.83e+01	7.43e-04*1.19e+01	6.63e-03*2.72e+01	61.1		2.01E-06	8.00E-07	3.9	4.1

a. Geometric mean is related to geometric standard deviation by multiplication and division, represented by “*”.

b. Percentage of observations with below detection limit (BDL) values.

c. Mean (centre) composition for pyrolysis and flaming combustion canisters based on concentration.

d. Percentage of total (metric) variance (239.518) contributed by pyrolyzate.

Table 20. Variation array of gas composition for pyrolysis and flaming combustion measured in a wind tunnel. Mean log-ratio and log-ratio variance ($\hat{\tau}_{ij}$) for each pair of gases are found below and above the diagonal, respectively.

	CO ₂	CO	H ₂	CH ₄	C ₂ H ₆	C ₂ H ₄	C ₂ H ₂	C ₃ H ₈	C ₃ H ₆	propyne	butane	isobutane	t butene	isobutene	trans2butene	cis2butene	C ₄ H ₆	pentane	isopentane	C ₅ H ₁₀	trans2pentene	cis2pentene
Pyrolysis																						
CO ₂		1.4 ^b	2.4	1.6	3.1	4.4	4.2	4.6	5.9	4.1	3.3	30.6	2.9	2.4	6.5	3.3	3.9	12.7	19.0	3.4	5.3	6.3
CO	-3.0 ^a		2.0	2.5	2.7	3.2	4.7	4.2	6.9	3.3	3.6	25.9	2.6	3.0	5.3	3.7	4.6	10.6	15.8	3.7	5.1	6.0
H ₂	-4.1	-1.2		1.1	1.2	1.7	2.9	3.1	6.1	1.4	1.8	25.7	1.2	1.6	4.1	3.8	2.8	8.9	15.1	2.6	3.5	4.4
CH ₄	-5.0	-2.1	-0.9		0.7	1.5	2.5	2.1	5.4	1.5	1.1	26.0	0.8	1.0	3.5	3.2	2.4	8.6	15.0	1.3	2.7	3.2
C ₂ H ₆	-8.1	-5.2	-4.0	-3.1		0.4	2.4	1.3	5.7	0.8	1.0	23.7	0.3	1.2	2.3	3.4	2.7	7.2	13.5	1.2	2.3	2.8
C ₂ H ₄	-6.2	-3.2	-2.1	-1.2	1.9		2.7	1.9	6.4	0.6	1.4	22.8	0.8	1.9	2.5	4.6	3.3	6.9	13.6	2.0	2.8	3.0
C ₂ H ₂	-7.6	-4.6	-3.4	-2.5	0.6	-1.4		6.4	1.6	2.1	1.7	35.9	1.9	1.4	7.2	3.0	1.3	13.7	23.4	3.6	5.2	5.1
C ₃ H ₈	-9.3	-6.3	-5.2	-4.3	-1.2	-3.1	-1.7		10.7	2.8	3.3	19.8	2.1	3.4	2.5	6.4	6.2	7.0	10.5	2.4	3.1	4.5
C ₃ H ₆	-9.4	-6.4	-5.2	-4.3	-1.2	-3.2	-1.8	-0.1		5.4	4.8	43.7	4.9	3.7	11.7	3.5	3.2	18.7	30.2	6.2	8.8	8.8
propyne	-9.7	-6.7	-5.5	-4.7	-1.6	-3.5	-2.1	-0.4	-0.3		1.2	24.8	0.9	1.7	3.8	4.0	2.3	7.2	15.3	2.3	3.2	3.2
butane	-10.6	-7.7	-6.5	-5.6	-2.5	-4.4	-3.0	-1.3	-1.2	-0.9		27.7	1.1	1.2	3.7	3.3	1.8	9.3	16.6	1.8	3.0	4.0
isobutane	-12.9	-10.0	-8.8	-7.9	-4.8	-6.7	-5.3	-3.6	-3.5	-3.2	-2.3		25.5	30.1	18.7	34.4	35.3	17.7	18.2	25.3	23.8	22.7
butene	-9.9	-7.0	-5.8	-4.9	-1.8	-3.7	-2.4	-0.6	-0.6	-0.2	0.7	3.0		1.0	2.9	3.1	2.2	8.0	14.3	1.0	2.6	2.8
isobutene	-10.6	-7.7	-6.5	-5.6	-2.5	-4.4	-3.1	-1.3	-1.3	-0.9	0.0	2.3	-0.7		4.7	2.4	0.8	10.4	17.5	1.6	3.2	4.4
trans2butene	-11.2	-8.2	-7.0	-6.2	-3.1	-5.0	-3.6	-1.9	-1.8	-1.5	-0.6	1.7	-1.3	-0.6		6.8	7.1	5.0	10.5	2.8	3.3	4.1
cis2butene	-12.2	-9.3	-8.1	-7.2	-4.1	-6.0	-4.6	-2.9	-2.9	-2.5	-1.6	0.7	-2.3	-1.6	-1.0		2.7	13.5	22.2	3.8	6.1	6.0
C ₄ H ₆	-10.2	-7.2	-6.0	-5.1	-2.0	-4.0	-2.6	-0.8	-0.8	-0.5	0.5	2.8	-0.2	0.5	1.0	2.1		13.3	22.2	3.3	5.2	5.9
pentane	-12.2	-9.3	-8.1	-7.2	-4.1	-6.0	-4.7	-2.9	-2.9	-2.5	-1.6	0.7	-2.3	-1.6	-1.0	0.0	-2.1		12.0	7.3	8.4	8.0
isopentane	-13.5	-10.5	-9.3	-8.4	-5.3	-7.3	-5.9	-4.2	-4.1	-3.8	-2.9	-0.6	-3.5	-2.8	-2.3	-1.2	-3.3	-1.2		14.4	13.7	16.5
C ₅ H ₁₀	-11.7	-8.7	-7.5	-6.6	-3.5	-5.5	-4.1	-2.4	-2.3	-2.0	-1.1	1.2	-1.7	-1.0	-0.5	0.6	-1.5	0.6	1.8		3.3	3.5
trans2pentene	-12.6	-9.6	-8.4	-7.5	-4.4	-6.4	-5.0	-3.3	-3.2	-2.9	-2.0	0.3	-2.6	-1.9	-1.4	-0.3	-2.4	-0.3	0.9	-0.9		4.9
cis2pentene	-12.9	-10.0	-8.8	-7.9	-4.8	-6.7	-5.4	-3.6	-3.6	-3.3	-2.3	0.0	-3.0	-2.3	-1.8	-0.7	-2.8	-0.7	0.5	-1.3	-0.4	
Flaming Combustion																						
CO ₂		1.7	2.1	1.4	3.8	4.4	3.6	5.8	4.8	4.5	3.1	23.0	3.6	3.0	6.9	4.0	4.5	17.0	28.3	3.5	7.9	6.4
CO	-3.2		2.8	2.5	4.1	4.3	3.6	7.1	4.7	4.9	3.6	23.4	4.3	3.7	8.2	5.7	5.2	18.1	30.5	4.9	9.1	8.2
H ₂	-4.9	-1.7		1.4	2.0	2.7	2.8	4.4	4.2	2.4	1.8	20.8	2.0	2.1	4.8	4.0	3.3	17.1	25.6	3.3	7.7	6.3
CH ₄	-5.3	-2.1	-0.4		1.4	2.1	3.2	2.9	5.5	2.1	1.2	17.5	1.3	1.6	3.6	2.4	2.3	13.3	23.0	1.9	5.4	5.1
C ₂ H ₆	-8.7	-5.5	-3.8	-3.4		0.9	2.7	1.6	5.7	1.5	1.0	16.4	0.6	1.5	2.4	3.2	1.8	14.1	20.2	2.6	5.7	5.3
C ₂ H ₄	-6.7	-3.5	-1.7	-1.3	2.0		2.8	2.8	5.9	2.0	1.7	15.7	1.7	2.4	3.0	4.2	2.2	15.1	20.8	3.5	7.4	6.8
C ₂ H ₂	-7.8	-4.6	-2.8	-2.4	0.9	-1.1		7.3	1.9	3.3	2.1	27.1	3.4	2.9	7.5	4.7	2.7	22.3	31.6	5.6	11.1	9.6
C ₃ H ₈	-10.0	-6.8	-5.0	-4.6	-1.3	-3.3	-2.2		10.6	3.5	3.2	12.8	1.9	3.8	2.3	4.8	4.4	12.3	16.4	3.8	5.5	6.0
C ₃ H ₆	-9.8	-6.6	-4.9	-4.5	-1.1	-3.1	-2.1	0.1		5.1	4.3	34.4	5.4	3.9	10.8	6.4	4.4	27.7	39.9	8.0	13.6	11.3
propyne	-10.1	-6.9	-5.2	-4.8	-1.4	-3.5	-2.4	-0.2	-0.3		0.8	18.9	0.8	1.2	3.1	3.2	2.4	16.8	23.9	3.2	7.3	6.4
butane	-11.0	-7.8	-6.1	-5.7	-2.3	-4.3	-3.2	-1.0	-1.2	-0.9		19.2	1.0	1.4	3.1	2.4	2.1	15.8	24.2	2.7	7.3	6.3

isobutane	-12.8	-9.6	-7.9	-7.5	-4.1	-6.1	-5.0	-2.8	-3.0	-2.7	-1.8		17.3	20.7	13.5	19.9	22.1	14.0	13.0	15.3	19.3	18.5
butene	-10.6	-7.4	-5.6	-5.2	-1.9	-3.9	-2.8	-0.6	-0.7	-0.4	0.4	2.2		0.7	2.5	2.3	1.9	14.8	21.5	2.1	4.9	4.8
isobutene	-11.2	-8.0	-6.3	-5.9	-2.5	-4.5	-3.5	-1.3	-1.4	-1.1	-0.2	1.6	-0.7		3.7	2.7	2.0	17.3	25.7	2.6	5.4	5.3
trans2butene	-11.7	-8.5	-6.8	-6.4	-3.0	-5.0	-3.9	-1.7	-1.9	-1.6	-0.7	1.1	-1.1	-0.5		4.2	4.4	12.2	16.2	3.8	6.8	5.5
cis2butene	-12.5	-9.3	-7.5	-7.1	-3.8	-5.8	-4.7	-2.5	-2.6	-2.3	-1.5	0.3	-1.9	-1.2	-0.8		3.6	16.1	25.8	2.5	6.7	6.9
C ₄ H ₆	-10.8	-7.6	-5.9	-5.5	-2.1	-4.1	-3.0	-0.8	-1.0	-0.7	0.2	2.0	-0.2	0.4	0.9	1.7		17.6	25.2	4.2	7.1	7.0
pentane	-13.6	-10.5	-8.7	-8.3	-5.0	-7.0	-5.9	-3.7	-3.8	-3.5	-2.6	-0.8	-3.1	-2.4	-1.9	-1.2	-2.8		15.4	12.4	11.8	11.2
isopentane	-15.0	-11.8	-10.1	-9.7	-6.3	-8.3	-7.2	-5.0	-5.2	-4.9	-4.0	-2.2	-4.4	-3.8	-3.3	-2.5	-4.2	-1.4		20.5	20.2	18.5
C ₅ H ₁₀	-12.3	-9.1	-7.4	-7.0	-3.6	-5.7	-4.6	-2.4	-2.5	-2.2	-1.3	0.5	-1.8	-1.1	-0.6	0.1	-1.5	1.3	2.7		5.2	4.3
trans2pentene	-13.6	-10.4	-8.7	-8.3	-4.9	-6.9	-5.8	-3.6	-3.8	-3.5	-2.6	-0.8	-3.1	-2.4	-1.9	-1.2	-2.8	0.0	1.4	-1.3		4.7
cis2pentene	-13.9	-10.8	-9.0	-8.6	-5.3	-7.3	-6.2	-4.0	-4.1	-3.8	-2.9	-1.1	-3.4	-2.7	-2.2	-1.5	-3.1	-0.3	1.1	-1.6	-0.3	

a. Geometric mean of log ratio.

b. $\hat{\tau}_{ij} = \text{var}(\ln(x_i/x_j))$ where x_i and x_j are gases in the composition and var is the usual sample variance. $\exp(-\hat{\tau}_{ij}^2/2)$ has been suggested as a measure of proportionality between two gases [115,190].

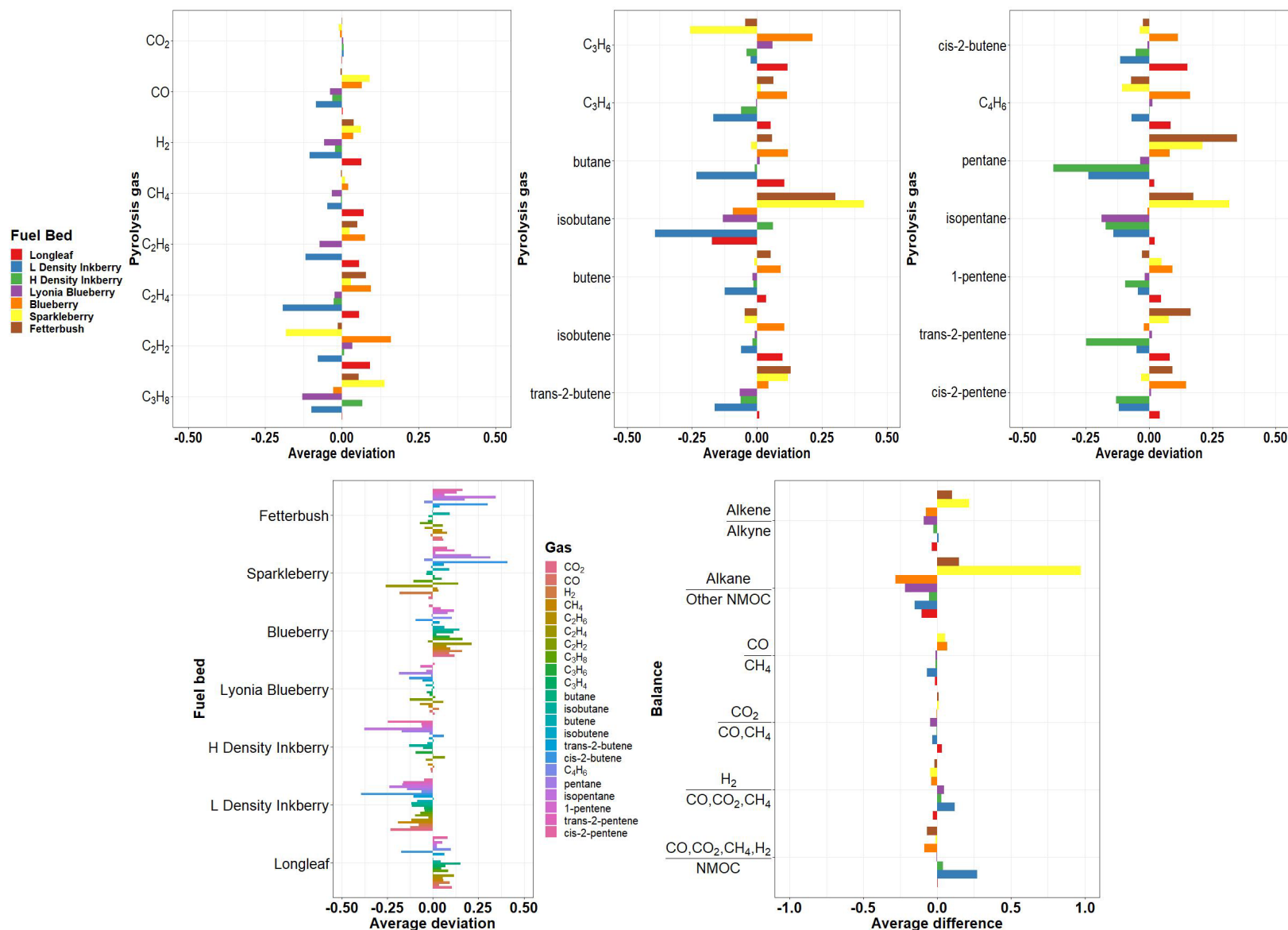


Figure 41. Deviations of fitted geometric mean to overall geometric mean (in log-ratio scale) for fuel beds organized by individual gas (upper) and for individual gases organized by fuel bed (lower left), and differences in mean balances (group versus overall) between gases for fuel beds (lower right).

Table 21. Influence of fuel bed type and environmental variables on the composition of pyrolysis gases measured in a wind tunnel.

Source	df ^a	Pillai's ^b trace	Hypothesis tests			Pr(>F)
			F ^c	Num df	Den df	
Fuel bed	6	1.90	1.35	126	366	0.02
Air temperature	1	0.31	2.65	21	56	0.27
Dead fuel moisture	1	0.36	1.74	21	56	0.12
Relative humidity	1	0.22	0.53	21	56	0.77

^a Degrees of freedom of effect. Natural logarithms of air temperature, dead fuel moisture and relative humidity were used because they are ratio scale variables (van den Boogaart and Tolosana-Delgado 2013).

^b Pillai's trace used to test equality of means.

^c F-statistic associated with Pillai's trace. Numerator df is the df for the effect multiplied by $D-1$.

Table 22. Custom balances of gases for wind tunnel and field experiments determined by sequential binary partition. “+” and “-” denote gases in the numerator and denominator, respectively.

Balance	H ₂	CO	CO ₂	CH ₄	Alkanes	Alkenes	Alkynes
Zhou vs NMOC ^a	+	+	+	+	-	-	-
H ₂ vs CO ₂ , CO, CH ₄ ^b	+	-	-	-			
CO ₂ vs CO, CH ₄		-	+	-			
CO vs CH ₄		+		-			
Alkanes vs other NMOC ^c					+	-	-
Alkenes vs Alkynes						+	-

^a Zhou refers to a reduced combustion mechanism containing H₂, CO, CO₂, and CH₄ [191]. NMOC is non-methane organic compounds.

^b H₂ compared to the gases in Westbrook-Dryer combustion mechanism [192].

^c Alkanes - C₂H₆, C₃H₈, C₄H₁₀, C₅H₁₂; alkenes - C₂H₄, C₃H₆, C₄H₈, C₅H₁₀; alkynes - C₂H₂, C₃H₄, C₄H₆

Table 23. Pairwise comparisons of fuel bed effect on selected balances of pyrolysis gases measured in a wind tunnel. For each balance, fuel beds that did not differ are indicated by the same letter with the letter values ordered from smallest to largest. P-values adjusted to control for false discovery rate at 0.05 [132].

Balance ^a	Longleaf	Low Inkberry	High Inkberry	Fetterbush Blueberry	Blueberry	Sparkleberry	Fetterbush
Zhou vs NMOC	13.6 ^a	14.9 ^a	14.0 ^a	13.6 ^a	12.6 ^a	13.6 ^a	12.9 ^a
H ₂ vs CO ₂ , CO, CH ₄	3.2 ^a	4.2 ^a	3.6 ^a	4.0 ^a	3.1 ^a	2.9 ^a	3.4 ^a
CO ₂ vs CO, CH ₄	0.0 ^a	-0.4 ^a	-0.1 ^a	-0.4 ^a	-0.2 ^a	0.0 ^a	0.0 ^a
CO vs CH ₄	1.3 ^a	1.2 ^a	1.4 ^a	1.4 ^a	1.8 ^a	2.1 ^a	1.5 ^a
Alkanes vs other NMOC	-2.3 ^{ab}	-3.1 ^a	-1.4 ^{ab}	-3.3 ^{ab}	-2.9 ^{ab}	3.4 ^c	0.4 ^{bc}
Alkenes vs Alkynes	-2.8 ^a	-2.3 ^{ab}	-2.7 ^a	-2.8 ^{ab}	-3.2 ^a	-1.1 ^b	-1.9 ^{ab}

^a See Table 22.

4.2.5 Canister composition of wind tunnel versus field

Based on the number of canisters collected, the probability that a wind tunnel sample was pyrolysis was 86/153 or 0.562. All wind tunnel fires were used to fit a logistic model to predict whether a sample was from pyrolysis or flaming combustion. The logistic model using the *ilr* coordinates as predictors was significant ($\chi^2=41.77$, $df=21$, $p\text{-value}=0.004$). The fitted logistic regression model correctly classified 49 of 67 wind tunnel flaming samples and 68 of 86 pyrolysis samples for an overall classification rate of 117/153 or 76 percent which we considered acceptable. When applied to the field canisters the model classified 17 (2 Tall Timbers, 15 Ft. Jackson) and 25 (6 Tall Timbers, 19 Ft. Jackson) of the 42 field samples as flaming and pyrolysis samples, respectively. Using this predicted classification of the field samples, the composition of pyrolysates in the canisters between the wind tunnel experiments and the Ft. Jackson burns was compared. A comparison across all three scales will be limited to the permanent gases (H₂, CO, CO₂, CH₄); comparison of the wind tunnel and field canisters with FTIR measurements of CO, CO₂, CH₄, C₂H₂, C₂H₄, C₂H₆, C₃H₆, isobutene and 1,3-butadiene reported in [193,194] is underway. Fire phase and location (wind tunnel, Tall Timbers, Fort Jackson) affected the *ilr* coordinates of the canister gas samples (Table 24), as did the interaction between location and fire phase.

Generally, the relative gas concentrations measured in the field at Ft. Jackson were less than the concentrations measured in the wind tunnel as indicated by average deviations less than zero (Figure 42). Recall that CO₂ comprised more than 92 percent of the samples (Table 19). While it dominated the composition, there was relatively little difference between the locations as indicated by the average deviations being close to zero. In contrast, H₂ differed appreciably between Ft. Jackson and the wind tunnel. More H₂ was present in the wind tunnel samples relative to the Ft. Jackson samples. This trend was noted for 14 of the 22 measured gases including CO and CH₄, the other two dominant gases and can be easily seen in Figure 43.

Table 24. Effects of air temperature, fire phase and location on composition of gases measured

Source	df ^a	Pillai's ^b trace	Hypothesis tests		Den df	Pr(>F)
			F ^c	Num df		
Location	2	0.53	2.98	42	344	<0.0001
Fire phase	1	0.33	4.08	21	171	<0.0001

^a Degrees of freedom of effect. Natural logarithms of air temperature, dead fuel moisture and relative humidity were used because they are ratio scale variables (van den Boogaart and Tolosana-Delgado 2013).

^b Pillai's trace used to test equality of means.

^c F-statistic associated with Pillai's trace. Numerator df is the df for the effect multiplied by *D-1*.

Since the balances (normalized ratios between geometric means of subsets of the gases) and the default *ilr* transformation are simply orthogonal rotations to each other, the ANOVA results contained in Table 24 apply to both forms of the data. Greater *ilr* coordinates for the concentration of dominant gases (CO, CO₂, CH₄, H₂) relative to NMOC and of H₂ relative to the other dominant gases were observed at Ft. Jackson compared to the wind tunnel. The balances of CO₂ relative to CO and CH₄, of CO relative to CH₄ and of alkanes relative to other NMOCs were greater in the wind tunnel (Table 25) compared to Ft. Jackson. The balances for the relative amounts of dominant gases vs NMOC, CO vs CH₄ and alkenes vs alkynes did not differ between the wind tunnel and field canisters.

In the wind tunnel experiment, the fuel bed mass was dominated by longleaf pine needles. The percentage of mass of the fuel bed that consisted of live plants is unknown, but it was probably less than 30 percent given the relatively small size of the plants. In several burns, we added in extra plants in hope of producing a stronger signal due to the presence of the plants. This was successful because the composition of the gases in the wind tunnel differed between fuel beds. The relative amounts of each gas changed; however, some groupings by fuel bed were noted. Historical work on the chemistry of wildland fuels noted differences in the chemical composition of the extractives, and our more recent lab-scale work has also confirmed that the composition of both the fuel and the resulting gases released by pyrolysis does differ.

The composition of gases also differed between the wind tunnel samples and the samples collected from prescribed burns conducted under operational conditions in longleaf pine stands in Georgia (Pebble Hill Plantation) and South Carolina (Ft. Jackson). While the overstory at both locations was dominated by longleaf pine, the understory composition differed. The composition of the understory vegetation at the Tall Timbers Pebble Hill Plantation was typical southern xeric longleaf woodland vegetation while the Ft. Jackson site was typical of fall line xeric longleaf woodland vegetation found in the Sand Hills region [195]. Sparkleberry is a deciduous shrub in the fall line longleaf type which does not contribute to fire behavior during dormant season burns (no foliage), but the foliage can significantly enhance fire behavior during the growing season. Due to sampling design, any differences due to vegetation at Tall Timbers and Ft. Jackson were confounded with all other site variables.

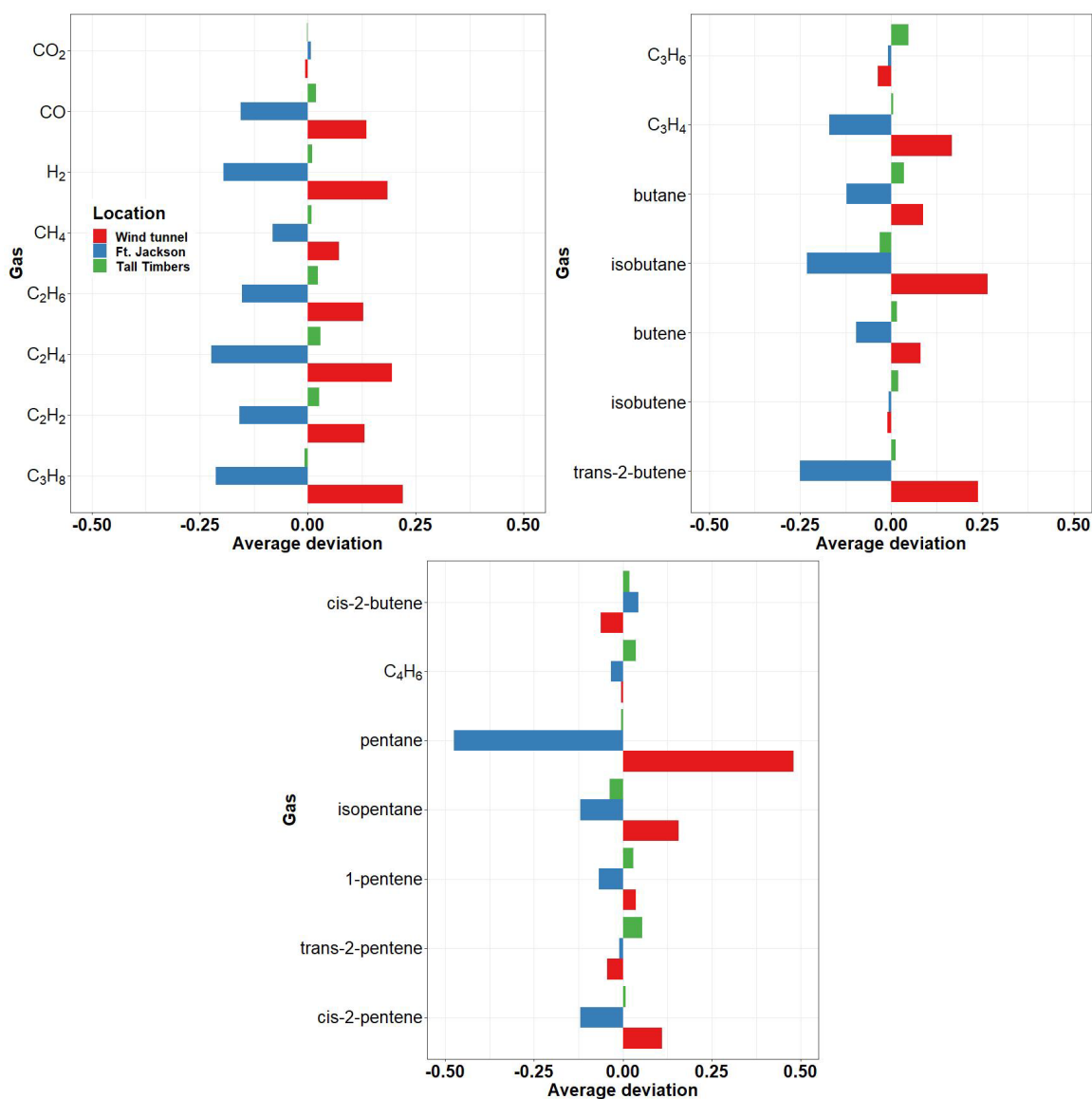


Figure 42. Effect of location on gas composition of pyrolysis samples collected in a wind tunnel and in prescribed burns in longleaf pine stands located at Tall Timbers Pebble Hill Plantation and Fort Jackson in the southeastern U.S. Composition expressed as deviation (log-ratio scale) from overall geometric mean by gas. Values below zero indicate gas concentrations less than the overall mean and values above zero indicate greater concentrations.

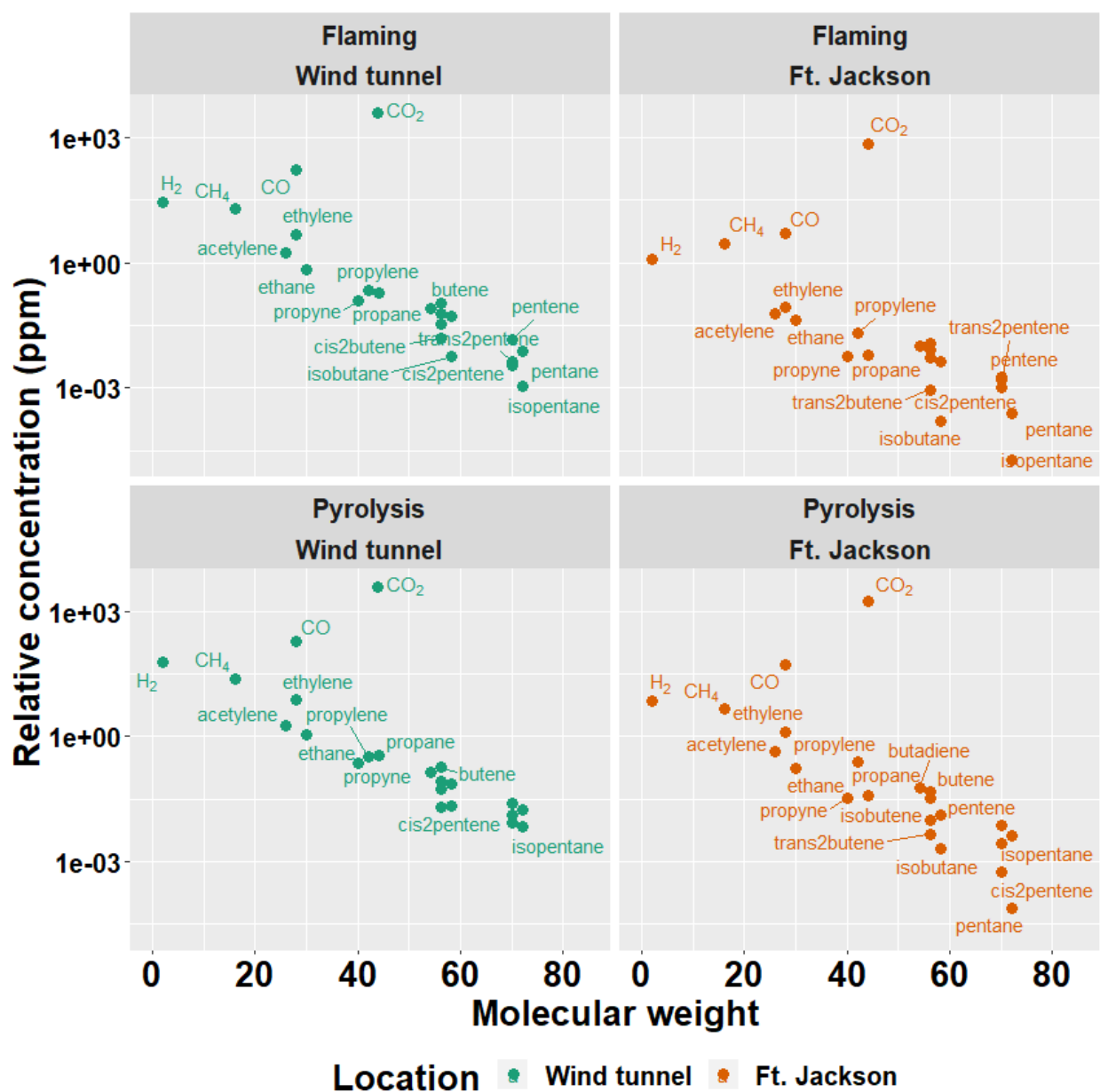


Figure 43. Observed relative concentration of gases in canister samples analyzed by GCMS from pyrolysis and flaming combustion in wind tunnel and field burns in longleaf pine fuel beds.

Table 25. Pairwise comparisons of location and fire phase effects on selected balances of gases measured in canisters. For each balance, effects that did not differ are indicated by the same letter with the letter values ordered from smallest to largest. P-values adjusted to control for false discovery rate at 0.05 [132].

Balance ^a	Location			Phase	
	Wind tunnel	Ft. Jackson	Tall Timbers	Flaming	Pyrolysis
Zhou vs NMOC	13.9 ^a	14.3 ^a	13.7 ^a	14.4 ^b	13.7 ^a
H ₂ vs CO ₂ , CO, CH ₄	3.7 ^a	4.6 ^b	3.5 ^a	4.1 ^b	3.6 ^a
CO ₂ vs CO, CH ₄	-0.3 ^b	-0.7 ^a	-0.5 ^{ab}	-0.6 ^a	-0.2 ^b
CO vs CH ₄	1.5 ^a	1.1 ^a	1.6 ^a	1.3 ^a	1.5 ^a
Alkanes vs other NMOC	-1.5 ^b	-3.4 ^a	-3.4 ^{ab}	-2.3 ^a	-1.7 ^a
Alkenes vs Alkynes	-2.5 ^a	-2.1 ^a	-2.3 ^a	-2.4 ^a	-2.4 ^a

^a See Table 22.

The consistent results showing that the *ilr* coordinates of all gases except CO₂ were greater in the pyrolysis samples relative to the flaming samples was not surprising (Figure 44). The proportion of the total amount of gas pyrolyzed that was sampled in the wind tunnel and in the field is unknown. Flaming samples in the wind tunnel were collected from the flame at approximately midflame height in a very turbulent environment. Pyrolysis gas sampling in the wind tunnel prior to flame arrival and at the base of the flame in the field may not be equivalent sampling locations. Such an effect--gas sampling location which was confounded with location of the experiment interacting with the fire phase—would be contained in the fire phase-location interaction term which was significant. The temperatures of the sampled gases were unknown. We have no reason to suspect that the sampling apparatus affected the composition as very similar equipment was used in the wind tunnel and field (suction pump, metal tubing, etc.). The relative amount of CO₂ decreased in the pyrolysis samples causing the relative concentrations of other gases to increase.

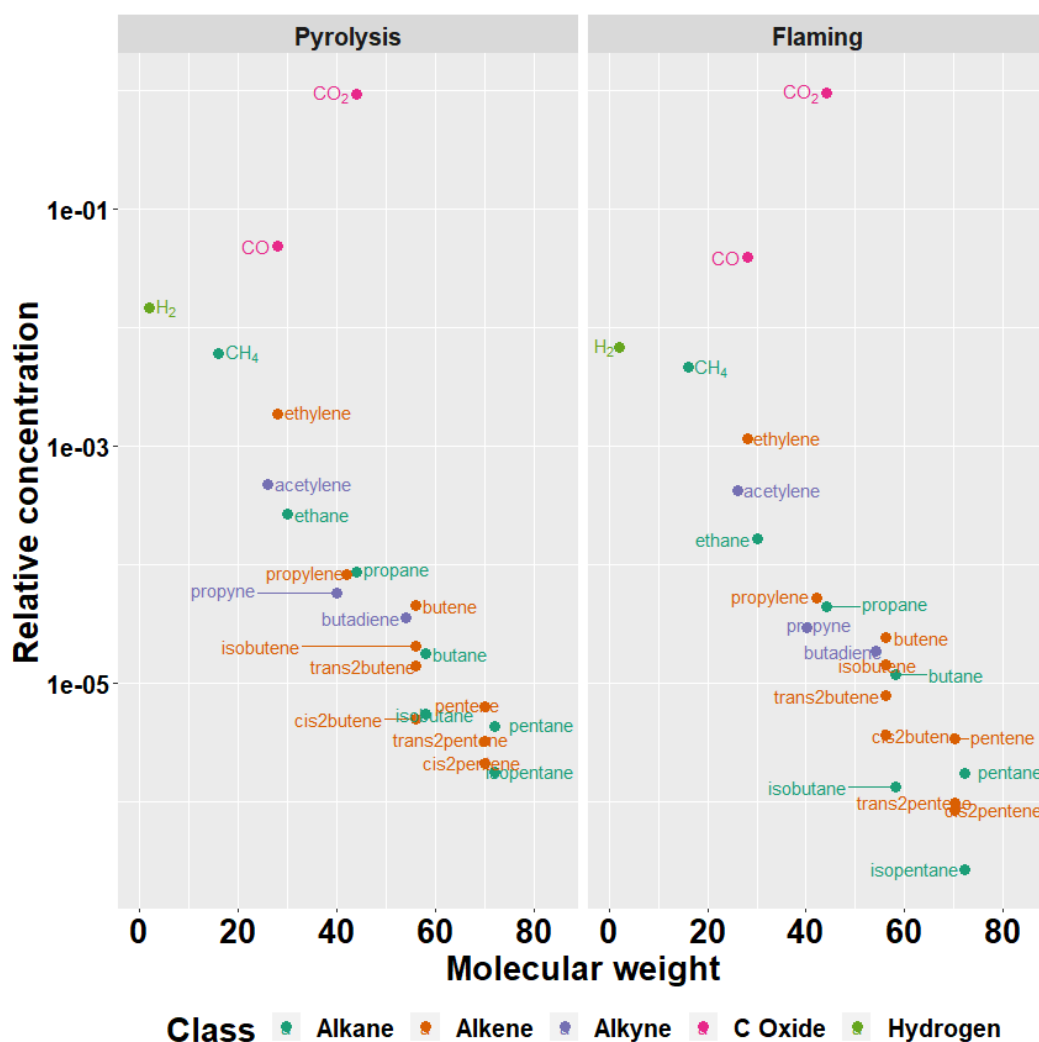


Figure 44. Observed mean composition of samples of pyrolysis and flaming combustion gases in wind tunnel fires by chemical type after closure.

The fuel beds in the wind tunnel were relatively simple compared to the fuel bed structure in the field. The heating rates and maximum fuel temperatures, two factors known to influence the yield and composition of pyrolysis gases, were quite similar in the wind tunnel and field (Table 10). The longleaf pine litter fuel moistures were also similar. The total consumption of longleaf pine needles (450 g m^{-2}) in the wind tunnel experiments fell within the estimated 95 percent confidence interval for the consumed litter during the fires at Ft. Jackson (Table 13). Given the similarities in heating rates, maximum fuel temperatures and fuel consumption, we feel that the wind tunnel and field fires at Ft. Jackson were similar enough to warrant comparison between the gas composition.

4.2.6 Static and dynamic FTIR measurements

To accomplish these measurements, many experimental techniques were employed to detect gas-phase chemicals and their (relative) concentrations, including optical methods such as Fourier Transform Infrared (FTIR) technology, and to a lesser extent Quantum Cascade Laser (QCL) spectroscopy. FTIR was used on multiple occasions to non-intrusively measure the composition and concentration of the pyrolysis gases. This includes identifying the gases from i) heating single leaf samples in a simple flat-flame burner system at BYU, ii) heating nursery plants with flames in the wind tunnel experiment during the late spring of 2018 and iii) heating shrubs in prescribed burns at

Ft. Jackson, SC. Two types of FTIR devices were used for these experiments, an open path device (OPAG) and the T37 laboratory instrument coupled to a long path gas cell. The T37 was deployed at the May 2018 Ft. Jackson burns in lab space made available by a colleague at the University of South Carolina and in the wind tunnel experiments. The T37/White cell measured the gas chemical composition by extracting the gases into the apparatus (or into a canister that is used to later transfer the pyrolysis gases to the instrument). In this mode the FTIR technique has delivered great success – the technique has quantified dozens of known pyrolysis and combustion species and also identified ½-dozen species for the first time using this method [196]. The QCL laser system was not able to identify as many species, but did make seminal measurements at higher acquisition rates, enabling dynamics at the second and even millisecond time scale.

For that reason, two acquisition modes were used. In the extractive mode, the inlet/outlet of the system were simply valved off such that a moderate pressure was achieved in the cell (ca. 700-740 Torr and for lower pressures ca. 400-430 Torr). A total of 22 burns were recorded using the static acquisition mode (Table 26). In this static mode the gas was then studied using the full resolution (0.6 cm^{-1}) of the spectrometer with an extended acquisition of ca. 30 minutes to achieve the best signal/noise possible. At the higher resolution and better signal/noise some of the best results of the campaign were achieved.

Table 26. Experimental wind tunnel fires measured by Bruker T37 spectrometer using static or dynamic mode.

T37 sampling mode	Wind tunnel fire number
Static	11, 13, 16, 20, 21, 22, 31, 38, 42, 44, 48, 49, 76, 78, 80, 82, 84, 88, 89, 90, 94, 95
Dynamic	3, 4, 5, 6, 7, 77, 79, 81, 83, 85, 86, 87, 92, 93, 97

Figure 45 shows the advantages of using a higher resolution to acquire data; displaying the measured spectrum, reference spectra of naphthalene (C_{10}H_8) and acetylene (C_2H_2) within a region dominated by the former, and the corresponding residuals with and without naphthalene subtracted from the a) original spectrum recorded at 0.6 cm^{-1} and the following deresolved spectra b) 1 cm^{-1} , c) 2 cm^{-1} and d) 4 cm^{-1} . With the reference spectra for the original 0.6 cm^{-1} measurement and the 1 cm^{-1} deresolved spectrum (Figure 45a and b), the absorption lines for C_2H_2 and naphthalene overlap, with the 782 cm^{-1} feature from naphthalene still slightly visible in the original spectra. The naphthalene peak appears clearly in the residuals when it is not included in the fitting process, but when naphthalene is included in the fitting process the feature is removed from the residual. However, as the resolution is further reduced (Figure 45c and d), the features broaden, and the distinction of the naphthalene peak from C_2H_2 is compromised and virtually disappears as seen in Figure 45d. The specificity between compounds is lost and confidence in the identification/quantification of the target species, particularly for the weaker absorbers, diminishes as the resolution decreases.

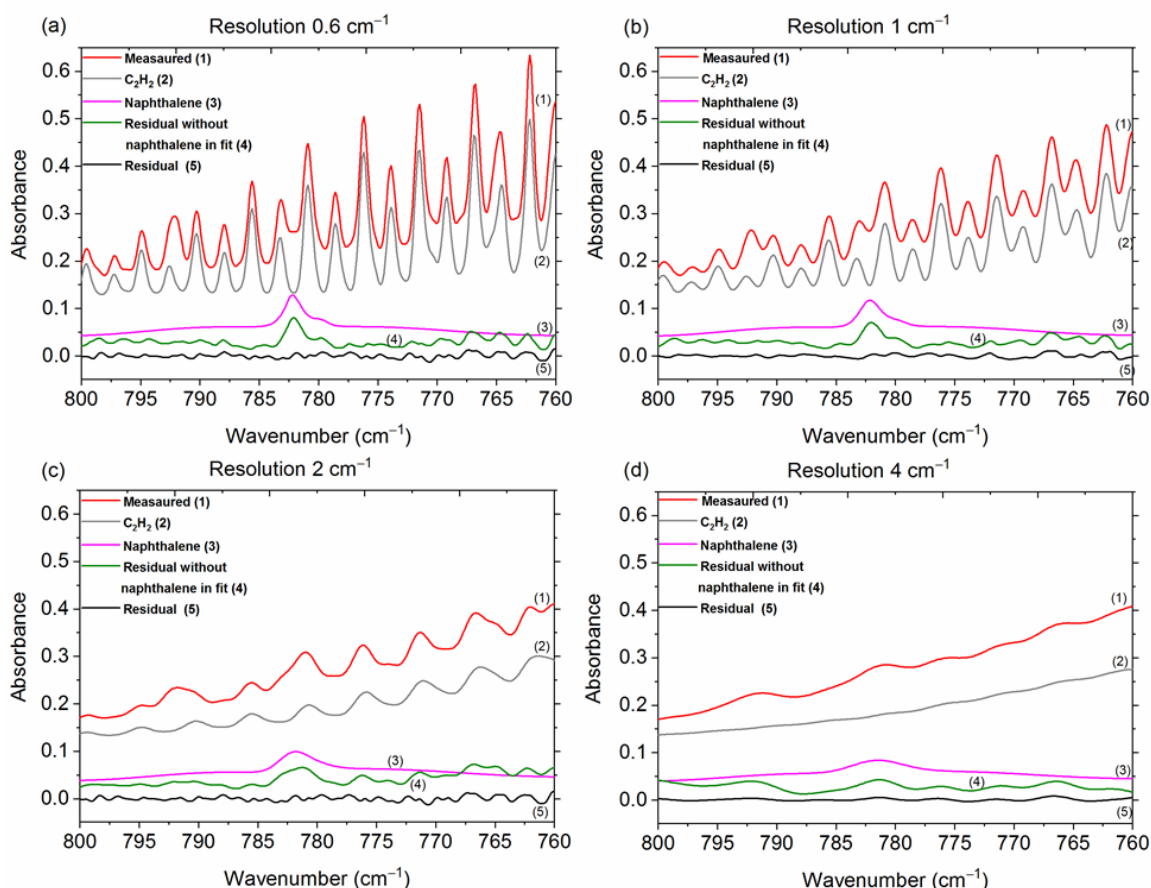


Figure 45. Measured and scaled reference spectra for C₂H₂ and naphthalene, and corresponding residuals with and without naphthalene included in the fit for the a) original spectrum collected at 0.6 cm⁻¹ and the deresolved spectra at b) 1 cm⁻¹, c) 2 cm⁻¹, and d) 4 cm⁻¹. The reference spectra for CO₂, HCN and H₂O are not shown (HCN was not included in fit when the resolution was 4 cm⁻¹; for resolutions 1, 2 and 4 cm⁻¹, H₂O was not included in the fit when naphthalene was removed from the fit). Spectra are offset for clarity.

Chemicals that are characteristically high absorbers, such as water, carbon dioxide, carbon monoxide, ethene, methane, methanol, and acetylene are visibly dominant. Using the MALT software, high absorbers were subtracted from the measured spectra leaving a residual allowing for smaller chemicals buried in the complex spectra to be identified. These smaller compounds, such as naphthalene, formaldehyde, formic acid, acetic acid, nitrous acid, furan, phenol, benzene and isoprene, that would typically be obscured by chemicals with higher absorptivity were identified and quantified; with MALT serving as a set of optical tweezers. As many as 30 different gas-phase molecules could be identified and quantified in the spectra.

One constraint to the static method, however, is the restriction of only being able to capture one “snapshot” of the fire rather than the entirety of it. In this way, the experimental technique is dependent on when the inlet valve is closed to capture the emissions coming from the wind tunnel. If the inlet valve from the wind tunnel is shut too early, such that atmospheric conditions are captured, or too late, such that the flaming stage is captured, then the target pyrolysis phase would not be recorded. To adjust for this potential in error, an individual would observe the burn from above and call out when to valve off the instrument to capture the desired phase. In this way, the emissions captured from the burn were expected to be taken during the pyrolysis phase of the burn.

In the dynamic mode, attempts were made to capture some of the chemical changes occurring i.e.,

pyrolysis to flaming combustion, and during some burns smoldering combustion. A total of 15 fires were measured in dynamic mode (Table 26). The spectral resolution was downgraded to either 1.0, 2.0 or 4.0 cm^{-1} (resulting in better signal-to-noise) but fewer scans were acquired (poorer signal-to-noise) to try to detect those species associated with different phases of the flame. Rather than averaging for 30 minutes, continuous acquisition of spectra was taken with 40-80 interferometer scans (depending on the duration of the burn) yielded a spectrum every 2.5 seconds for 1.0 cm^{-1} resolution, 1.5 seconds for 2.0 cm^{-1} resolution and every 0.5 seconds for 4.0 cm^{-1} resolution respectively.

Data acquisition during this experimental mode required the inlet valve to be open for the duration of the burn to achieve a continuous flow of emissions to the T37/gas cell device. Scanning would start as the flame front approached the undergrowth species and would continue scanning until the flame passed the extractive probe. Figure 46 displays Burn 86 during the time-resolved phase of the experiment. Measured IR for regions 1150-800 cm^{-1} and 2250-2000 cm^{-1} are shown respectively. The top series of spectra show ethene (C_2H_4), propene (C_3H_6) and nitrous acid (HONO) continue to increase as the flame front approaches the extraction probe and plant. The chemical species are evident in the pyrolysis phase of the fire and reach their highest mixing ratios as can be seen during scans 15-20. As the flaming and smoldering combustion phase takes over, the respective species begin to dissipate; ammonia (NH_3), in turn, begins to increase in mixing ratio during these phases of the fire (scans 25-35). The bottom series of spectra depicts the progression of the burn relative to carbon monoxide (CO), with mixing ratios rapidly increasing. For a typical burn, mixing ratios for CO would be on the order of 11,500 ppm during its highest recorded data point. To date only a few of the experimental fires have been analyzed in such a fashion. No PNNL funding remained to complete this work which was complex and took longer to complete than originally anticipated and budgeted. Future work funded outside of RC-2640 will integrate the dynamic measurements with the FLIR infrared camera measurements as done in [194] under a separately funded agreement with UCR; PNNL personnel will consult with UCR subject to availability.

The PNNL extractive method relies on transporting the analyte volume of gas to the instrument and is thus limited in its temporal resolution (the valves in Figure 16 must be opened/closed by hand). Moreover, the source in the spectrometer is an infrared glow bar source with limited brightness which is not an issue during the static mode when data is acquired over a period of 30 minutes. However, data acquired during the dynamic mode does not have the benefit of longer scanning periods, thus increase with noise. The noisy spectra in turn causes difficulty in data analysis using the MALT software as noise peaks make be mistaken as actual artifacts and vice versa.

Wavelength-swept ECQCL systems provided rapid detection of CO_2 and CO in the MWIR spectral region, and other reduced species in the LWIR spectral region. Specifically, the two broadly-tunable swept-ECQCL systems were used with the first laser tuned over the range 2089 to 2262 cm^{-1} (4.42 – 4.79 μm) to measure spectra of CO_2 , H_2O , and CO and the second LWIR laser was tuned over the range of 920 to 1150 cm^{-1} (8.70 – 10.9 μm) to measure spectra of ammonia (NH_3), ethene (C_2H_4), and methanol (MeOH). Absorption spectra were measured continuously at a 100 Hz rate throughout the burn process, including inhomogeneous flame regions, and analyzed to determine time-resolved gas concentrations and temperature. We note, however, that to improve the signal-noise, in almost all cases the 100 Hz measurements were averaged (binned) to 10 Hz for analysis, providing $\sim 3\times$ (i.e. $\sqrt{10}$) lower noise levels. The results provide *in situ*, dynamic information regarding gas-phase species as they are generated, close to the biomass fuel source.

Chemical species were measured throughout the dynamic burn experiment and showed the evolution of temperature and gas concentrations over fast and slow time scales. Temporal correlations between gas species, temperature, and emission intensity on sub-second time scales indicated the presence of localized high temperature regions dominated by combustion gases CO_2 and H_2O . Uncorrelated

variations in CO and NH₃ indicate that they exist in cooler localized regions along the measurement path and were likely generated from upwind regions of previously burned material. The results are consistent with observed variations in MCE during the burn process. Examples of the measured QCL spectra and fits to the QCL laser data are seen for the MWIR and LWIR domains in Figure 47 left and right frames, respectively.

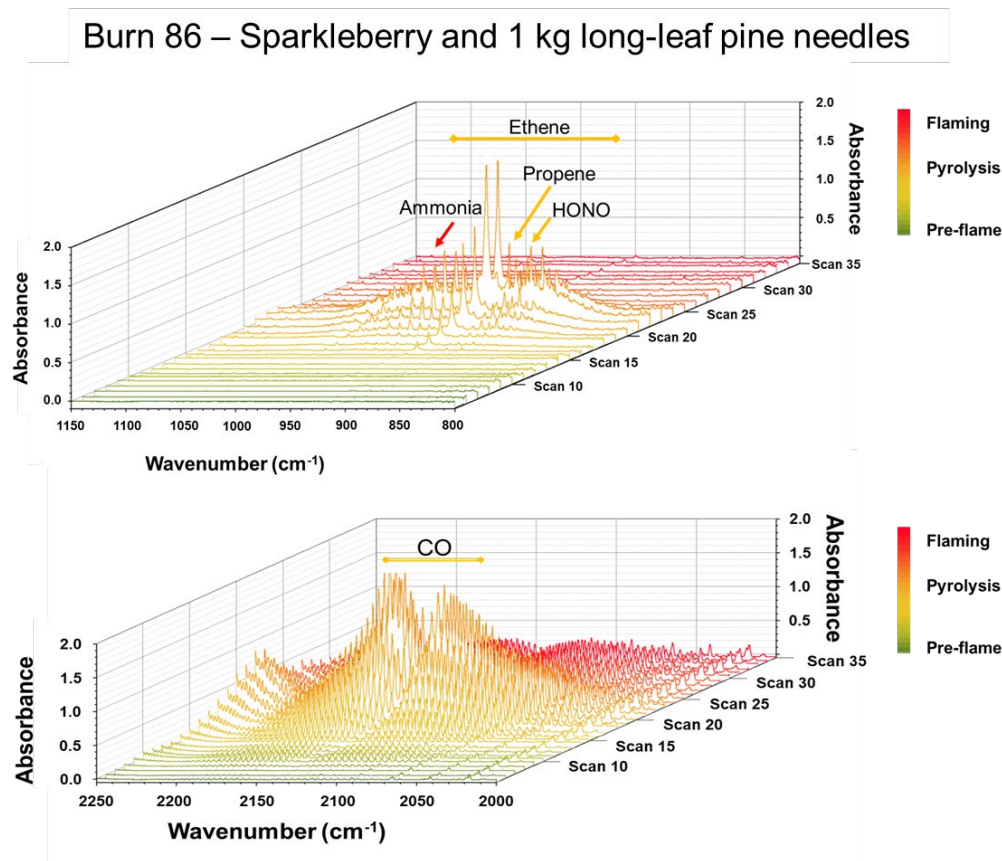


Figure 46. Burn 86 time-resolved measured IR spectra (November 2018) for regions 1150-800 cm⁻¹ and 2250-2000 cm⁻¹ respectively. The top series of spectra show the presence of ethene (C₂H₄), propene (C₃H₆) and nitrous acid (HONO) become more evident during the pyrolysis phase of the burn and reach their highest mixing ratios as seen in scans 15-20, and ammonia (NH₃) at its highest mixing ratio during the flaming and smoldering phases of the fire. The bottom series of spectra depicts the progression of the burn relative to carbon monoxide (CO), with mixing ratios increasing and peaking during the pyrolysis phase while decreasing during the flaming portion of the flame. Spectra were taken at 1 cm⁻¹ resolution every 2.5 seconds.

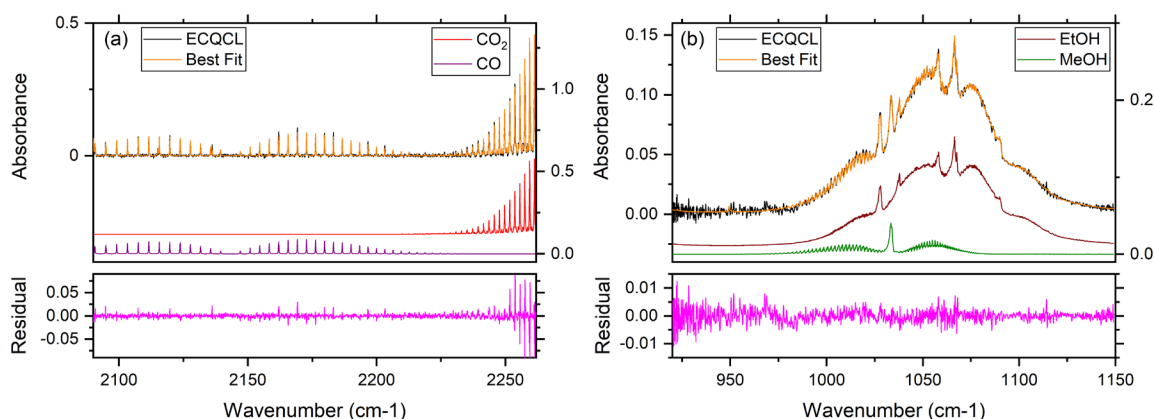


Figure 47. (a) MWIR absorption spectrum shortly after ignition (10:40:41.9 - 0.1 s average). Concentrations from the fit Figure 13 are 893 ppm CO₂, 10 ppm CO, 2690 ppm H₂O, and T_{fit}=314 K. (b) LWIR absorption spectrum (10:39:59.3 - 0.1 s average) showing plume from denatured alcohol used to ignite the flame. Concentrations from the fit are 6 ppm MeOH and 72 ppm EtOH, and T=298 K (fixed). For both (a) and (b), the top panel (left axis) shows the experimental absorbance (black) and the best fit (orange). The top panel (right axis) shows selected library spectra, offset for clarity. The bottom panel shows the fit residuals.

The swept-ECQCL measurements demonstrated a new tool for *in situ* study of biomass burning dynamics on faster time scales than have been previously studied and have been published [197]. The high spectral radiance of the ECQCL permitted measurement through high-temperature flame regions which is needed to access spatial regions close to the fuel source where transient species may be present. The results presented in that study focused primarily on gases with highest concentrations and infrared cross-sections, with NH₃, C₂H₄, and MeOH being identified unambiguously. The broad tuning range of each swept-ECQCL did provide for multi-species detection by using multiple ECQCL systems simultaneously to access different wavelength regions. It was hoped that in addition to CO and CO₂ two dozen or more (oxygenated) volatile organic compounds would be detected with the QCL systems, thus elucidating for the first time some of the truly complex chemistry of pyrolysis and the effects these species can have on both health and the atmosphere. However, only six chemical species were definitively identified, with several others at or just below the detection limit of the current system. This knowledge can be used in future experiments to modify the method to increase the sensitivity by increasing the spectral path length (for the QCLs) from ca. 2.5 meters to 50 meters or more using standard multi-pass optics. This should gain at least an order of magnitude greater sensitivity. The QCL method and results did provide some of the “first ever” such laser measurements applied to chemical measurement of wildland fire phenomena with some advancement of both environmental and optical sciences.

Of the 88 wind tunnel fires, 22 were measured using the static mode and 15 were measured using the dynamic mode. The mixing ratio for the 35 compounds observed by the T37 ranged over several orders of magnitude (Table 27). It is important to remember that these data are relative. CoDA techniques are being used to compare the FTIR measurements with the canister measurements. The compounds observed in both 2018 and 2019 will be the focus of comparison. The geometric mean and standard deviation show that the dominant components of the measured pyrolysis mixture were H₂O, CO₂, CO, CH₄ (Table 28). Phenol (C₆H₅OH), while present, was observed in relative amounts like other trace gases. Recall that the confidence interval for the geometric mean is an exponential function (4.1.3). While tempting to draw conclusions based on these relative amounts as is commonly done, the relative amounts are based solely on the compounds in the composition. CoDA analyses will be used to draw conclusions about the effects of the experimental factors on the FTIR measurements as well as comparison with the canister samples.

Table 27. Mixing ratios for compounds identified using a Bruker T37 spectrometer in experimental wind tunnel fires in static mode. Values are ppm except H₂O and CO₂ (%), pph).

Burn ¹	H ₂ O	CO ₂	CO	N ₂ O	CH ₄	C ₂ H ₂	C ₂ H ₄	C ₂ H ₆	C ₃ H ₆	allene	1,3-butadiene	isobutene
11	3.1	1.9	1324.6		31.6	41.1	42.2	0.0	31.8	0.5	0.0	0.0
13	2.7	0.8	1177.8		34.2	2.8	9.6	1.9	1.5	1.2	0.0	0.0
16	6.8	6.7	11352.1		1388.8	358.7	1089.4	81.2	108.6	20.8	56.5	0.0
20	7.9	8.2	12907.5		853.0	655.7	538.5	35.6	41.4	11.3	24.7	0.0
21	7.1	11.6	12517.4		4211.7	383.7	3596.5	250.5	526.6	51.7	257.0	9.7
22	2.8	1.1	1400.0		66.8	19.0	43.4	4.4	4.7	1.5	0.0	0.0
31	1.3	0.9	2212.9		105.7	16.9	45.2	7.7	8.6	3.7	3.3	0.0
38	7.5	4.0	6311.3		282.9	140.3	188.1	19.2	21.1	10.6	7.8	0.0
42	16.0	3.9	13099.4		924.2	445.8	712.1	62.7	79.9	12.5	32.1	0.0
44	1.4	0.1	43.8		4.6	0.1	1.0	0.0	0.0	0.1	0.0	0.0
48	7.5	4.2	7693.6		781.7	399.7	627.5	47.1	65.1	10.1	28.3	0.1
49	9.7	3.7	6135.9		98.7	12.3	30.4	5.7	0.0	3.0	0.0	0.0
76	1.24	0.06	1.45	0.35	2.27	0.01	0.07			0.17		
78	1.05	0.09	3.90	0.34	2.21	0.06	0.05					
80	3.23	2.06	808	1.21	45.3	23.8	29.3	0.83	4.02	0.64	1.63	0.75
82	2.03	0.48	192	0.50	10.7	4.52	7.05		0.99	0.29	0.37	
84	3.54	1.51	1089	1.28	54.5	23.4	39.9		5.55	1.12	1.98	0.74
88	3.08	2.06	1057	1.79	50.3	23.2	39.3	2.76	5.48	1.21	2.07	0.52
89	3.46	1.36	391	0.44	15.4	8.82	9.66		0.75	0.25	0.26	
90	1.82	0.34	160	0.41	11.3	5.62	6.52	4.E-04	0.77	0.12	0.43	
94	6.21	4.60	7506	3.22	682	351	452	24.2	61.3	8.69	28.1	3.16
95	4.10	2.08	2651	1.78	198	96.5	133	6.29	18.1	2.30	7.57	1.07

	Burn	isoprene	CH ₃ OH	C ₂ H ₅ OH	acetic acid	HCOOH	CH ₃ CHO	C ₄ H ₄ O	C ₃ H ₄ O	C ₄ H ₃ OCHO	NH ₃	NO	NO ₂
11		2.4	0.0		0.0	4.8	0.0	0.0	0.0	0.0	9.6	13.0	2.1
13		0.0	4.7		0.9	0.7	0.1	0.3	14.8	0.7	10.0	206.5	4.4
16		10.7	49.7		8.0	8.4	57.3	0.0	8.4	17.0	0.0	212.9	0.6
20		5.3	26.3		4.9	8.5	12.0	2.5	17.9	5.6	0.6	0.0	10.9
21		77.1	155.5		72.7	11.6	162.1	0.0	42.7	34.0	0.0	18.0	4.3
22		0.0	5.2		0.0	4.4	0.3	0.2	27.1	0.0	8.2	22.9	1.0
31		0.0	12.3		12.1	9.4	0.1	1.0	28.2	0.8	26.8	140.2	4.3
38		0.0	20.9		6.8	18.4	6.3	1.3	71.5	1.8	81.8	46.3	4.3
42		20.3	70.9		38.1	14.0	65.4	7.9	0.0	11.9	8.6	0.1	1.4
44		0.0	0.6		0.0	0.9	0.0	0.0	6.9	0.0	1.7	46.5	5.4
48		19.8	45.3		16.9	6.7	53.5	4.8	14.5	5.4	2.4	60.0	4.0
49		0.0	20.8		12.5	13.7	0.0	1.3	0.0	5.1	17.8		
76			0.89	1.37	0.07						0.10		
78			0.24								0.29		
80		1.78	6.81		5.93	15.9	5.87	0.75	2.59	0.65	0.19		
82		0.39	1.53		3.55	5.14	1.69		1.29	0.06	1.29		
84		1.72	6.92		13.4	32.35	7.62	0.39	3.99		1.79		
88		1.43	9.44		13.8	35.3	8.65	0.54	4.35		0.88		
89		0.31	1.66		11.0	9.20	1.51		0.98		1.08		
90		0.32	0.93		2.49	3.64	0.94		0.00	0.13	0.41		
94		11.7	42.3		13.4	130	73.6	3.07	26.0	3.34	0.58		
95		4.22	18.0		9.62	73.6	22.6	1.16	9.53	1.24	0.57		

Burn	HCHO	HONO	HCN	C ₆ H ₆	C ₁₀ H ₈	C ₆ H ₅ OH	(CH ₃) ₂ CO	CH ₃ ONO	SO ₂	HNCO	C ₄ H ₆ O
11	10.2	14.6	8.8		1.7	0.0	4.5	0.0	2.1		
13	258.5	5.3	4.3		0.0	0.4	47.8	5.4	9.1		
16	101.3	64.8	171.8		12.8	16.2	22.0	3.8	3.6		
20	532.0	24.8	143.0		19.7	8.3	92.1	5.4	0.8		
21	21.1	86.6	369.2		16.2	30.2	10.6	1.5	3.1		
22	30.7	9.3	9.6		1.9	6.8	20.3	0.2	2.5		
31	69.4	7.6	8.4		0.7	4.8	40.5	2.1	5.5		
38	271.5	30.4	41.9		4.0	8.0	67.8	4.2	2.3		
42	1.1	23.9	73.0		7.5	18.4	0.0	0.2	1.9		
44	186.8	0.4	0.4		0.2	0.9	34.9	2.6	1.7		
48	51.7	21.5	70.9		8.1	5.1	117.2	0.0	1.3		
49		25.4	9.2		0.4	12.9					
76											
78	0.08	0.11									
80	13.6	9.40	5.84	4.08	4.48	0.90				1.89	1.51
82	4.31	2.53	2.19	2.23	1.06	0.30				0.67	0.54
84	21.3	9.72	8.25	5.19	3.60	1.36				2.61	
88	22.5	12.7	6.94	4.24	4.80	1.63				2.94	
89	5.41	8.92	3.36	1.93	3.40	1.75				1.27	0.73
90	3.33	1.75	1.69	1.48	0.82	0.37				0.70	0.17
94	114	26.9	64.2	61.3	14.6	2.19				5.37	9.97
95	52.8	11.3	21.0	18.6	1.42	1.63				1.98	5.64

1. See Table 10 for more information on experimental fires.

Table 28. Geometric mean, standard deviation, and 95% confidence interval for pyrolysis gases measured in wind tunnel using Bruker T37 spectrometer. Note that the geometric mean and standard deviation were calculated from the data after closure [120]. Pyrolysates are sorted in decreasing order based on mean relative amount.

Pyrolysate	Geometric mean	Geom. Stand. Deviation	95% CI	
			Lower	Upper
H ₂ O	6.44E-01	1.29	6.42E-01	6.46E-01
CO ₂	2.46E-01	1.96	2.44E-01	2.48E-01
CO	1.82E-02	5.66	1.78E-02	1.87E-02
CH ₄	1.40E-03	3.75	1.37E-03	1.42E-03
C ₂ H ₄	6.36E-04	8.08	6.18E-04	6.54E-04
(CH ₃) ₂ CO	4.59E-04	3.59	4.48E-04	4.72E-04
HCHO	4.15E-04	7.18	4.04E-04	4.27E-04
NO	4.07E-04	16.05	3.85E-04	4.31E-04
C ₂ H ₂	3.27E-04	9.20	3.17E-04	3.37E-04
HCN	2.18E-04	2.89	2.15E-04	2.21E-04
C ₃ H ₆	1.79E-04	3.65	1.76E-04	1.83E-04
C ₃ H ₄ O	1.54E-04	3.09	1.52E-04	1.57E-04
HONO	1.53E-04	2.39	1.51E-04	1.55E-04
HCOOH	1.49E-04	3.13	1.47E-04	1.51E-04
CH ₃ OH	1.41E-04	2.58	1.39E-04	1.42E-04
C ₆ H ₆	1.10E-04	2.31	1.08E-04	1.12E-04
C ₂ H ₅ OH	1.06E-04			
CH ₃ COOH	1.04E-04	2.94	1.02E-04	1.05E-04
CH ₃ CHO	8.35E-05	5.71	8.13E-05	8.58E-05
C ₂ H ₆	8.13E-05	13.13	7.79E-05	8.48E-05
1,3-butadiene	5.97E-05	5.96	5.80E-05	6.14E-05
isoprene	4.50E-05	2.86	4.42E-05	4.58E-05
C ₁₀ H ₈	4.37E-05	2.41	4.31E-05	4.43E-05
C ₆ H ₅ OH	4.34E-05	2.45	4.28E-05	4.40E-05
NH ₃	3.96E-05	5.41	3.86E-05	4.05E-05
NO ₂	3.83E-05	3.79	3.73E-05	3.93E-05
HNCO	3.63E-05	1.34	3.61E-05	3.66E-05
SO ₂	3.21E-05	3.81	3.13E-05	3.30E-05
allene	3.00E-05	3.16	2.95E-05	3.05E-05
C ₄ H ₆ O	2.84E-05	2.60	2.76E-05	2.91E-05
N ₂ O	2.28E-05	1.45	2.26E-05	2.30E-05
CH ₃ ONO	2.26E-05	5.75	2.18E-05	2.35E-05
C ₅ H ₄ O ₂	1.98E-05	4.16	1.93E-05	2.03E-05
C ₄ H ₄ O	1.46E-05	1.96	1.44E-05	1.48E-05

4.2.7 Field pyrolysis measurements at Ft. Jackson

The analysis of the canister samples analyzed by GC-MS including the effects of location (wind tunnel, field) on the samples are described above. The pairwise comparisons between the wind tunnel and two field locations are contained in Table 25.

Isolating the gas-phase pyrolysis species was challenging as they often blended with the background atmosphere and are rapidly mixed with other gases at the onset of combustion. One must thus isolate

“the pyrolysis molecules” either optically, mechanically, or temporally. In the Ft. Jackson experiments we selectively probed the pyrolysis gases (Figure 18). While not a perfect solution, the information gathered in this study added important insights into the primary products generated during pyrolysis and other early-stage processes [193,198].

In the Ft. Jackson experiments, the pyrolysis gases were analyzed in a manner somewhat like the Riverside wind November 2017 using an extractive method to bring the gas to spectrometer / long-path gas cell. Rather than locating the FTIR in the middle of the burn, however, canister samples were obtained using an extractive wand and small pump onsite (Figure 18). The canisters were then transported to a nearby chemical laboratory at the University of South Carolina which had better infrastructure to support the measurements. The FTIR system was again a T37 spectrometer coupled to a long path gas cell, very similar to that pictured in Figure 16. The methods and parameters used for spectral acquisition and spectral analysis are similar to that described above and are detailed in [193,198].

A great deal was learned from the Ft. Jackson studies, including about the technique itself. First amongst these is that when using IR spectroscopy deriving the mixing ratios from the congested spectra obtained from wildland smoke samples is far more challenging than in other applications due to multiple overlapping spectral features such as those seen in Figure 13. Sophisticated software and analysis are required with careful iterative analysis carried out in selected spectral “microwindows”. However, using such methods, successful analysis was carried out that resulted in first infrared detection of five compounds generated during prescribed forest fire burns. These include the gas phase compounds methyl nitrite ($\text{CH}_3\text{ON}=\text{O}$); allene (1,2-propadiene, $\text{CH}_2=\text{C}=\text{CH}_2$); the aromatic compound naphthalene (C_{10}H_8); as well as the two aldehydes acrolein ($\text{CH}_2=\text{CHCHO}$) and acetaldehyde (CH_3CHO). The seminal IR detections of the five molecules as ambient measurements of wildland emissions was reported [198]. Most of the compounds (excluding acetaldehyde), had their primary features become apparent only after the larger spectral features had been fitted and subtracted. A comparison of the new infrared-spectroscopy based measurements to other methods in previous reports is reproduced (Table 29).

A total of 25 compounds were identified in the Ft. Jackson FTIR canisters (Table 30). After closure of the data, the dominant compounds were CO_2 , H_2O , CO , and CH_4 in descending order (Table 31). The geometric standard deviation of the 10 canister samples was relatively constant across the 25 gases unlike the results from the wind tunnel fires. It is interesting to note that relatively more CO_2 compared to H_2O was observed in the field measurements when compared to the wind tunnel measurements (Table 28). Analysis is underway to compare the composition of the wind tunnel FTIR measurements to the field measurements as well as comparing the results from both locations with the GCMS measurements. This analysis will be like that presented above for the GCMS canisters. As stated above, comparison of wind tunnel and field pyrolysis results is appropriate given the similarities in heating rate, maximum fuel temperature and fuel conditions (4.2.5). At the 2019 IPR, a slide (15) presented emission ratios (with CO) measured at Ft. Jackson for pyrolysis and reported emission ratios of the same gases reported in the literature for combustion. The slide suggested differences (based on standard deviations plotted on the bar plots) for C_2H_4 and C_2H_2 ; however, the plot suggested no difference for CH_4 . In the presentation we did not assert that there were differences. Presenting compositional data in this manner does not reflect the relative nature of the data so the results cannot be compared in this fashion as has been shown recently [106,114,126]. For hypothesis H_8 , gas concentrations varied between the different experimental scales. Future work outside this project will examine the linkages between the 3 scales using compositional data techniques.

Table 29. Emission ratios relative to CO (ppb/ppm) and standard deviations (1σ) for the present study of the five compounds detected for the first time via IR and for three other previous biomass burning studies.

Target compounds	This study	Emission ratios relative to CO					
		[199]	[200]	[201]	SW [202]	SE[202]	Northern[202]
Method	FTIR	PTR-ToF-MS	GC-FID ^a	PTR-ToF-MS	GC-MS	GC-MS	GC-MS
Naphthalene	0.79 ± 0.47	0.20 ± 0.16	n/a	n/a	0.0070 ± 0.004	0.0040 ± 0.00	0.022 ± 0.012
Methyl nitrite	0.94 ± 0.85	n/a	n/a	n/a	0.9 ± 1.1	0.52 ± 0.51	0.76 ± 0.90
Acrolein	4.0 ± 1.8	5.4 ± 3.0	n/a	3.14 ± 0.12	0.82 ± 0.68	1.31 ± 0.88	3.5 ± 1.7
Acetaldehyde	9.4 ± 3.6	7.4 ± 5.2	n/a	37.3 ± 1.4	1.6 ± 1.2	2.8 ± 1.8	5.5 ± 3.6
Allene	1.05 ± 0.24	n/a	0.1 ± 0.1	8.73 ± 0.28	n/a	n/a	n/a

^a GC-FID is gas chromatography with flame ionization detector

Table 30. Mixing ratios for compounds identified using a Bruker T37 spectrometer in experimental prescribed burns at Ft. Jackson, SC. Values are ppm.

Plot ¹	H ₂ O	CO ₂	CO	CH ₄	C ₂ H ₂	C ₂ H ₄	C ₂ H ₆	C ₃ H ₆	allene	1,3-butadiene	isobutene	isoprene	CH ₃ OH
24B	24373.68	13637.00	2927.97	306.39	79.54	184.59	24.56	27.29	2.38	4.16	0.64		56.45
24A	16206.12	64314.65	18563.38	2070.78	784.64	1395.91	118.87	258.37	23.63	101.11	21.81	80.62	240.07
24A	30487.00	84045.90	27337.98	2471.22	1249.10	1767.32	155.35	262.04	38.27	130.16	20.56	86.43	98.61
24A	15804.88	52943.85	7899.99	786.28	246.45	421.56	55.45	88.01	6.61	29.02	6.89	10.28	32.23
16D5	10073.41	67507.70	11207.08	1261.10	593.25	821.51	55.94	113.69	15.69	41.92	8.71	12.17	42.73
16D6	11793.49	68706.80	18957.16	2684.18	1145.33	1154.89	78.14	115.01	21.74	41.95	4.00	5.25	48.18
16D6	6739.91	41994.60	5998.38	600.39	242.44	373.98	34.59	62.88	7.11	17.11	3.66	2.33	23.00
16D1	11257.20	29879.50	4376.10	432.05	180.60	278.88	22.01	36.45	4.72	10.94	2.01	1.95	24.43
16D1	17057.80	35095.65	6574.80	466.38	194.09	304.95	31.90	52.06	5.45	15.81	2.63	2.62	11.69
16D1	18262.36	55924.45	9749.44	839.89	367.01	463.88	31.14	61.37	8.84	22.63	3.63	4.10	35.67

Plot	acetic acid	HCOOH	CH ₃ CHO	C ₄ H ₄ O	C ₃ H ₄ O	C ₄ H ₃ OCHO	HCHO	HONO	HCN	C ₁₀ H ₈	(CH ₃) ₂ CO	CH ₃ ONO
24B	61.09	5.08	47.33	5.37	25.45	13.08	45.64	4.60	20.10	1.02	21.63	6.06
24A	40.46	13.28	252.20	24.15	125.81	58.72	86.26	1.36	97.57	3.65	67.98	4.33
24A	43.50	12.80	264.46	18.65	99.84	34.40	63.08	1.99	176.95	16.49	53.09	12.41
24A	11.80	5.40	89.96	11.65	34.63	5.19	48.99	2.08	46.16	1.45	31.92	21.30
16D5	16.70	8.25	94.27	6.35	37.74	7.47	17.65	0.61	103.38	6.49	24.97	3.43
16D6	7.05	3.62	87.86	7.20	28.01	12.66	8.81	1.01	161.34	20.37	23.22	8.40
16D6	5.65	2.71	56.14	5.32	24.62	5.05	4.50	0.64	46.11	7.35	15.71	2.24
16D1	11.55	4.55	34.52	2.83	14.73	5.66	6.78	0.69	34.28	6.97	9.55	3.98
16D1	11.76	5.41	46.83	4.79	19.57	2.82	12.36	2.52	47.88	5.44	14.16	6.56
16D1	12.03	4.96	51.01	3.61	21.00	10.54	12.79	2.89	81.86	10.84	17.41	20.59

1. See Table 10 for more information on experimental fires.

Table 31. Geometric mean, standard deviation, and 95% confidence interval for pyrolysis gases measured in experimental prescribed burns in longleaf pine at Ft. Jackson, SC using Bruker T37 spectrometer. Note that the geometric mean and standard deviation were calculated from the data after closure [120]. Pyrolysates are sorted in decreasing order based on mean relative amount. Number of samples = 10.

Pyrolysate	Geometric mean	Geom. Stand. Deviation	95% CI	
			Lower	Upper
CO ₂	6.05E-01	1.26	6.02E-01	6.08E-01
H ₂ O	1.95E-01	1.66	1.93E-01	1.97E-01
CO	1.20E-01	1.37	1.19E-01	1.21E-01
CH ₄	1.20E-02	1.51	1.19E-02	1.21E-02
C ₂ H ₄	7.24E-03	1.49	7.19E-03	7.30E-03
C ₂ H ₂	4.76E-03	1.70	4.71E-03	4.82E-03
C ₃ H ₆	1.09E-03	1.51	1.08E-03	1.10E-03
CH ₃ CHO	1.05E-03	1.52	1.04E-03	1.06E-03
HCN	8.69E-04	1.41	8.63E-04	8.75E-04
C ₂ H ₆	6.44E-04	1.41	6.40E-04	6.49E-04
CH ₃ OH	5.61E-04	1.99	5.53E-04	5.69E-04
C ₃ H ₄ O	4.38E-04	1.62	4.33E-04	4.42E-04
1,3-Butadiene	3.50E-04	1.93	3.46E-04	3.55E-04
(CH ₃) ₂ CO	3.09E-04	1.50	3.06E-04	3.11E-04
HCHO	2.59E-04	2.54	2.54E-04	2.64E-04
CH ₃ COOH	2.14E-04	2.33	2.11E-04	2.18E-04
C ₅ H ₄ O ₂	1.32E-04	2.12	1.30E-04	1.34E-04
allene	1.28E-04	1.63	1.27E-04	1.29E-04
isoprene	1.04E-04	3.17	1.01E-04	1.06E-04
C ₄ H ₄ O	9.32E-05	1.65	9.23E-05	9.42E-05
CH ₃ ONO	9.02E-05	2.03	8.89E-05	9.15E-05
HCOOH	7.65E-05	1.51	7.58E-05	7.71E-05
C ₁₀ H ₈	7.45E-05	2.26	7.33E-05	7.57E-05
isobutene	6.10E-05	2.11	6.01E-05	6.20E-05
HONO	1.94E-05	2.31	1.91E-05	1.97E-05

In addition to the first detections by FTIR of the five gases listed above, a larger objective of the study was to collect and quantify gas-phase compounds emitted ahead of the flame front (prior to the onset of combustion) in prescribed burns conducted in a pine forest, and what are the relationships of these gases relative to other gases in the mix, as well as the gas-phase composition of the fire at later stages, e.g., during combustion or smoldering phases. Some of the primary observations from the Ft. Jackson study [193] can be summarized as follows: First, the estimated ratio of high to low temperature volatile organic compound (VOC) emissions suggest that the samples were indeed extracted when the high temperature pyrolysis process was dominant (Figure 18). The acetylene/furan ratio suggested by Sekimoto [203] was nearly 10x higher than previous studies. This is consistent with previous work as previous works all had longer collection times, and, in some cases, fire-averaged values. Moreover, the significantly increase emission ratios (ERs) observed for specific compounds, e.g., lightweight HCs such as ethene and acetylene as well as unoxidized aromatics such as naphthalene all support the hypothesis that the grab samples were collected prior to onset of decomposition, recombination or combustion reactions. That is, the unoxidized species gases do in fact represent pyrolytic processes. For the oxidized organics, acetaldehyde and methanol

consistently had the highest ER values relative to CO for this collection of pyrolysis gases. The ERs for acetic acid and formaldehyde were found to be high in some instances, but this appeared to be related to fuel composition of the individual burn site. During the Ft. Jackson studies the primary nitrogen-bearing-component released was HCN, while ammonia (NH₃) was not observed. This is consistent with the collected gases representing species associated with the high temperature pyrolysis process. The absence of NH₃ in our analysis must be considered while bearing in mind that detection of amines and ammonia in such systems is always problematic due to wall adhesion; there were several walls in the current method including those of the wand, the canister, the gas cell, etc. It would be interesting to study the effects of initial pyrolysis gas composition ratios on the composition of the downwind plume [87,88].

Project RC-2640 has greatly expanded the scope of understanding of products and mechanisms of pyrolysis by extending the number of southern fuels examined under more realistic conditions [63,83]. We have used multiple methods such as bench-scale pyrolysis measurements to better understand the composition of tars and condensates, but also gas chromatography-mass spec (GC/MS), methods, infrared spectroscopy and particle analysis and other extractive methods for the laboratory- and field-scale burns. The project has largely succeeded in i) seeing what pyrolysis species can be identified by the various techniques (see for example Table 32); ii) maximizing the number of identified species using careful chemometric or signal extraction from the acquired data; iii) using the various methods to determine the degree of oxidation/combustion, i.e. pyrolysis characterization; iv) making first attempts to quantify the rates of evolution of pyrolysis products for certain species; and importantly, v) determining if differences exist between the pyrolysis emissions for different plant species. Application of FTIR spectroscopy to static and dynamic gas samples yielded new insight into the evolution of pyrolysis gases. A methodology to link fuel temperature measurements in the wind tunnel experiments to dynamic gas samples was developed. Both the loss of trained personnel due to pursuit of graduate education and lack of budget for salary sufficient to train new personnel to apply the methodology to additional dynamic samples prevented full analysis of the dynamic gas samples from the wind tunnel experiments. An abbreviated analysis of these samples is being pursued in conjunction with a separate study funded by the Forest Service.

The relative compositions of the wind tunnel and field gas mixtures as related to molecular weight after applying the CoDA closure operation can be seen in Figure 48.

Table 32. Partial list of gas-phase compounds detected by infrared absorption spectroscopy during the laboratory-scale and field-scale experiments conducted as part of SERDP project RC-2640.

CO ₂	NO	methanol	phenol	HCOOH
CO	NO ₂	acetic acid	furaldehyde	peroxyacetyl nitrate**
CH ₄	HONO	SO ₂	hydroxyacetone	limonene
C ₂ H ₂	NH ₃	Furan	1,3-butadiene	carbonyls as glyoxal
C ₂ H ₄	HCN	H ₂ O	acetone	carbonyl sulfide
C ₃ H ₆	HCl	N ₂ O	isoprene	2-methylfuran*
C ₄ H ₈	O ₃ **	HCHO	glycolaldehyde	MVE (methyl vinyl ether)

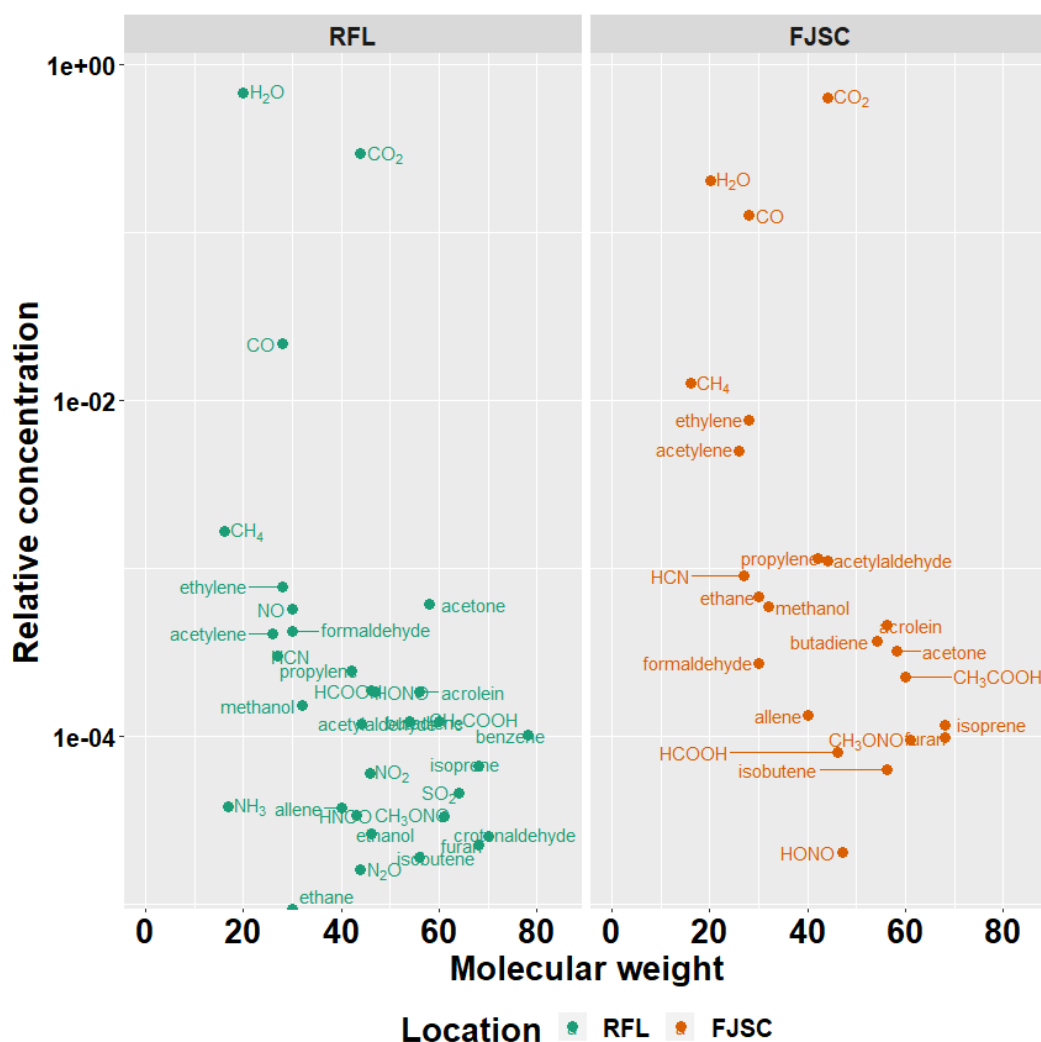


Figure 48. Relative concentrations of gases measured using FTIR in wind tunnel (RFL) and field burns (FJSC). RFL samples are known to be pyrolysis samples. FJSC samples have not yet been classified as flaming or pyrolysis samples using logistic regression as in section 4.2.5.

4.3 Objective 2 – Determining effects of heat transfer

4.3.1 Bench-scale tests

Infrared images taken using an IR camera during the pyrolysis of the leaves indicate that the leaves did not heat isothermally under convective heating (Figure 49). At the beginning of the experiments, there were temperature gradients within the leaves; the edges of the leaves had higher temperatures than the middle of the leaves. As time passed, the heat traveled from the edges towards the center until the temperature was uniform across the entire leaf.

Non-uniformity of the temperature within the leaves may be caused by: (1) the formation of a convective boundary layer across the surface of the leaves that reduces the heat transfer from the hot gases to the surface of the leaves; (2) characteristic differences between the edges and the centers of the leaves, such as moisture content and thickness. A similar observation has been reported for similar heating experiments conducted in the FFB [80]. Plants with smaller thickness and a lower moisture content reached a uniform temperature within a shorter time. The live plants were found to have similar heating patterns during the pyrolysis experiments. The maximum fuel surface

temperature measured during the convection-only experiments was 750 °C which is similar to maximum temperatures reported for vertically-oriented manzanita (*Arctostaphylos glandulosa* Eastw.) leaves [80]. In order to compare the temperature evolution in these experiments with the field-scale measurement of leaf temperature (Figure 91), temperature data will need to be extracted from the IR videos for future analysis of the temperature distributions spatially and temporally [80].

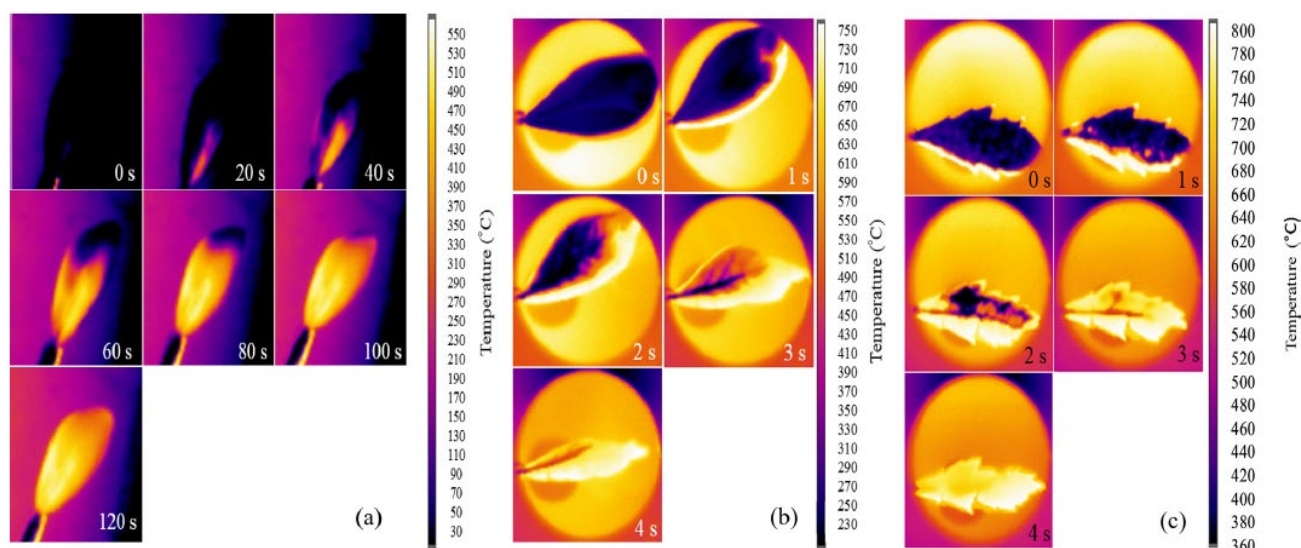
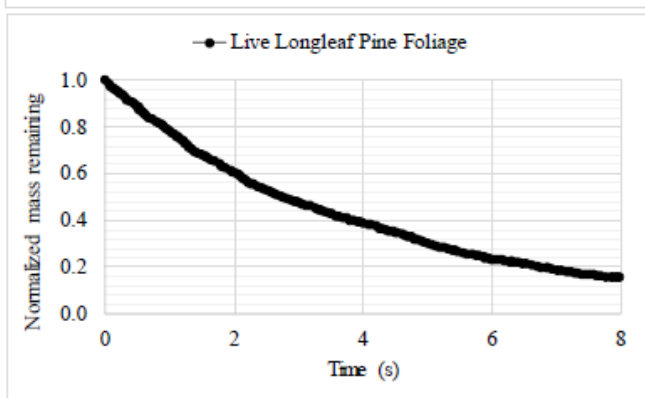
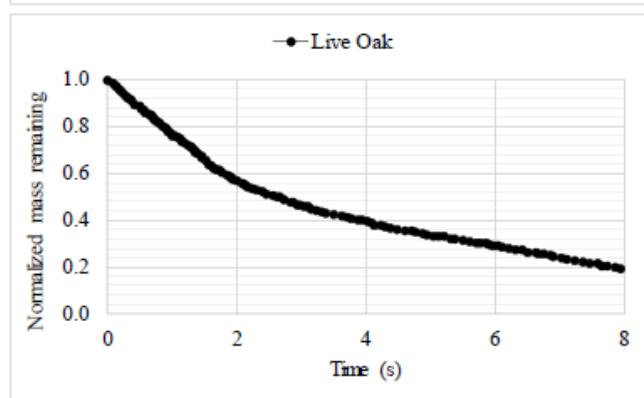
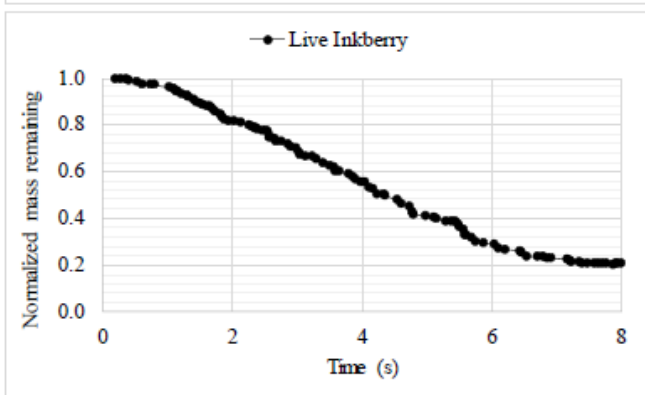
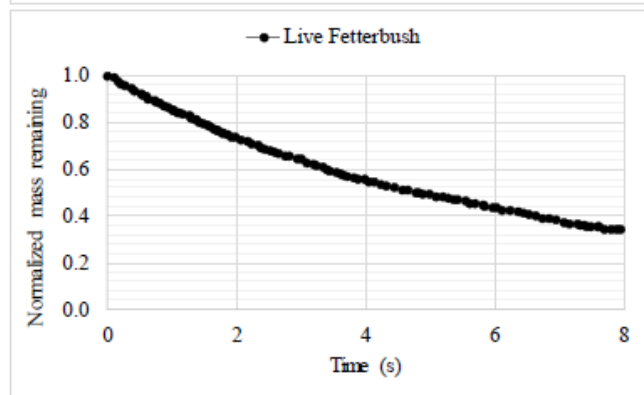
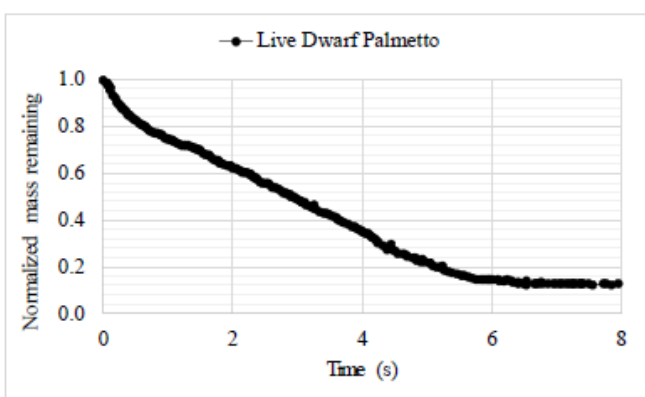
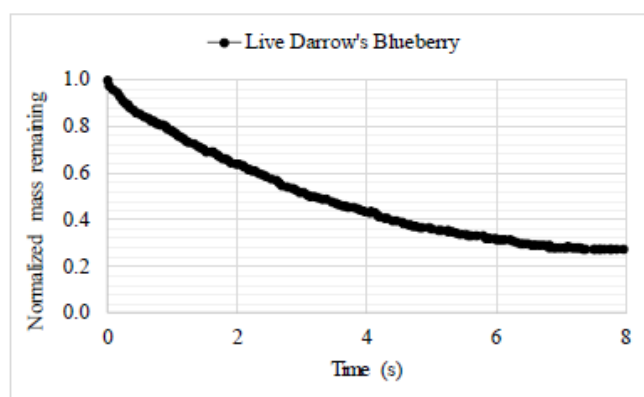


Figure 49. Fuel surface temperatures for (a) radiation-only (inkberry), (b) convection-only (inkberry) and (c) combined convection and radiation (wax myrtle) heating modes ([125]). Note that the temperature color ramps differ due to automatic camera selection of scale.

In the high-heating rate experiments, observed mass loss of the live foliage samples was similar between the convection only and the combined radiative and convective heating modes for the different plant species (Figure 50, Figure 51).



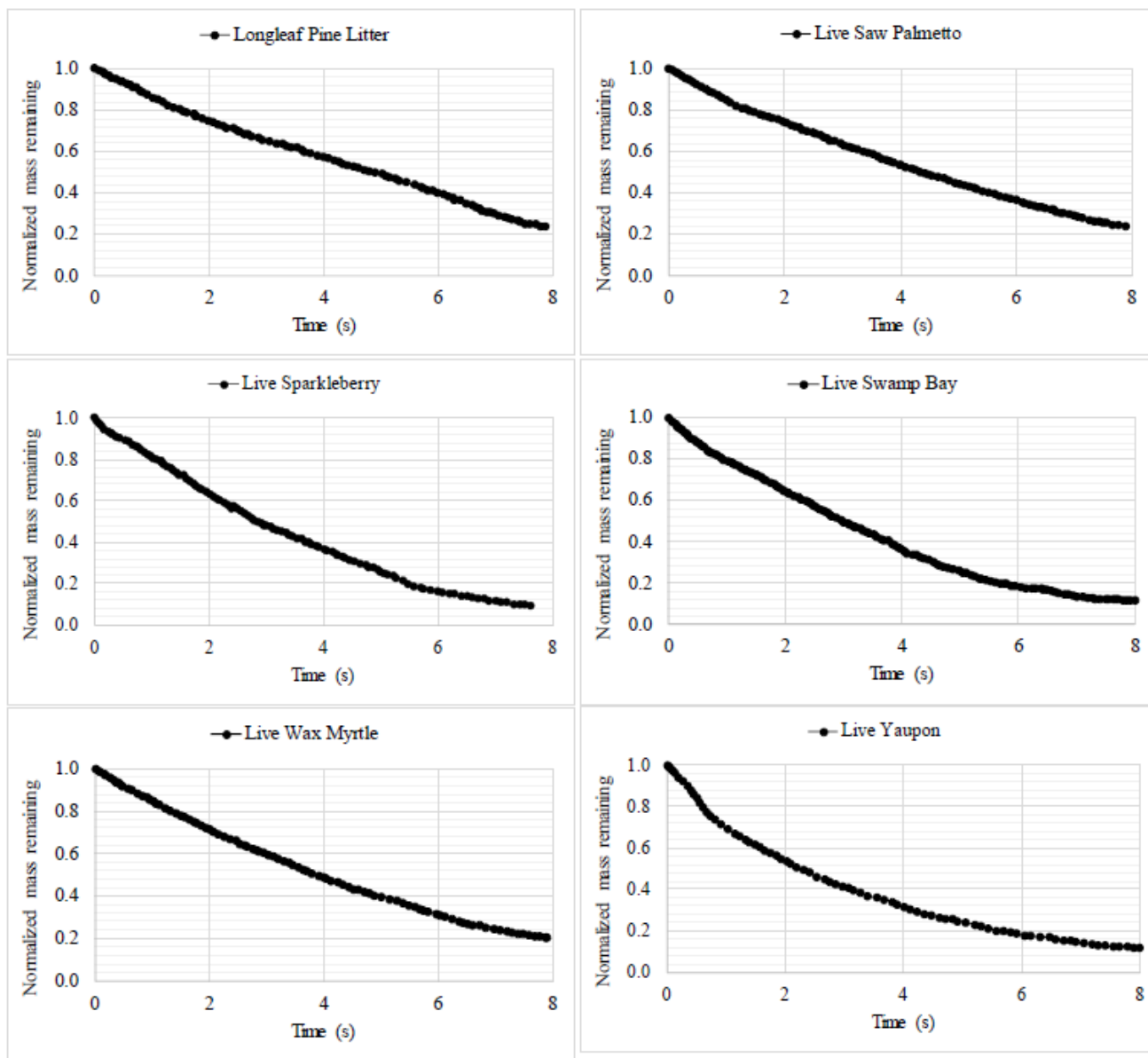
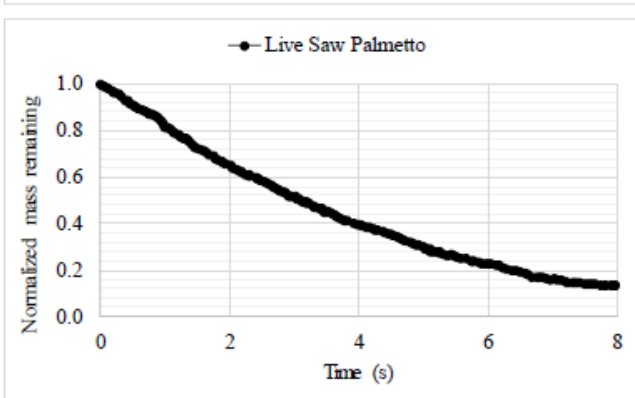
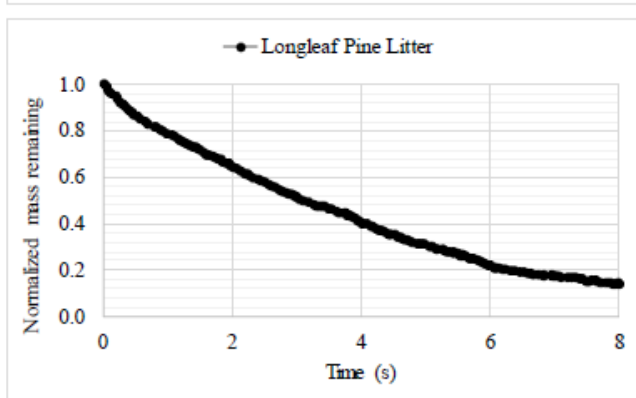
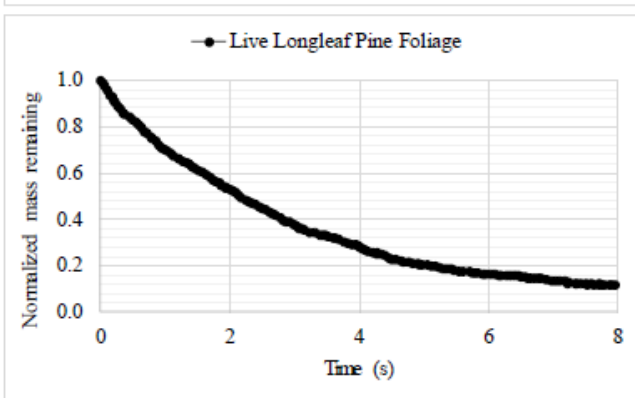
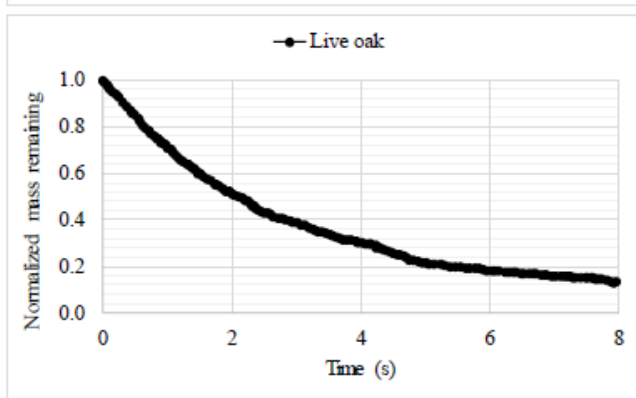
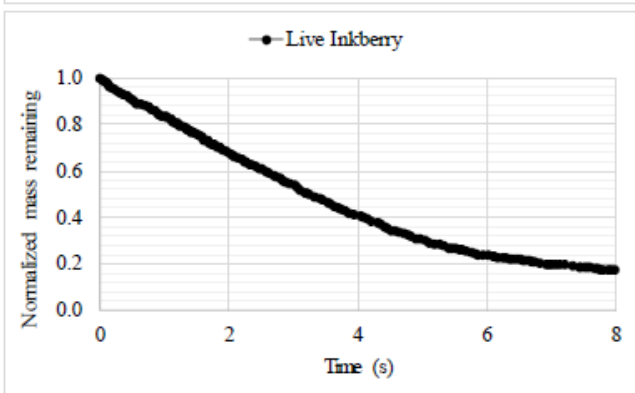
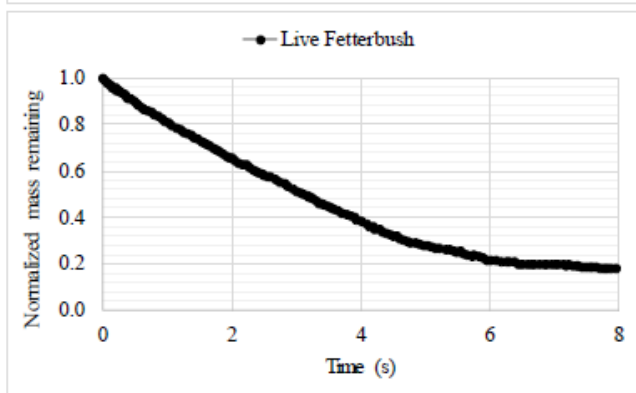
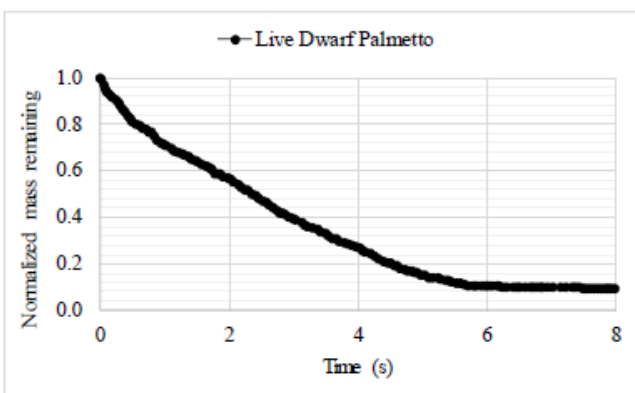
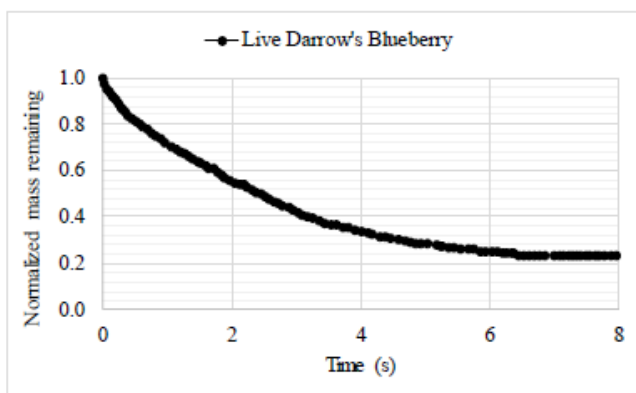


Figure 50. Mass loss over time for live foliage samples heated by convection only in a flat-flame burner.



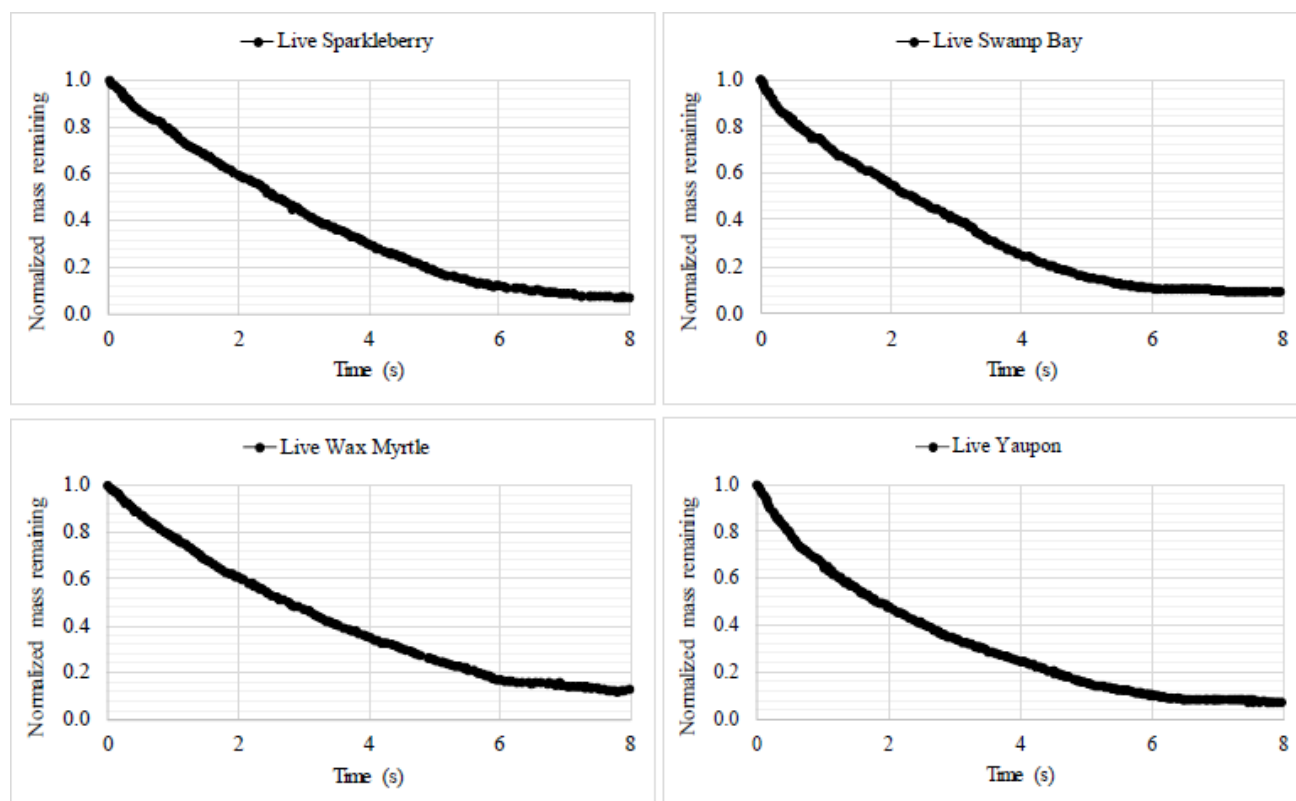


Figure 51. Mass loss over time for live foliage samples heated by convection and radiation in a flat-flame burner/radiant panel apparatus.

Heating mode. The balances (Table 4) provided insight into the effects of heating mode on the pyrolysis products (Figure 52). For the 1st three balances involving the permanent gases, eight of nine of the pairwise differences between the Slow heating mode and the three FFB modes were positive and significant [126]. This means that the FFB modes produced more tars relative to permanent gases (PG), more CO relative to H₂, CO₂ and CH₄ and more H₂ relative to CH₄. Within the FFB results, the Conv mode produced more tars relative to PG compared to Rad and RadConv. RadConv produced the most CO relative to the other PG. The Slow mode produced the least amount of H₂ relative to CH₄ compared to the higher heating rates of the FFB; it also produced relatively less tar than phenol for Rad and Conv. The combined mode (RadConv) produced relatively less tar than phenol compared to Rad and Conv modes alone. The amount of phenol relative to the other tars did not differ between the pyrolyzer (Slow) and the RadConv heating modes nor did it differ between Rad and Conv modes singly. Ledesma et al. [204] reported maximum yield of phenol produced by the pyrolysis of 1,2-benzenediol at 800 °C, the yield of benzene and 2-8 ring polyaromatic hydrocarbons began to increase at 700 °C which would decrease the amount of phenol relative to other tars. Recall that the temperatures of the 4 modes were 105 °C for Rad and 500 to 800 °C for Slow, Conv, and RadConv.

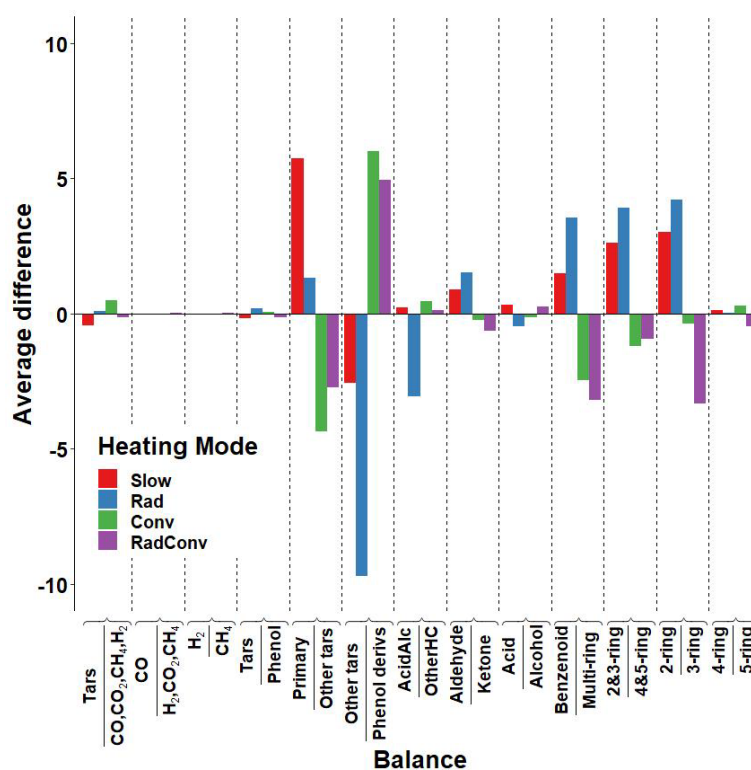


Figure 52. Influence of heating mode on selected balances of pyrolysis gases. Average difference for a balance is the difference between mean value for heating mode and overall mean value. Average difference less than 0 indicates either relatively less in the numerator or relatively more in the denominator; positive values, vice-versa.

As heating rate increased, lower amounts of primary tars were produced relative to other tars (negative differences for all pairwise comparisons except RadConv - Conv). For the FFB modes, the Rad mode produced the greatest amount of primary tars relative to other tars (excluding phenol) which decreased as environmental temperature (but not heat flux) increased. Several authors report an increase in tar production as temperature increases followed by a reduction with an increase in gas products due to cracking of the tars [e.g. 205]. This behavior may explain the increase in the relative amount of tar to gas followed by a decrease in the FFB apparatus for these high heating rates. Similarly, increased heating rate produced relatively less benzenoid compounds relative to the multiring tars and generally smaller quantities of 3-ring tars relative to 2-ring tars. This confirms that both heating rate and the environmental temperature at which pyrolysis occurs are important factors that influence the composition of pyrolysis products.

When the ring compounds are considered, the pyrolyzer generally produced smaller ring compounds as indicated by more benzenoid (single ring) relative to multiple ring, more 2 and 3-ring compounds relative to 4 and 5-ring compounds and more 2-ring relative to 3-ring compounds. In contrast, the FFB modes produced much less benzenoid relative to multiple ring compounds. The Rad mode produced more 2 and 3-ring relative to 4 and 5-ring and more 2-ring relative to 3-ring. However, the Conv and RadConv modes produced much less benzenoid relative to the multi-ring tars, much less 2 and 3-ring relative to 4 and 5-ring and much less 2-ring relative to 3-ring. Recall that these relative ratios change whenever the numerator or the denominator of the balance changes. These results related to heating modes and pyrolysis gas composition, in agreement with many of the results presented in the original papers, are based on statistical tests and methodology that are appropriate to the nature of the data. As such, the results will not change if a subset or superset of the data were analyzed which is not the case for our original work.

4.3.2 Wind tunnel fires

IR imagery was collected on all of the wind tunnel fires. To date all of the imagery has been processed to identify the fuel temperature below the sampling tube used to gather pyrolysis gases for processing by the Bruker T37. The preheating of the longleaf pine needles in advance of the flame and the progression from preheating and pyrolysis to combustion and post-flame combustion can be determined from the temperatures ($^{\circ}\text{C}$) (Figure 53).

The temperatures of the fuel below the sample tube were calculated from measured radiance and an assumed emissivity of 0.98. Time plots of the evolution of fuel temperature (primarily longleaf pine needles with interspersed nursery plants) were generally consistent (Figure 54). Maximum radiometric temperatures ranged from about 300 to 600 $^{\circ}\text{C}$. There was a consistent rapid rise in temperature as the flame front approached followed by a reasonably rapid decrease following the passage of the flame front. There was a wide range in the observed maximum fuel temperatures. Recall that fires 51 to 73 simulated dormant season fires with lower air temperatures and somewhat higher relative humidity (Table 10). There is some suggestion that the maximum temperatures may be lower for the dormant season fires. This could also be due to the slightly higher atmospheric water content which can attenuate radiant emissions. However, in a modeling study radiant emissions from a 1 m flame were attenuated by only 9 percent when relative humidity was 100 percent [206] which was not achieved in this experiment. Fuel temperature did not significantly affect the composition of the gases collected in the canisters in the wind tunnel.

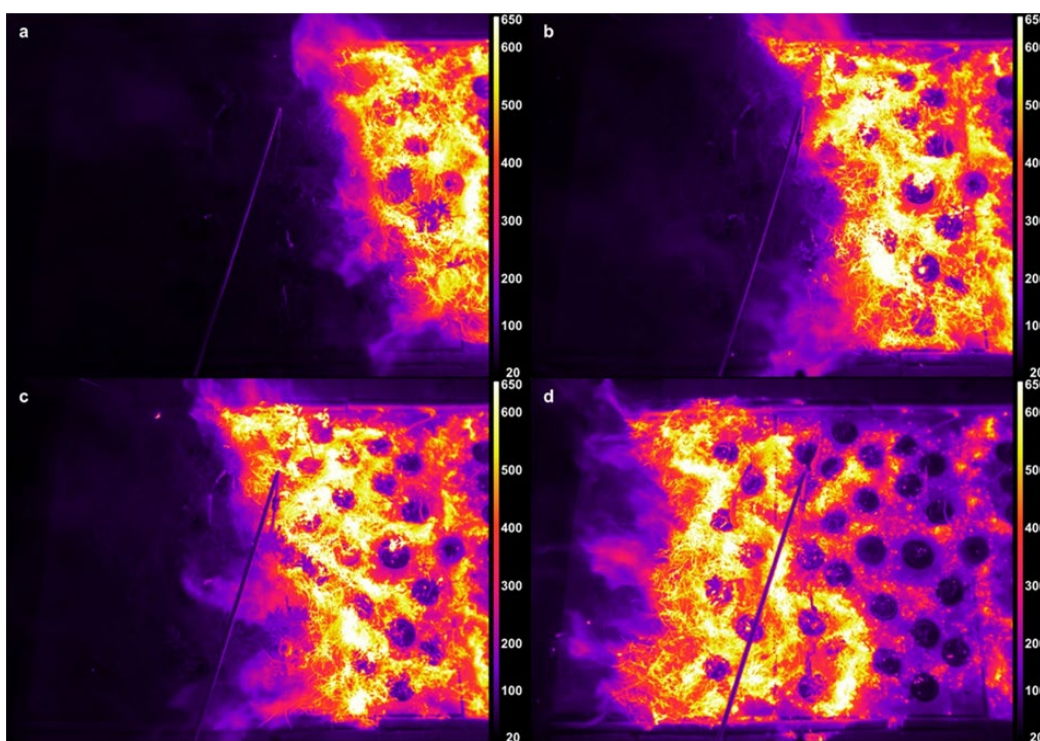


Figure 53. Example of long wave infrared imagery collected in experimental fires in wind tunnel experiments in fuel beds of longleaf pine needles and small shrubs. Dark circles indicate location of plants.

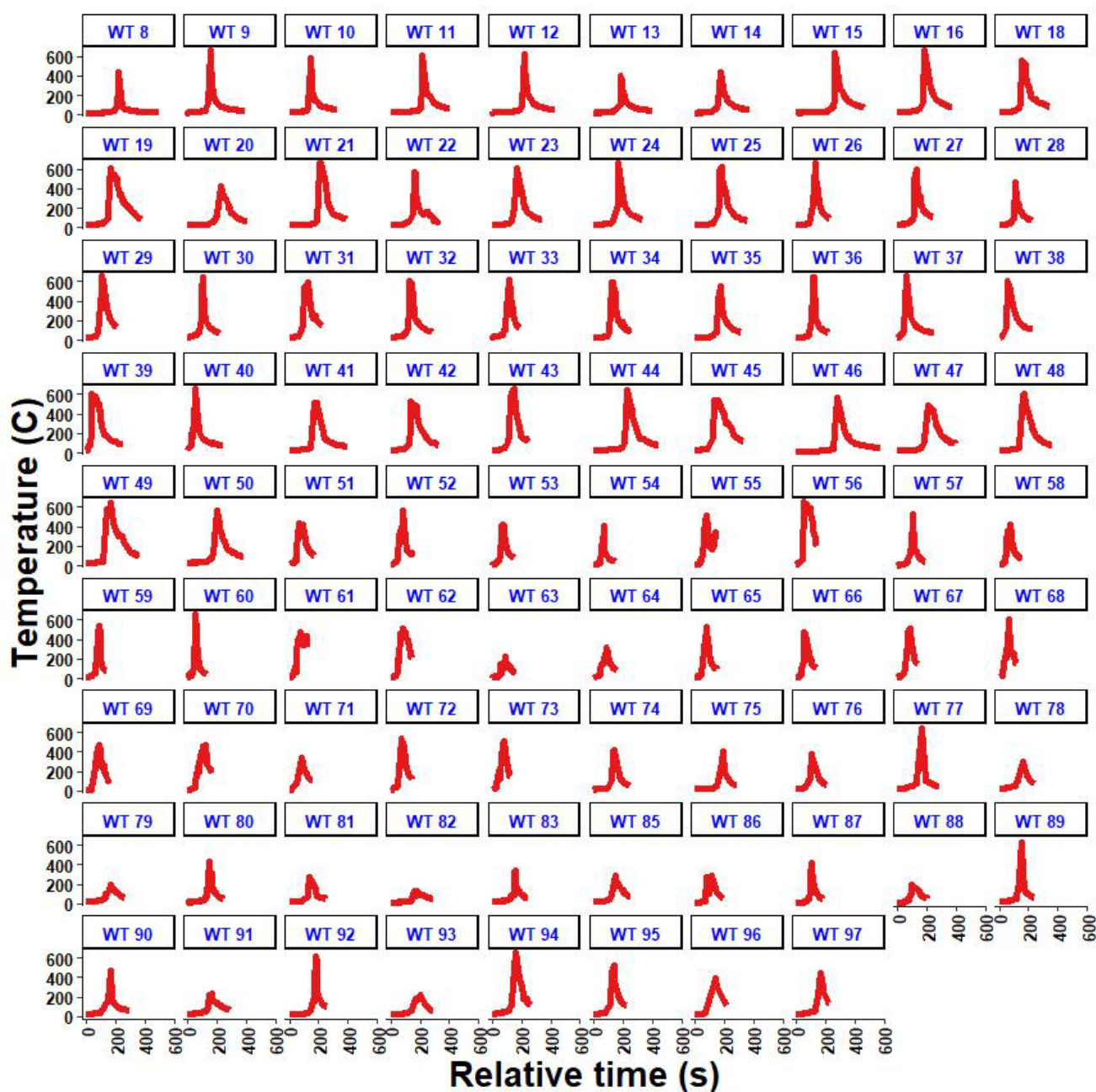


Figure 54. Time trace of surface fuel temperature below FTIR sample probe determined from FLIR thermal camera. Fuel bed composed on longleaf pine needles and small shrubs.

Mass loss of a single plant in the wind tunnel was measured. The mass loss was generally a smooth function (Figure 55); however, the rate was quite variable depending on the experimental configuration. The mass of the individual plant which included the soil, soil water, roots, stem and foliage ranged between 140 and 220 g (Figure 56). Actual mass loss observed ranged between 1 and 7 g. We assume that this mass loss was primarily the above ground stem and foliar biomass. It was not possible to determine below-ground mass loss in this experimental setup; however, we assume it to be relatively small due to soil insulating properties and the relatively short residence time of the fires (6 to 12 seconds to traverse the 6 cm diameter of the plant holder). Mass loss rate ranged between 0.07 and 0.32 g s⁻¹.

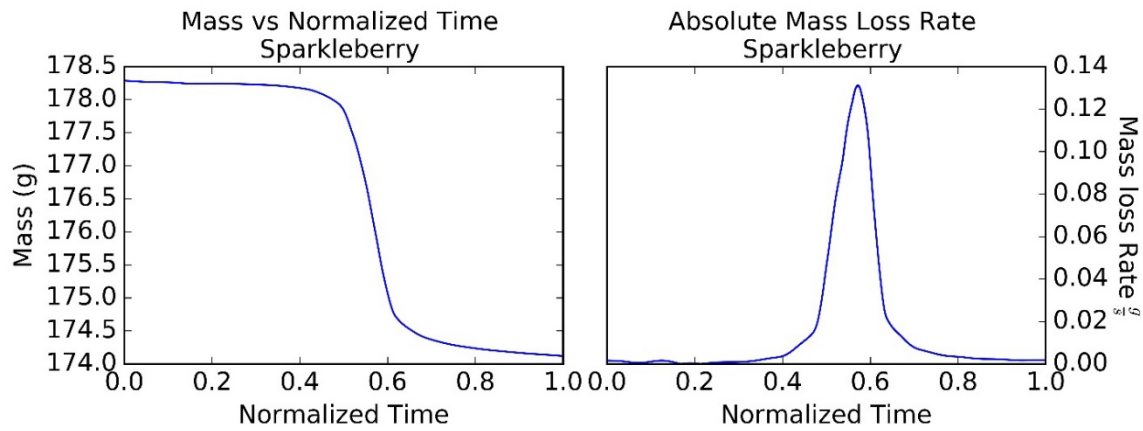


Figure 55. Example of mass and mass loss rate of a single plant in a fuel bed of longleaf pine needles measured in a wind tunnel experiment.

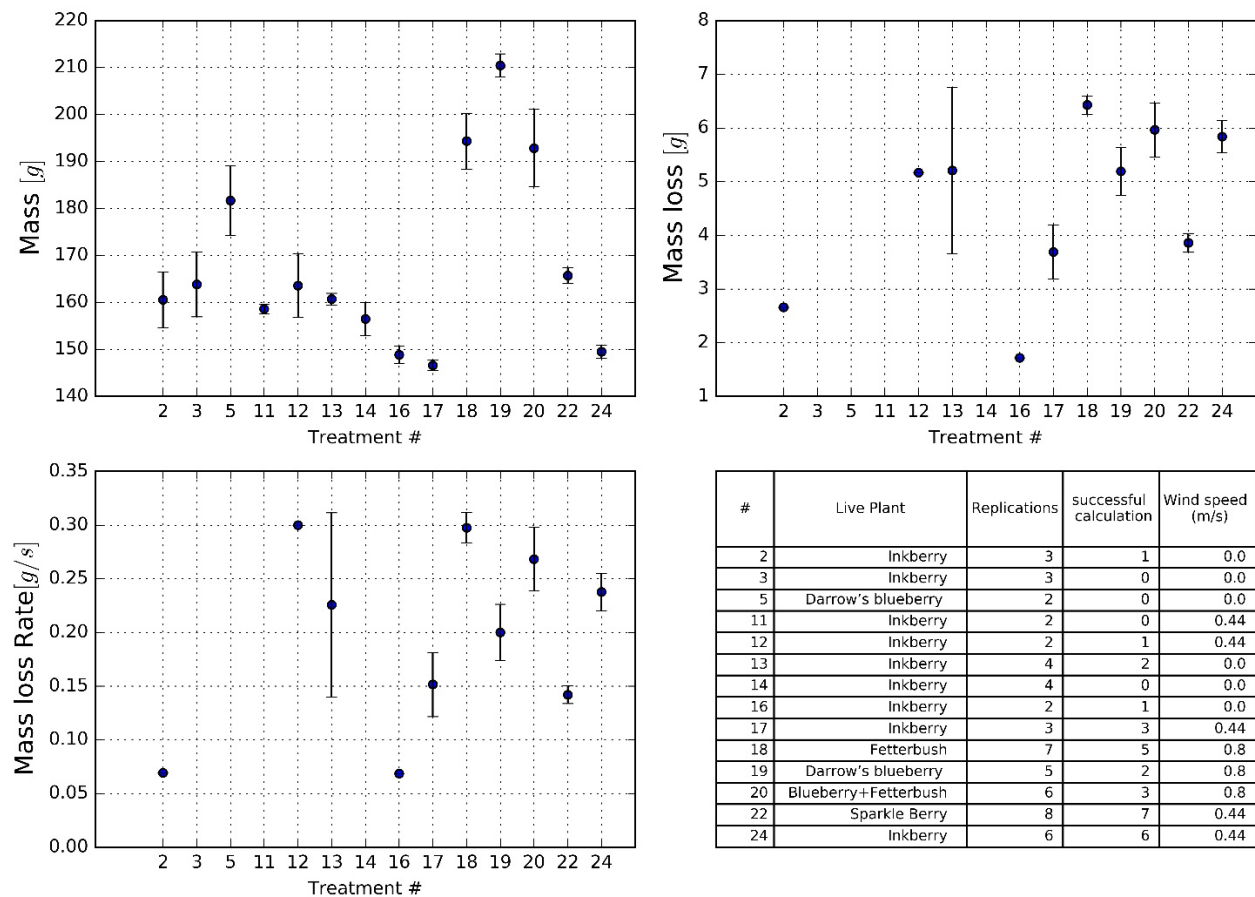


Figure 56. Summary of mass and mass loss data for different fuel bed configurations of longleaf pine needles with nursery shrubs. Treatment number refers to the combination of plant species and wind speed.

A thermocouple array of 2 vertical layers of 4 thermocouples each oriented horizontally in 90° increments measured temperatures as experienced by a plant in the wind tunnel. An example of the observed temperatures shows little difference between the two vertical layers (Figure 57). Temperatures varied little between the various fuel bed configurations.

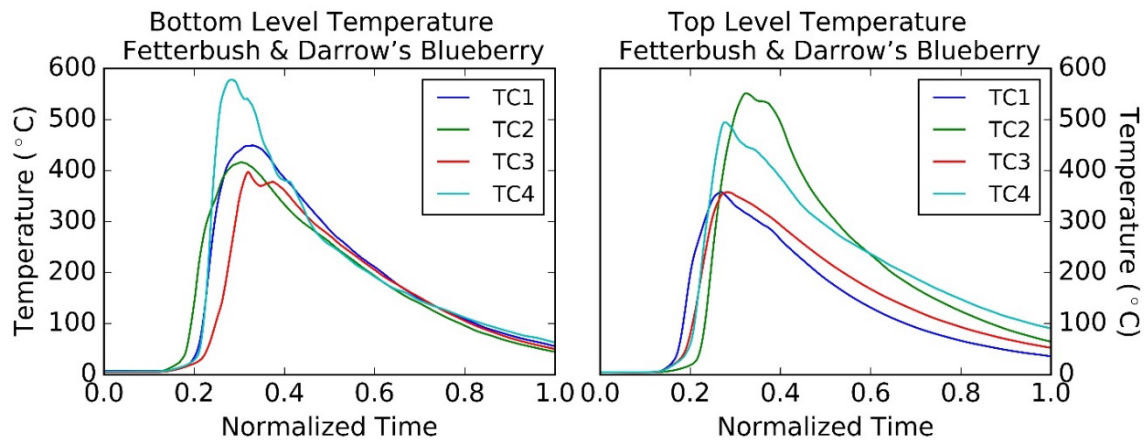


Figure 57. Example of temperatures measured by thermocouple tree array (Figure 22) in wind tunnel fires.

The Medtherm sensors were installed to capture total and radiant heat flux absorbed by the surface fuel as the fire propagated through the fuel bed. The sample results for output of these sensors can be seen in Figure 58. When looking into the heat flux sensor data, it can be seen that the amount of radiation and total heat flux varied greatly. The reason for this difference relates back to the position of the sensors. The sensors were positioned to capture heat flux on the surface of the fuel bed but were commonly covered by the longleaf pine needles. As a result, the total heat flux measurement included conduction from the needles. The needles also limited the view factor between the radiometer and the flame which resulted in a small amount of radiation to be recorded.

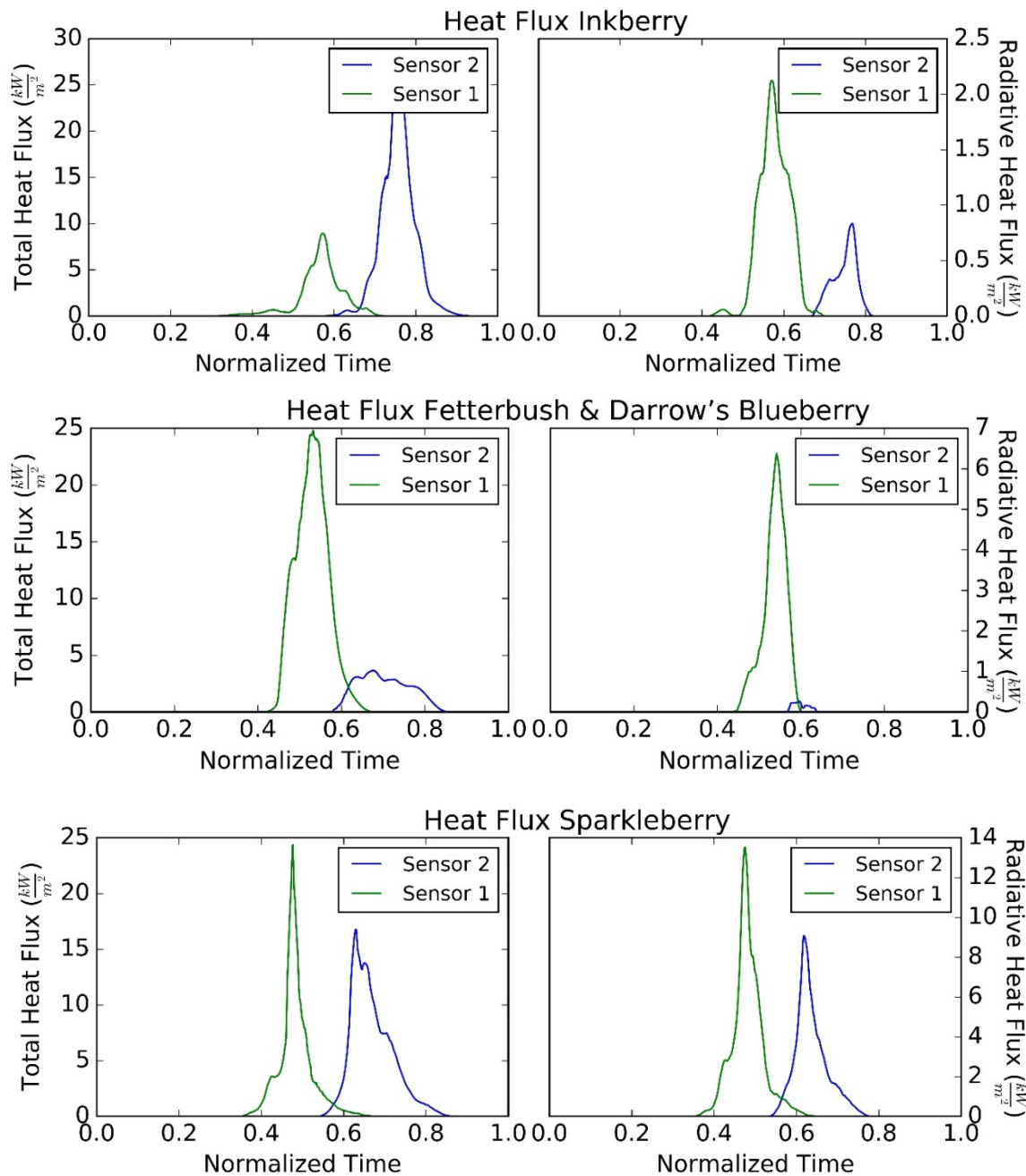


Figure 58. Total and radiant heat flux measured by sensors placed below the fuel bed upwind and downwind of mass loss plant in a wind tunnel experiment (Figure 21).

A neighborhood of 100 x 100 pixels was selected to capture convective heat flux caused by the flame using methodology detailed elsewhere [139,161]. Figure 59 shows a sample signal obtained by this process applied to four experimental fires in similar fuels. The results are shown in Figure 60 shows how the convective heat flux changed in different experimental configurations. These values are an estimate of the amount of convective heat transfer caused by the fire in the direction that it propagates. As it has also been discussed various assumptions were made to estimate convective heat flux, and these assumptions may cause uncertainty in the results shown in Figure 60. One of the major assumptions was using 2D BOS to study a 3D phenomenon, consequently the images and data were a planar projection of a 3D phenomenon. All the values obtained assumed that when a linear flame was present, all the properties did not change in the direction of line of sight. As the flame front deviates from linear, this assumption could cause uncertainty on the quantitative results. Thus,

the computed values may not be exact. However, this methodology still can provide a general understanding of the convective heat transfer for example, as demonstrated here, how it changes in different wind conditions.

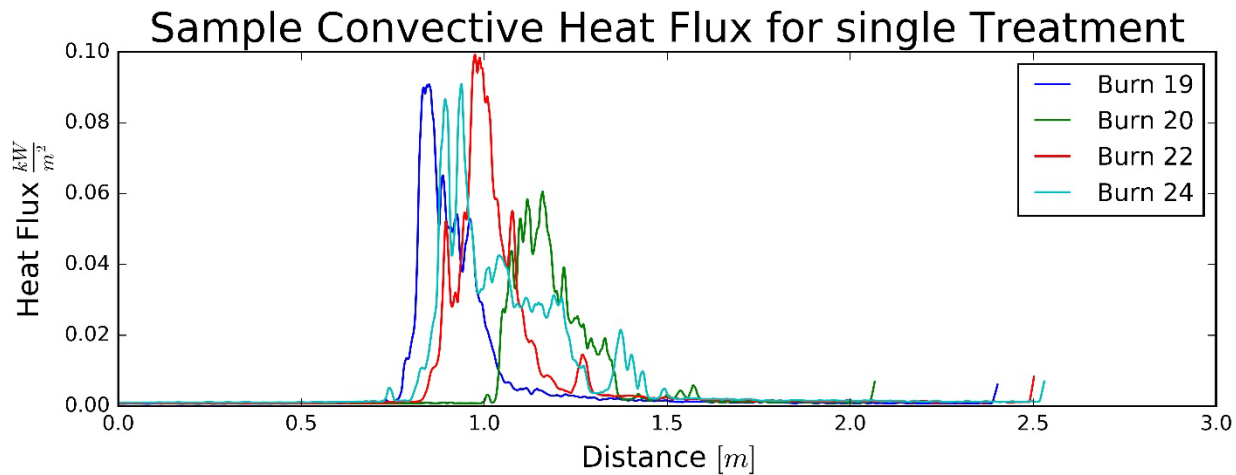


Figure 59. Convective heat flux estimated using Background-Oriented Schlieren methods for 4 replicate burns in a wind tunnel.

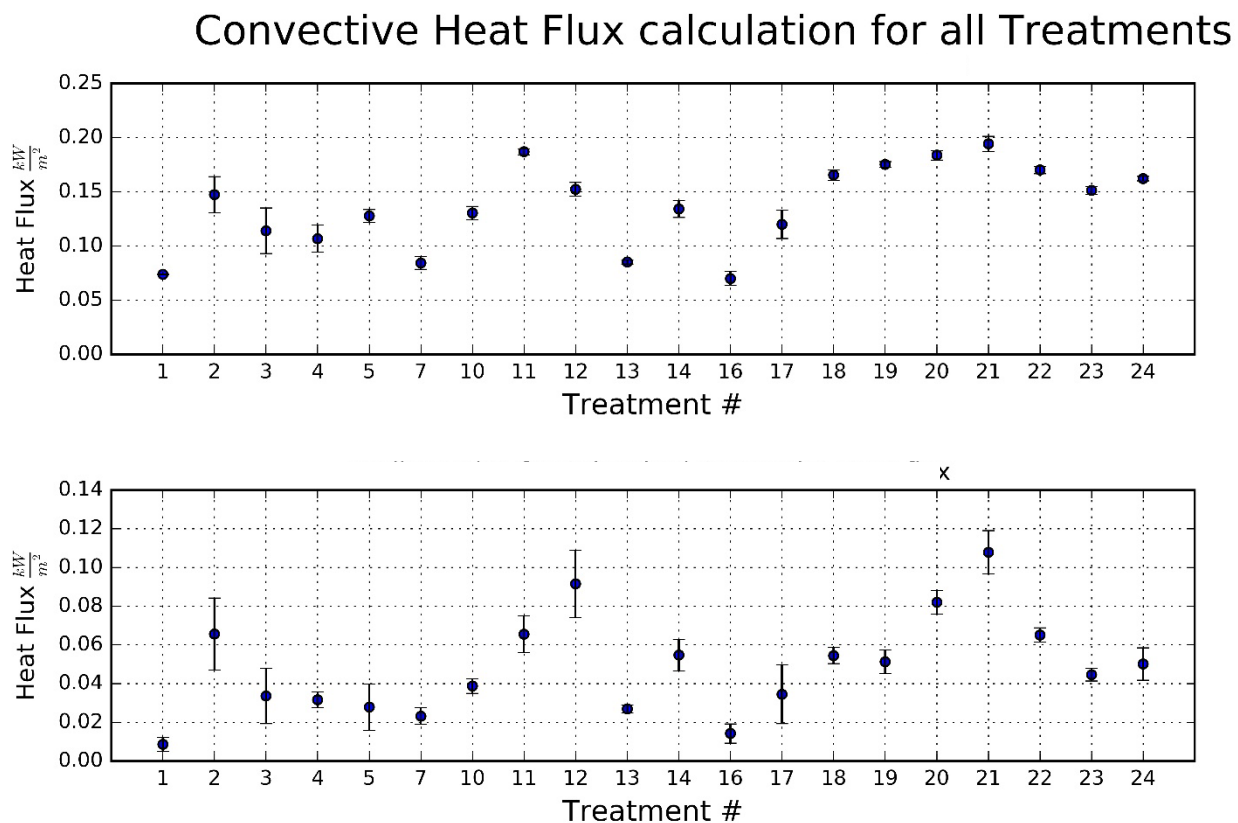


Figure 60. Maximum (top) and median (bottom) convective heat fluxes estimated using Background-Oriented Schlieren for all fuel bed configurations for experimental wind tunnel fires.

Recent findings elaborate on the importance of convective heat transfer in fire propagation in vegetative fuels. In this research, the effect of convective heat transfer mechanism on the pyrolysis process and fire propagation was studied. To quantify convection ahead of the flame, Background Oriented Schlieren (BOS) was used as a simple method of flow visualization around the fire. BOS

made it possible to visualize the thermal plume associated with the fire as the flame propagated through the fuel bed. This enabled us to effortlessly see how in a wind-driven fire, the wind forces the thermal plume ahead of the flame while in the non-wind driven fire the thermal plume is attached to the flame itself. Next, we demonstrated that by applying Density Gradient Image Velocimetry (DGIV) to the result of BOS the flow associated with the thermal plume could be visualized as well. Finally, it was shown that comparing consecutive frame of images makes it possible to visualize and quantify convective heat transfer.

After visualizing convective heat around a fire, a procedure was developed to model convective heat transfer ahead of the fire using the concept of eddy diffusivity. The eddy diffusivity was defined using an algebraic equation, which used turbulent mixing length and mixing time scale. The result of evaluating eddy diffusivity in different experimental configuration, demonstrated how the presence of external wind affected the mixing length and thus eddy diffusivity. To summarize external wind effects on eddy diffusivity, the eddy diffusivity was plotted against non-dimensional Froude number defined as

$$Fr = \left[\frac{(U_w - ROS)^2}{g \frac{\Delta H_c}{H_\infty} W_f} \right]^2 \quad (2)$$

This Froude number expression provides a measure of the ratio of the kinetic energy of the air over the sensible heat flux provided by the fire. Here, U_w is the wind speed, ROS is the rate of spread of the fire, g is the gravity and W_f is the width of flame. The convective buoyancy is expressed as $\Delta H_c/H_\infty$, where ΔH_c is enthalpy of combustion and H_∞ is the ambient enthalpy. The Froude number shown in equation (2) is very similar to the convective Froude number previously defined [11,207,208]. For this study, to estimate the heat of combustion, ΔH_c , the heat release of longleaf pine needles was only considered. Figure 61 shows the plotted values of eddy diffusivity against the calculated Froude number.

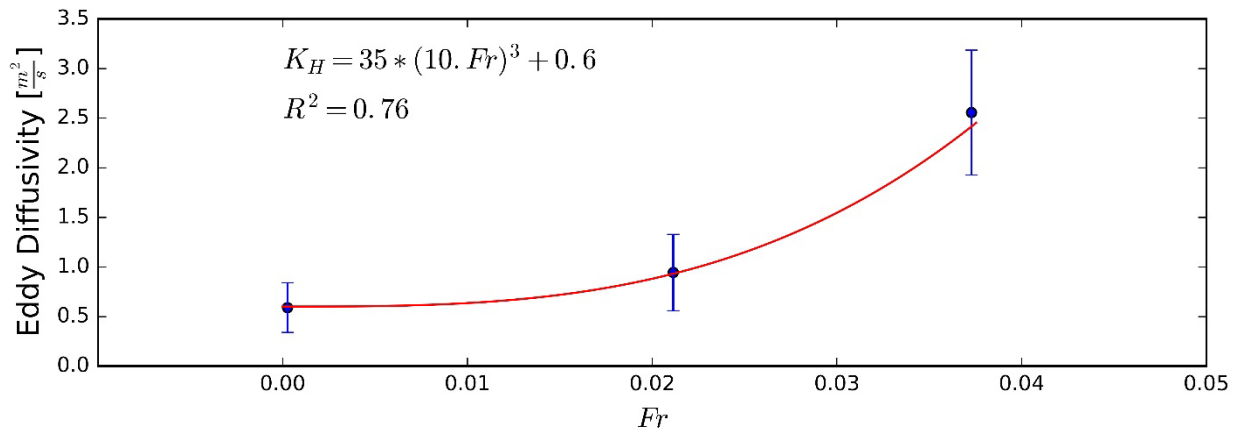


Figure 61. Relationship between eddy diffusivity against convective Froude number.

The same procedure can be taken to evaluate the effect of the Froude number on convective heat flux measured ahead of the flame using BOS (Figure 62). The fitted model did not account for as much of the variation in convective heat flux.

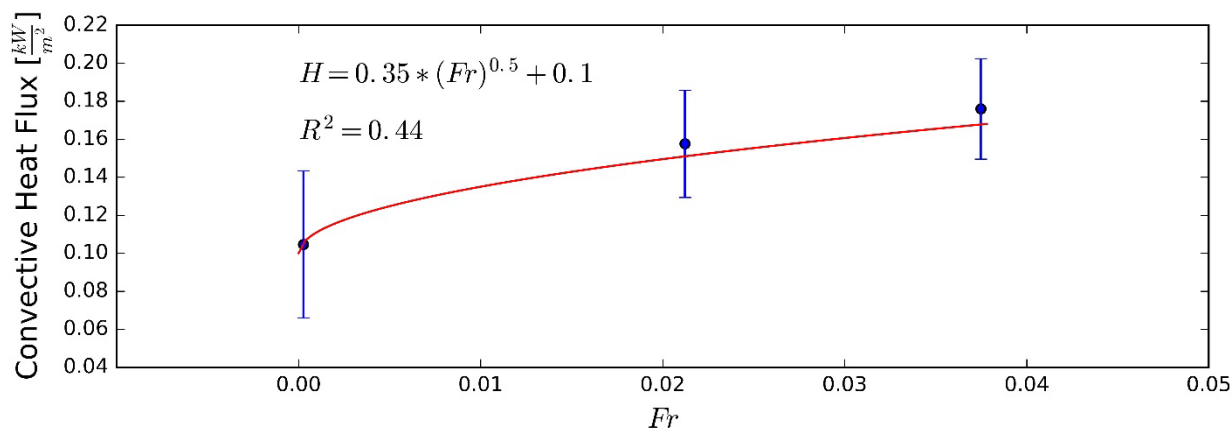


Figure 62. Relationship between convective heat flux and convective heat Froude number.

In calculating convective heat flux, it was assumed when a linear flame is present, all the properties do not change in the direction of line of sight, As the flame front deviates from linear this assumption could cause uncertainty on the quantitative results. Thus, the computed values may not be exact. However, when looking at the order of magnitude of measured values, it is comparable to some numerical models [209]. Nevertheless, this methodology still can provide a general understanding of the convective heat transfer for example, as demonstrated here, how it changes in different wind condition.

Combining these heat flux measurements and fuel temperatures with the pyrolysis composition results will be a portion of the future analysis of the wind tunnel canister and FTIR comparison. If possible, the temperature data will be combined with the dynamic FTIR data as in Figure 46.

4.3.3 *Ft. Jackson field burns*

Sensors and cameras were deployed in seven burns at Fort Jackson and four burns at Pebble Hill Plantation (Figure 63 - Figure 73). Number of sensors deployed in a plot ranged from one to eight. A total of 43 measurements were collected for the experimental burns. The horizontal flow sensor in FBP 5 failed on fire 24Bs and the air temperature sensor in FBP 11 failed in fire 16D5. The instantaneous velocities and air temperature were similar across all seven fires (Figure 74, Figure 75). Across all burns average total energy incident at the face of the sensor was 8.3 kW/m^2 with an average maximum of 17 kW/m^2 (Figure 76). Average radiant flux was 4.4 kW/m^2 with an average peak value of 10.4 kW/m^2 . Convective heating on the sensor face can be extracted by accounting for transmission through the radiant window and correcting for the difference between the total and radiant heating levels. Using this method average convective heating the surface of the sensors was 5.2 kW/m^2 , with peak average value of 9.6 kW/m^2 (Figure 76). Average air temperature at the sensor location 473 C with an average peak of 743 C (Figure 77). Average vertical air velocity at the sensor location was 1.8 m/s while average peak velocity for all burns was 3.7 with average downward velocity of -0.13 m/s (Figure 77). Similarly, average horizontal velocity into the face of the sensor was 1.2 m/s with average peak of 3.9 and minimum of -2 m/s . From an individual burn point of view burns 24Bs, 24At and 16D1 produced the highest heating and temperatures. The overall peak energy level recorded was nearly 30 kW/m^2 of total heating for burn 24Bs.

These heating values are representative of those reported elsewhere for similar vegetation and environments [210]. They are quantitatively at the low end of the energy release spectrum and suggest that burning conditions were largely low intensity. Impacts to surrounding vegetation and soil would be expected to be low. The low heat values reflect the relatively low fuel consumption that occurred (Table 11).



Figure 63. Fire behavior package 6 set up for plot 24Bt.



Figure 64. Fire behavior package 6 during burn in 24Bt. This package saw a peak total heat flux of 10.9 kW m^{-2} , peak air temperature of 423°C , and registered a peak wind speed of 3 m s^{-1} .



Figure 65. Fuel loading on plot 24Bs. A peak total heat flux of 30kW m^{-2} was registered for this burn along with a peak air temperature of $1042\text{ }^{\circ}\text{C}$ and a peak horizontal wind speed of 4m s^{-1} .



Figure 66. An example of fuel loading in plot 24As.



Figure 67. Fire behavior in 24As where a peak total heat flux value of 17.5 kW m^{-2} was registered along with a peak air temperature of $954 \text{ }^{\circ}\text{C}$ and peak wind speed of 4.5 m s^{-1} .



Figure 68. A sensor package set up to monitor fire behavior in the reference plots of plot 24At.



Figure 69. Fire behavior in the reference plots of plot 24At. Instruments registered a peak total heat flux of 19.3 kW m^{-2} , a peak air temperature of $714 \text{ }^{\circ}\text{C}$, and a peak horizontal wind speed of 3.6 m s^{-1} .



Figure 70. Instrumentation set up to monitor fire behavior in plot 16D5 reference plots.



Figure 71. Fire behavior in plot 16D5 reference plots. A peak total heat flux of 10.9kW m^{-2} was registered for burn 5 along with a peak air temperature of $511\text{ }^{\circ}\text{C}$, peak horizontal wind speed of 3.8m s^{-1} .



Figure 72. Fuel loading in plot 16D6. A peak total heat flux of 12.4 kW m^{-2} was registered along with a peak air temperature of $631 \text{ }^{\circ}\text{C}$ and peak horizontal wind speeds of 4 m s^{-1} .



Figure 73. Fuel loading for plot 16D1. A peak total heat flux of 17.8 kW m^{-2} was registered along with a peak air temperature of $930 \text{ }^{\circ}\text{C}$ and peak horizontal wind speeds of 4.3 m s^{-1} .

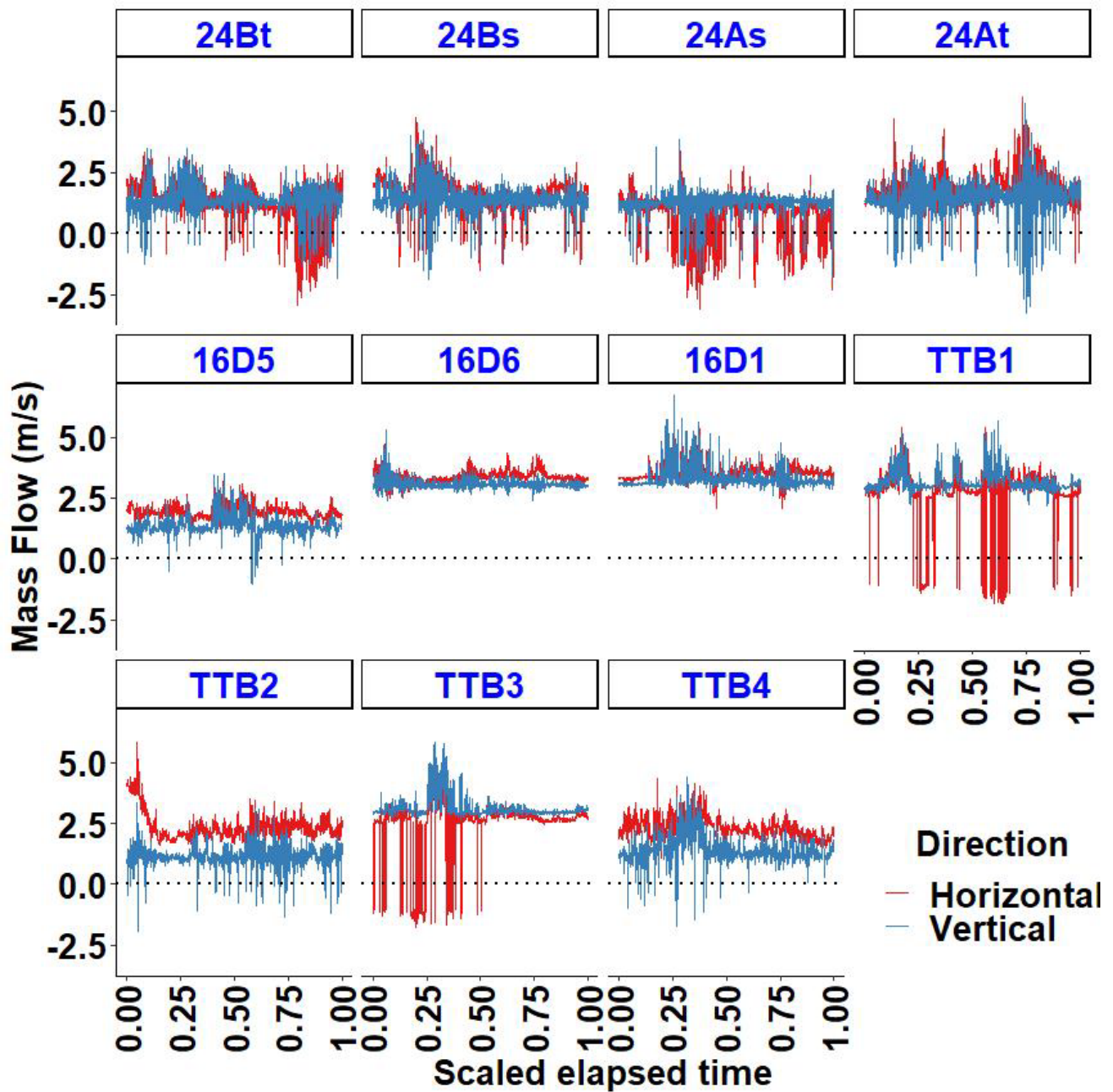


Figure 74. Instantaneous horizontal and vertical air flow measured by FBPs in low intensity prescribed burns in longleaf pine at Ft. Jackson, SC and Tall Timbers Pebble Hill Plantation. Note that positive horizontal flow is into the FBP and negative vertical flow is parallel to the gravity vector.

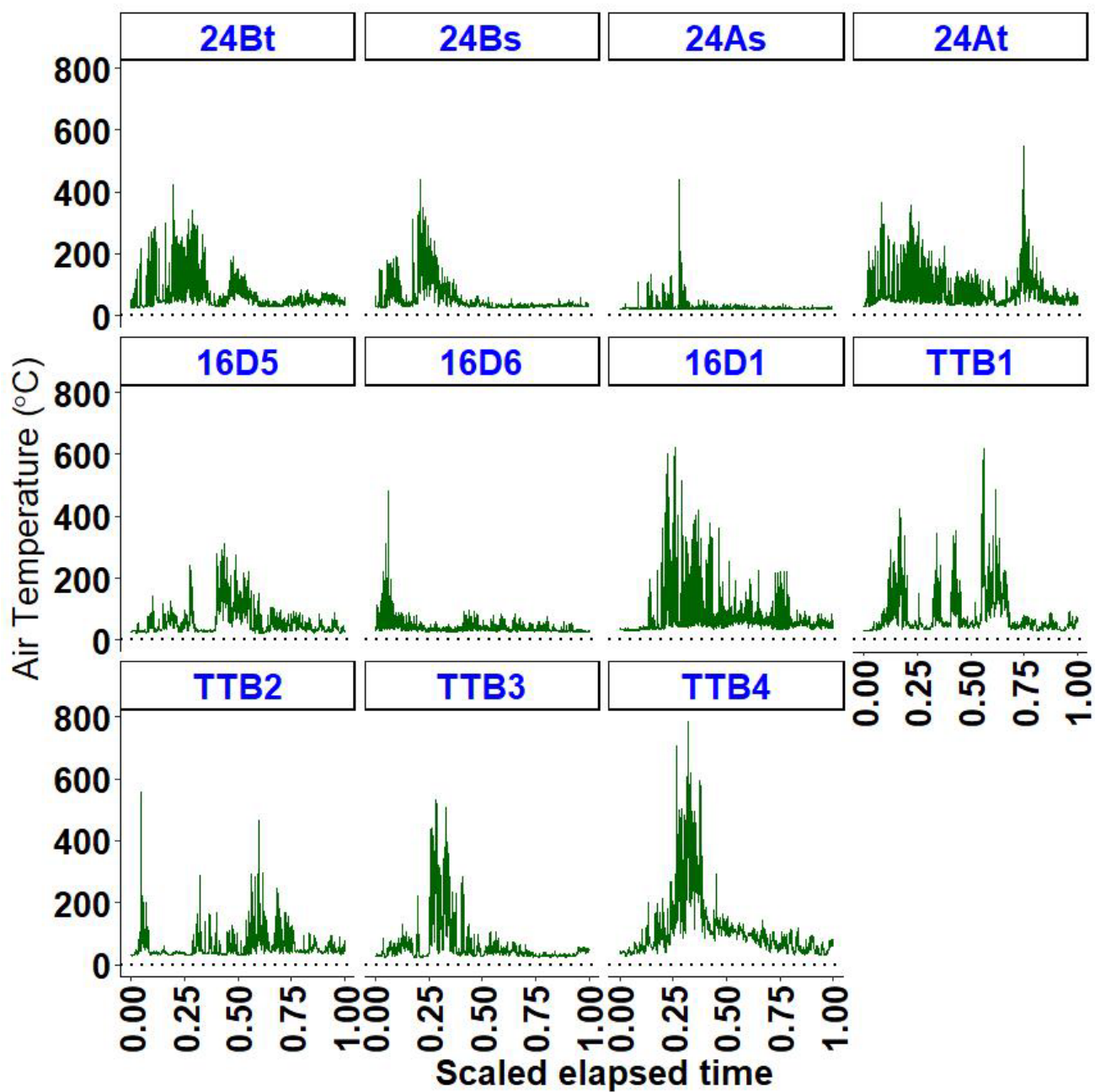


Figure 75. Instantaneous air temperature measured with FBPs in low intensity prescribed burns in longleaf pine at Ft. Jackson, SC, and Tall Timbers Pebble Hill Plantation.

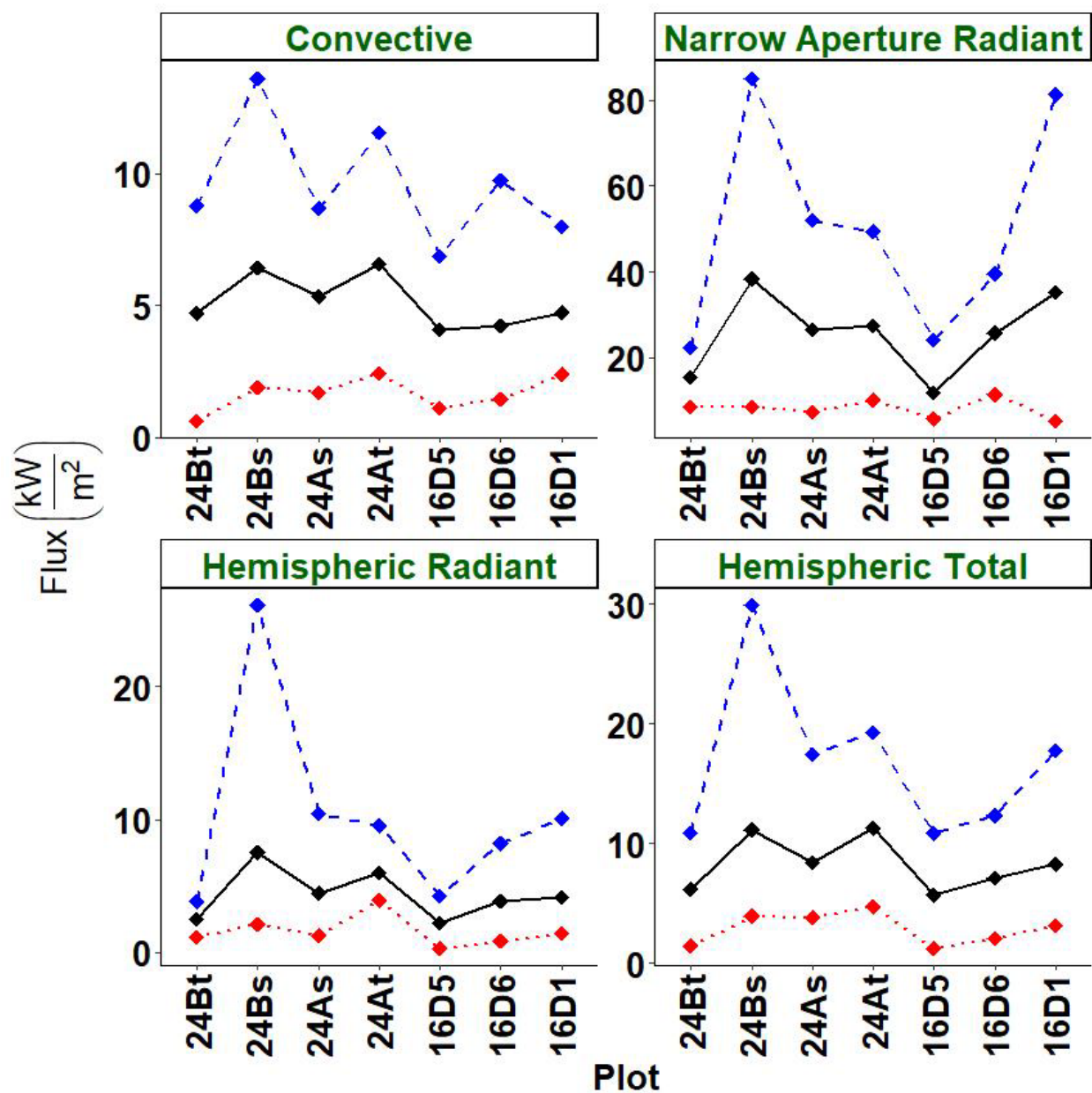


Figure 76. Maximum, arithmetic mean and minimum heat fluxes measured during experimental prescribed fires in longleaf pine at Ft. Jackson, SC.

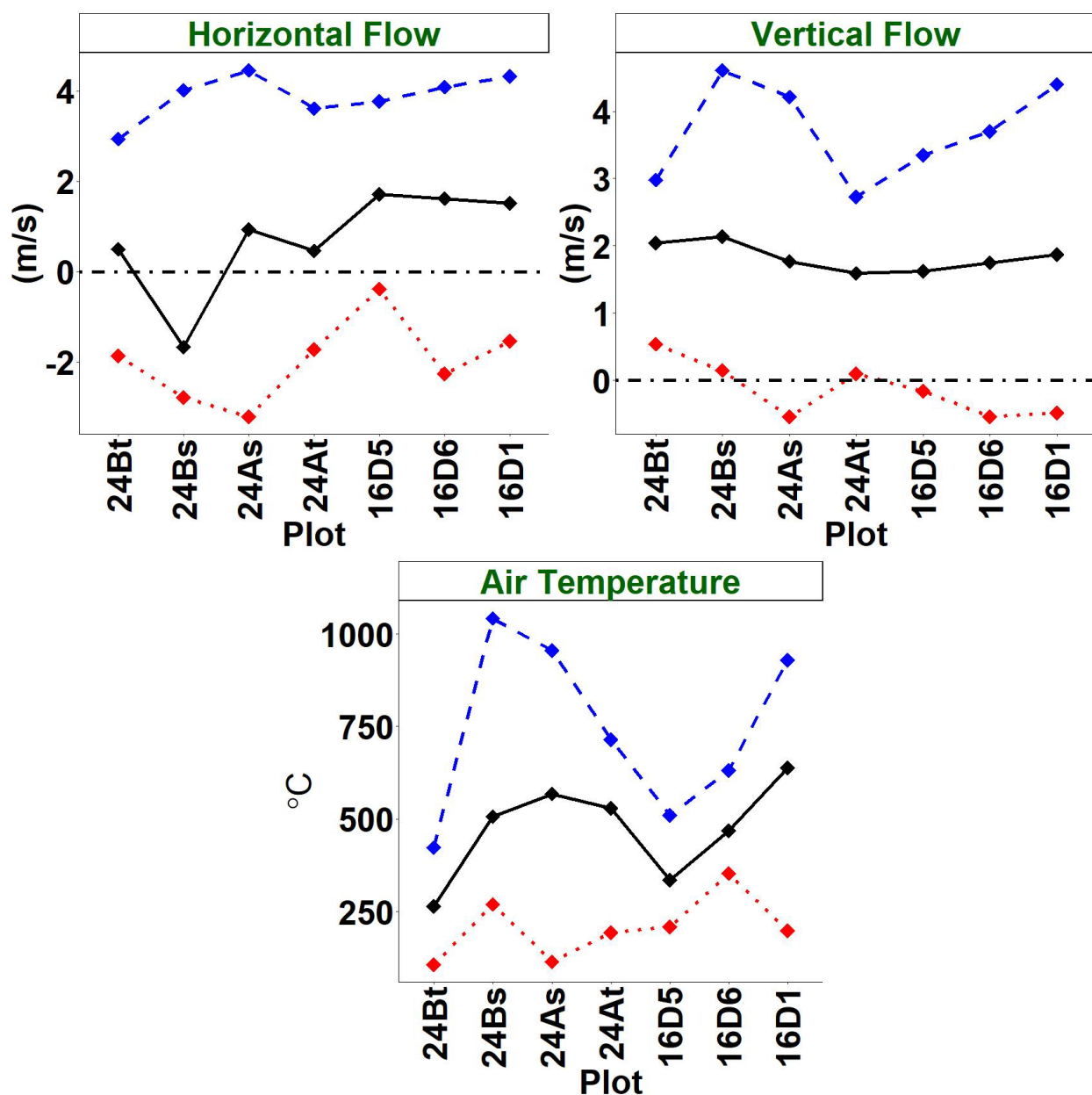


Figure 77. Components of air flow and air temperatures measured during experimental prescribed fires in longleaf pine at Ft. Jackson, SC.

An alternative summary of the information collected by the FBP packages was performed by calculating the harmonic means of the fluxes and air velocities. FBP logger 5 on burn 24Bs was excluded from this analysis because the horizontal wind sensor failed. This resulted in 38 usable sets of usable observations. The heat fluxes are rates ($\text{kJ s}^{-1} \text{m}^{-2}$) and the harmonic mean was used to estimate the mean of rates where time (s) is fixed and the quantity varies (kJ m^{-2}) [211–213]. The arithmetic mean which can be used with both positive and negative numbers was applied in Figure 76 and Figure 77; however, the geometric (for proportions) and harmonic (for rates) means can only be used with positive values. We previously used the geometric mean extensively in the analysis of the compositional data (gases, fuel loading, etc.). While the initial analysis of the velocity data assigned a negative value for horizontal flow away from the sensor face and a negative value for vertical flow downward (same direction as gravity), the velocity data were converted to positive values and direction of flow was treated as a circular variable (0 to 360°) [214] in polar coordinates with 0° indicating flow into the sensor face and 90° indicating vertical flow opposite the gravity

vector. The maximum values of the different fluxes occurred at different times. To illustrate, the maximum values of total, radiant, convective and NAR heat fluxes were determined for each FBP within a fire. The values of the other fluxes at the time of the observed maximum as well as the mean wind velocity and direction of flow were attached to the maximum value (Table 33). For example, in Plot 16D1, the mean maximum total heat flux was 6.3 kW m^{-2} with a 95 percent confidence interval of 6.19 to 6.41 kW m^{-2} . The mean radiant flux and mean convective fluxes which occurred at the time of the total flux in each FBP were 0.23 and 0.60 of the mean maximum total flux, the magnitude of the wind velocity was 3.7 m s^{-1} and the direction was 36° indicating that it was principally into the FBP. Similarly, for plot 16D1, the maximum convective flux was 3.84 kW m^{-2} with a confidence interval of 6.79 to 6.90 and the total and radiant fluxes at the time of the maximum were 1.62 and 0.37 the size of the convective flux, respectively. The magnitude of the wind was 3.4 and the direction was 28° which indicated that the horizontal flow was relatively larger than when the maximum total flux occurred. When viewed this way, the convective flux was generally smaller when the maximum radiant flux occurred as measured by the hemispherical sensor and the hemispherical radiant flux was smaller when the maximum convective flux occurred. The narrow angle radiometer consistently estimated higher heat fluxes than the hemispherical heat flux sensor. The 95 percent confidence intervals, based on the number of FBPs deployed in each burn, were quite variable (Figure 78). For harmonic means, confidence intervals spanning 0 are undefined since the data are strictly positive which is reflected in the lack of confidence intervals for several fluxes. The relatively small sample size (number of FBPs in a plot) also required larger t-values (ranged from 2.36 to 12.71 for 7 to 1 degree of freedom) to compute the 95 percent confidence intervals.

The distribution of the magnitude of the instantaneous wind velocity was similar between the burns. In Figure 79, the frequency of the velocity magnitude is plotted in a conventional stacked bar plot. As can be seen, the velocity generally was less than 9 m s^{-1} . Determining the dominant direction of the flow is more easily seen when the data were plotted as polar coordinates (Figure 80). Most of the flow was directed into the sensor as indicated by the angle midpoint of 22.5° .

In addition to the FBPs which have been used extensively to characterize heat fluxes and air flow in wildland fire, two experimental sensors were also deployed in the experimental fires at Ft. Jackson. These experimental sensor packages measure 1) heat flux with a radiometer, 2) fine wire thermocouples and 3D air flow with a disk anemometer (HF package, Figure 81) and 2) flame residence time using a flame ionization detector (FID package, Figure 82). These experimental sensor packages were deployed successfully in burns 24Bs, 24As, 24At, 16D5, 16D6 and 16D1. The HF package recorded radiant heat fluxes similar in magnitude to the NAR (narrow angle radiometer) contained in the FBP package (Figure 83). Wind flow data were also collected during the fires; however, the disk anemometers have not been calibrated so the data are not currently available to compare with the FBP flow data. Voltage from the flame ionization detector, which determines how long the flame resides over the sensor based on gas ionization, was variable in the 5 fires it was deployed in (Figure 84). Defining flame residence time as the time that the voltage exceeded the background level resulted in flame residence times ranging from approximately 30 to 330 seconds. While there is discussion surrounding what is meant by flame residence time [215], the values observed by the FID packages fall within the range of values reported for wildland fuels [215,216]. In constructed fuel beds of longleaf and slash pine needles burned under a range of wind speeds ($0.4 - 26 \text{ m s}^{-1}$), flame residence time ranged from 61 to 15 s [217]. The value in 24As includes a lengthy time when the FID values were low (at background levels) and the value in 16D1 is larger than that reported for litter fuels. This could be due, in part, to flaming combustion of the duff component of the fuel bed (Table 12) which would produce longer residence times. Despite these shortcomings, these results suggest that the approach to measuring flame residence time may be feasible.

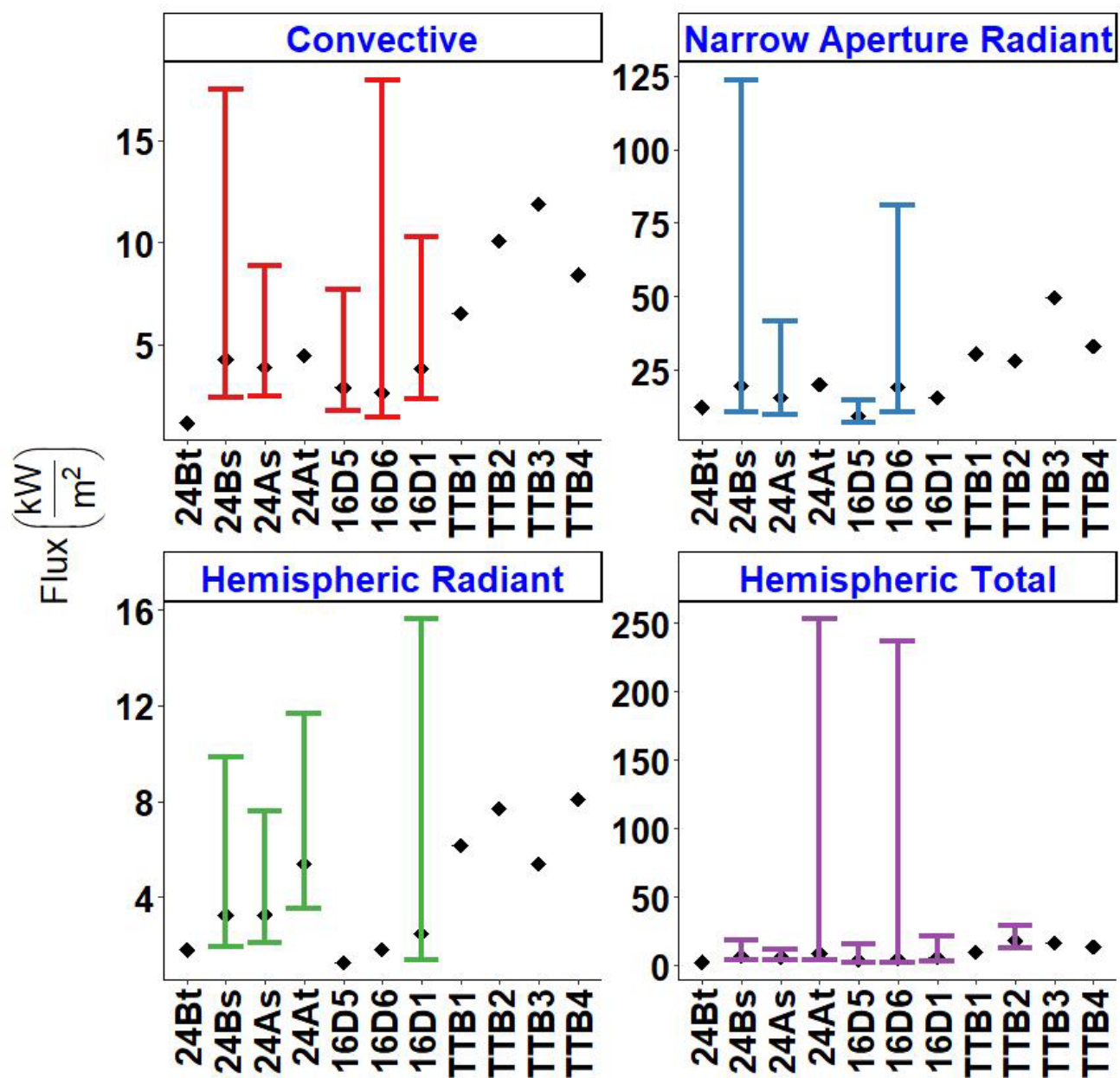


Figure 78. Heat fluxes measured using Fire Behavior Packages in prescribed burns in longleaf pine at Ft. Jackson, SC, and Tall Timbers Research Station Pebble Hill Plantation. Harmonic mean with 95 percent confidence interval shown.

Table 33. Mean maximum heat flux for each heat transfer mode and associated fluxes (expressed as proportion of maximum) and wind information observed at same time as maximum. Harmonic mean and 95 percent confidence interval shown. Fluxes in kW m⁻², wind velocity m s⁻¹, angle in degrees. Flow into face of sensor, away from face, upward and downward is 0°, 180°, 90° and 270°, respectively.

Plot	Type	Flux			Associated Fluxes and Air Flow					
		Max	Lower	Upper	Total	Radiant	Convective	NAR	Wind	Angle
24Bt	Total	2.69				0.49	0.39	1.12	2.9	45
24Bs		6.81	3.78	34.24		0.30	0.35	0.66	3.3	38
24As		6.61	4.59	11.77		0.39	0.30	0.81	2.9	77
24At		8.72	4.41	404.27		0.60	0.25	1.22	2.2	70
16D5		4.10	2.36	15.69		0.19	0.64	0.95	2.3	43
16D6		5.07	2.57	191.69		0.26	0.41	0.92	2.8	45
16D1		6.30	3.67	22.02		0.23	0.60	0.64	3.7	36
TTB1		10.2				0.56	0.43	2.11	5.4	48
TTB2		18.7	14.2	27.1		0.37	0.54	0.66	5.3	26
TTB3		17.4				0.29	0.68	0.46	3.5	109
TTB4		14.4				0.41	0.57	1.67	3.4	42
24Bt	Radiant	3.27	2.09	7.57	1.18		0.11	1.62	2.7	42
24Bs		5.41	3.52	11.64	1.28		0.23	2.23	2.1	47
24As		1.28			1.41		0.34	2.52	2.3	73
24At		1.81			1.49		0.36	1.87	2.3	69
16D5		2.49	1.35	15.63	2.18		0.89	4.63	2.2	38
16D6		6.16			1.27		0.10	3.93	2.1	45
16D1		7.70			1.82		0.54	2.05	3.1	30
TTB1		5.40			1.30		0.28	2.83	4.0	49
TTB2		8.08			1.72		0.67	2.02	4.9	27
TTB3		3.27	2.09	7.57	2.33		1.27	1.97	6.6	52
TTB4		5.41	3.52	11.64	1.18		0.11	1.62	3.5	42
24Bt	Convective	1.16			2.27	1.05		2.61	2.8	45
24Bs		4.01	2.09	49.72	1.34	0.28		0.66	3.0	49
24As		3.88	2.48	8.85	1.62	0.50		1.23	3.3	44
24At		4.46			1.47	0.43		1.67	2.5	67
16D5		2.90	1.78	7.69	1.39	0.24		1.23	2.4	41
16D6		2.64	1.43	17.89	1.83	0.49		1.71	2.8	45
16D1		3.84	2.36	10.31	1.62	0.37		1.06	3.4	28

TTB1		6.54			1.33	0.29		1.05	5.6	45
TTB2		10.10			1.85	0.69		1.21	5.3	26
TTB3		11.87			1.47	0.43		0.67	3.5	109
TTB4		8.43			1.31	0.27		0.84	2.8	35
24Bt	NAR	8.63			0.11	0.09	0.01		2.4	55
24Bs		18.90			0.06	0.21	0.03		2.5	38
24As		15.85	9.79	41.63	0.15	0.11	0.03		2.1	62
24At		20.17			0.32	0.20	0.09		2.2	58
16D5		9.62	7.08	14.98	0.18	0.17	0.12		2.2	41
16D6		13.90			0.07	0.15	0.06		2.4	42
16D1		15.76			0.13	0.08	0.04		2.4	48
TTB1		30.66			0.24	0.19	0.05		4.6	48
TTB2		28.41			0.36	0.20	0.11		5.0	33
TTB3		49.73			0.03	0.02	0.01		4.3	49
TTB4		33.18			0.23	0.14	0.08		4.2	35

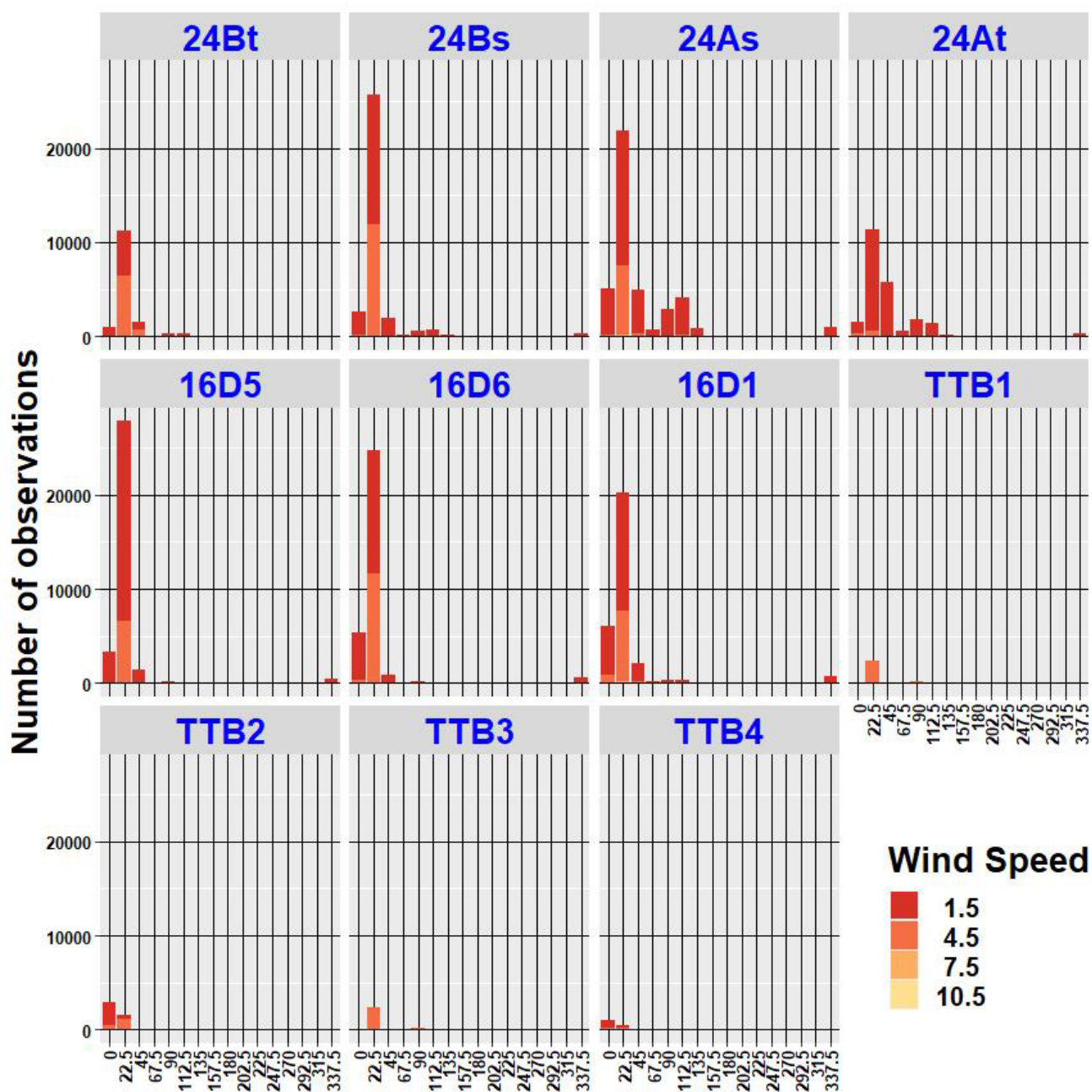


Figure 79. Frequency distribution of wind speed (m s^{-1}) into sensor by direction categories summarized by plot from FBPs deployed in experimental burns in longleaf pine at Ft. Jackson, SC and Tall Timbers Pebble Hill Plantation shown as bar charts.

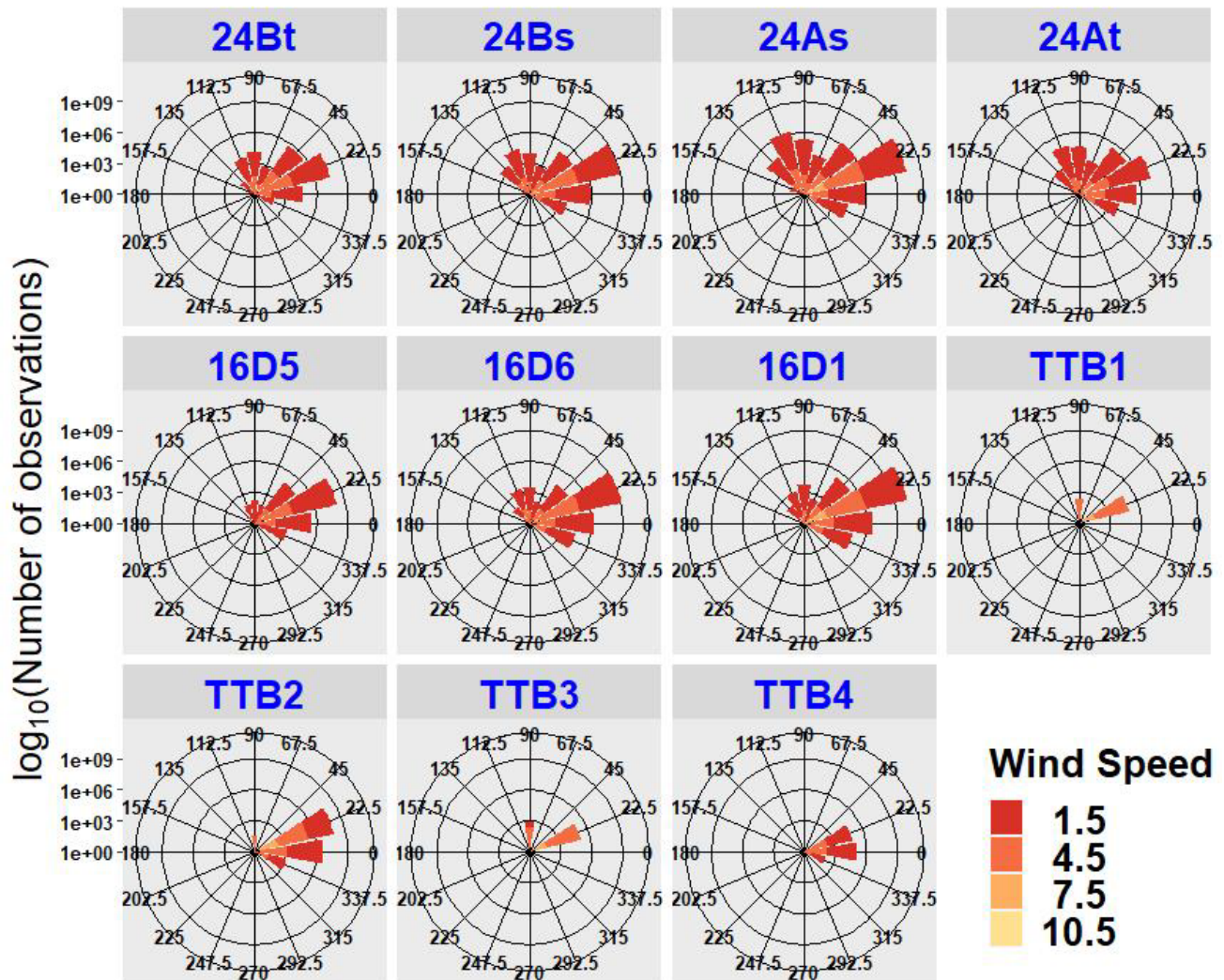


Figure 80. Frequency distribution of wind speed (m s^{-1}) into sensor by direction categories from FBPs deployed summarized by experimental burns in longleaf pine at Ft. Jackson, SC and Tall Timbers Pebble Hill Plantation shown in polar coordinates.



Figure 81. New heat flux package consisting of radiometer, a disk anemometer and thermocouples deployed in experimental prescribed burns in longleaf pine at Ft. Jackson, SC.



Figure 82. Flame ionization detector used to estimate flame residence time buried in longleaf pine forest floor at Ft. Jackson, SC. Red arrow indicates detector.

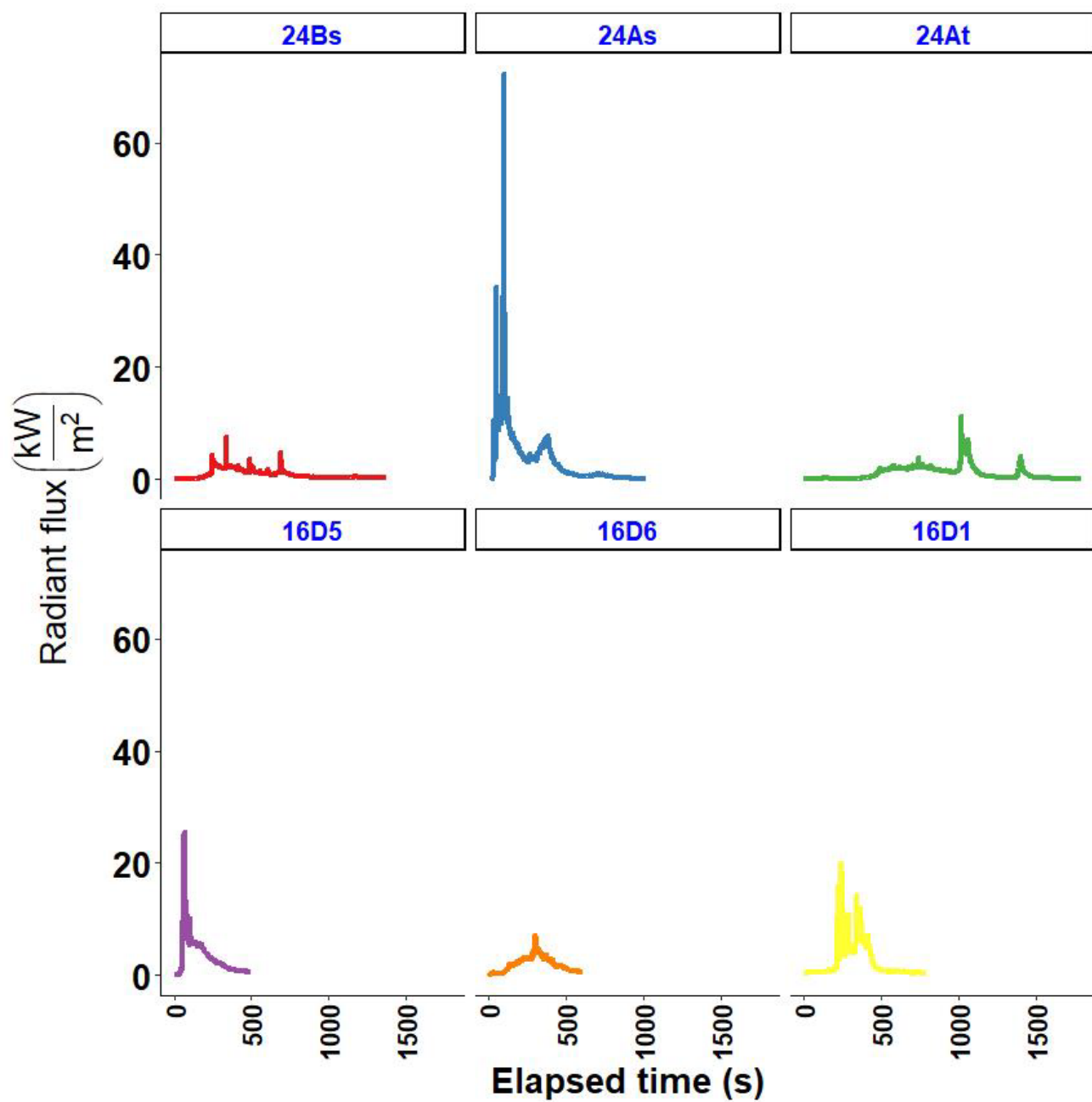


Figure 83. Uncorrected radiant flux measured in experimental prescribed fires in longleaf pine at Ft. Jackson, SC with new heat flux (HF) package.

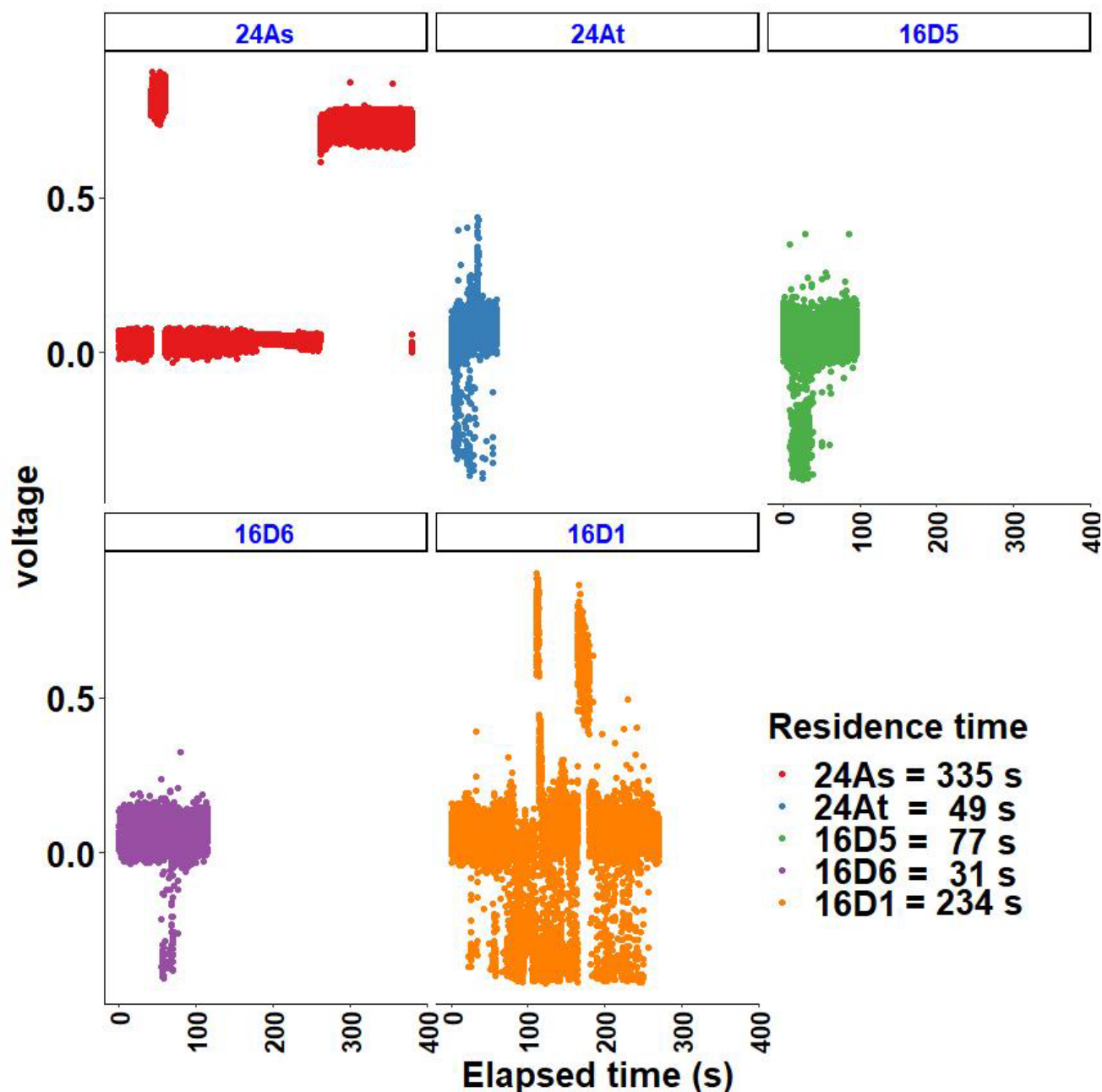


Figure 84. Flame residence time estimated by new flame ionization detector in experimental prescribed fires in longleaf pine, Ft. Jackson, SC.

For the leaf temperature measurements, Figure 85 and Figure 86 indicate the position of the shrubs and leaves sampled in two of the seven burns. In the false color IR images (Figure 87 - Figure 89) of the sample frames in Plots 16D1, 16D5 and 16D6, the colors are a temperature scale. Purple indicates cool foliage (transpiration/high water content), orange indicates warm spots in the litter (surface fuels) caused by sun flecks. The lavender is litter in the shade. The threshold between orange and purple is about 30 °C, the warmest fuels in the sun were up to 50 °C, shaded fuel about 28 °C and the leaves about 20 °C. Figure 90 shows an example thermal image during the prescribed burn from which the leaf temperature data were extracted.



Figure 85. Location (red circles) of foliage sampled for leaf temperature during prescribed burn 24A in longleaf pine at Ft. Jackson, SC.



Figure 86. Location (red circles) of foliage sampled for leaf temperature during prescribed burn 24A in longleaf pine at Ft. Jackson, SC.

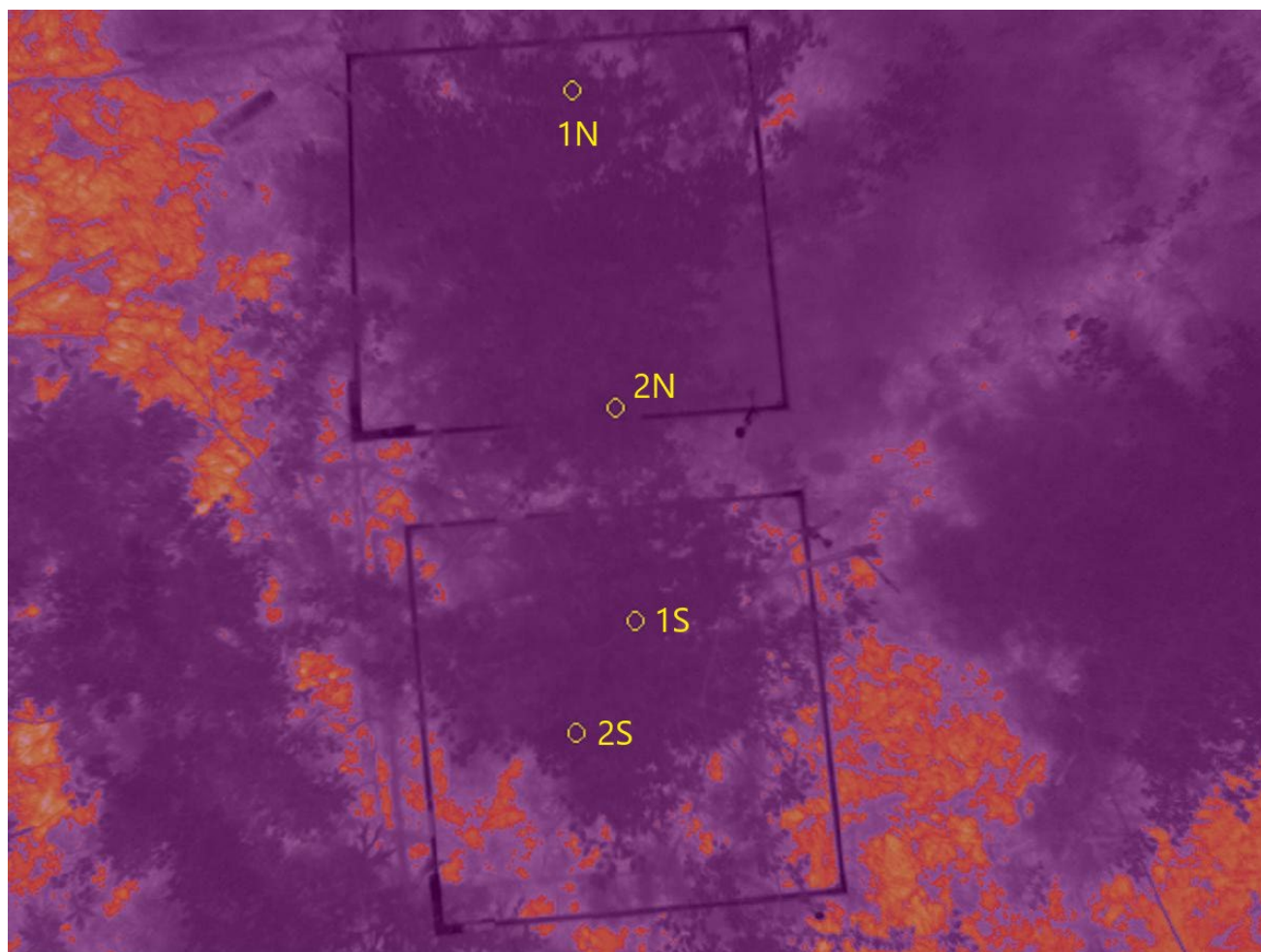


Figure 87. LWIR (7-14 μm) false color image of leaf temperature sampling locations during prescribed burn 16D1 in longleaf pine at Ft. Jackson, SC. Purple indicates high water content foliage, orange indicates sun flecks in litter, lavender is shaded litter.

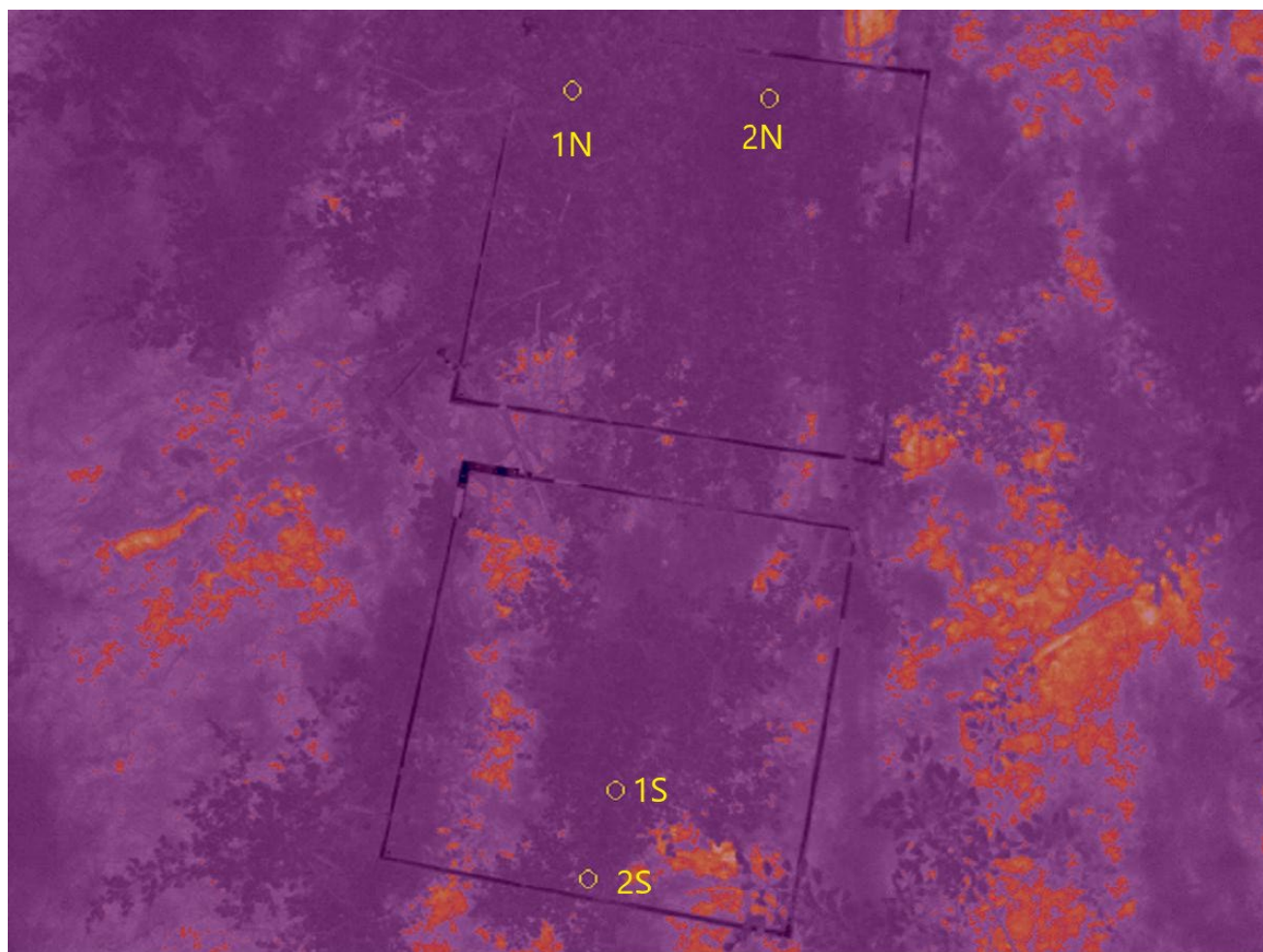


Figure 88. IR image of leaf temperature sampling locations during prescribed burn 16D5 in longleaf pine at Ft. Jackson, SC.

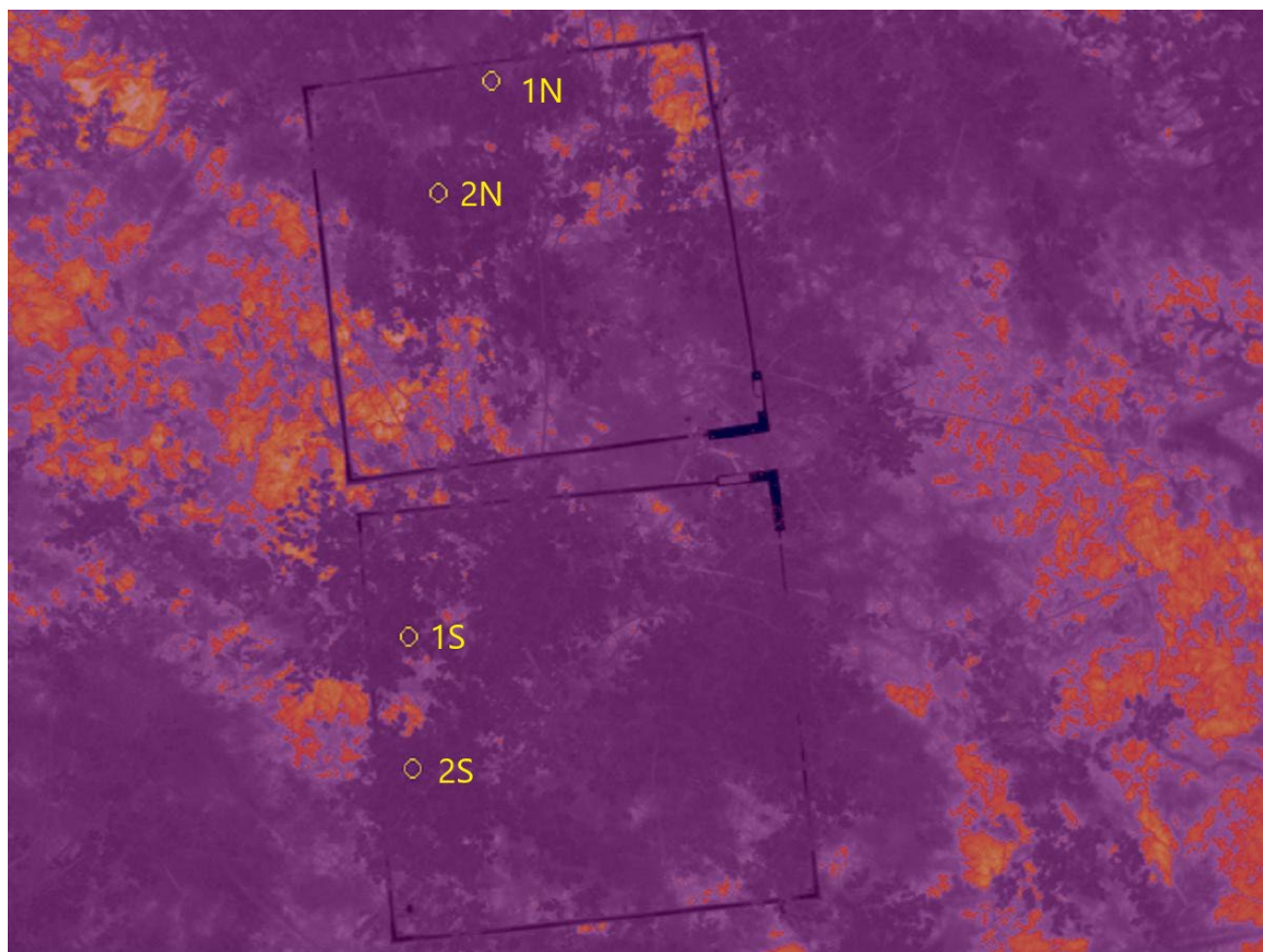


Figure 89. IR image of leaf temperature sampling locations during prescribed burn 16D6 in longleaf pine at Ft. Jackson, SC.



Figure 90. Example thermal image of plot 24A. The gas sampling wand is visible in the lower left.

The time series of the average leaf surface temperatures in the areas denoted in Figure 85 and Figure 86 are plotted in Figure 91. Only values that occurred prior to any leaf consumption are shown. Recall that these are radiometric temperatures [218] which assumed a high emissivity value (0.98) for fuels based on emissivity measurements of vegetation at ambient temperatures. The maximum temperatures observed in plots 24A and 24B approached 600 °C while the temperatures in plots 16D1, 16D5 and 16D6 were substantially lower. Maximum leaf temperatures in plots 24A and 24B are lower than the maximum leaf temperatures observed in the bench-scale tests (750 °C).

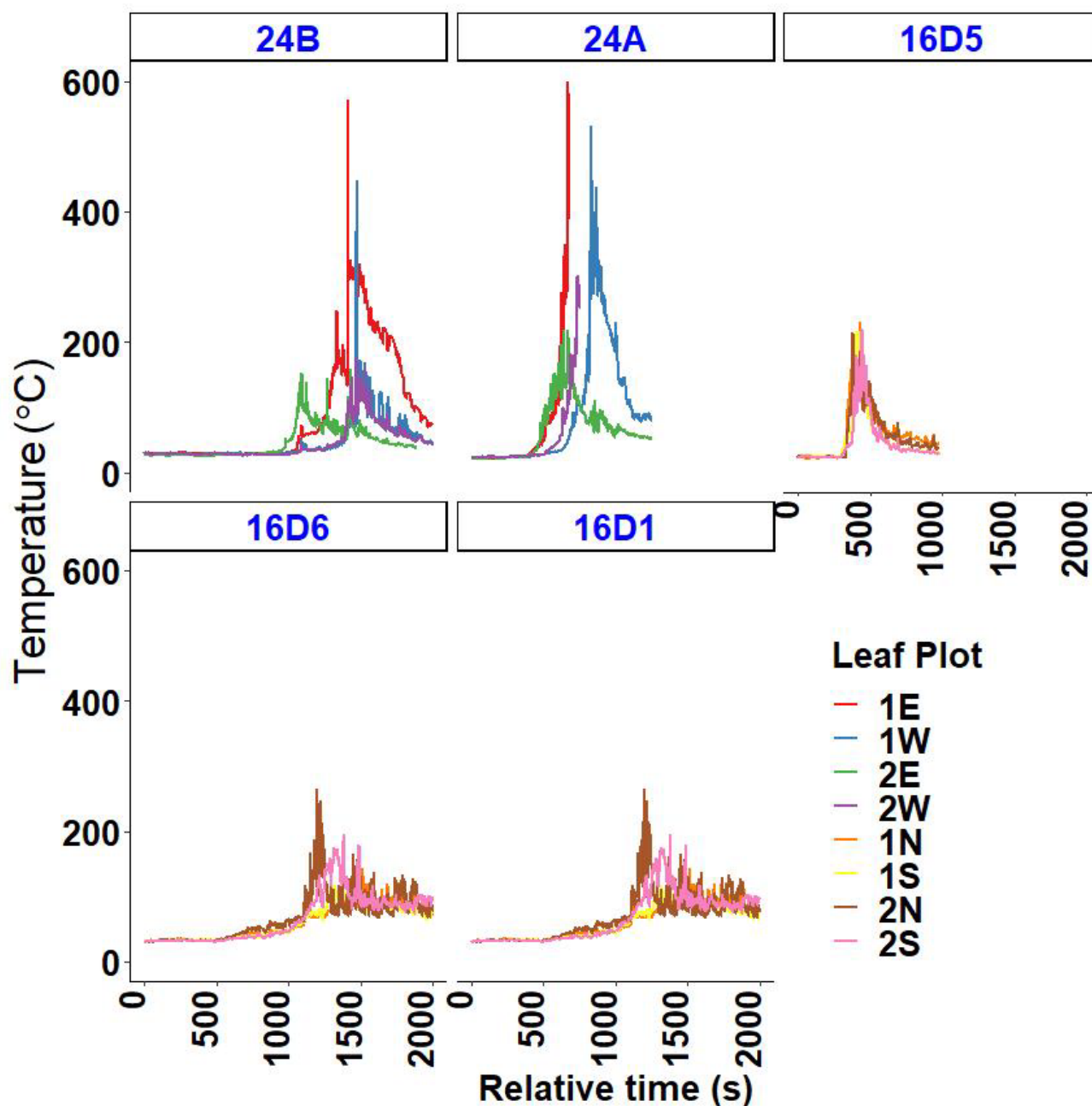


Figure 91. Shrub leaf temperatures estimated from IR images during experimental prescribed burns in longleaf pine at Ft. Jackson, SC.

4.4 Objective 3 – High-fidelity physics-based modeling

4.4.1 *Gpyro* & *FDS* bench-scale

The model was validated against experimental data [148] for horizontally oriented leaves. A comparison between the modeled and measured time evolutions of the fuel mass and the mass loss rate (MLR) showed a reasonably good match between the numerical results and the experimental data (Figure 92) [150]. The modeling effort provided more insight into the thermochemical evolution of the heated leaf and the role the fluid dynamics plays in this process.

Time evolution of the leaf mass, starting from the onset of heating was characterized in four consecutive time intervals for all considered FMC cases. In the initial interval, the fuel heated up

without losing much of mass. Duration of this interval was almost identical for all three modeled FMC cases. After the solid fuel temperature increased sufficiently, moisture started evaporating from the fuel and the second interval began. In this interval, the fuel mass decreased almost linearly versus time. This process commenced around the same time for all considered moisture contents. However, since the initial masses of all three modeled fuels were close, it took longer for a fuel with a larger FMC to complete the moisture evaporation process. The third interval started with a rapid decrease of mass and continued until the fuel mass versus time leveled off. In this interval, pyrolysis gases were released, ignition took place, a flame was formed and eventually extinguished. In the fourth interval, while the FFB continued heating the fuel, the mass and the temperature field of the fuel remained unchanged over time. It is noted that since no char oxidation was reported in the experiment, this process was not accounted for in the model.

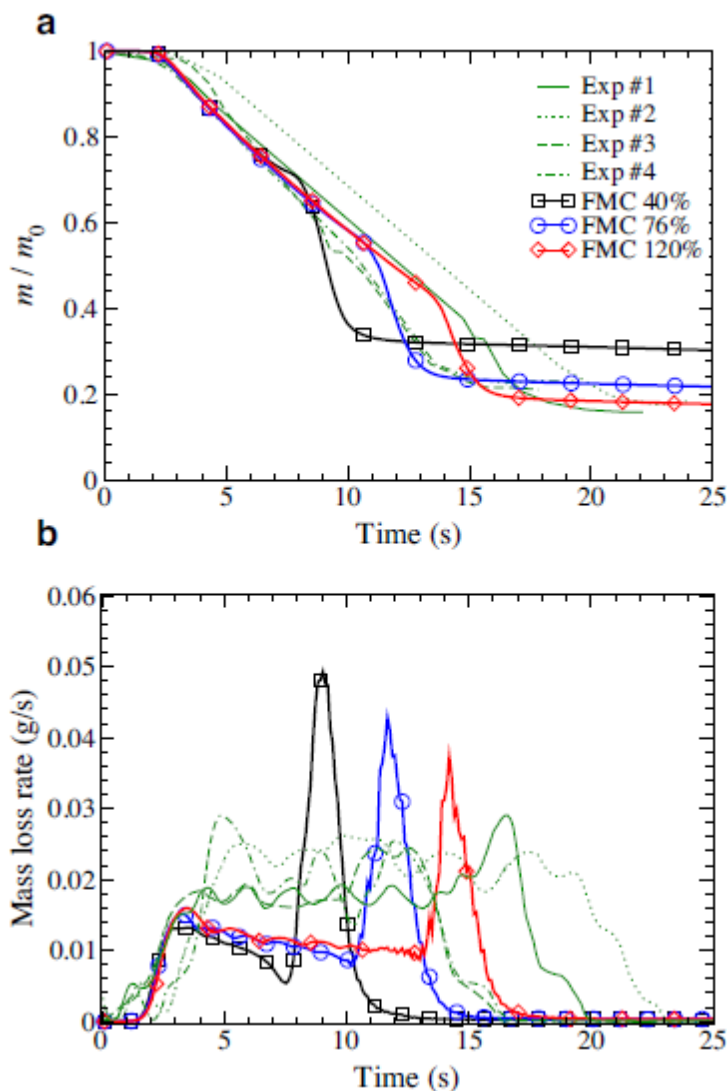


Figure 92. Time histories of (a) mass normalized by initial mass and (b) mass loss rate. Exp #1-4 are for experiments performed on four manzanita leaves with unspecified FMCs [148]. FMC 40%/76%/120% are the three FMCs modeled in the study.

The simulation results revealed a distinct role that the fluid dynamics played in moisture evaporation, pyrolysis, ignition, combustion and burnout behavior of leaves. The horizontally oriented leaf (with two longer dimensions of the leaf perpendicular to the flat flame burner exit flow) acted as a bluff

body in the upstream flow of hot gases exiting the FFB with a stagnation point formed on the upstream sided of the leaf and vortical structures formed in the opposite side (Figure 93). Simulations further revealed the distinct role that the flow vortices played in the nonuniform distribution of temperature around the fuel. This effect in turn resulted in a nonuniform release of moisture and pyrolysis gases from the leaf. Consequently, it affected the time and location of ignition and the overall burning behavior.

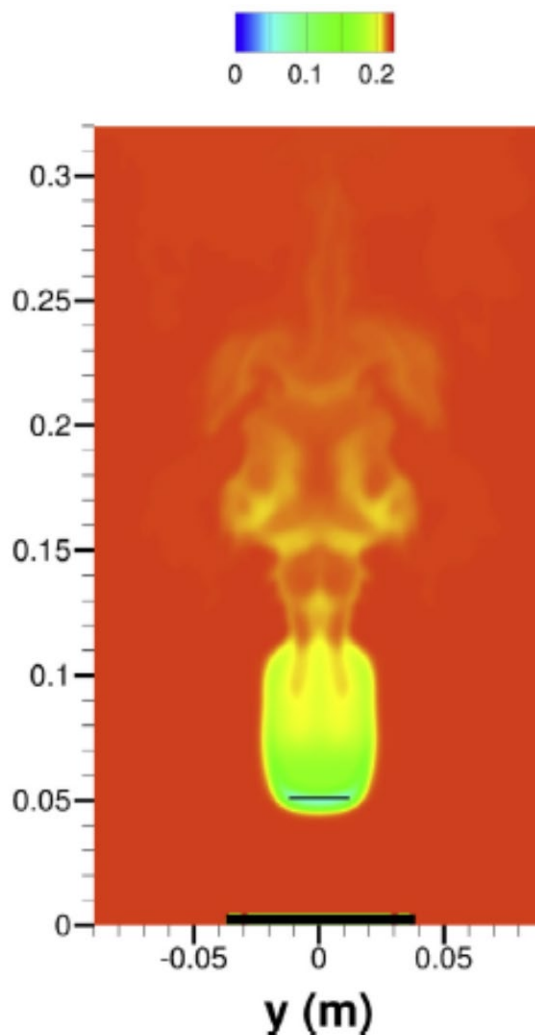


Figure 93. Color contours of oxygen mass fraction at $t=11.5$ s for a simulated horizontal manzanita leaf heated in a flat flame burner.

In the vertically oriented leaf simulations [153], the fuel condition was set identical to the horizontally oriented leaf simulations except for the orientation and FMC of the leaf. Four different treatments of dry dead (FMC 4%), rehydrated dead (26%), dehydrated live (34%) and fresh live (63%) which were previously studied in the FFB [219], were simulated. Until the time when the fuel lost nearly 50% of its initial mass, the model somewhat overpredicted the experimentally measured mass but after this time, the model somewhat underpredicted it for dead leaves (Figure 94). For live leaves, the model performed very well until the time when 25% and 50% of the initial mass were lost for the dehydrated and fresh leaves, respectively. Then, the model underpredicted measured mass with an increasing difference over time. The mass loss rate at the ignition time increased with FMC whereas the fuel temperature at the ignition time was not very sensitive to FMC. The ignition times obtained in simulations were found in very good agreement with the ones determined by empirical correlations for all FMCs. On the other hand, the predicted burnout times were shorter than the

empirically determined ones.

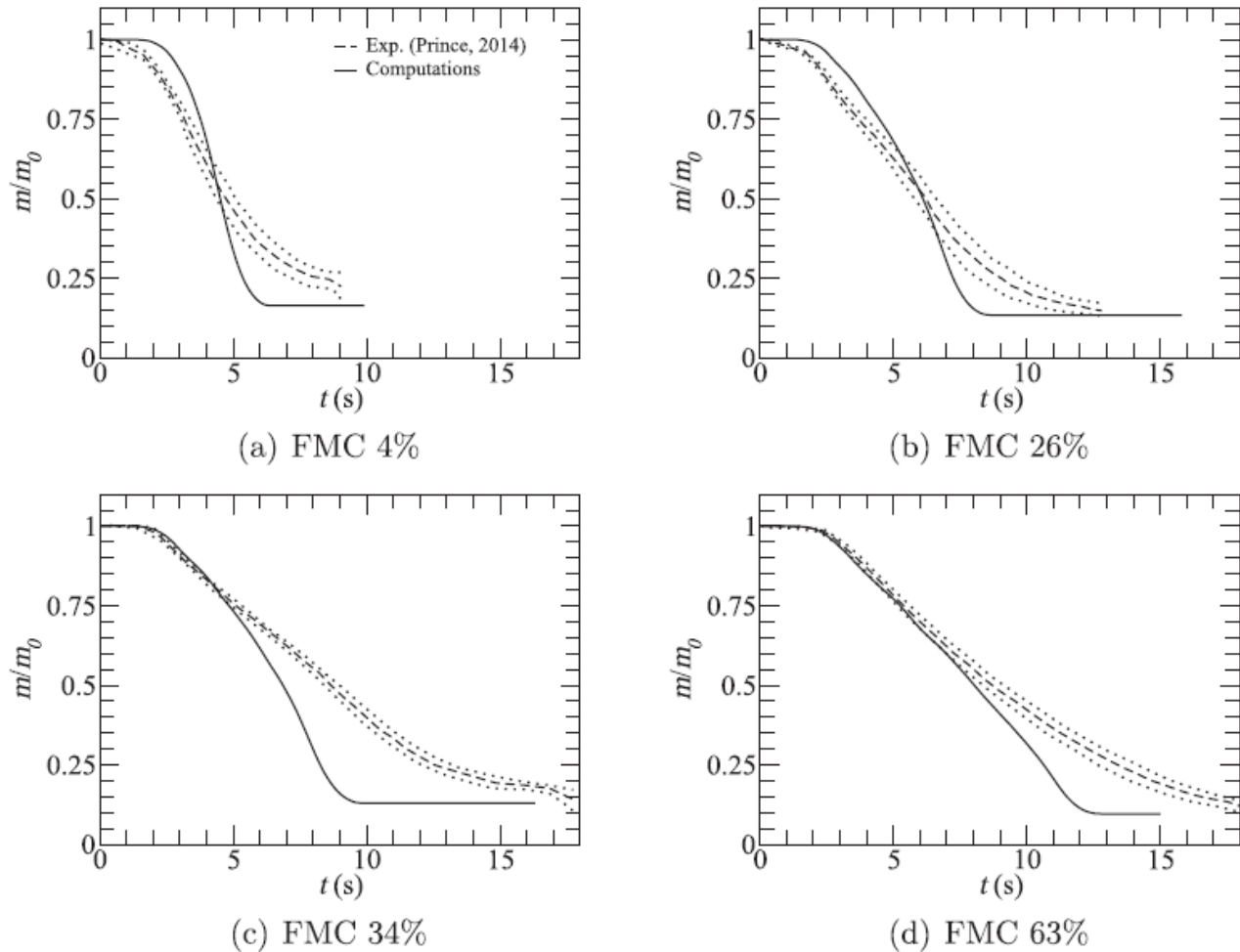


Figure 94. Time evolution of vertically oriented leaf normalized mass. Dotted lines indicate 95% confidence intervals for experimental data [219].

Simulations revealed that the flow near the leaf was characterized by two laminar boundary layers formed on the faces of the vertically oriented leaf. They played a critical role in heating, moisture evaporation and pyrolysis, as demonstrated by the simulations. There was a lack of any vortical structures near the flow, which made the flow characteristics here completely different from that in the horizontally oriented leaf. Recall that no boundary layers were formed on the faces of the horizontally oriented leaves. An evaporation front propagating inward from the edges was noted inside the leaf. After ignition, appreciable moisture remained in the leaf. Release of water vapor and pyrolysis gases because of the leaf moisture evaporation and pyrolysis, displaced oxygen in the leaf neighborhood and reduced the oxygen concentration therein. After ignition occurred, gas phase combustion further decreased oxygen concentration in the vicinity of the leaf. The flaming pattern was qualitatively in agreement with previously reported experimental observations.

From the study examining the effect of heating mode on vertically oriented leaves [154], Figure 95 shows the time evolution of the normalized fuel mass computed in the current study and the one in the previous experiments [46] for the convection-only and combined convection and radiation heating modes. Comparing the left and right panels reveals that the additional heat flux supplied by the radiant panel caused the leaf to lose mass faster in the combined mode. The time to reach 50% of the initial mass was determined as 7.3 s and 8.1 s for the experiments and the computations, respectively, in the convection-only mode. It is nearly identical and equal to 6.2 s for both

experiments and computations in the combined mode. Time (mean of 12 monthly measurements) for live manzanita leaves to reach 50% of the initial mass was reported as 8.8 s and 5.8 s for convection-only and combined modes, respectively [155]. The simulations slightly underpredicted the mass of the fuel remaining at the conclusion of the experiments (residual mass) (Figure 95). From Figure 95, it could be also understood that in light of the parametric values pertinent to the heating sources, the convective heating seemed to have more impact than the radiative heating on the pyrolysis and burning process of the leaf. It took about 9 s for the leaf to be completely pyrolyzed when the combined mode was applied. As a result, at the end of ~ 9 s of the combined heating, the leaf lost $\sim 90\%$ of its initial mass. When the heating mode was convection-only, as in Figure 95a, the leaf loses $\sim 60\%$ of its initial mass after 9 s. The ignition times were calculated ~ 3.4 s and ~ 3.0 s in the convection heating and the combined heating, respectively. Unlike these modes, the radiation-only heating mode did not result in ignition in the simulations, which is the confirmation of no ignition reported in the experiments for this mode. The mass versus time was not reported in the previous experiments for this mode. In the simulation, it smoothly dropped by around 30% by the end 15s in the radiation only heating mode. For brevity, the mass was not plotted versus time for this mode.

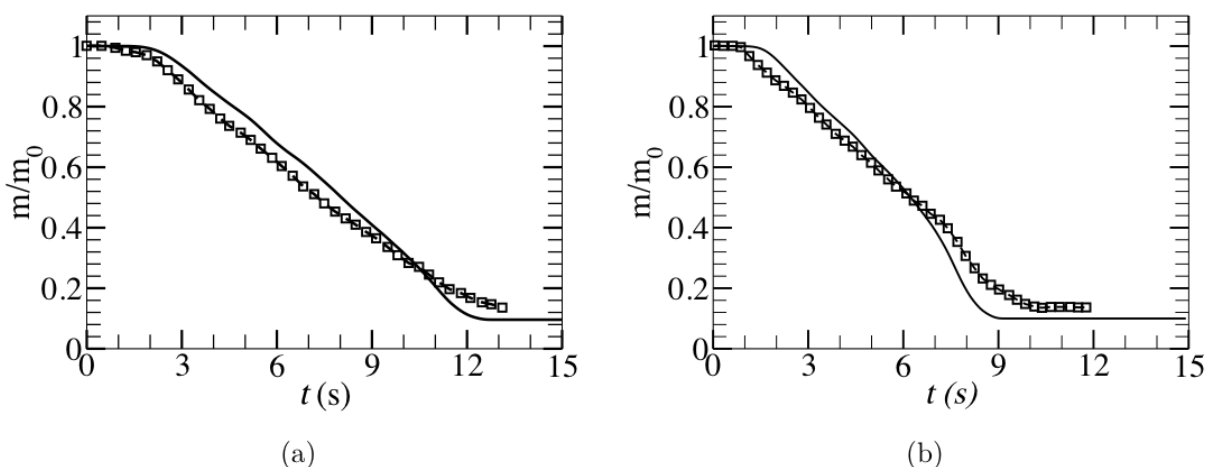


Figure 95. Time evolution of the leaf mass normalized by the leaf initial mass for (a) convection-only and (b) combined convection and radiation heating modes in the previous experiments [46] (symbolized dashed line) and the current computations (solid line).

Figure 96 shows gas temperature, gas vertical velocity, and oxygen volume fraction versus y in the line passing the middle of the leaf (where $z = 0.045$ m and $x = 0$ m planes intersect) in the gas (FDS) domain for the combined heating mode. The spatial distributions of gas temperature, gas vertical velocity and oxygen volume fraction exhibit an asymmetry as the variables in the left and right sides of the leaf are compared. The reason for this asymmetric behavior is that the left face of the leaf is opposite to the radiant panel. Hence, the left face heats up faster than the right face and the physical and thermochemical processes lag on the right side of the leaf. For instance, referring to Figure 96(a), the gas temperature peak on the left side is $\sim 1150^{\circ}\text{C}$ which is about 75°C higher than that on the right side and indicates that the combustion reaction rate is higher on the left side. As a result, oxygen is consumed faster an overall lower amount in the left side as can be seen in Figure 96c. Moreover, as shown in Figure 96b, the peak of the vertical velocity which occurs in the reaction zone, is higher on the left side of the leaf mostly because the peak temperature is higher therein compared to that on the right side. In the convection-only mode (not shown in the figure), the variables plotted in Figure 96 showed quite a symmetric distribution.

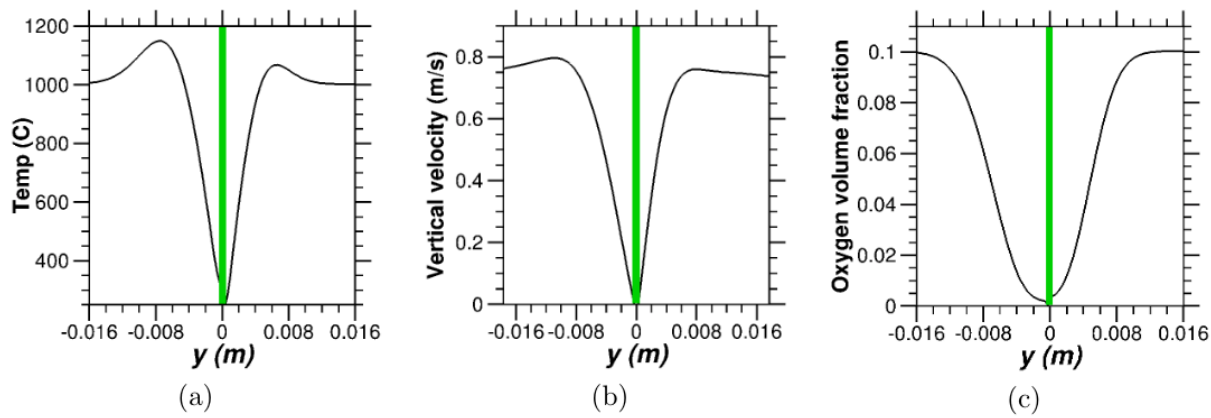


Figure 96. (a) Temperature; (b) vertical (z-component) velocity; and (c) oxygen volume fraction versus y at $x=0$ m and $z=0.045$ m in the gas domain surrounding the leaf at $t = 6$ s for the combined heating modes of convection and radiation. The thick line in the middle indicates the horizontal position of the leaf.

In the fuel moisture evaporation study which permitted the solid fuel to shrink, evaporation generally preceded and significantly influenced the pyrolysis and burning processes and the fuel [220]. Hence, an accurate representation of the moisture evaporation is critical in the physical modeling of fires, especially when live fuels, which are characterized by high FMC, are involved.

With the equilibrium model, a steep evaporation front where evaporation rate, moisture mass fraction and temperature profiles were found to exhibit abrupt changes. On the other hand, profiles obtained using the Arrhenius model were found to be smooth throughout the slab. This behavior was mainly attributed to the evaporation rate equation of the Arrhenius model. It was noted that the drying dynamics described by the equilibrium model was more consistent with the physics of evaporation. The equilibrium model showed a distinct evaporation front, and more accurately captured the effect of FMC on the drying dynamics. The impact of the evaporation model on the amount of fuel shrinkage was not appreciable for low fuel FMC but it was significant for high FMC.

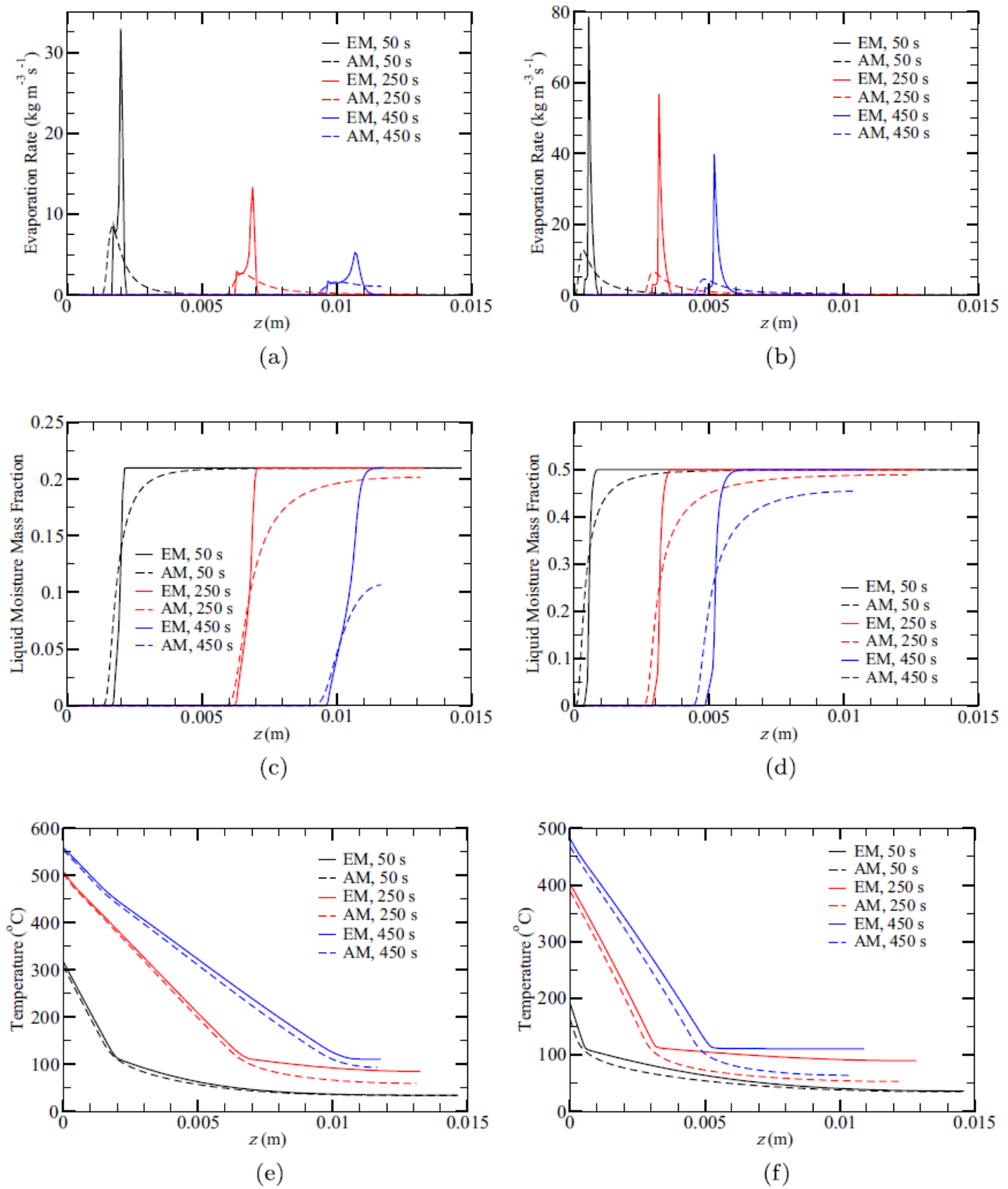


Figure 97. Profiles of evaporation (a,b), liquid moisture mass fraction (c,d) and temperature (e,f) for an external radiant flux of 40 kW m^{-2} . FMC = 26 and 100 %, left and right, respectively. EM is equilibrium model and AM is Arrhenius model.

4.4.2 FDS wind tunnel scale

For the single step reaction scheme for a no wind fire, the simulation resulted in a maximum

temperature greater than 900 °C with a flame height of roughly 0.5 m (Figure 98). Maximum simulated vertical velocity exceeded 3 m s^{-1} .

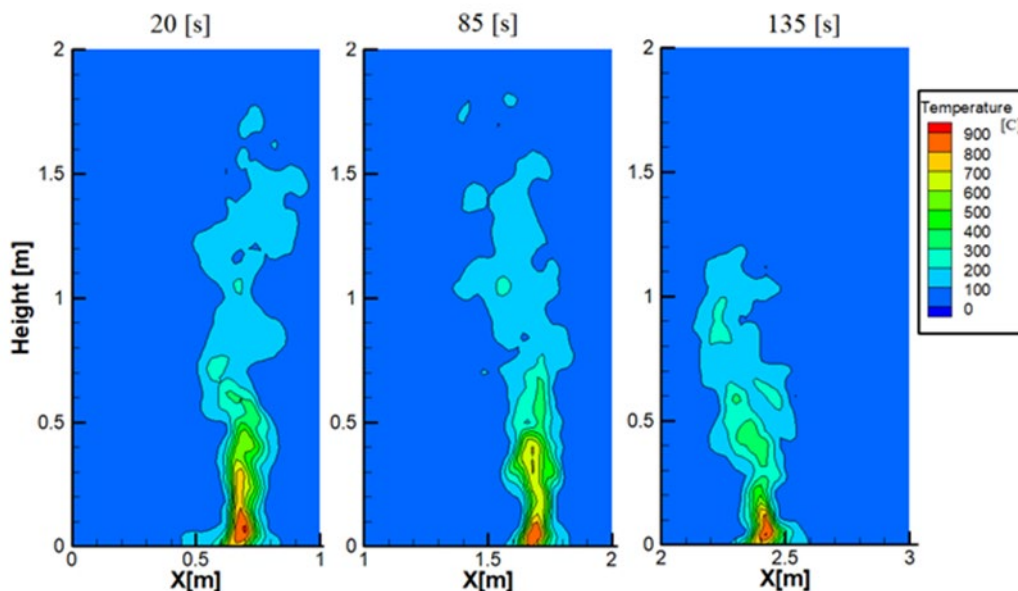


Figure 98. Contour plot of temperature at different time steps estimated using a single step pyrolysis scheme in a longleaf pine fuel bed under no wind conditions.

The comparison of observed fuel temperature with the single-step and multi-step simulations yielded several results (Figure 99). The temperature was reported for a point at the fuel bed surface at the center line. The temperature rise and drop indicate the leading and trailing edges of the flame, respectively. In all three wind conditions, there was a rapid rise in temperature; as wind speed increased; the flame depth increased as indicated by the increased breadth of the temperature curve. The temperature profiles for the single-step simulations were similar to the experimental results for the no wind and low wind (0.44 m s^{-1}) conditions. The model overpredicted maximum temperature for high wind (1 m s^{-1}). The larger width of the peak for the single reaction compared to the experiment indicates that the simulated flame width of the simulation was larger than the experiment.

In the case of single step reaction modeling, the peak temperatures for no wind, 0.44 m/s and 1.0 m/s wind speeds are approximately $760 \text{ }^{\circ}\text{C}$, $680 \text{ }^{\circ}\text{C}$ and $740 \text{ }^{\circ}\text{C}$, respectively. Also, the relative temperature error between model prediction and experimental data were 17.6%, 16.6% and 45% for no wind, 0.44 m/s and 1.0 m/s wind speeds conditions, respectively. The multi-step reaction modeling improved the maximum temperature prediction compared to single-step reaction. The width of the peak curve is more similar to the experimental measurements. The peak temperature for no wind, 0.44 m/s and 1.0 m/s cases are $665 \text{ }^{\circ}\text{C}$, $552 \text{ }^{\circ}\text{C}$ and $658 \text{ }^{\circ}\text{C}$, respectively. The relative temperature error between model prediction and experimental data are 2.8%, 4.8% and 29%. Compared to the single step model, the results of multi-step model indicated that the multi-step reaction model is more capable of predicting the temperature profile. However, the multi-step reaction model was incapable to predict the temperature profile for the 1 m s^{-1} wind velocity.

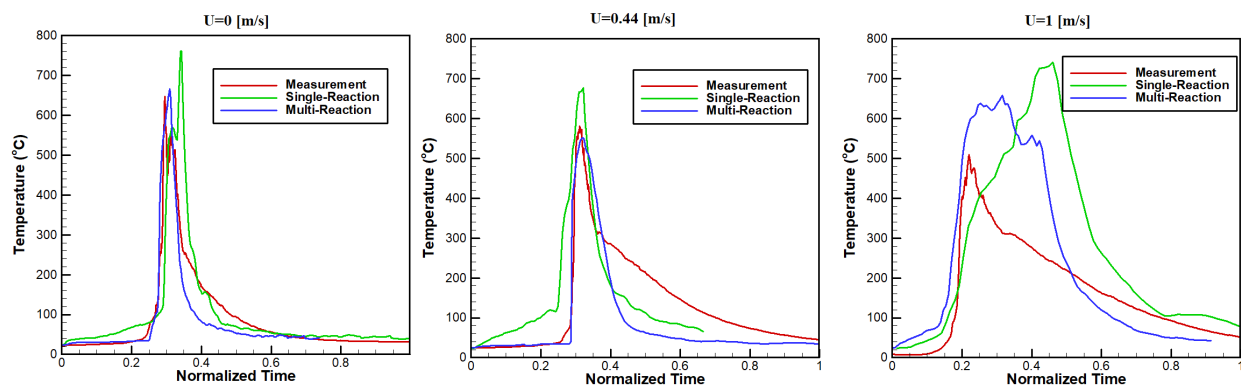


Figure 99. Comparison of measured fuel bed surface temperature with simulations using single step and multi-step pyrolysis schemes for longleaf pine needle fuel beds burned under 3 wind velocities (none, 0.44 m s^{-1} , 1 m s^{-1}) in a wind tunnel.

Figure 100 shows the contour of temperature at a vertical plane in the middle of the wind tunnel for different wind conditions and different modeling schemes. According to the contours, an increase in the wind speed made the flame larger and reduced the angle between flame plume and unburned fuel as is well-established [e.g. 221]. Comparing the results of single-step reaction and multi-step reaction showed that the size of flame was bigger for the single-step reaction modeling (Figure 100). From this result we can conclude that fire spread rate and maximum flame temperature were higher for the single-step reaction.

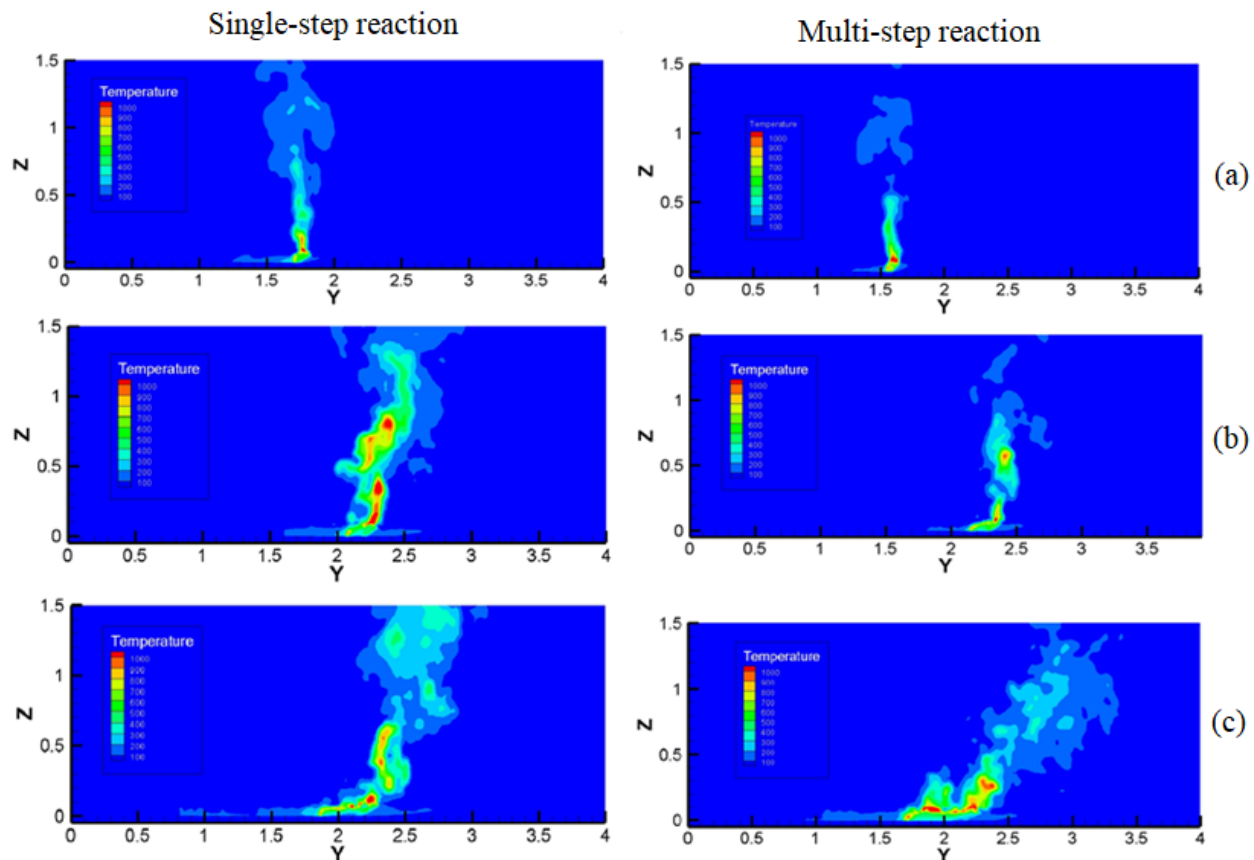


Figure 100. Temperature contours in a vertical plane in the wind tunnel centerline for single and multistep pyrolysis schemes for 3 wind velocities: (a) 0 m s^{-1} , (b) 0.44 m s^{-1} , (c) 1 m s^{-1} .

While every attempt was made in the experiments to produce a linear flame front, curvature of the flame front inevitably occurred as the fire progressed in the wind tunnel. Both reaction schemes and the flow dynamics simulated in the wind tunnel by FDS resulted in curvature of the flame front (not shown) that was similar to the no and low wind speed conditions. The high wind speed simulation did not match the observed flame front shape. The simulated flame depth (width) was relatively constant along the flame front (Figure 101). The flame width for single-step reaction is larger compared to the multi-step reaction. For the single-step reaction the flame width varied around 0.15 m, while the flame width for the multi-step reaction varied around 0.1 m. These data could be potentially compared to measurements taken with the IR camera after extracting the data from the videos.

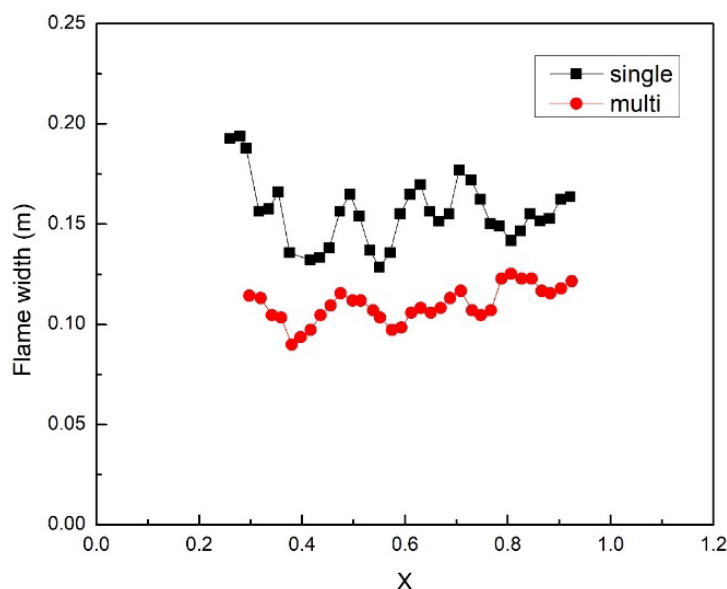


Figure 101. Simulated flame zone width (depth) along the fire front for single and multi-step pyrolysis schemes.

The simulated pine needle mass loss differed between the single step and multi-step reaction schemes at different wind speeds (Figure 102). Mass loss rate increased with wind speed. The constant mass loss rate for the no wind condition indicated that the combustion process was stable. As wind speed increased, the mass loss rate fluctuated suggesting that the flame changed. For the multi-step scheme, the burning time was 550 s, 295 s and 130 s for wind speeds of 0, 0.44 and 1.0 m s⁻¹, respectively. Residual mass differed between the reaction schemes under no wind conditions; the single-step scheme resulted in less fuel consumption (Figure 102) indicating incomplete combustion.

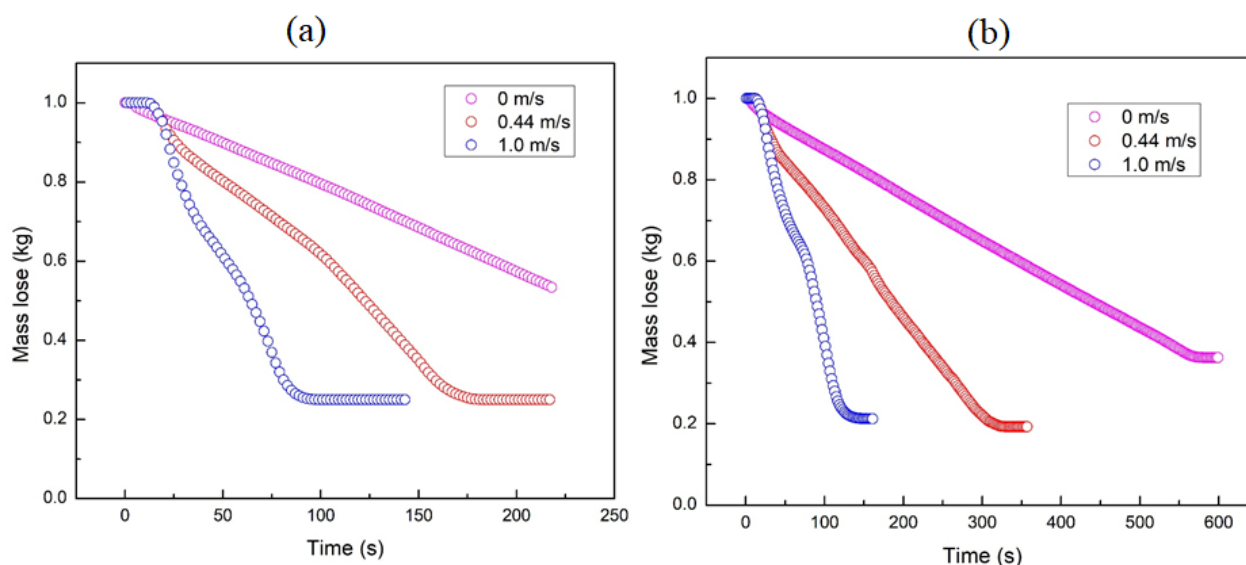


Figure 102. The mass loss with time for different wind speeds a): single-step reaction. b): multi-step reaction.

Table 34 compares the experimental fire spread rate with simulated spread rate for the single step and multi-step schemes. Simulated spread rates were calculated based on the fuel mass loss rate and the flame front location. For the single step scheme, the predicted fire spread rate was much faster compared to the experiment since some endothermic reactions were neglected. The difference between observed and simulated rate of spread was much smaller for the multi-step scheme.

Table 34. Experimental and simulated rate of spread in longleaf pine needle fuel beds burned in a low speed wind tunnel.

Wind velocity (m s ⁻¹)	Rate of spread (m s ⁻¹)		
	Experimental	Single step	Multi-step
0	0.0058	0.0086 (+48.9%)	0.0051 (-12.1%)
0.44	0.0104	0.0167 (+60.7%)	0.0095 (-8.4%)
1.0	0.0208	0.0351(+68.7%)	0.0213 (2.4%)

4.4.3 Specific heat and Vegetation module

Results with the 12 leaf species show a linear variation of heat capacity of dried leaf with temperature up to around 200°C with apparent and reversing heat capacities in agreement within error limits of triplicate testing, and including the correlation with the 12 components individual heat capacities (Figure 103). For temperatures from around 200°C to 440°C the reversing specific heat capacity, as corrected for sample mass loss, could be modeled as constant (within error bounds), whereas the positive difference between reversing heat capacity and apparent heat capacity suggests the exothermic heat of charring for multiple components of the fresh leaf [paper being prepared]. This behavior of the heat capacity and the heat of pyrolysis during leaf degradation is in stark contrast to that of current pyrolysis modeling, including that in the vegetation module of FDS and GPYRO.

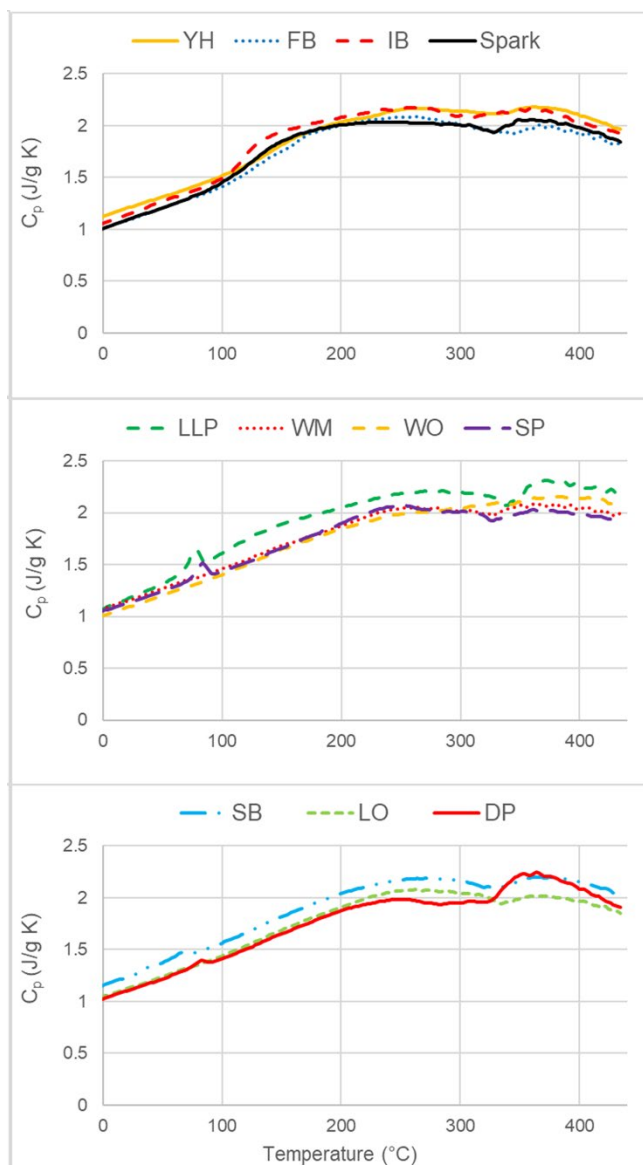


Figure 103. Specific heat capacity measured in a DSC for foliage from 11 species of plants native to the southeastern U.S. [163]

Complementing the work on measuring tars and gases in a flat flame burner/radiant panel environment, we measured tars, soot, and gases along with mass loss rate and heat release rate and their estimation during smoldering/pyrolysis tests and during piloted ignition tests under irradiance of 35 kWm^{-2} in the iCone calorimeter, and reported specifically for the longleaf pine needles [188]. Several leaves (around 50 for needles) were laid as a single layer between two wire screens to take advantage of a uniform radiant heat flux on a circular area of 132 cm^2 (Figure 3). Thermocouples were placed on the shaded and exposed side of the leaves held in place by coarse thin wire screens. Replication of leaf pyrolysis/smoldering experiments was done to provide tars onto filters and into bottles of solvent for GC2xTOFMS characterization. To date, the GC2xTOFMS analysis for *Lyonia lucida* isolated nearly 2000 compounds, many of which have yet to be identified; a publication with the results for a majority of the plant species has been recently published [222,223]. Results from the iCone calorimeter confirm that for longleaf pine litter, fuel gases were only a small mass fraction of the combusting fuel (Figure 104).

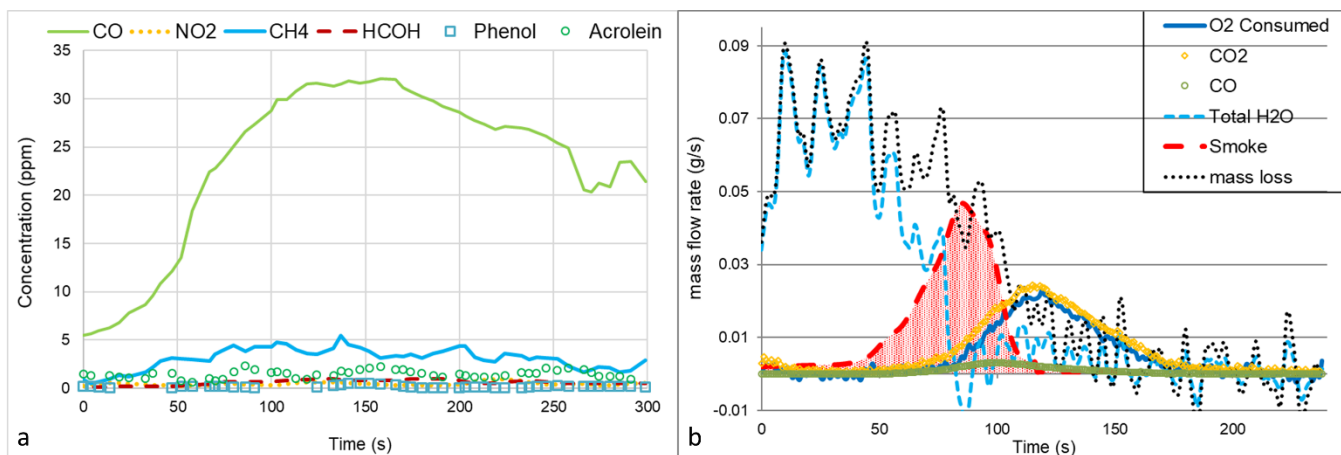


Figure 104. Pyrolysis emissions: a) trace gases b) major mass flows derived.

It is seen that the CH₄ molar concentration averaged to 14% of CO concentration in Figure 104a. CO in turn has mass concentration that is around 1% that of the fuel mass loss at the beginning of smoldering (mostly char oxidation) and pyrolysis at around 200°C, moving up to around 10% of the fuel mass loss as the white smoke ends and glowing peaks, for temperatures of 400°C to 600°C, which is optimum for maximizing tar production. This simplifies determination of tar mass (white smoke that is escaping combustion) evolved as fraction of fuel mass loss as a function of time as follows. From the rates of O₂ consumption, production rates of CO₂, CO, and black smoke, and sample mass loss rate, it was determined the char fuel composition during the complete glow combustion is that of lignin/phenol [64]. With thermocouple showing temperatures around 100°C up to 50 s test time, the weight loss data is the initial mass loss primarily that of the absorbed moisture (180% dry basis), as shown in Figure 104b. Specific extinction area of smoke was calibrated to compute the remainder fuel mass, which is tar mass rate as function of time, as shaded pink in Figure 1b (shaded area is 71% of leaf dry mass). The tar global elemental composition was derived as a difference between the live leaf composition (from Ultimate Analysis [64]) and the derived glowing char composition, assuming hydrocarbon fuel gases are negligible.

Mass loss rates for water, tar, and char oxidation (Figure 104b) were predicted well using pyrolysis kinetics derived with TGA measurements in nitrogen and air and using the exposed and shaded temperatures measured with time from the cone calorimeter test [Paper being prepared]. The data from the exposed and shaded temperatures was used in the inverse heat conduction approximation method to estimate the transport properties of surface emissivity, convective heat transfer coefficient, and thermal conductivity as function of leaf composition, moisture, temperature, and degradation of leaf components [Paper being prepared]. All of the leaf thermal and mass properties and pyrolysis kinetics for moisture, tar, and char oxidation were derived independently of the pyrolysis models in GPYRO and FDS, as the intent is to replace the vegetation module in the FDS with a more general pyrolysis model [164]. A spark plug ignition with a piloted ignition criteria of 24 kWm⁻² converted the white smoke (tars) into combustion products of CO₂, CO, H₂O, and soot that were measured in the early phase of the project with standard cone calorimeter testing [188].

Fundamental pyrolysis thermal and kinetics properties for live vegetation that are essential to CFD modeling of pyrolysis and flammability were obtained from a series of small-scale tests for live and dead vegetation. The complexity of live leaf composition was recently documented allowing analysis of 12 crude compounds. Model simplification required a practical grouping into contents of (0) moisture, (1) lipids, (2) digestives (glucose, fructose, and protein), (3) hemicellulose (xylan and pectin), (4) glucan (cellulose and starch), (5) phenolic (lignin and tannins), and (6) inert (silicate and mineral), along with the use of higher reaction orders to accommodate the wide pyrolysis peaks, and of biproduction of volatiles (tar/gas) and char from each pyrolysis group. Extensive TGA tests in

nitrogen and air were used to derive oxidative pyrolysis kinetics of the celluloses and of the char, which is also suitable for smolder modeling. Moisture desorption was based on phase change kinetics coupled with the moisture isotherm relationship and heat of desorption for bound water to add generality over that of the common first-order Arrhenius kinetics relationship. Extensive DSC tests in nitrogen flow provided leaf heat capacity and estimates of the exothermic heat of pyrolysis (primarily charring) reactions over a range of temperatures. The heat of combustion remains established as a correlation based on the oxygen consumption principle whether as a volatile or a char. Finally, the transport properties of leaf surface emissivity and convective heat transfer coefficient, in conjunction with a semi-theoretical expression for the leaf thermal conductivity varying with composition, temperature, moisture content, and material degradation was obtained via an inverse heat conduction approximation method with a specialized vegetation test using leaf surface thermocouples in the cone calorimeter. This paper provides the summary of such formulations and properties that could replace or supplement existing formulations in the vegetation module in the CFD modeling of wildland fires, e.g., Fire Dynamics Simulator (FDS).

Results of the testing of the remaining hypotheses follow.

H₁₀: Inclusion of an advanced pyrolysis mechanism for live and dead wildland fuels does not improve fire behavior predictions by the high-fidelity physics-based models.

H₁₁: Improving the evaporation mechanism for moisture content in wildland fuels does not improve fire behavior predictions by the high-fidelity physics-based models.

Inclusion of an improved pyrolysis mechanism and an improved evaporation mechanism improved the modeling of pyrolysis and combustion when compared with data from previous experiments.

H₁₂: Simulation of pyrolysis and ignition of wildland fuels is not improved with 3D fuels characterization and can be just as effectively simulated in 2D.

It was not possible to test this hypothesis since the focus of the high-fidelity modeling was on well-described experiments involving single fuel particles. A framework to improve the modeling of physical vegetation characteristics based on the detailed compositional analysis was developed. Analysis to correlate fuel consumption derived from 3D measurements with observed pyrolysis gas composition is underway.

5 Conclusions and Implications for Future Research/Implementation

This study has shown that the composition and relative amount of pyrolysates differed between common plant species native to the southern United States. While the permanent gases (CO, CO₂, H₂ and CH₄) were common to all species, some trace gases, notably phenol, was present at relatively higher levels in some species. The relative amount of H₂ in the pyrolysate composition was shown to be greater than CH₄. The impact of these relative differences on fire spread model output is currently unknown so it is not possible to determine if a common pyrolysis scheme can be used. While it has been known for some time that the composition of pyrolysates is affected by heating rate which has typically been done in a fashion to eliminate heat transfer affects, this work has shown that both heating rate and heating mode affect the composition of pyrolysates in intact fuels, particularly in terms of tar composition. These differences have potential implications for fire spread modeling; however, most physically based fire models do not currently model secondary pyrolysis due to its complex nature and unknown chemical pathways. Additionally, differences in tar composition have important implications since the tars condense and form particulate matter.

While water is a major component that is released as vegetation is heated and is also a combustion product, its relative amount has not typically been described in analytical methods used to describe

pyrolysate composition. In this study, using FTIR spectroscopy, the amount of H₂O present in pyrolysate composition has been described under actual fire conditions. It is potentially a significant component and prior modeling described conditions under which an idealized flame could fail to form due to high water content. Analysis of the composition of pyrolysates from the FTIR measurements is underway and should allow us to determine if H₂O affected the relative amounts of other pyrolysates. Our modeling of pyrolysis using Gpyro improved the modeling of evaporation and the presence of H₂O. The implication of the improved modeling in models such as FDS has not been explored. As indicated in the original proposal, future modeling work is necessary to determine if the knowledge gained and improvements made in modeling pyrolysis improve our ability to model fire behavior in support of prescribed fire operations.

Comparison of the pyrolysate composition between wind tunnel and field fires based on GCMS canister samples showed that the composition was affected by this factor. Future statistical analyses of the canister samples analyzed by GCMS and composition determined by FTIR while including additional variables such as heat fluxes and fuel loading are planned outside of this project. The results from these analyses will allow us to determine applicability of lab results to the field.

6 Literature Cited

- [1] S. Cohen, J. Hall, J.K. Hiers, Fire Science Strategy, Strategic Environmental Research and Development Program, Resource Conservation and Climate Change Program Area, Washington, D.C., 2014. <https://serdp-estcp.org/content/download/30210/291748/file/Fire%20Science%20Strategy.pdf>.
- [2] R.C. Rothermel, A mathematical model for predicting fire spread in wildland fuels, USDA Forest Service, Intermountain Forest and Range Experiment Station, Ogden, UT, 1972. http://www.fs.fed.us/rm/pubs_int/int_rp115.pdf.
- [3] W.L. Fons, Analysis of fire spread in light forest fuels, *Journal of Agricultural Research*. 72 (1946) 92–121.
- [4] F.A. Albini, A physical model for firespread in brush, *Symposium (International) on Combustion*. 11 (1967) 553–560. [https://doi.org/10.1016/S0082-0784\(67\)80180-2](https://doi.org/10.1016/S0082-0784(67)80180-2).
- [5] P.J. Pagni, T.G. Peterson, Flame spread through porous fuels, *Symp. (Int.) Combust.* 14 (1973) 1099–1107. [https://doi.org/10.1016/S0082-0784\(73\)80099-2](https://doi.org/10.1016/S0082-0784(73)80099-2).
- [6] W.A. Hough, F.A. Albini, Predicting fire behavior in palmetto-gallberry fuel complexes, USDA Forest Service, Southeastern Forest Experiment Station, Asheville, NC, 1978. http://www.srs.fs.fed.us/pubs/rp/rp_se174.pdf.
- [7] R.E. Martin, J.D. Dell, Planning for prescribed burning in the inland northwest, USDA Forest Service Pacific Northwest Forest and Range Experiment Station, Portland, OR, 1978. <http://www.treesearch.fs.fed.us/pubs/25146>.
- [8] B.M. Kilgore, The ecological role of fire in Sierran conifer forests, *Quaternary Research*. 3 (1973) 496–513. [https://doi.org/10.1016/0033-5894\(73\)90010-0](https://doi.org/10.1016/0033-5894(73)90010-0).
- [9] T.A. Waldrop, S.L. Goodrick, Introduction to prescribed fires in southern ecosystems, USDA Forest Service, Southern Research Station, Asheville, NC, 2012. <http://www.treesearch.fs.fed.us/pubs/41316>.
- [10] H.E. Mobley, ed., Southern forestry smoke management guidebook, USDA Forest Service, Southeastern Forest Experiment Station, Asheville, NC, 1976. <http://www.treesearch.fs.fed.us/pubs/683>.
- [11] G.M. Byram, Combustion of forest fuels, in: K.P. Davis (Ed.), *Forest Fire: Control and Use*, 1st ed., McGraw-Hill, New York, 1959: pp. 61–89.
- [12] R.M. Nelson Jr., C.W. Adkins, Flame characteristics of wind-driven surface fires, *Canadian Journal of Forest Research*. 16 (1986) 1293–1300. <https://doi.org/10.1139/x86-229>.
- [13] R.M. Nelson Jr., C.W. Adkins, A dimensionless correlation for the spread of wind-driven fires, *Canadian Journal of Forest Research*. 18 (1988) 391–397. <https://doi.org/10.1139/x88-058>.
- [14] R.M. Nelson Jr., B.W. Butler, D.R. Weise, Entrainment regimes and flame characteristics of wildland fires, *International Journal of Wildland Fire*. 21 (2012) 127–140. <https://doi.org/10.1071/WF10034>.
- [15] W.A. Hough, Caloric value of some forest fuels of the southern United States, USDA Forest Service, Southeastern Forest Experiment Station, Asheville, NC, 1969. <http://www.treesearch.fs.fed.us/pubs/2778>.
- [16] A. Behm, M.L. Duryea, A.J. Long, W.C. Zipperer, Flammability of native understory species in pine flatwood and hardwood hammock ecosystems and implications for the wildland–urban interface, *International Journal of Wildland Fire*. 13 (2004) 355–365. <https://doi.org/10.1071/WF03075>.
- [17] R.A. Susott, Characterization of the thermal properties of forest fuels by combustible gas analysis, *For. Sci.* 28 (1982) 404–420.
- [18] R.E. Burgan, R.A. Susott, Influence of sample processing techniques and seasonal variation on quantities of volatile compounds of gallberry, saw-palmetto and wax myrtle, *International*

- Journal of Wildland Fire. 1 (1991) 57–62. <https://doi.org/10.1071/WF9910057>.
- [19] J.M. Rogers, R.A. Susott, R.G. Kelsey, Chemical composition of forest fuels affecting their thermal behavior, *Can. J. For. Res.* 16 (1986) 721–726. <https://doi.org/10.1139/x86-129>.
 - [20] F. Shafizadeh, P.P.S. Chin, W.F. DeGroot, Effective heat content of green forest fuels, *Forest Science*. 23 (1977) 81–89.
 - [21] L. Buessing, J.L. Goldfarb, Energy along Interstate I-95: Pyrolysis kinetics of Floridian cabbage palm (*Sabal palmetto*), *Journal of Analytical and Applied Pyrolysis*. 96 (2012) 78–85. <https://doi.org/10.1016/j.jaap.2012.03.008>.
 - [22] M.A. Melvin, 2012 National Prescribed Fire Use Survey Report, Coalition of Prescribed Fire Councils, Inc., 2012. http://www.stateforesters.org/sites/default/files/publication-documents/2012_National_Prescribed_Fire_Survey.pdf.
 - [23] E. Marino, M. Guijarro, J. Madrigal, C. Hernando, C. Diez, Assessing fire propagation empirical models in shrub fuel complexes using wind tunnel data, in: J. de las Heras, C.A. Brebbia, D. Viegas, V. Leone (Eds.), *Modelling, Monitoring and Management of Forest Fires*, WITPress, Wessex, UK, 2008: pp. 121–130. <https://doi.org/10.2495/FIVA080131>.
 - [24] E.A. Catchpole, W.R. Catchpole, R.C. Rothermel, Fire behavior experiments in mixed fuel complexes, *Int. J. Wildland Fire*. 3 (1993) 45–57. <https://doi.org/10.1071/WF9930045>.
 - [25] D.V. Sandberg, C.L. Riccardi, M.D. Schaaf, Reformulation of Rothermel’s wildland fire behaviour model for heterogeneous fuelbeds, *Can. J. For. Res.* 37 (2007) 2438–2455. <https://doi.org/10.1139/X07-094>.
 - [26] D.E. Ward, Particulate matter emissions for fires in the palmetto-gallberry fuel type, *Forest Science*. 29 (1983) 761–770.
 - [27] J.C. Sparks, R.E. Masters, D.M. Engle, G.A. Bukenhofer, Season of burn influences fire behavior and fuel consumption in restored shortleaf pine-grassland communities, *Restoration Ecology*. 10 (2002) 714–722. <https://doi.org/10.1046/j.1526-100X.2002.01052.x>.
 - [28] G.M. Byram, H.B. Clements, M.E. Bishop, R.M.Jr. Nelson, Project Fire Model - an experimental study of model fires, USDA Forest Service, Southeastern Forest and Range Experiment Station, Asheville, NC, 1966. <http://www.treesearch.fs.fed.us/pubs/45219>.
 - [29] W.R. Anderson, E.A. Catchpole, B.W. Butler, Convective heat transfer in fire spread through fine fuel beds, *International Journal of Wildland Fire*. 19 (2010) 284–298. <https://doi.org/10.1071/WF09021>.
 - [30] P.A. Santoni, P. Bartoli, A. Simeoni, J.L. Torero, Bulk and particle properties of pine needle fuel beds – influence on combustion, *International Journal of Wildland Fire*. 23 (2014) 1076–1086. <https://doi.org/10.1071/WF13079>.
 - [31] D.R. Weise, G.S. Biging, Effects of wind velocity and slope on fire behavior, in: *Fire Safety Science - Proceedings of the 4th International Symposium*, International Association of Fire Safety Science, Ottawa, Canada, 1994: pp. 1041–1051. <https://doi.org/10.3801/IAFSS.FSS.4-1041>.
 - [32] D.R. Weise, X. Zhou, L. Sun, S. Mahalingam, Fire spread in chaparral—‘go or no-go?’, *Int. J. Wildland Fire*. 14 (2005) 99–106. <https://doi.org/10.1071/WF04049>.
 - [33] J.D. Cohen, M.A. Finney, An examination of fuel particle heating during fire spread, in: D.X. Viegas (Ed.), *Proceedings of the VI International Conference on Forest Fire Research*, University of Coimbra, Coimbra, Portugal, 2010: p. 13. <http://www.treesearch.fs.fed.us/pubs/39350>.
 - [34] D. Frankman, B.W. Webb, B.W. Butler, D.J. Latham, Fine fuel heating by radiant flux, *Combustion Science and Technology*. 182 (2010) 215–230. <https://doi.org/10.1080/00102200903341538>.
 - [35] J.R. Gallacher, Implementation of Measured Seasonal Variations of the Ignition Behavior of Live Fuels and a Fundamental 3-D Shrub Geometry Description Method in a Semi-Empirical

- Fire Spread Model, (2015).
- [36] X. Zhou, S. Mahalingam, D. Weise, Experimental study and large eddy simulation of effect of terrain slope on marginal burning in shrub fuel beds, *Proceedings of the Combustion Institute*. 31 (2007) 2547–2555. <https://doi.org/10.1016/j.proci.2006.07.222>.
 - [37] S.S. McAllister, M.A. Finney, Convection ignition of live forest fuels, in: *Draft Proceedings of the Eleventh International Symposium, International Association for Fire Safety Science*, 2014: pp. 1–14. <http://www.iafss.org/publications/fss/11/139/view>.
 - [38] D. Frankman, B.W. Webb, B.W. Butler, D. Jimenez, J.M. Forthofer, P. Sopko, K.S. Shannon, J.K. Hiers, R.D. Ottmar, Measurements of convective and radiative heating in wildland fires, *International Journal of Wildland Fire*. 22 (2013) 157–167. <https://doi.org/10.1071/WF11097>.
 - [39] R.D. Ottmar, C.B. Clements, B.W. Butler, M.B. Dickinson, B. Potter, J. O'Brien, Data set for fuels, fire behavior, smoke, and fire effects model development and evaluation—the RxCADRE Project, Joint Fire Science Program, 2014. http://www.firescience.gov/projects/11-2-1-11/project/11-2-1-11_final_report.pdf.
 - [40] M.E. Alexander, Perspective on experimental fires in canadian forestry research., *Mathl. Comput. Modelling*. Vol. 13. (1990) 17–26.
 - [41] J.K. Hiers, J.J. O'Brien, R.J. Mitchell, J.M. Grego, E.L. Loudermilk, The wildland fuel cell concept: an approach to characterize fine-scale variation in fuels and fire in frequently burned longleaf pine forests, *International Journal of Wildland Fire*. 18 (2009) 315. <https://doi.org/10.1071/WF08084>.
 - [42] B.J. Stocks, M.E. Alexander, B.M. Wotton, C.N. Stefner, M.D. Flannigan, S.W. Taylor, N. Lavoie, J.A. Mason, G.R. Hartley, M.E. Maffey, G.N. Dalrymple, T.W. Blake, M.G. Cruz, R.A. Lanoville, Crown fire behaviour in a northern jack pine - black spruce forest, *Canadian Journal of Forest Research*. 34 (2004) 1548–1560. <https://doi.org/10.1139/x04-054>.
 - [43] W.R. Catchpole, E.A. Catchpole, B.W. Butler, R.C. Rothermel, G.A. Morris, D.J. Latham, Rate of spread of free-burning fires in woody fuels in a wind tunnel, *Comb. Sci. Tech.* 131 (1998) 1–37. <https://doi.org/10.1080/00102209808935753>.
 - [44] D. Morvan, J.L. Dupuy, Modeling the propagation of a wildfire through a Mediterranean shrub using a multiphase formulation, *Combustion and Flame*. 138 (2004) 199–210. <https://doi.org/10.1016/j.combustflame.2004.05.001>.
 - [45] K. McGrattan, S. Hostikka, J. Floyd, H. Baum, R. Rehm, W. Mell, R. McDermott, *Fire Dynamics Simulator (Version 5): Technical Reference Guide*, U.S. Department of Commerce, National Institute of Standards and Technology, 2007.
 - [46] B.L. Yashwanth, B. Shotorban, S. Mahalingam, D.R. Weise, An investigation of the influence of heating modes on ignition and pyrolysis of woody wildland fuel, *Combustion Science and Technology*. 187 (2015) 780–796. <https://doi.org/10.1080/00102202.2014.973948>.
 - [47] T. Kan, V. Strezov, T.J. Evans, Lignocellulosic biomass pyrolysis: A review of product properties and effects of pyrolysis parameters, *Renewable and Sustainable Energy Reviews*. 57 (2016) 1126–1140. <https://doi.org/10.1016/j.rser.2015.12.185>.
 - [48] M.B. Pecha, M. Garcia-Perez, Pyrolysis of lignocellulosic biomass: oil, char, and gas, in: *Bioenergy*, Elsevier, 2020: pp. 581–619. <https://doi.org/10.1016/B978-0-12-815497-7.00029-4>.
 - [49] A.P. Dimitrakopoulos, Thermogravimetric analysis of Mediterranean plant species, *Journal of Analytical and Applied Pyrolysis*. 60 (2001) 123–130. [https://doi.org/10.1016/S0165-2370\(00\)00164-9](https://doi.org/10.1016/S0165-2370(00)00164-9).
 - [50] W. Mell, A. Maranghides, R. McDermott, S.L. Manzello, Numerical simulation and experiments of burning douglas fir trees, *Combustion and Flame*. 156 (2009) 2023–2041. <https://doi.org/10.1016/j.combustflame.2009.06.015>.
 - [51] S.C. Ferguson, A. Dahale, B. Shotorban, S. Mahalingam, D.R. Weise, The role of moisture on

- combustion of pyrolysis gases in wildland fires, *Combustion Science and Technology*. 185 (2013) 435–453. <https://doi.org/10.1080/00102202.2012.726666>.
- [52] W.M. Jolly, A.M. Hadlow, K. Huguet, De-coupling seasonal changes in water content and dry matter to predict live conifer foliar moisture content, *International Journal of Wildland Fire*. 23 (2014) 480–489. <https://doi.org/10.1071/WF13127>.
- [53] A.M.S. Smith, W.T. Tinkham, D.P. Roy, L. Boschetti, R.L. Kremens, S.S. Kumar, A.M. Sparks, M.J. Falkowski, Quantification of fuel moisture effects on biomass consumed derived from fire radiative energy retrievals, *Geophysical Research Letters*. 40 (2013) 6298–6302. <https://doi.org/10.1002/2013GL058232>.
- [54] F. Shafizadeh, *Pyrolysis and Combustion of Cellulosic Materials*, in: *Advances in Carbohydrate Chemistry*, Elsevier, 1968: pp. 419–474. <http://linkinghub.elsevier.com/retrieve/pii/S0096533208601733> (accessed September 17, 2015).
- [55] H. Stiles, R. Kandiyoti, Secondary reactions of flash pyrolysis tars measured in a fluidized bed pyrolysis reactor with some novel design features, *Fuel*. 68 (1989) 275–282. [https://doi.org/10.1016/0016-2361\(89\)90087-2](https://doi.org/10.1016/0016-2361(89)90087-2).
- [56] C.A. Koufopoulos, A. Lucchesi, G. Maschio, Kinetic modelling of the pyrolysis of biomass and biomass components, *The Canadian Journal of Chemical Engineering*. 67 (1989) 75–84. <https://doi.org/10.1002/cjce.5450670111>.
- [57] K. Raveendran, A. Ganesh, K.C. Khilar, Pyrolysis characteristics of biomass and biomass components, *Fuel*. 75 (1996) 987–998. [https://doi.org/10.1016/0016-2361\(96\)00030-0](https://doi.org/10.1016/0016-2361(96)00030-0).
- [58] R.S. Miller, J. Bellan, A generalized biomass pyrolysis model based on superimposed cellulose, hemicellulose and lignin kinetics, *Combustion Science and Technology*. 126 (1997) 97–137. <https://doi.org/10.1080/00102209708935670>.
- [59] T.H. Fletcher, H.R. Pond, J. Webster, J. Wooters, L.L. Baxter, Prediction of tar and light gas during pyrolysis of black liquor and biomass, *Energy & Fuels*. 26 (2012) 3381–3387. <https://doi.org/10.1021/ef300574n>.
- [60] A.D. Lewis, T.H. Fletcher, Prediction of Sawdust Pyrolysis Yields from a Flat-Flame Burner Using the CPD Model, *Energy & Fuels*. 27 (2013) 942–953. <https://doi.org/10.1021/ef3018783>.
- [61] P.J. DiNenno, D. Drysdale, C.L. Beyler, W.D. Walton, R.L.P. Custer, J.R. Hall Jr., J.M. Watts Jr., eds., *SFPE handbook of fire protection engineering*, 3rd ed, National Fire Protection Association ; Society of Fire Protection Engineers, Quincy, MA : Bethesda, MD, 2002.
- [62] R.A. Susott, Effect of heating rate on char yield from forest fuels, USDA Forest Service, Intermountain Forest and Range Experiment Station, Ogden, UT, 1980. <https://ia800707.us.archive.org/15/items/effectofheatingr295suso/effectofheatingr295suso.pdf>.
- [63] M.-S. Safdari, M. Rahmati, E. Amini, J.E. Howarth, J.P. Berryhill, M. Dietenberger, D.R. Weise, T.H. Fletcher, Characterization of pyrolysis products from fast pyrolysis of live and dead vegetation native to the Southern United States, *Fuel*. 229 (2018) 151–166. <https://doi.org/10.1016/j.fuel.2018.04.166>.
- [64] F.J. Matt, M.A. Dietenberger, D.R. Weise, Summative and ultimate analysis of live leaves from southern U.S. forest plants for use in fire modeling, *Energy Fuels*. (2020) 4703–4720. <https://doi.org/10.1021/acs.energyfuels.9b04107>.
- [65] B.C. Bright, E.L. Loudermilk, S.M. Pokswinski, A.T. Hudak, J.J. O'Brien, Introducing close-range photogrammetry for characterizing forest understory plant diversity and surface fuel structure at fine scales, *Canadian Journal of Remote Sensing*. 42 (2016) 460–472. <https://doi.org/10.1080/07038992.2016.1229598>.
- [66] A.T. Hudak, A. Kato, B.C. Bright, E.L. Loudermilk, C. Hawley, J.C. Restaino, R.D. Ottmar, G.A. Prata, C. Cabo, S.J. Prichard, E.M. Rowell, D.R. Weise, Towards spatially explicit

- quantification of pre- and postfire fuels and fuel consumption from traditional and point cloud measurements, *Forest Science*. 66 (2020) 428–442. <https://doi.org/10.1093/forsci/fxz085>.
- [67] D.R. Weise, Fundamental measurements and modeling of prescribed fire behavior in the naturally heterogeneous fuel beds of southern pine forests - RC2640 Interim Technical Report, USDA Forest Service, Pacific Southwest Research Station, Albany, CA, 2018.
- [68] S.J. Prichard, E.C. Karau, R.D. Ottmar, M.C. Kennedy, J.B. Cronan, C.S. Wright, R.E. Keane, Evaluation of the CONSUME and FOFEM fuel consumption models in pine and mixed hardwood forests of the eastern United States, *Can. J. For. Res.* 44 (2014) 784–795. <https://doi.org/10.1139/cjfr-2013-0499>.
- [69] R.D. Ottmar, R.E. Vihnanek, Volume VI: Longleaf pine, pocosin, and marshgrass in the Southeast United States, National Wildfire Coordinating Group, National Interagency Fire Center, Boise, ID, 2000.
- [70] C.M. Hawley, E.L. Loudermilk, E.M. Rowell, S. Pokswinski, A novel approach to fuel biomass sampling for 3D fuel characterization, *MethodsX*. 5 (2018) 1597–1604. <https://doi.org/10.1016/j.mex.2018.11.006>.
- [71] R.E. Martin, L.S. Davis, Temperatures near the ground during prescribed burning, *Papers of the Michigan Academy of Science, Arts, and Letters*. 46 (1961) 239–249.
- [72] B.W. Butler, J. Cohen, D.J. Latham, R.D. Schuette, P. Sopko, K.S. Shannon, D. Jimenez, L.S. Bradshaw, Measurements of radiant emissive power and temperatures in crown fires, *Canadian Journal of Forest Research*. 34 (2004) 1577–1587. <https://doi.org/10.1139/x04-060>.
- [73] B. Butler, C. Teske, D. Jimenez, J. O'Brien, P. Sopko, C. Wold, M. Vosburgh, B. Hornsby, E. Loudermilk, Observations of energy transport and rate of spreads from low-intensity fires in longleaf pine habitat – RxCADRE 2012, *International Journal of Wildland Fire*. 25 (2016) 76–89. <https://doi.org/10.1071/WF14154>.
- [74] W. Tachajapong, J. Lozano, S. Mahalingam, X. Zhou, D.R. Weise, An investigation of crown fuel bulk density effects on the dynamics of crown fire initiation in shrublands, *Combustion Science and Technology*. 180 (2008) 593–615. <https://doi.org/10.1080/00102200701838800>.
- [75] C. Huggett, Heating rates in fire experiments, *Journal of Fire Sciences*. 2 (1984) 257–259. <https://doi.org/10.1177/073490418400200401>.
- [76] J.D. Cohen, Fuel particle heat exchange during wildland fire spread, PhD Thesis, University of Idaho, 2015.
- [77] M.A. Finney, J.D. Cohen, J.M. Forthofer, S.S. McAllister, M.J. Gollner, D.J. Gorham, K. Saito, N.K. Akafuah, B.A. Adam, J.D. English, Role of buoyant flame dynamics in wildfire spread, *Proceedings of the National Academy of Sciences*. (2015) 201504498. <https://doi.org/10.1073/pnas.1504498112>.
- [78] B. Moghtaderi, The state-of-the-art in pyrolysis modelling of lignocellulosic solid fuels, *Fire Mater.* 30 (2006) 1–34. <https://doi.org/10.1002/fam.891>.
- [79] J.D. Engstrom, J.K. Butler, S.G. Smith, L.L. Baxter, T.H. Fletcher, D.R. Weise, Ignition behavior of live California chaparral leaves, *Combustion Science and Technology*. 176 (2004) 1577–1591. <https://doi.org/10.1080/00102200490474278>.
- [80] D.R. Prince, T.H. Fletcher, Differences in burning behavior of live and dead leaves - part 1: measurements, *Combustion Science and Technology*. 186 (2014) 1844–1857. <https://doi.org/10.1080/00102202.2014.923412>.
- [81] T.H. Fletcher, R. Gillis, J. Adams, T. Hall, C.L. Mayne, M.S. Solum, R.J. Pugmire, Characterization of macromolecular structure elements from a Green River oil shale, II. Characterization of pyrolysis products by ¹³C NMR, GC/MS, and FTIR, *Energy & Fuels*. 28 (2014) 2959–2970. <https://doi.org/10.1021/ef500095j>.
- [82] J.L. Hillier, T.H. Fletcher, M.S. Solum, R.J. Pugmire, Characterization of macromolecular structure of pyrolysis products from a Colorado Green River oil shale, *Industrial &*

- Engineering Chemistry Research. 52 (2013) 15522–15532. <https://doi.org/10.1021/ie402070s>.
- [83] E. Amini, M.-S. Safdari, J.T. DeYoung, D.R. Weise, T.H. Fletcher, Characterization of pyrolysis products from slow pyrolysis of live and dead vegetation native to the southern United States, *Fuel*. 235 (2019) 1475–1491. <https://doi.org/10.1016/j.fuel.2018.08.112>.
- [84] V. Gold, ed., *The IUPAC Compendium of Chemical Terminology: The Gold Book*, 4th ed., International Union of Pure and Applied Chemistry (IUPAC), Research Triangle Park, NC, 2019. <https://doi.org/10.1351/goldbook>.
- [85] D.W.T. Griffith, MALT5 User guide, Version 5.5.9, 2016.
- [86] D.W.T. Griffith, Synthetic calibration and quantitative analysis of gas-phase FT-IR spectra, *Appl. Spectrosc.* 50 (1996) 59–70.
- [87] T.J. Johnson, T. Masiello, S.W. Sharpe, The quantitative infrared and NIR spectrum of CH₂I₂ vapor: vibrational assignments and potential for atmospheric monitoring, *Atmos. Chem. Phys.* 6 (2006) 2581–2591. <https://doi.org/10.5194/acp-6-2581-2006>.
- [88] T.J. Johnson, R.L. Sams, S.D. Burton, T.A. Blake, Absolute integrated intensities of vapor-phase hydrogen peroxide (H₂O₂) in the mid-infrared at atmospheric pressure, *Anal Bioanal Chem.* 395 (2009) 377–386. <https://doi.org/10.1007/s00216-009-2805-x>.
- [89] R. Lindenmaier, N.K. Scharko, R.G. Tonkyn, K.T. Nguyen, S.D. Williams, T.J. Johnson, Improved assignments of the vibrational fundamental modes of *ortho*-, *meta*-, and *para*-xylene using gas- and liquid-phase infrared and Raman spectra combined with *ab initio* calculations: quantitative gas-phase infrared spectra for detection, *Journal of Molecular Structure*. 1149 (2017) 332–351. <https://doi.org/10.1016/j.molstruc.2017.07.053>.
- [90] L.T.M. Profeta, R.L. Sams, T.J. Johnson, S.D. Williams, Quantitative infrared intensity studies of vapor-phase glyoxal, methylglyoxal, and 2,3-butanedione (diacetyl) with vibrational assignments, *The Journal of Physical Chemistry A*. 115 (2011) 9886–9900. <https://doi.org/10.1021/jp204532x>.
- [91] S.W. Sharpe, T.J. Johnson, R.L. Sams, P.M. Chu, G.C. Rhoderick, P.A. Johnson, Gas-phase databases for quantitative infrared spectroscopy, *Appl. Spectrosc.* 58 (2004) 1452–1461.
- [92] I.E. Gordon, L.S. Rothman, C. Hill, R.V. Kochanov, Y. Tan, P.F. Bernath, M. Birk, V. Boudon, A. Campargue, K.V. Chance, B.J. Drouin, J.-M. Flaud, R.R. Gamache, J.T. Hodges, D. Jacquemart, V.I. Perevalov, A. Perrin, K.P. Shine, M.-A.H. Smith, J. Tennyson, G.C. Toon, H. Tran, V.G. Tyuterev, A. Barbe, A.G. Császár, V.M. Devi, T. Furtenbacher, J.J. Harrison, J.-M. Hartmann, A. Jolly, T.J. Johnson, T. Karman, I. Kleiner, A.A. Kyuberis, J. Loos, O.M. Lyulin, S.T. Massie, S.N. Mikhailenko, N. Moazzen-Ahmadi, H.S.P. Müller, O.V. Naumenko, A.V. Nikitin, O.L. Polyansky, M. Rey, M. Rotger, S.W. Sharpe, K. Sung, E. Starikova, S.A. Tashkun, J.V. Auwera, G. Wagner, J. Wilzewski, P. Wcisło, S. Yu, E.J. Zak, The HITRAN2016 molecular spectroscopic database, *Journal of Quantitative Spectroscopy and Radiative Transfer*. 203 (2017) 3–69. <https://doi.org/10.1016/j.jqsrt.2017.06.038>.
- [93] R.J. Yokelson, D.W.T. Griffith, D.E. Ward, Open-path Fourier transform infrared studies of large-scale laboratory biomass fires, *Journal of Geophysical Research*. 101 (1996) 21067. <https://doi.org/10.1029/96JD01800>.
- [94] S.K. Akagi, I.R. Burling, A. Mendoza, T.J. Johnson, M. Cameron, D.W.T. Griffith, C. Paton-Walsh, D.R. Weise, J. Reardon, R.J. Yokelson, Field measurements of trace gases emitted by prescribed fires in southeastern US pine forests using an open-path FTIR system, *Atmospheric Chemistry and Physics*. 14 (2014) 199–215. <https://doi.org/10.5194/acp-14-199-2014>.
- [95] S.K. Akagi, R.J. Yokelson, I.R. Burling, S. Meinardi, I. Simpson, D.R. Blake, G.R. McMeeking, A. Sullivan, T. Lee, S. Kreidenweis, S. Urbanski, J. Reardon, D.W.T. Griffith, T.J. Johnson, D.R. Weise, Measurements of reactive trace gases and variable O₃ formation rates in some South Carolina biomass burning plumes, *Atmospheric Chemistry and Physics*. 13 (2013) 1141–1165. <https://doi.org/10.5194/acp-13-1141-2013>.

- [96] I.R. Burling, R.J. Yokelson, S.K. Akagi, S.P. Urbanski, C.E. Wold, D.W.T. Griffith, T.J. Johnson, J. Reardon, D.R. Weise, Airborne and ground-based measurements of the trace gases and particles emitted by prescribed fires in the United States, *Atmospheric Chemistry and Physics*. 11 (2011) 12197–12216. <https://doi.org/10.5194/acp-11-12197-2011>.
- [97] I.R. Burling, R.J. Yokelson, D.W.T. Griffith, T.J. Johnson, P. Veres, J.M. Roberts, C. Warneke, S.P. Urbanski, J. Reardon, D.R. Weise, W.M. Hao, J. de Gouw, Laboratory measurements of trace gas emissions from biomass burning of fuel types from the southeastern and southwestern United States, *Atmos. Chem. Phys.* 10 (2010) 11115–11130. <https://doi.org/10.5194/acp-10-11115-2010>.
- [98] T.J. Johnson, R.J. Yokelson, S.K. Akagi, I.R. Burling, D.R. Weise, S.P. Urbanski, C.E. Stockwell, J. Reardon, E.N. Lincoln, L.T.M. Profeta, and 13 others, Strategic Environmental Research and Development Program Final Report for RC-1649: Advanced chemical measurements of smoke from DoD-prescribed burns, Pacific Northwest National Laboratory, Richland, WA, 2014. <https://www.serdp-estcp.org/content/download/24314/252130/file/RC-1649-FR.pdf>.
- [99] T.J. Johnson, L.T.M. Profeta, R.L. Sams, D.W.T. Griffith, R.L. Yokelson, An infrared spectral database for detection of gases emitted by biomass burning, *Vibrational Spectroscopy*. 53 (2010) 97–102. <https://doi.org/10.1016/j.vibspec.2010.02.010>.
- [100] R. Lindenmaier, N.M. Tipton, R.L. Sams, C.S. Brauer, T.A. Blake, S.D. Williams, T.J. Johnson, Assignment of the fundamental modes of hydroxyacetone using gas-phase infrared, far-infrared, Raman and *ab initio* methods: band strengths for atmospheric measurements, *The Journal of Physical Chemistry A*. 120 (2016) 5993–6003. <https://doi.org/10.1021/acs.jpca.6b05045>.
- [101] R. Lindenmaier, S.D. Williams, R.L. Sams, T.J. Johnson, Quantitative infrared absorption spectra and vibrational assignments of crotonaldehyde and methyl vinyl ketone using gas-phase mid-infrared, far-infrared, and liquid Raman spectra: *s-cis* vs *s-trans* composition confirmed via temperature studies and *ab Initio* methods, *The Journal of Physical Chemistry A*. 121 (2017) 1195–1212. <https://doi.org/10.1021/acs.jpca.6b10872>.
- [102] D.E. Ward, L.F. Radke, Emissions measurement from vegetation fires: a comparative evaluation of methods and results, in: P.J. Crutzen, J.G. Goldammer (Eds.), *Fire in the Environment: The Ecological, Atmospheric, and Climatic Importance of Vegetation Fires: Report of the Dahlem Workshop, Held in Berlin, 15-20 March 1992*, John Wiley & Sons Ltd., 1993: pp. 53–76. http://www.fs.fed.us/rm/pubs_other/rmrs_1993_ward_d001.pdf.
- [103] D.E. Ward, H.B. Clements, R.M. Nelson Jr., Particulate matter emission factor modeling for fire in southeastern fuels, in: *Sixth Conference on Fire and Forest Meteorology*, American Meteorological Society, Seattle, WA, 1980: pp. 276–284.
- [104] D.E. Ward, W.M. Hao, Projections of emissions from burning of biomass for use in studies of global climate and atmospheric chemistry, in: *Air and Waste Management Association*, Vancouver, British Columbia, Canada, 1991: p. 19. <http://www.treesearch.fs.fed.us/pubs/43258>.
- [105] R.J. Yokelson, R. Susott, D.E. Ward, J. Reardon, D.W.T. Griffith, Emissions from smoldering combustion of biomass measured by open-path Fourier transform infrared spectroscopy, *J. Geophys. Res.-Atmos.* 102 (1997) 18865–18877. <https://doi.org/10.1029/97JD00852>.
- [106] D.R. Weise, J. Palarea-Albaladejo, T.J. Johnson, H. Jung, Analyzing wildland fire smoke emissions data using compositional data techniques, *J. Geophys. Res. Atmos.* 125 (2020) e2019JD032128. <https://doi.org/10.1029/2019JD032128>.
- [107] L. Mertz, Auxiliary computation for Fourier spectrometry, *Infrared Physics*. 7 (1967) 17–23. [https://doi.org/10.1016/0020-0891\(67\)90026-7](https://doi.org/10.1016/0020-0891(67)90026-7).
- [108] F.J. Harris, On the use of windows for harmonic analysis with the discrete Fourier transform,

- Proceedings of the IEEE. 66 (1978) 51–83. <https://doi.org/10.1109/PROC.1978.10837>.
- [109] A. Hugli, G. Villares, S. Blaser, H.C. Liu, J. Faist, Mid-infrared frequency comb based on a quantum cascade laser, *Nature*. 492 (2012) 229–233. <https://doi.org/10.1038/nature11620>.
 - [110] D.K.W. Wang, C.C. Austin, Determination of complex mixtures of volatile organic compounds in ambient air: canister methodology, *Anal Bioanal Chem*. 386 (2006) 1099–1120. <https://doi.org/10.1007/s00216-006-0466-6>.
 - [111] J.C. Evans, J.L. Huckaby, A.V. Mitroshkov, J.L. Julya, J.C. Hayes, J.A. Edwards, L.M. Sasaki, 32-week holding-time study of SUMMA polished canisters and triple sorbent traps used to sample organic constituents in radioactive waste tank vapor headspace, *Environ. Sci. Technol*. 32 (1998) 3410–3417. <https://doi.org/10.1021/es9803153>.
 - [112] W.A. McGlenny, J.D. Pleil, G.F. Evans, K.D. Oliver, M.W. Holdren, W.T. Winberry, Canister-Based Method for Monitoring Toxic VOCs in Ambient Air, *Journal of the Air & Waste Management Association*. 41 (1991) 1308–1318. <https://doi.org/10.1080/10473289.1991.10466924>.
 - [113] D.R. Weise, T.H. Fletcher, M.-S. Safdari, E. Amini, J. Palarea-Albaladejo, Effect of plant species, moisture content and heating mode on composition of pyrolysis products – a new approach using compositional data analysis, (2020).
 - [114] D.R. Weise, H. Jung, J. Palarea-Albaladejo, Compositional data analysis of smoke emissions from debris piles with low-density polyethylene, (2020).
 - [115] K.G. van den Boogaart, R. Tolosana-Delgado, *Analyzing compositional data with R*, Springer, Heidelberg, 2013.
 - [116] J.J. Egozcue, V. Pawlowsky-Glahn, Groups of parts and their balances in compositional data analysis, *Mathematical Geology*. 37 (2005) 795–828. <https://doi.org/10.1007/s11004-005-7381-9>.
 - [117] G. Mateu-Figueras, V. Pawlowsky-Glahn, J.J. Egozcue, The Principle of Working on Coordinates, in: V. Pawlowsky-Glahn, A. Buccianti (Eds.), *Compositional Data Analysis*, John Wiley & Sons, Ltd, Chichester, UK, 2011: pp. 31–42. <https://doi.org/10.1002/9781119976462.ch3>.
 - [118] V. Pawlowsky-Glahn, J.J. Egozcue, R. Tolosana-Delgado, *Modelling and analysis of compositional data*, Wiley, Chichester, West Sussex, U.K., 2015.
 - [119] F.A. Graybill, *Matrices with applications in statistics*, Duxbury, Belmont, 2002.
 - [120] J. Aitchison, *The statistical analysis of compositional data*, Chapman and Hall, London ; New York, 1986.
 - [121] P. Filzmoser, K. Hron, M. Templ, *Applied compositional data analysis: with worked examples in R*, Springer Berlin Heidelberg, New York, NY, 2018.
 - [122] V. Pawlowsky-Glahn, A. Buccianti, eds., *Compositional data analysis: theory and applications*, Wiley, Chichester, West Sussex, U.K., 2011.
 - [123] M.J. Greenacre, *Compositional data analysis in practice*, CRC Press, Taylor and Francis Group, Boca Raton, 2019.
 - [124] M.-S. Safdari, E. Amini, D.R. Weise, T.H. Fletcher, Heating rate and temperature effects on pyrolysis products from live wildland fuels, *Fuel*. 242 (2019) 295–304. <https://doi.org/10.1016/j.fuel.2019.01.040>.
 - [125] M.-S. Safdari, E. Amini, D.R. Weise, T.H. Fletcher, Comparison of pyrolysis of live wildland fuels heated by radiation vs. convection, *Fuel*. 268 (2020) 117342. <https://doi.org/10.1016/j.fuel.2020.117342>.
 - [126] D.R. Weise, T.H. Fletcher, M.-S. Safdari, E. Amini, J. Palarea-Albaladejo, Application of compositional data analysis to determine the effects of heating mode, moisture status and plant species on pyrolysates, *International Journal of Wildland Fire*. (2021) 22. <https://doi.org/10.1071/WF20126>.

- [127] J. Palarea-Albaladejo, J.A. Martín-Fernández, zCompositions — R package for multivariate imputation of left-censored data under a compositional approach, *Chemometrics and Intelligent Laboratory Systems*. 143 (2015) 85–96.
<https://doi.org/10.1016/j.chemolab.2015.02.019>.
- [128] J. Palarea-Albaladejo, J.A. Martín-Fernández, Values below detection limit in compositional chemical data, *Analytica Chimica Acta*. 764 (2013) 32–43.
<https://doi.org/10.1016/j.aca.2012.12.029>.
- [129] K. Pearson, Mathematical contributions to the theory of evolution.--on a form of spurious correlation which may arise when indices are used in the measurement of organs, *Proceedings of the Royal Society of London (1854-1905)*. 60 (1896) 489–498.
<https://doi.org/10.1098/rspl.1896.0076>.
- [130] R Core Team, R: A Language and Environment for Statistical Computing, R Foundation for Statistical Computing, Vienna, Austria, 2021. <https://www.R-project.org/>.
- [131] J.J. Egozcue, V. Pawłowsky-Glahn, G. Mateu-Figueras, C. Barceló-Vidal, Isometric logratio transformations for compositional data analysis, *Mathematical Geology*. 35 (2003) 279–300.
<https://doi.org/10.1023/A:1023818214614>.
- [132] Y. Benjamini, Y. Hochberg, Controlling the false discovery rate: a practical and powerful approach to multiple testing, *Journal of the Royal Statistical Society. Series B (Methodological)*. 57 (1995) 289–300.
- [133] X. Zhou, L. Sun, S. Mahalingam, D.R. Weise, Thermal particle image velocity estimation of fire plume flow, *Combustion Science and Technology*. 175 (2003) 1293–1316.
<https://doi.org/10.1080/00102200302376>.
- [134] J. Lozano, W. Tachajapong, D.R. Weise, S. Mahalingam, M. Princevac, Fluid dynamic structures in a fire environment observed in laboratory-scale experiments, *Combustion Science and Technology*. 182 (2010) 858–878. <https://doi.org/10.1080/00102200903401241>.
- [135] T. Maynard, M. Princevac, D.R. Weise, A study of the flow field surrounding interacting line fires, *Journal of Combustion*. 2016 (2016) 1–12. <https://doi.org/10.1155/2016/6927482>.
- [136] G. Meier, Computerized background-oriented schlieren, *Experiments in Fluids*. 33 (2002) 181–187. <https://doi.org/10.1007/s00348-002-0450-7>.
- [137] H. Richard, M. Raffel, Principle and applications of the background oriented schlieren (BOS) method, *Measurement Science and Technology*. 12 (2001) 1576–1585.
<https://doi.org/10.1088/0957-0233/12/9/325>.
- [138] M. Raffel, Background-oriented schlieren (BOS) techniques, *Experiments in Fluids*. 56 (2015). <https://doi.org/10.1007/s00348-015-1927-5>.
- [139] A. Aminfar, J. Cobian-Iñiguez, M. Ghasemian, N. Rosales Espitia, D.R. Weise, M. Princevac, Using background-oriented schlieren to visualize convection in a propagating wildland fire, *Combustion Science and Technology*. 192 (2020) 2259–2279.
<https://doi.org/10.1080/00102202.2019.1635122>.
- [140] J.S. Barrows, Fire Behavior in Northern Rocky Mountain Forests, Forest Service- Station Paper NO.29. (1951) 1–103.
- [141] N.P. Cheney, J.S. Gould, W.R. Catchpole, The influence of fuel, weather and fire shape variables on fire-spread in grasslands, *International Journal of Wildland Fire*. 3 (1993) 31–44.
<https://doi.org/10.1071/WF9930031>.
- [142] W.L. Fons, Analysis of fire spread in light fuels, *Journal of Agricultural Research*. (1946) 93–121.
- [143] P.A. Call, F.A. Albini, Aerial and Surface Fuel Consumption in Crown Fires, *International Journal of Wildland Fire*. 7 (1997) 259. <https://doi.org/10.1071/WF9970259>.
- [144] R. Linn, J. Reisner, J.J. Colman, J. Winterkamp, Studying wildfire behavior using FIRETEC, *International Journal of Wildland Fire*. 11 (2002) 233–246. <https://doi.org/10.1071/WF02007>.

- [145] W. Mell, M.A. Jenkins, J. Gould, P. Cheney, A physics-based approach to modelling grassland fires, *International Journal of Wildland Fire*. 16 (2007) 1–22. <https://doi.org/10.1071/WF06002>.
- [146] B.J. Stocks, T.J. Lynham, B.D. Lawson, M.E. Alexander, C.E.V. Wagner, R.S. McAlpine, D.E. Dubé, The Canadian Forest Fire Danger Rating System: An Overview, *The Forestry Chronicle*. 65 (1989) 450–457. <https://doi.org/10.5558/tfc65450-6>.
- [147] B. Butler, D. Jimenez, J. Forthofer, P. Sopko, K. Shannon, J. Reardon, In-situ characterization of wildland fire behavior, in: D.D. Wade, M.L. Robinson (Eds.), *Proceedings of 3rd Fire Behavior and Fuels Conference*, International Association of Wildland Fire, Birmingham, AL, 2010: p. 11. http://www.fs.fed.us/rm/pubs_other/rmrs_2010_butler_b006.pdf.
- [148] B.M. Pickett, C. Isackson, R. Wunder, T.H. Fletcher, B.W. Butler, D.R. Weise, Experimental measurements during combustion of moist individual foliage samples, *International Journal of Wildland Fire*. 19 (2010) 153–162. <https://doi.org/10.1071/WF07121>.
- [149] T.H. Fletcher, B.M. Pickett, S.G. Smith, G.S. Spittle, M.M. Woodhouse, E. Haake, D.R. Weise, Effects of moisture on ignition behavior of moist California chaparral and Utah leaves, *Combust. Sci. Technol.* 179 (2007) 1183–1203. <https://doi.org/10.1080/00102200601015574>.
- [150] B. Shotorban, B.L. Yashwanth, S. Mahalingam, D.J. Haring, An investigation of pyrolysis and ignition of moist leaf-like fuel subject to convective heating, *Combustion and Flame*. 190 (2018) 25–35. <https://doi.org/10.1016/j.combustflame.2017.11.008>.
- [151] C. Lautenberger, Gpyro- a generalized pyrolysis model for combustible solids, Reax Engineering, Berkeley, CA, 2014.
- [152] K. McGrattan, S. Hostikka, R. McDermott, J. Floyd, C. Weinschenk, K. Overholt, *Fire Dynamics Simulator: Technical Reference Guide Volume 1: Mathematical Model*, U.S. Department of Commerce, National Institute of Standards and Technology, 2013.
- [153] P.R. Borujerdi, B. Shotorban, S. Mahalingam, A computational study of burning of vertically oriented leaves with various fuel moisture contents by upward convective heating, *Fuel*. 276 (2020) 118030. <https://doi.org/10.1016/j.fuel.2020.118030>.
- [154] P.R. Borujerdi, B. Shotorban, Pyrolysis and combustion characteristics of leaf-like fuel under convection and radiation heating, *Combustion Science & Technology*. (In press) 43.
- [155] J.R. Gallacher, The influence of season, heating mode and slope angle on wildland fire behavior, Ph.D., Brigham Young University, 2016.
- [156] J.R. Gallacher, V. Lansinger, S. Hansen, D. Jack, D.R. Weise, T.H. Fletcher, Effects of season and heating mode on ignition and burning behavior of three species of live fuel measured in a flat-flame burner system, in: Pasadena, CA, 2014: p. 14.
- [157] D.K. Shen, M.X. Fang, Z.Y. Luo, K.F. Cen, Modeling pyrolysis of wet wood under external heat flux, *Fire Safety Journal*. 42 (2007) 210–217. <https://doi.org/10.1016/j.firesaf.2006.09.001>.
- [158] P.R. Borujerdi, B. Shotorban, S. Mahalingam, D.R. Weise, Influence of pyrolysis gas composition and reaction kinetics on leaf-scale fires, (2021).
- [159] J.W. Deardorff, Stratocumulus-capped mixed layers derived from a three-dimensional model, *Boundary-Layer Meteorol.* 18 (1980) 495–527. <https://doi.org/10.1007/BF00119502>.
- [160] S.B. Pope, *Turbulent flows*, Cambridge University Press, Cambridge ; New York, 2000.
- [161] M. Princevac, A. Aminfar, M. Ghasemian, Final Report for Agreement 16JV11272167026, University of California - Riverside, 2019.
- [162] Y. Qi, W.M. Jolly, P.E. Dennison, R.C. Kropp, Seasonal relationships between foliar moisture content, heat content and biochemistry of lodgepole pine and big sagebrush foliage, *International Journal of Wildland Fire*. 25 (2016) 574–578. <https://doi.org/10.1071/WF15156>.
- [163] C.R. Boardman, M.A. Dietenberger, D.R. Weise, Specific heat capacity of wildland foliar fuels to 434 °C, *Fuel*. 292 (2021) 120396. <https://doi.org/10.1016/j.fuel.2021.120396>.

- [164] M.A. Dietenberger, C.R. Boardman, B. Shotorban, W. Mell, D.R. Weise, Thermal degradation modeling of live vegetation for fire dynamic simulator. In: , 20 p, in: Proceedings, 2020 Spring Technical Meeting, Central States Section of the Combustion Institute, University of Alabama in Huntsville, AL, 2020: p. 20. <https://www.fs.usda.gov/treearch/pubs/60852>.
- [165] J.M. Varner, J.K. Hiers, R.D. Ottmar, D.R. Gordon, F.E. Putz, D.D. Wade, Overstory tree mortality resulting from reintroducing fire to long-unburned longleaf pine forests: the importance of duff moisture, *Can. J. For. Res.* 37 (2007) 1349–1358. <https://doi.org/10.1139/X06-315>.
- [166] W.H. McNab, M.B. Edwards Jr., W.A. Hough, Estimating fuel weights in slash pine-palmetto stands, *Forest Science.* 24 (1978) 345–358. <https://doi.org/10.1093/forestscience/24.3.345>.
- [167] B.M. Butler, J. Palarea-Albaladejo, K.D. Shepherd, K.M. Nyambura, E.K. Towett, A.M. Sila, S. Hillier, Mineral–nutrient relationships in African soils assessed using cluster analysis of X-ray powder diffraction patterns and compositional methods, *Geoderma.* 375 (2020) 114474. <https://doi.org/10.1016/j.geoderma.2020.114474>.
- [168] S.M. Haase, S.S. Sackett, Effects of prescribed fire in giant sequoia-mixed conifer stands in Sequoia and Kings Canyon National Parks, in: T.L. Pruden, L.A. Brennan (Eds.), *Tall Timbers Fire Ecology Conference Proceedings*, Tall Timbers Research Station, Tallahassee, FL, 1998: pp. 236–243. <https://www.fs.usda.gov/treearch/pubs/43412>.
- [169] S.S. Sackett, S.M. Haase, Two case histories for using prescribed fire to restore ponderosa pine ecosystems in northern Arizona, in: *Tall Timbers Fire Ecology Conference -- Fire In Ecosystem Management: Shifting the Paradigm from Suppression to Prescription*, 1998: pp. 380–389. <https://www.fs.usda.gov/treearch/pubs/23291>.
- [170] J.J. O’Brien, J. Kevin Hiers, R.J. Mitchell, J.M. Varner, K. Mordecai, Acute Physiological Stress and Mortality Following Fire in a Long-Unburned Longleaf Pine Ecosystem, *Fire Ecol.* 6 (2010) 1–12. <https://doi.org/10.4996/fireecology.0602001>.
- [171] M.S. Safdari, Characterization of Pyrolysis Products from Fast Pyrolysis of Live and Dead Vegetation, Dissertation, Brigham Young University, 2018.
- [172] R.K. Peet, D.J. Allard, Longleaf pine vegetation of the southern Atlantic and eastern Gulf Coast regions: a preliminary classification, in: S.M. Hermann (Ed.), *Proceedings of the Tall Timbers Fire Ecology Conference*, No. 18, *The Longleaf Pine Ecosystem: Ecology, Restoration and Management*, 1993: pp. 45–81. https://talltimbers.org/wp-content/uploads/2018/09/45-PeetandAllard1993_op.pdf.
- [173] T.E. Ostertag, K.M. Robertson, A comparison of native versus old-field vegetation in upland pinelands managed with frequent fire, south Georgia, USA, in: R.E. Masters, K.L.M. Galley (Eds.), *Proceedings of the 23rd Tall Timbers Fire Ecology Conference: Fire in Grassland & Shrubland Ecosystems*, Tall Timbers Research Station, Tallahassee, FL, 2007: pp. 109–120. <https://talltimbers.org/wp-content/uploads/2018/09/109-OstertagandRobertson2007.pdf>.
- [174] A. Signorell, DescTools: Tools for Descriptive Statistics, 2020. <https://cran.r-project.org/package=DescTools>.
- [175] E. Rowell, E.L. Loudermilk, C. Hawley, S. Pokswinski, C. Seielstad, Ll. Queen, J.J. O’Brien, A.T. Hudak, S. Goodrick, J.K. Hiers, Coupling terrestrial laser scanning with 3D fuel biomass sampling for advancing wildland fuels characterization, *Forest Ecology and Management.* 462 (2020) 117945. <https://doi.org/10.1016/j.foreco.2020.117945>.
- [176] S.J. Prichard, R. Keane, E. Rowell, A. Hudak, E.L. Loudermilk, D. Lutes, L. Chappell, B. Hornsby, J. Hall, R.D. Ottmar, *US Forest Service National Smoke Assessment: Fuels and Consumption*, (In review).
- [177] E. Amini, M.-S. Safdari, D.R. Weise, T.H. Fletcher, Pyrolysis kinetics of live and dead wildland vegetation from the southern United States, *Journal of Analytical and Applied Pyrolysis.* 142 (2019) 104613. <https://doi.org/10.1016/j.jaap.2019.05.002>.

- [178] A.C. Davison, D.V. Hinkley, *Bootstrap methods and their application*, Cambridge University Press, New York, NY, USA, 1997.
- [179] E. Amini, M.-S. Safdari, N. Johnson, D.R. Weise, T.H. Fletcher, Pyrolysis kinetics of wildland vegetation using model-fitting methods, *Journal of Analytical and Applied Pyrolysis*. (2021) 12. <https://doi.org/10.1016/j.jaap.2021.105167>.
- [180] W.L. Fons, H.B. Clements, P.M. George, Scale effects on propagation rate of laboratory crib fires, *Symposium (International) on Combustion*. 9 (1963) 860–866. [https://doi.org/10.1016/S0082-0784\(63\)80092-2](https://doi.org/10.1016/S0082-0784(63)80092-2).
- [181] E.B. Snyder, J.M. Hamaker, Needle characteristics of hybrids of some species of southern pine, *Silvae Genetica*. 27 (1978) 184–188.
- [182] M.E. Alexander, M.G. Cruz, Interdependencies between flame length and fireline intensity in predicting crown fire initiation and crown scorch height, *International Journal of Wildland Fire*. 21 (2011) 95–113. <https://doi.org/10.1071/WF11001>.
- [183] R.M. Nelson Jr., *Flame characteristics for fires in southern fuels*, USDA Forest Service, Southeastern Forest Experiment Station, Asheville, NC, 1980. http://www.srs.fs.fed.us/pubs/rp/rp_se205.pdf.
- [184] D. Wade, Thinning young loblolly pine stands with fire, *Int. J. Wildland Fire*. 3 (1993) 169. <https://doi.org/10.1071/WF9930169>.
- [185] C.A. Banach, A.M. Bradley, R.G. Tonkyn, O.N. Williams, J. Chong, D.R. Weise, T.L. Myers, T.J. Johnson, Dynamic infrared gas analysis from longleaf pine fuel beds burned in a wind tunnel: observation of phenol in pyrolysis and combustion phases, *Atmos. Meas. Tech*. 14 (2021) 2359–2376. <https://doi.org/10.5194/amt-14-2359-2021>.
- [186] A. Aminfar, *Application of computer vision to transport phenomena*, Ph.D., University of California, 2019.
- [187] A. Aminfar, M. Princevac, Final report: experimental measurements of convective heat flux ahead of fire., (2019).
- [188] M.A. Dietenberger, C.R. Boardman, D.R. Weise, New methods for pyrolysis and combustion properties of forest litter: enhanced cone calorimetry with longleaf pine needles, in: S.M. Hood, S. Drury, T. Steelman, R. Steffens (Eds.), *Proceedings of the Fire Continuum Conference*, USDA Forest Service Rocky Mountain Research Station, Ft. Collins, CO, 2020: pp. 72–83. <https://www.fs.usda.gov/treearch/pubs/60630>.
- [189] C. Di Blasi, Modeling chemical and physical processes of wood and biomass pyrolysis, *Progress in Energy and Combustion Science*. 34 (2008) 47–90. <https://doi.org/10.1016/j.pecs.2006.12.001>.
- [190] J. Aitchison, *A concise guide to compositional data analysis*, (2003). <http://ima.udg.edu/activitats/codawork03/>.
- [191] X. Zhou, S. Mahalingam, Evaluation of reduced mechanism for modeling combustion of pyrolysis gas in wildland fire, *Combustion Science and Technology*. 171 (2001) 39–70. <https://doi.org/10.1080/00102200108907858>.
- [192] C.K. Westbrook, F.L. Dryer, Simplified reaction mechanisms for the oxidation of hydrocarbon fuels in flames, *Combustion Science and Technology*. 27 (1981) 31–43. <https://doi.org/10.1080/00102208108946970>.
- [193] N.K. Scharko, A.M. Oeck, T.L. Myers, R.G. Tonkyn, C.A. Banach, S.P. Baker, E.N. Lincoln, J. Chong, B.M. Corcoran, G.M. Burke, R.D. Ottmar, J.C. Restaino, D.R. Weise, T.J. Johnson, Gas-phase pyrolysis products emitted by prescribed fires in pine forests with a shrub understory in the southeastern United States, *Atmos. Chem. Phys*. 19 (2019) 9681–9698. <https://doi.org/10.5194/acp-19-9681-2019>.
- [194] C.A. Banach, O.N. Williams, A.M. Bradley, R.G. Tonkyn, J. Chong, D.R. Weise, T.L. Myers, T.J. Johnson, *Dynamic Infrared Gas Analysis from Longleaf Pine Fuelbeds Burned in a*

- WindTunnel: Observation of Phenol in Pyrolysis and Combustion Phases, Gases/Laboratory Measurement/Data Processing and Information Retrieval, 2020. <https://doi.org/10.5194/amt-2020-332>.
- [195] N.L. Christensen, Vegetation of the Southeastern Coastal Plain, in: M.G. Barbour, W.D. Billings (Eds.), *North American Terrestrial Vegetation*, 2nd ed., Cambridge University Press, New York, NY, 2000: pp. 397–448.
 - [196] N.K. Scharko, A.M. Oeck, R.G. Tonkyn, S.P. Baker, E.N. Lincoln, J. Chong, B.G. Corcoran, G.M. Burke, D.R. Weise, T.L. Myers, T.J. Johnson, Identification of Gas-phase Pyrolysis Products in a Prescribed Fire: Seminal Detections Using Infrared Spectroscopy for Naphthalene, Methyl Nitrite, Allene, Acrolein and Acetaldehyde, (2018).
 - [197] M.C. Phillips, T.L. Myers, T.J. Johnson, D.R. Weise, In-situ measurement of pyrolysis and combustion gases from biomass burning using swept wavelength external cavity quantum cascade lasers, *Opt. Express*. 28 (2020) 8680. <https://doi.org/10.1364/OE.386072>.
 - [198] N.K. Scharko, A.M. Oeck, R.G. Tonkyn, S.P. Baker, E.N. Lincoln, J. Chong, B.M. Corcoran, G.M. Burke, D.R. Weise, T.L. Myers, C.A. Banach, D.W.T. Griffith, T.J. Johnson, Identification of gas-phase pyrolysis products in a prescribed fire: first detections using infrared spectroscopy for naphthalene, methyl nitrite, allene, acrolein and acetaldehyde, *Atmospheric Measurement Techniques*. 12 (2019) 763–776. <https://doi.org/10.5194/amt-12-763-2019>.
 - [199] A.R. Koss, K. Sekimoto, J.B. Gilman, V. Selimovic, M.M. Coggon, K.J. Zarzana, B. Yuan, B.M. Lerner, S.S. Brown, J.L. Jimenez, J. Krechmer, J.M. Roberts, C. Warneke, R.J. Yokelson, J. de Gouw, Non-methane organic gas emissions from biomass burning: identification, quantification, and emission factors from PTR-ToF during the FIREX 2016 laboratory experiment, *Atmos. Chem. Phys.* 18 (2018) 3299–3319. <https://doi.org/10.5194/acp-18-3299-2018>.
 - [200] R.J. Ferek, J.S. Reid, P.V. Hobbs, D.R. Blake, C. Liou, Emission factors of hydrocarbons, halocarbons, trace gases and particles from biomass burning in Brazil, *Journal of Geophysical Research: Atmospheres*. 103 (1998) 32107–32118. <https://doi.org/10.1029/98JD00692>.
 - [201] F. Brilli, B. Gioli, P. Ciccioli, D. Zona, F. Loreto, I.A. Janssens, R. Ceulemans, Proton Transfer Reaction Time-of-Flight Mass Spectrometric (PTR-TOF-MS) determination of volatile organic compounds (VOCs) emitted from a biomass fire developed under stable nocturnal conditions, *Atmospheric Environment*. 97 (2014) 54–67. <https://doi.org/10.1016/j.atmosenv.2014.08.007>.
 - [202] J.B. Gilman, B.M. Lerner, W.C. Kuster, P.D. Goldan, C. Warneke, P.R. Veres, J.M. Roberts, J.A. de Gouw, I.R. Burling, R.J. Yokelson, Biomass burning emissions and potential air quality impacts of volatile organic compounds and other trace gases from fuels common in the US, *Atmospheric Chemistry and Physics*. 15 (2015) 13915–13938. <https://doi.org/10.5194/acp-15-13915-2015>.
 - [203] K. Sekimoto, A.R. Koss, J.B. Gilman, V. Selimovic, M.M. Coggon, K.J. Zarzana, B. Yuan, B.M. Lerner, S.S. Brown, C. Warneke, R.J. Yokelson, J.M. Roberts, J. de Gouw, High- and low-temperature pyrolysis profiles describe volatile organic compound emissions from western US wildfire fuels, *Atmospheric Chemistry and Physics*. 18 (2018) 9263–9281. <https://doi.org/10.5194/acp-18-9263-2018>.
 - [204] E.B. Ledesma, N.D. Marsh, A.K. Sandrowitz, M.J. Wornat, An experimental study on the thermal decomposition of catechol, *Proceedings of the Combustion Institute*. 29 (2002) 2299–2306. [https://doi.org/10.1016/S1540-7489\(02\)80280-2](https://doi.org/10.1016/S1540-7489(02)80280-2).
 - [205] L. Fagbemi, L. Khezami, R. Capart, Pyrolysis products from different biomasses, *Applied Energy*. 69 (2001) 293–306. [https://doi.org/10.1016/S0306-2619\(01\)00013-7](https://doi.org/10.1016/S0306-2619(01)00013-7).
 - [206] D. Frankman, B.W. Webb, B.W. Butler, Influence of Absorption by Environmental Water

- Vapor on Radiation Transfer in WildLand Fires, *Combustion Science and Technology*. 180 (2008) 509–518. <https://doi.org/10.1080/00102200701741400>.
- [207] T.L. Clark, M.A. Jenkins, J.L. Coen, D.R. Packham, A coupled atmosphere-fire model: role of the convective Froude number and dynamic fingering at the fireline, *International Journal of Wildland Fire*. 6 (1996) 177–190. <https://doi.org/10.1071/WF9960177>.
- [208] A.M. Grishin, Mathematical modeling of forest fires and new methods of fighting them, Novosibirsk. “Nauka” Publisher. Translation from russian (1992) 1–450.
- [209] B. Porterie, S. Nicolas, J.L. Consalvi, J.C. Loraud, F. Giroud, C. Picard, MODELING THERMAL IMPACT OF WILDLAND FIRES ON STRUCTURES IN THE URBAN INTERFACE. PART 1: RADIATIVE AND CONVECTIVE COMPONENTS OF FLAMES REPRESENTATIVE OF VEGETATION FIRES, *Numerical Heat Transfer, Part A: Applications*. 47 (2005) 471–489. <https://doi.org/10.1080/10407780590891434>.
- [210] D. Frankman, B.W. Webb, B.W. Butler, D. Jimenez, J.M. Forthofer, P. Sopko, K.S. Shannon, J.K. Hiers, R.D. Ottmar, Measurements of convective and radiative heating in wildland fires, *International Journal of Wildland Fire*. 22 (2013) 157–167. <https://doi.org/10.1071/WF11097>.
- [211] W.F. Ferger, The nature and use of the harmonic mean, *Journal of the American Statistical Association*. 26 (1931) 36–40. <https://doi.org/10.1080/01621459.1931.10503148>.
- [212] F.M. Buckingham, The harmonic mean in forest mensuration, *The Forestry Chronicle*. 45 (1969) 104–106. <https://doi.org/10.5558/tfc45104-2>.
- [213] F.M. Fujioka, Estimating wildland fire rate of spread in a spatially nonuniform environment, *Forest Science*. 31 (1985) 21–29.
- [214] N.I. Fisher, Statistical analysis of circular data, Cambridge University Press, Cambridge, England, 1995.
- [215] R.M. Nelson Jr., Reaction times and burning rates for wind tunnel headfires, *International Journal of Wildland Fire*. 12 (2003) 195–211. <https://doi.org/10.1071/WF02041>.
- [216] B.M. Wotton, J.S. Gould, W.L. McCaw, N.P. Cheney, S.W. Taylor, Flame temperature and residence time of fires in dry eucalypt forest, *International Journal of Wildland Fire*. 21 (2012) 270. <https://doi.org/10.1071/WF10127>.
- [217] B. Butler, S. Quarles, C. Standohar-Alfano, M. Morrison, D. Jimenez, P. Sopko, C. Wold, L. Bradshaw, L. Atwood, J. Landon, J. O’Brien, B. Hornsby, N. Wagenbrenner, W. Page, Exploring fire response to high wind speeds: fire rate of spread, energy release and flame residence time from fires burned in pine needle beds under winds up to 27 ms⁻¹, *Int. J. Wildland Fire*. 29 (2020) 81. <https://doi.org/10.1071/WF18216>.
- [218] J.J. O’Brien, E.L. Loudermilk, B. Hornsby, A.T. Hudak, B.C. Bright, M.B. Dickinson, J.K. Hiers, C. Teske, R.D. Ottmar, High-resolution infrared thermography for capturing wildland fire behaviour: RxCADRE 2012, *Int. J. Wildland Fire*. 25 (2016) 62. <https://doi.org/10.1071/WF14165>.
- [219] D.R. Prince, Measurement and modeling of fire behavior in leaves and sparse shrubs, PhD Thesis, Brigham Young University, 2014. <http://scholarsarchive.byu.edu/etd/5545>.
- [220] P.R. Borujerdi, B. Shotorban, S. Mahalingam, D.R. Weise, Modeling of water evaporation from a shrinking moist biomass slab subject to heating: Arrhenius approach versus equilibrium approach, *International Journal of Heat and Mass Transfer*. 145 (2019) 118672. <https://doi.org/10.1016/j.ijheatmasstransfer.2019.118672>.
- [221] G.M. Byram, Forest fire behavior, in: K.P. Davis (Ed.), *Forest Fire : Control and Use*, 1st ed., McGraw-Hill, New York, NY, 1959: pp. 90–123.
- [222] R.K. Moore, D. Mann, F. Matt, M. Dietenberger, D. Weise, Characterization of fetterbush *Lyonia lucida* liquid extractions, USDA Forest Service, Forest Products Laboratory, Madison, WI, 2020. <https://www.fs.usda.gov/treesearch/pubs/61073>.
- [223] R.K. Moore, M.A. Dietenberger, D.H. Mann, P.K. Lebow, D.R. Weise, Utilizing two-

dimensional gas chromatography time of flight mass spectrometry (GCxGC TOFMS) to characterize volatile products from pyrolysis of living vegetation foliage, *Bioresources*. 17 (2022) 862–889.

Appendices:

Supporting Data and Analyses:

This project generated a large quantity of data and model simulations. The data will be archived in the Forest Service Research Data Archive. The data sets that will be included in the archive are described in Table 35. Modifications to computer code is available from the faculty at UA Huntsville (Shotorban) and UC Riverside (Princevac).

Table 35. Data sets created by SERDP project RC-2640 to be archived in the Forest Service Research Data Archive (<https://www.fs.usda.gov/rds/archive/>).

Data set name	Objective	Category	Originator	Measurements
Physical properties	0	data	Dietenberger	
	0	data	Fletcher	
Wind tunnel fuels	0	data	Weise	
Ft. Jackson fuel data	0	data	Hudak, Ottmar	
Pyrolysate composition – bench scale	1	data	Fletcher	
Pyrolysate composition – wind tunnel canister	1	data	Hao/Baker	
Pyrolysate composition – wind tunnel FTIR	1	data	Johnson/Myers	
Pyrolysate composition – Ft. Jackson canister	1	data	Hao/Baker	
Pyrolysate composition – Ft. Jackson FTIR	1	data	Johnson/Myers	
Flame gas composition - RFL		data	Hao/Baker/Johnson/Fletcher	measurements collected as additional data
Bench-scale heating, foliage temperatures	2	data	Fletcher	
Wind tunnel heat fluxes	2	data	Princevac/Weise	

Ft. Jackson heat fluxes	2	data	Butler/McAllister/Weise	
Ft. Jackson foliage temperatures	2	data	O'Brien	
Ft. Jackson fuel consumption	2	data	Hudak/Ottmar	

List of Scientific/Technical Publications:

Peer-reviewed journal articles

1. Aminfar, A., Cobian-Iñiguez, J., Ghasemian, M., Rosales, Espitia N.R., Weise, D.R., Princevac, M. 2019. Using Background-Oriented Schlieren to visualize convection in a propagating wildland fire. *Combustion Science and Technology* 1–21. doi:10.1080/00102202.2019.1635122
2. Amini, E., M.-S. Safdari, D.R. Weise, and T.H. Fletcher. 2019. Pyrolysis kinetics of live and dead wildland vegetation from the southern United States. *Journal of Analytical and Applied Pyrolysis*, 142:104613, 10.1016/j.jaap.2019.05.002
3. Amini, E., Safdari, M.-S., DeYoung, J.T., Weise, D.R., & Fletcher, T.H. 2019. Characterization of pyrolysis products from slow pyrolysis of live and dead vegetation native to the southern United States. *Fuel*, 235, 1475-1491, doi: 10.1016/j.fuel.2018.08.112
4. Amini, E., Safdari, M.-S., Johnson, N., Weise, D.R., Fletcher, T.H. 2021. Pyrolysis kinetics of wildland vegetation using model-fitting methods. *Journal of Analytical and Applied Pyrolysis*. doi: 10.1016/j.jaap.2021.105167
5. Banach, C.A., Williams, O.N., Bradley, A.M., Tonkyn, R.G., Chong, J., Weise, D.R., Myers, T.L., Johnson, T.J. 2021. Dynamic infrared gas analysis from longleaf pine fuelbeds burned in a wind tunnel: observation of phenol in pyrolysis and combustion phases, *Atmospheric Measurement Techniques*, 14, 2359-2376, doi: [10.5194/amt-2020-332](https://doi.org/10.5194/amt-2020-332)
6. Boardman, C.R., Dietenberger, M.A., Weise, D.R. 2021. Specific heat capacity of wildland foliar fuels to 434 °C, *Fuel*, 292, 120396. doi: 10.1016/j.fuel.2021.120396
7. Borujerdi, P.R., Shotorban, B. 2021. Pyrolysis and combustion characteristics of leaf-like fuel under convection and radiation heating, *Combustion Science and Technology*, doi: 10.1080/00102202.2021.1890055.
8. Borujerdi, P.R., Shotorban, B., Mahalingam, S. 2020. A computational study of burning of vertically oriented leaves with various fuel moisture contents by upward convective heating, *Fuel*, 276 (September): 118030. doi: [10.1016/j.fuel.2020.118030](https://doi.org/10.1016/j.fuel.2020.118030)
9. Borujerdi, P.M., Shotorban, B., Mahalingam, S., Weise, D.R. 2019. Modeling of water evaporation from a shrinking moist biomass slab subject to heating: Arrhenius approach versus equilibrium approach. *International Journal of Heat and Mass Transfer*, 145, 118672. doi: 10.1016/j.ijheatmasstransfer.2019.118672
10. Cobian-Iñiguez, J., Aminfar, A.H., Weise, D.R., Princevac, M. 2019. On the use of semi-empirical flame models for spreading chaparral crown fire. *Frontiers in Mechanical Engineering*, Vol. 5, Article 50, doi:10.3389/fmech.2019.00050

11. Gordon I.E., Rothman, L.S., Hill, C., Kochanov, R.V., Tan, Y., Bernath, P.F., Birk, M., et al. 2017. The HITRAN2016 Molecular Spectroscopic Database. *Journal of Quantitative Spectroscopy and Radiative Transfer*, 203,3-69. doi:10.1016/j.jqsrt.2017.06.038
12. Hudak, A.T., Kato, A., Bright, B.C., Loudermilk, E.L., Hawley, C., Restaino, J., Ottmar, R.D., Prata, G.A., Cabo, C., Prichard, S.J., Rowell, E.M., Weise, D.R. 2020. Towards spatially explicit quantification of pre- and post-fire fuels and fuel consumption from traditional and point cloud measurements. *Forest Science*, 66(4), 428-442, doi: 10.1093/forsci/fxz085
13. Johnson, T.J., Aker, P.M., Scharko, N.K., & Williams, S.D. 2018. Quantitative Infrared and Near-Infrared Gas-Phase Spectra for Pyridine: Absolute Intensities and Vibrational Assignments. *Journal of Quantitative Spectroscopy and Radiative Transfer*, 206 (February), 355–66, doi: 10.1016/j.jqsrt.2017.11.023
14. Kochanov R.V., I.E. Gordon, L.S. Rothman, K.P. Shine, K.P. Shine, S.W. Sharpe, and T.J. Johnson, et al. 2019. "Infrared absorption cross-sections in HITRAN2016 and beyond: Expansion for climate, environment, and atmospheric applications." *Journal of Quantitative Spectroscopy and Radiative Transfer* 230, doi:10.1016/J.JQSRT.2019.04.001
15. Lindenmaier, R., Scharko, N.K., Tonkyn, R.G., Nguyen, K.T., Williams, S.D., Johnson, T.J. 2017. Improved assignments of the vibrational fundamental modes of ortho -, meta -, and para -xylene using gas- and liquid-phase infrared and Raman spectra combined with *ab initio* calculations: quantitative gas-phase infrared spectra for detection. *Journal of Molecular Structure* 1149 (December):332–51, doi: [10.1016/j.molstruc.2017.07.053](https://doi.org/10.1016/j.molstruc.2017.07.053).
16. Lindenmaier, R., Tipton, N.M., Sams, R.L., Brauer, C.S., Blake, T.A., Williams, S.D., Johnson, T.J. 2016. Assignment of the fundamental modes of hydroxyacetone using gas-phase infrared, far-infrared, Raman and *ab initio* methods: band strengths for atmospheric measurements." *The Journal of Physical Chemistry A* 120 (30):5993–6003, doi: [10.1021/acs.jpca.6b05045](https://doi.org/10.1021/acs.jpca.6b05045).
17. Lindenmaier, R., Williams, S.D., Sams, R.L., Johnson, T.J. 2017. Quantitative infrared absorption spectra and vibrational assignments of crotonaldehyde and methyl vinyl ketone using gas-phase mid-infrared, far-infrared, and liquid Raman spectra: s-cis vs s-trans composition confirmed via temperature studies and *ab initio* methods." *The Journal of Physical Chemistry A* 121 (6):1195–1212, [10.1021/acs.jpca.6b10872](https://doi.org/10.1021/acs.jpca.6b10872).
18. Matt, F., Dietenberger, M.A., Weise, D.R. 2020. Summative and ultimate analysis of live leaves from southern U.S. forest plants for use in fire modeling. *Energy and Fuels*, 34:4703-4720. doi: 10.1021/acs.energyfuels.9b04107
19. Maynard, T., Princevac, M., Weise, D.R. 2016. A study of the flow field surrounding interacting line fires." *Journal of Combustion* 2016:1–12, doi: [10.1155/2016/6927482](https://doi.org/10.1155/2016/6927482).
20. Moore, R.K., Dietenberger, M.A., Mann, D.H., Lebow, P.K., Weise, D.R. 2022. Utilizing two-dimensional gas chromatography time of flight mass spectrometry (GCxGC ToFMS) to characterize volatile products from pyrolysis of living vegetation foliage. *BioResources* 17(1):862-889, doi: [10.15376/biores.17.1.862-889](https://doi.org/10.15376/biores.17.1.862-889).
21. Phillips, M.C., Myers, T.L., Johnson, T.J., Weise, D.R. In-situ measurement of pyrolysis and combustion products from biomass burning using swept external cavity quantum cascade lasers. *Optics Express*, 28:6. doi: 10.1364/OE.386072
22. Safdari, M.-S., Amini, E., Weise, D.R., Fletcher, T.H. 2020. Comparison of pyrolysis of live wildland fuels heated by radiation vs. convection. *Fuel*, 268, doi: 10.1016/j.fuel.2020.117342

23. Safdari, M.-S., E. Amini, D.R. Weise, and T.H. Fletcher. 2019. Heating rate and temperature effects on pyrolysis products from live wildland fuels. *Fuel*, 242:295–304, doi: 10.1016/j.fuel.2019.01.040
24. Safdari, M.-S., Rahmati, M., Amini, E., Howarth, J.E., Berryhill, J.P., Dietsberger, M., Weise, D.R., & Fletcher, T.H. (2018) Characterization of pyrolysis products from fast pyrolysis of live and dead vegetation native to the Southern United States. *Fuel* 229,151–166, doi: 10.1016/j.fuel.2018.04.166
25. Scharko, N.K., Oeck, A.M., Tonkyn, R.G., Baker, S.P., Lincoln, E.N., Chong, J., Corcoran, B.M., Burke, G.M., Weise, D.R., Myers, T.L., Banach, C.A., Johnson, T.J. 2019. Identification of gas-phase pyrolysis products in a prescribed fire: first detections using infrared spectroscopy for naphthalene, methyl nitrite, allene, acrolein and acetaldehyde. *Atmospheric Measurement Techniques* 12:763-776, doi: 10.5194/amt-12-763-2019
26. Scharko, N.K., Oeck, A.M., Myers, T.L., Tonkyn, R.G., Banach, C.A., Baker, S.P., Lincoln, E.N., Chong, J., Corcoran, B.M., Burke, G.M., Ottmar, R.D., Restaino, J.C., Weise, D.R., Johnson, T.J. 2019. Gas-phase pyrolysis products emitted by prescribed fires in pine forests with a shrub understory in the southeastern United States. *Atmospheric Chemistry and Physics*, 19: 9681-9698, doi: [10.5194/acp-19-9681-2019](https://doi.org/10.5194/acp-19-9681-2019).
27. Scharko, N. K., Oeck, A.M., Tonkyn, R.G., Baker, S.P., Lincoln, E.N., Chong, J., Corcoran, B.M., Burke, G.M., Weise, D.R., Myers, T.L., Banach, C.A., Johnson, T.J. 2018. Identification of gas-phase pyrolysis products in a prescribed fire: seminal detections using infrared spectroscopy for naphthalene, methyl nitrite, allene, acrolein and acetaldehyde, *Atmospheric Measurement Technique Discussions*. 31 p.
28. Scharko, N.K., Oeck, A.M., Myers, T.L., Tonkyn, R.G., Banach, C.A., Baker, S.P., Lincoln, E.N., Chong, J., Corcoran, B.M., Burke, G.M., Ottmar, R.D., Restaino, J.C., Weise, D.R., Johnson, T.J., 2019. Gas-phase pyrolysis products emitted by prescribed fires in pine forests with a shrub understory in the southeastern United States. *Atmospheric Chemistry and Physics Discussions* 2019, 1–46.
29. Shotorban, B., Yashwanth, B.L., Mahalingam, S., Haring, D.J. 2018. An investigation of pyrolysis and ignition of moist leaf-like fuel subject to convective heating. *Combustion and Flame* 190 (April):25–35, doi: [10.1016/j.combustflame.2017.11.008](https://doi.org/10.1016/j.combustflame.2017.11.008).
30. Weise, D.R., Fletcher, T.H., Cole, W., Mahalingam, S., Zhou, X., Sun, L., Li, J. (2018). Fire behavior in chaparral – evaluating flame models with laboratory data. *Combustion and Flame* 191, 500-512, 10.1016/j.combustflame.2018.02.012
31. Weise, D.R., Palarea-Albaladejo, J., Johnson, T.J., Jung, H. 2020. Analyzing fire smoke emissions data using compositional data techniques. *Journal of Geophysical Research–Atmospheres*, 125:6, doi: 10.1029/2019JD032128
32. Weise, David R., Jung, H., Palarea-Albaladejo, J., Cocker, D.R. 2020. Compositional data analysis of smoke emissions from debris piles with low-density polyethylene. *Journal of Air and Waste Management*, 70(8):834-845. doi: 10.1080/10962247.2020.1784309
33. Weise, D.R., Fletcher, T.H., Safdari, M.-S., Amini, E., Palarea-Albaladejo, J. 2021. Effect of plant species on composition of pyrolysis products. *International Journal of Wildland Fire*, 31(1), 24-45. doi: 10.1071/WF20126
34. Weise, D.R., Hao, W.M., Baker, S., Princevac, M., Aminfar, A.-H., Palarea-Albaladejo, J., Ottmar, R.D., Hudak, A.M., Restaino, J., O'Brien, J.J. Comparison of fire-produced gases from wind tunnel and small field experimental burns. 2022. *International Journal of Wildland*

Technical reports

1. Aminfar, AmirHessam. 2019. Application of Computer Vision to Transport Phenomena. Ph.D. dissertation, Department of Mechanical Engineering, University of California - Riverside, 175 p.
2. Amini, Elham. 2020 Characterization of Slow Pyrolysis Behavior of Live and Dead Vegetation. Ph.D. dissertation. Department of Chemical Engineering, Brigham Young University, Provo, UT. 203 p.
3. Borujerdi, Peyman Rahimi. Anticipated Summer 2021. Physics-based modeling of pyrolysis and combustion of live leaves in wildland fires. Ph.D. dissertation. Department of Mechanical Engineering, University of Alabama in Huntsville. 182 p.
4. Safdari, M.S. 2018. Characterization of pyrolysis products from fast pyrolysis of live and dead vegetation. Ph.D. dissertation. Department of Chemical Engineering, Brigham Young University. 176 p.
5. Moore, Roderiquita K.; Mann, Doreen; Matt, Frederick; Dietenberger, Mark; Weise, David. 2020. Characterization of fetterbush (*Lyonia lucida*) liquid extractions. Res. Note FPL-RN-0385. Madison, WI: U.S. Department of Agriculture, Forest Service, Forest Products Laboratory. 10 p.

Manuscripts under development or review

1. Borujerdi, P.R., Shotorban, B., Mahalingam, S., Weise, D.R. Influence of pyrolysis gas composition and reaction kinetics on leaf-scale fires (in review).
2. Herzog, M.M., Hudak, A.T., Weise, D.R., Bradley, A.M., Tonkyn, R.G., Banach, C.A., Myers, T.L., Bright, B.C., Batchelor, J., Kato, A., Johnson, T.J. LIDAR methods for spatial modeling of understory fuel distribution and quantification of fuel consumption in prescribed burns (in review).
3. Weise, D.R., Johnson, T.J., Myers, T.L., Hao, W.M., Baker, S., Palarea-Albaladejo, J. A comparison of two methods to measure pyrolysis gases in a wind tunnel and in prescribed burns. International Conference on Forest Fire Research ebook.
4. Weise, D.R., Johnson, T.J., Myers, T.L., Hao, W.M., Baker, S., Palarea-Albaladejo, J., Scharko, N., Bradley, A.M., Banach, C., Tonkyn, R.G. Comparing two methods to measure pyrolysis gases in a wind tunnel and in prescribed burns. (in review)
5. Weise, D.R., Fletcher, T.H., Johnson, T.J., Hao, W.M., Dietenberger, M., Princevac, M., Butler, B., McAllister, S., O'Brien, J.J., Loudermilk, E.L., Ottmar, R.D., Hudak, A.T., Kato, A., Shotorban, B., Mahalingam, S., Mell, W.E., Boardman, C.R., Myers, T.L., Baker, S.P., Bright, B.C., Restaino, J.C. Scaling bench-scale pyrolysis experiments to field scale. (in preparation).

Conference or symposium proceedings scientifically recognized and referenced.

1. Dietenberger, M.A., Boardman, C.R., Weise, D.R. 2020. New methods for pyrolysis and combustion properties of forest litter: enhanced cone calorimetry with longleaf pine needles. Pp. 72-83 In Hood, Sharon; Drury, Stacy; Steelman, Toddi; Steffens, Ron, tech. eds. The fire continuum—preparing for the future of wildland fire: Proceedings of the Fire Continuum Conference. 21-24 May 2018, Missoula, MT. Proc. RMRS-P-78. Fort Collins, CO: U.S.

Department of Agriculture, Forest Service, Rocky Mountain Research Station. 358 p.

2. Diitenberger, M.A., C.R. Boardman, B. Shotorban, W. Mell, and D.R. Weise. 2020. Thermal Degradation Modeling of Live Vegetation for Fire Dynamic Simulator. Spring Technical Meeting, Central States Section of the Combustion Institute, May 17-19, 2020, Huntsville, Alabama. 20 p.
3. Weise, D.R., Johnson, T.J., Hao WM., Princevac, M., Scharko, N., Oeck, A., Myers, T.L., Baker, S., Lincoln, E., Aminfar, A. 2018. Measurement of pyrolysis products from mixed fuel beds during fires in a wind tunnel. Pp. 534-541 In Viegas, D.X. (ed.) *Advances in Forest Fire Research 2018*, Imprensa da Universidade de Coimbra, doi: 10.14195/978-989-26-16-506_59.
4. Weise; D.R., Fletcher, T.H., Johnson, T.J., Hao, WM., Diitenberger, M., Princevac, M., Butler, B., McAllister, S., O'Brien, J., Loudermilk, L., Ottmar, R., Hudak, A., Kato, A., Shotorban, B., Mahalingam, S., Mell, W.E. 2018. A project to measure and model pyrolysis to improve prediction of prescribed fire behavior. Pp. 308-318 In Viegas, D.X. (ed.) *Advances in Forest Fire Research 2018*, Imprensa da Universidade de Coimbra, doi: 10.14195/978-989-26-16-506_33.
5. Fletcher, T.H., Safdari, M.-S., Amini, E., Weise, D.R. 2018. Bench-scale measurement of pyrolysis products from intact live fuels. Pp. 1223-1226 In Viegas, D.X. (ed.) *Advances in Forest Fire Research 2018*, Imprensa da Universidade de Coimbra, doi: 10.14195/978-989-26-16-506_143.

Conference or symposium abstracts

1. Safdari, M.-S., M. Rahmati, E. Amini, and T. H. Fletcher, "Analysis of Pyrolysis Products from Live Shrub Fuels," 10th National Combustion Institute Meeting, University of Maryland (April 23-26, 2017).
2. Weise, D., T. H. Fletcher, B. Shotorban, B. Butler, M. Princevac, T. J. Johnson, M. Diitenberger, W. Mell, R. Ottmar, A. Hudak, S. McAllister, W. M. Hao, J. O'Brien, S. Mahalingam, and J. Reardon, "Measuring and Modeling Pyrolysis to Improve Prediction of Prescribed Fire Behavior," poster presented at the 10th National Combustion Institute Meeting, University of Maryland (April 23-26, 2017). Also presented at 2nd International Smoke Symposium, Nov. 14-17, 2016, Long Beach, CA.
3. Weise, D.R.; Mell, W.E.; Zhou, X.; Mahalingam, S. 2017. Comparison of thermal decomposition models in chaparral fuels. 10th National Combustion Institute Meeting, University of Maryland (April 23-26, 2017).
4. Shotorban, B., Yashwanth, B. L., Mahalingam, S., Haring, D. J., and Rahimi Borujerdi, P. *, Pyrolysis and burning of leaf-like fuel by convective heating: A computational study. The 10th U.S. National Meeting on Combustion, College Park, Maryland, April 2017
5. Weise, D. R., T. H. Fletcher, S. Mahalingam, Z. Zhou, and L. Sun, "Fire Spread in Chaparral: Comparison of Data with Flame-Mass Loss Relationships," presented at the Eighth International Symposium on Scale Modeling (ISSM-8), Portland, Oregon (Sept 12-14, 2017).
6. Amini, E., M.-S. Safdari, M. Rahmati, J. Howarth, J. DeYoung, and T. H. Fletcher, "Pyrolysis of Live Vegetation at Slow Heating Rates," Western States Section of the Combustion Institute, University of Wyoming, Laramie, WY (October 2-3, 2017).
7. Safdari, M.-S., J. Howarth, M. Rahmati, and T. H. Fletcher, "Study of Pyrolysis Products of

- Live and Dead Shrub Fuels from the Forest in the Southeastern United States,” 2017 AIChE Annual Meeting, Minneapolis, MN (October 29-November 3, 2017).
8. Scharko, N. K., M-S. Safdari, T. O. Danby, J. Howarth, T. N. Beiswenger, D. R. Weise, T. L. Myers, T. H. Fletcher, and T. J. Johnson, “Laboratory Measurements of Gas Phase Pyrolysis Products from Southern Wildland Fuels using Infrared Spectroscopy,” American Geophysical Union Conference, New Orleans (December 11-15, 2017).
 9. Aminfar, AmirHessam; Princevac, Marko; Espitia, N. Rosales; Weise, David R. Visualization and Measurements of Convective Mass Flux Around Fire Using Background Oriented Schlieren. Oral presentation. 12th Fire and Forest Meteorology Symposium, May 15-18, 2018, Boise, ID
 10. Amini, E., J. Howarth, J. DeYoung, and T. H. Fletcher, “Tar and Gas Composition from Slow Pyrolysis of 15 Live and Dead Plant Species from the Southeastern United States,” presented at the Fire Continuum Conference, Missoula, MT (May 21-24, 2018).
 11. Safdari, M-S., J. P. Berryhill, and T. H. Fletcher, “Fast Pyrolysis of 15 Live and Dead Plant Species at Heating Rates Typical of Wildland Fires,” presented at the Fire Continuum Conference, Missoula, MT (May 21-24, 2018).
 12. Scharko, Nicole K., Ashley M. Oeck, Tyler O. Danby, Joey Chong, Bonni Corcoran, Gloria Burke, Bruce E. Bernacki, David R. Weise, Tanya L. Myers, and Timothy J. Johnson. Gas-phase products from the pyrolysis of southeastern fuels using infrared spectroscopy. Oral presentation. The Fire Continuum Conference, May 21-24, 2018, Missoula, MT
 13. Oeck, Ashley M. Nicole K. Scharko, Joey Chong, Bonni Corcoran, Gloria Burke, David R. Weise, Tanya L. Myers, Timothy J. Johnson. 2018. Gas phase pyrolysis products of southern wildland fuels via extractive infrared spectroscopy. Poster presentation. The Fire Continuum Conference, May 21-24, 2018, Missoula, MT
 14. Dietenberger, Mark A.; Boardman, Charles R.; Weise, David R. New Methods for Pyrolysis and Combustion Properties of Forest Litter: Enhanced Cone Calorimetry with Longleaf Pine Needles. Oral presentation. The Fire Continuum Conference, May 21-24, 2018, Missoula, MT
 15. Aminfar, AmirHessam; Princevac, Marko; Weise, David R. Application of Background Oriented Schlieren on Visualization and Measurements of Convective Mass Flux Around Fire. Oral presentation. The Fire Continuum Conference, May 21-24, 2018, Missoula, MT
 16. Aminfar, A. N. Davoodzadeh, D. R. Weise, G. Aguilar and M. Princevac. Application of Computer Vision in Multi-Scale Flow Visualization Using Granular Light Patterns. Oral presentation. Pacific Division of the American Association for the Advancement of Science 99th Annual meeting, June 12-15, 2018, California State Polytechnic University, Pomona, CA.
 17. Yang, H., T. H. Fletcher, Y. Li, L. Jin, S. Li, Y. Shang, H. Hu, “Modeling the Influence of Changes in Aliphatic Structure on Char Surface Area during Coal Pyrolysis,” presented at the 37th International Symposium on Combustion, Dublin, Ireland (July 29-August 3, 2018).
 18. Safdari, M-S., J. Berryhill, D. R. Weise, and T. H. Fletcher, “Bench-scale Measurement of Pyrolysis Products from Intact Live Fuels,” 2019 AIChE Annual Meeting, Pittsburgh, PA (November 10-15, 2018).
 19. Weise, D. R., T. H. Fletcher, T. J. Johnson, W. Hao, M. Dietenberger, M Princevac, B. Butler, S. McAllister, J. O'Brien, L. Loudermilk, R. Ottmar, A. Hudak, A. Kato, B.

Shotorban, S. Mahalingam, W. E. Mell, “A Project to Measure and Model Pyrolysis to Improve Prediction of Prescribed Fire Behavior,” 8th International Conference on Forest Fire Research, Coimbra, Portugal (November 10-16, 2018).

20. Fletcher, T. H., M-S. Safdari, E. Amini, and D. R. Weise, “Bench-scale measurement of pyrolysis products from intact live fuels,” 8th International Conference on Forest Fire Research, Coimbra, Portugal (November 10-16, 2018).
21. Aminfar, AmirHessam, David R. Weise, Marko Princevac. Flow Visualization of Fire Propagation in Mixed Vegetative Fuel Beds. 11th U.S. National Combustion meeting, Mar. 24-27, 2019, Pasadena, CA. Presentation 3C09
22. Rahimi Borujerdi, Peyman Babak Shotorban, Shankar Mahalingam, and David R. Weise. A comparative study of moisture evaporation models in the drying and pyrolysis of moist solid fuels. 11th U.S. National Combustion meeting, Mar. 24-27, 2019, Pasadena, CA. Presentation 3D02
23. Weise, David R. Timothy J. Johnson, Javier Palarea-Albaladejo, Heejung Jung. Predicting smoke emissions using a compositional linear trend. 11th U.S. National Combustion meeting, Mar. 24-27, 2019, Pasadena, CA. Presentation 1K06

6th Fire Behavior and Fuels Conference, Apr. 30-May 2, 2019, Albuquerque, NM

Special Session: Deep Dive – Measuring and modeling pyrolysis in longleaf pine fuel beds to improve fire behavior models – David Weise, Moderator (#24-31)

24. An overview of the SERDP RC-2640 study to measure and model pyrolysis in longleaf pine forests. David R. Weise
25. Kinetic study of slow pyrolysis of live and dead wildland fuels. Elham Amini, Mohammad-Saeed Safdari, David R. Weise, Thomas H. Fletcher
26. Heats for evaporation, capacity, and combustion of fresh leaves and their relationships to leaf composition and moisture content. Mark Dietenberger, Charles Boardman, David R. Weise
27. Fire monitoring using 3D data from drone based PhoDAR and Terrestrial Laser Scanner. A. Kato, A. Hudak, J. Batchelor, L.M. Moskal, David R. Weise
28. Application of Background Oriented Schlieren to flow visualization in live vegetative fuel beds. Amirhessam Aminfar, David R. Weise, Marko Princevac
29. Analytical kinetics solutions with derived parameters for moisture desorption, pyrolysis, and char combustion for fresh leaves relative to compositions and moisture content. Mark Dietenberger, Charles Boardman, Babak Shortoban, David R. Weise
30. Physics based modeling of moisture evaporation in living leaves. P. Rahimi Borujerdi, B. Shotorban, S. Mahalingam, David R. Weise
31. Numerical Modeling of Fire Spread across pine needle fuel beds. Masoud Ghasemian, Yubiao Huang, AmirHessam Aminfar, Marko Princevac, David R. Weise
32. Weise, D.R. A new way to analyze the composition of materials – application to wildland fire gases.
33. Weise, D.R., Ottmar, R.D. Appropriate analysis of wildland fuel composition.
34. Hudak, A.T., R. McCarley, P. Fekety, B. Bright, A. Kato, L. Loudermilk, E. Rowell, C. Silva, J. Restaino, S. Prichard, R. Ottmar and D. Weise. 2019. Quantifying biomass and biomass change at multiple scales from TLS and ALS. Invited seminar, Universiti Kebangsaan Malaysia, Kuala Lumpur, Malaysia, 1 Aug 2019. (oral presentation, published abstract)

35. Amini, E., M-S. Safdari, D. R. Weise, and T. H. Fletcher, "Pyrolysis Kinetics of Live and Dead Wildland Vegetation from the Southern United States," presented at the AIChE Annual Meeting, Orlando, FL (November 10-15, 2019).
36. Weise, D.R., Johnson, T.J., Palarea-Albaladejo, J., Jung, H. Poster presentation – A new way to predict emission factors – a compositional data approach, 8th International Fire Ecology and Management Congress, 18-22 Nov. 2019, Tucson, AZ
37. Weise, D.R. Oral presentation – A new way to predict emission factors – a compositional data approach, 3rd International Smoke Symposium, 21 Apr 2020 (virtual)
38. Weise, D.R., Fletcher, T.H., Safdari, M.-S., Amini, E., and Palarea-Albaladejo, J. Poster presentation - Effect of plant species on composition of pyrolysis products, 3rd International Smoke Symposium, 21 Apr 2020
39. Moore, R., Mann, D., Dietenberger, M.A., Weise, D.R. Characterization of fetter bush *Lyonia lucida* extracts. Poster presentation, 43rd International Symposium on Capillary Chromatography & the 16th GCxGC Symposium, 12-17 May 2019, Fort Worth, TX
40. Rahimi Borujerdi, P., Shotorban, B., and Mahalingam, S., "Comparison of two evaporation models for drying dynamics in a biomass slab," 2018 Princeton University Summer School on Combustion, Princeton, NJ, June 2018.
41. Shotorban, B., and Mahalingam, S., "Modeling the role of fuel moisture on ignition in thin fuels," The Fire Continuum Conference, Missoula, MT, May 2018.
42. Scharko N.K., S. Safdari, T.O. Danby, H. Joel, T.N. Beiswenger, D. Weise, and T.L. Myers, et al. "Laboratory Measurements of Gas Phase Pyrolysis Products from Southern Wildland Fuels using Infrared Spectroscopy." 2017 AGU Fall Meeting, Dec. 11-15, 2017, New Orleans, Louisiana.
43. Johnson T.J., R.L. Sams, M.D. Schneider, L.T. Profeta, S.W. Sharpe, I.R. Burling, and S. Akagi, et al. "A Quantitative Infrared Database for Trace Gas Detection: Applications to Prescribed-Fire Biomass Burns at Select US Military Bases." Brigham Young University, Provo, Utah. 01/26/2017.
44. Kochanov R.V., I.E. Gordon, L.S. Rothman, K.P. Shine, K.P. Shine, S.W. Sharpe, and T.J. Johnson, et al. "Absorption Cross-Sections in HITRAN2016: Major Database Update for Atmospheric, Industrial, and Climate Applications. 72nd International Symposium on Molecular Spectroscopy, June 19-23, 2017, Champaign, Illinois.
<https://dx.doi.org/10.15278/isms.2017.TJ10>
45. Scharko N.K., S. Safdari, T.O. Danby, J. Howarth, A.M. Oeck, G. Burke, and B. Corcoran, et al. "Laboratory and Wind Tunnel Measurements of Gas Phase Products from Southern Wildland Fuels using Infrared Spectroscopy." 01/26/2018, SERDP Project Meeting, Fort Jackson, South Carolina.
46. Scharko N.K., A.M. Oeck, T.O. Danby, J. Chong, B. Corcoran, G. Burke, and B.E. Bernacki, et al. "Gas-Phase Products from the Pyrolysis of Southeastern Fuels using Open-Path Infrared Spectroscopy." Fire Continuum Conference, 05/23/2018 Missoula, Montana.
47. Weise D., T.J. Johnson, W. Hao, M. Princevac, N.K. Scharko, A.M. Oeck, and T.L. Myers, et al. "Measurement of pyrolysis products from mixed fuel beds during fires in a wind tunnel." Poster presentation, 8th International Conference on Forest Fire Research, 11/13/2018, Coimbra, Portugal.

48. Oeck A.M., N.K. Scharko, T.O. Danby, J. Chong, B. Corcoran, G. Burke, and B.E. Bernacki, et al. "Wind Tunnel Measurements of Gas Phase Pyrolysis Products from Southern Wildland Fuels using Extractive Infrared Spectroscopy." 05/23/2018, Fire Continuum Conference, Missoula, Montana.
49. Johnson T.J., T.L. Myers, S. Sharpe, R.L. Sams, R.G. Tonkyn, M.S. Taubman, and J.C. Birnbaum, et al. "PNNL Databases for Atmospheric Monitoring." 15th International HITRAN Conference, 06/13/2018, Cambridge, Massachusetts.
50. Weise D., N.K. Scharko, T.O. Danby, A.M. Oeck, and T.J. Johnson. "RC-2640 Measuring and Modeling Pyrolysis to Improve Prediction of Prescribed Fire Behavior." Presented by Timothy J Johnson at SERDP (Strategic Environmental Research & Development Program) 11/28/2017. Annual Meeting, Wash, District Of Columbia. PNNL-SA-131014.
51. Gaspar C.L., O.N. Williams, E.G. Stephan, T.L. Myers, and T.J. Johnson.. "Generation of a Website to Host Infrared Spectral Data for Biomass Burn Analysis and Other Similar Events." 08/23/2018, High School End of Internship Symposium, EMSL Auditorium, PNNL, Richland, Washington
52. Scharko N.K., A.M. Oeck, R.G. Tonkyn, S. Baker, E.N. Lincoln, J. Chong, and B. Corcoran, et al.. "Infrared Spectroscopy for Detection of Gas-Phase Pyrolysis." American Geophysical Union (AGU) Fall Meeting 2018, 12/10/2018, Washington, DC.
53. Oeck A.M., N.K. Scharko, J. Chong, B. Corcoran, G. Burke, D. Weise, and T.L. Myers, et al. "Gas Phase Pyrolysis Products of Southern Wildland Fuels via Extractive Infrared Spectroscopy." 08/21/2018, Richland, Washington
54. Williams O.N. 08/10/2018. "Environmental Analysis of Forest Fires Using Spectroscopy: It's All Smoke and Mirrors" O.N. Williams at SRAP student final presentation, Richland, Washington.
55. Johnson T.J., N.K. Scharko, A.M. Oeck, R.G. Tonkyn, S. Baker, E.N. Lincoln, and J. Chong, et al. "IR Spectroscopic Detection of Pyrolysis Gases in Southeastern US Pine Forest Prescribed Burns." 12/12/2018, Washington, DC.
56. Williams O.N. "Requisite Spectral Resolution for Infrared Spectra: Studies on Room Temperature Liquids and Solids." High School Interns Symposium, 05/23/2019, Richland, WA.
57. Banach C.A., A.M. Oeck, R.G. Tonkyn, N.K. Scharko, B.P. Stephen, E.N. Lincoln, and J. Chong, et al. "Pyrolysis Products Emitted by Prescribed Fires in Longleaf Pine Forests in the Southeastern United States." Post Graduate Research Symposium, 08/14/2019, Richland WA.